Computational Heterogeneous Catalysis Applied to Steam Methane Reforming over Nickel and Nickel/Silver Catalysts

by

Donnie Wayne Blaylock

B.S., Chemical Engineering
Tennessee Technological University (2003)

Submitted to the Department of Chemical Engineering in Partial Fulfillment of the Requirements for the Degree of

DOCTOR OF PHILOSOPHY IN CHEMICAL ENGINEERING

at the

MASSACHUSETTS INSTITUTE OF TECHNOLOGY

February 2011

Signature of Author: _____
Department of Chemical Engineering
January 28, 2011

Certified by: _____
William H. Green
Professor of Chemical Engineering
Thesis Supervisor

Accepted by: _____
William M. Deen
Professor of Chemical Engineering
Chairman, Committee for Graduate Students

This page is intentionally left blank.

Computational Heterogeneous Catalysis Applied to Steam Methane Reforming over Nickel and Nickel/Silver Catalysts

by

Donnie Wayne Blaylock

Submitted to the Department of Chemical Engineering
on January 28, 2011 in partial fulfillment of the requirements for the degree
Doctor of Philosophy in Chemical Engineering

ABSTRACT

The steam methane reforming (SMR) reaction is the primary industrial means for producing hydrogen gas. As such, it is a critical support process for applications including petrochemical processing and ammonia synthesis. In addition, SMR could be an important component of future energy infrastructures as a means for producing hydrogen as an energy carrier for applications including fuel cells in automobiles and direct combustion for electricity generation. Nickel is the preferred SMR catalyst; however, the efficiency of SMR over nickel can be severely hindered by carbon formation, which leads to the deactivation or even destruction of the catalyst particles. Thus, there is significant interest in catalysts that inhibit carbon formation yet retain activity to SMR. In order to develop improved catalysts for SMR, a thorough understanding of the processes occurring on the nickel surface is needed.

In this thesis, computational heterogeneous catalysis is applied to investigate steam methane reforming over nickel (Ni) and silver-alloyed nickel (Ni/Ag) catalysts. Electronic structure calculations using density functional theory (DFT) are employed to develop thermochemical landscapes describing the relative stabilities of SMR intermediates on the catalyst surfaces. In addition, DFT calculations are used to obtain kinetic parameters that describe elementary surface reactions taking place during SMR. A detailed statistical thermodynamics framework is developed to allow for the calculation of enthalpies, entropies, and free energies of the surface species at the temperatures and pressures relevant to industrial SMR.

The data from the DFT calculations are used to build detailed *ab inito* microkinetic models of SMR over the multi-faceted nickel catalyst. The resulting microkinetic models are used to provide insight into the processes occurring on the catalyst surface through identifying the most important intermediate species and reactions occurring on the catalyst. The effects of alloying the nickel catalyst with silver are predicted through modeling the dissociative methane adsorption reaction on multiple facets of the Ni/Ag surface with varying concentrations of silver. In addition, DFT calculations are used to investigate carbon formation on the Ni and Ni/Ag catalyst surfaces, including relative stabilities of various carbon-containing intermediates and the effects of alloying the nickel surface with silver on carbon formation.

Thesis Supervisor: William H. Green
Title: Professor of Chemical Engineering

Dedication

For Lindsay.

Acknowledgements

First, I would like to thank my wife, Lindsay. She selflessly joined me in coming to Boston just days after our wedding in 2005 and has worked to make it home since. I admire her strength, dedication, and work ethic – all of which she has put to constant use in making the most of our time here. She has made many sacrifices to help me reach this goal, and I am forever grateful.

I would also like to acknowledge my family. My mother and father have provided me with shining examples of how one should approach life. Their positive outlooks, care for others, dedication to family, and commitment to doing every job well have set a high bar. I am thankful for the support structure they have provided me with during my years of school and for their good-wishes at every step along the way. Also, thanks for that Go Kart you built for me at the end of 5th grade – it may have stopped running and disappeared long ago, but the encouragement I got from the understanding that you fully supported my nerdish ways hasn't. I would also like to thank Ron, my sister, brother-in-law, and nieces for their encouragement through this process as well as my extended family (the Vehr and Lolli families) for all they have done for Lindsay and me.

I also have many things for which to acknowledge my thesis supervisor, Professor William H. Green. He has been an excellent advisor through this process and I am thankful that I have had the opportunity to learn from him. The passion and joviality with which he approaches his work along with his dedication to both aspects of the phrase "research community" will serve as a model for me as I start my professional career. Also, thank you to Professors Sylvia T. Ceyer, Jefferson W. Tester, and Bernhardt L. Trout for serving on my thesis committee. I am very thankful for the advice and mentorship you provided along the way and your work to make my thesis a better product. I would also like to acknowledge my collaborators on this project from NTNU in Trondheim, Norway, Professors De Chen and Anders Holmen, Dr. Hongmin Wang, and Anh Dam. It was a wonderful experience working with them and they provided much valuable insight with regard to experimental catalysis.

When I returned to graduate school after having worked for a few years in industry, I came with a sense that great groups are important to quality work, and if you can find the right group, it will make reaching your goals and achieving success a much more likely scenario. I found that in the Green Group. I am thankful to Bill for fostering the excellent atmosphere that is present in the group and to all of the group members for maintaining it. I had the pleasure of working closely with two very talented and dedicated post-docs during my tenure in the Green Group. Thank you to (now) Professors Greg Beran and Teppei

Ogura. Your ideas and hard work helped shape many aspects of this thesis and I owe a debt of gratitude to each of you for the successes of this project. Also, I would like to thank former group member Dr. Franklin Goldsmith for his many helpful discussions regarding my research. I would also like to acknowledge Dr. Ujjal Das for his assistance in learning how to use the VASP simulation code, David Couling for his many helpful discussions regarding the nature of gas-solid interactions, Mike Harper for being my go-to "what do you think about this?" guy, and Dr. Richard West for helpful discussions – usually over excellent tea/coffee. I would also like to acknowledge Barbara Balkwill for all that she does to make our research experience in the Green Group as smooth as possible and for being a friend along the way.

My acknowledgements would not be complete without recognizing the important role that my colleagues-turned-friends have had in shaping this experience into many great memories. Mike, Chris, and Jon – the friendships we forged in first-year have stayed strong and were so important, not only to me but also to Lindsay, in adjusting to our new life in Boston. Thank you for all the memories and all the helpful discussions, whether with regard to research or life. Our Thanksgiving parties on Lake Street will, of course, be a lasting memory, and a tradition that I would love to revive upon occasion in the future. Also, I would like to thank Ryan and Megan for all they did to add to our experience here in Boston. You may have not been here for first-year, but it didn't take long once you arrived for Lindsay and me to know that we had found two close friends. You each have added many great memories to our time here.

Finally, I would like to acknowledge the community that is MIT. I can't imagine a better place to have conducted my thesis research. We are provided with a tremendous research support structure, from equipment to facilities to the people that make them go. I am grateful for the many tremendous speakers, lectures, and professors that I have had the opportunity to interact with and learn from during my time here. I am grateful for the administration and support structure that helped us (Al, Gerry, Lily, Mike, Megan, et al.) turn an IAP course in science policy into the Science Policy Initiative, a student organization for those like me that have no formal education in policy, but have a strong interest in the intersection between science/technology and public policy. I am grateful for MIT resources like Bill Bonvillian, Director of the Washington Office, who is so selfless with his time and energy, tireless in his dedication to the MIT community, and is someone I look to as both a mentor and friend. I am grateful for all of the opportunities that MIT and its community have given me to explore my interest, both professional and personal.

Table of Contents

Table of Figures

Table of Tables

Chapter 1. Introduction

The roots of catalysis can be traced to the early days of civilization, when man began to engage in the noble task of alcohol production via fermentation. Study of the then unnamed phenomenon consisted only of limited observations of events not fully understood. Over time, additional applications of catalysis began to emerge, such as sulfuric acid production from sulfur and humid air in the presence of nitric acid during the Middle Ages and the later use of sulfuric acid to catalyze the conversion of alcohol into ether in 1552.[1] A principle tenet of catalysis – that the catalytic species is conserved through the reaction – was first presented by Fulhame in 1794 when she noted that water, acting as a catalyst in oxidation of carbon monoxide, was unaffected by the chemical reaction.[2] An early example of heterogeneous catalysis is the 1817 discovery by Humphry Davy of the reaction between oxygen and coal gas in contact with hot platinum and palladium wires, which may have be the first clear evidence that gases can react on a metal surface without the metal being altered chemically.[3] An effort was made in the 1830s by Jöns Jacob Berzelius to collect and classify these historical observations, and gave the phenomenon the name *catalysis*, from the Greek words *kata,* meaning "down," and *lyein,* meaning "loosen".[2, 3]

The application of industrial catalysts grew rapidly in the early 20th century following the discovery of the Haber-Bosch process for ammonia synthesis – a technology that quickly revolutionized agriculture through the mass production of fertilizer and set the stage for a world-wide population explosion.[4] The industrial application of catalysts has been growing steadily since that time, leading to the field of catalysis today, which is responsible for 85-90% of the products of the chemical industry with applications including fuels, commodity and fine chemicals, and pollution prevention.[5] The fundamental understanding of catalysis grew more slowly than its application. Langmuir-Hinshelwood kinetics were developed in the mid-1920s, providing the basis for mechanism development and kinetic analysis that became essentially the sole source of fundamental understanding of catalysis for several decades. Fundamental understanding of catalysis began to grow considerably with the introduction of spectroscopy, first with infrared spectroscopy in the 1950s and followed by a range of surface science techniques including XPS, LEED, HREELS, TEM, and by the late 20th century, STM. These techniques allow for catalyst characterization, including structure and composition, as well as for the identification of adsorbed structures and intermediate species on the catalyst surface. However, a shortcoming of these techniques is that they are generally limited to low pressures and moderate temperatures, a parameter space in which catalyzed industrial reactions are not carried out. Though techniques are being developed

that can begin to probe catalyzed reactions at industrial operating conditions such as spectroscopy by sum frequency generation and high pressure/high temperature STM,[6] there still exists a pressure gap that limits our understanding of surface chemistry under the desired working conditions. Computational heterogeneous catalysis emerged in the late 20th century as a tool that can aid in bridging this gap.

The development of quantum theoretical methods has provided a better molecular-level understanding of the catalyst surface by allowing for the calculation of equilibrium structures, adsorption energies, and activation energies.[7] For catalyst surfaces, density functional theory (DFT) is currently the most widely-employed method for performing the quantum chemical calculations, balancing computational accuracy and computational expense. DFT provides a framework for calculating the ground state electron density and total energy through the solution of many one-electron time-independent Schrödinger equations at reduced computational expense. However, because catalytic systems consist of many atoms, including many-electron atoms such as transition metals, simplified models of the catalyst are employed to allow for quantum calculations at reasonable computational expense. Despite the complexity of catalytic systems and the simplifications made in modeling, there have been numerous examples of successful application of computational chemistry to model heterogeneous catalysis. For example, recent collaborative efforts combining DFT and experiments have led to a better understanding of ammonia synthesis over ruthenium catalysts and methanol decomposition on platinum.[8-10] While the accuracy of quantum chemical calculations may not yet be sufficient to consistently provide detailed quantitative information about reaction rates, theoretical studies can provide valuable information about the adsorption and reaction processes. Specifically, theoretical studies have proved useful for comparing systems and establishing trends among catalysts, which is valuable in the search for new catalysts with certain desired properties.

In this thesis, computational heterogeneous catalysis is applied to study the steam methane reforming (SMR) reaction over nickel and nickel/silver catalysts. The SMR reaction, which is detailed in Chapter 2, involves the conversion of methane and steam to carbon monoxide and hydrogen (a product that is often referred to as synthesis gas). It is the primary means by which hydrogen is produced and is also important to the operation of solid-oxide fuel cells. Historically, nickel is the preferred SMR catalyst because of its reasonably high activity and affordability relative to noble metal catalysts.[11] However, nickel is susceptible to deactivation via carbon formation. Concerns over carbon formation motivate interest in new catalysts that inhibit carbon formation while retaining activity to the steam reforming reaction. To aid in the search for improved SMR catalysts, a detailed understanding of the important reactions and intermediates on the nickel surface is desired.

The computational methods for obtaining thermochemical properties in heterogeneous catalysis are presented in Chapter 3. Density Functional Theory, which is the basis of all electronic structure calculations applied in this work, and the software packages used to perform the calculations are discussed. A discussion of the models used to simulate heterogeneous catalysis is also included. The quantities obtained from the electronic structure calculations are at a zero-Kelvin electronic energy level. In Chapter 3, the equations used to transform these quantities into thermodynamic properties at relevant temperatures and pressures are developed, including a discussion of partition functions, enthalpies, entropies, and Gibbs free energies for adsorbed species. A framework for treating weakly adsorbed, mobile species vs. tightly-bound, localized surface species is also presented.

In Chapter 4, the partition functions developed in Chapter 3 are used to derive rate expressions and rate coefficients for the reactions important to heterogeneous catalysis, including: molecular adsorption and desorption, dissociative adsorption and associative desorption, unimolecular and bimolecular reactions involving adsorbed surface species, and inter-facet diffusion of an adsorbed surface species. The process of combining these rate expressions into a microkinetic model and integrating the model with Continuously-Stirred Tank Reactor and Plug Flow Reactor models is also discussed.

The methods developed in Chapter 3 and Chapter 4 are applied to investigate the SMR reaction over multiple model catalysts. In Chapter 5, an *ab initio* microkinetic model for steam methane reforming over a Ni(111) catalyst is presented.[12] The model's predictions are compared to available Ni(111) single-crystal data and the impact of the statistical thermodynamic approach developed in Chapter 3 on the results is discussed. In addition, flux and sensitivity analysis are applied to identify the primary reforming pathways and rate-limiting reactions on the Ni(111) surface. In Chapter 6, the microkinetic model presented in Chapter 5 is expanded to include the effects of the Ni(100) and Ni(211) surface facets in addition to the Ni(111) surface. Methods for estimating the fraction of each surface facet present on a multi-faceted catalyst nanoparticle are applied to develop a mean-field microkinetic model of a commercial catalyst particle. Flux and sensitivity analysis are once again applied to determine the primary reforming pathways and rate-limiting reactions and the results are compared to previously-published experimental data.

In Chapter 7, the steam methane reforming reaction is investigated on the silver-alloyed nickel surface. Multiple Ni/Ag surface alloy configurations are investigated to determine the relative stabilities of the alloyed facets. The dissociative methane adsorption reaction is studied in detail on the multi-faceted Ni/Ag surface at various total concentrations of silver on the catalyst surface, taking into account the

information learned from the alloy stability analysis. The results of this analysis are then compared to experimental data obtained from collaborators at the Norwegian University of Science and Technology. In addition, the thermochemical properties of selected species on the Ni/Ag(111) surface alloyed at 1/4 monolayer (ML) silver coverage are presented in Chapter 7 along with the kinetics of the key reactions identified via sensitivity analysis in previous chapters.

A computational investigation of carbon formation of Ni and Ni/Ag catalysts is presented in Chapter 8. Equilibrated gas and a dynamic SMR conversion models are generated to describe the driving force for carbon formation during steam methane reforming from thermodynamic arguments. The driving force for carbon formation is shown to be a function of temperature, pressure, and gas composition. The dynamic SMR conversion model is used to highlight the importance of understanding the competition between carbon-carbon coupling and carbon oxidation. Also in Chapter 8, several metrics are presented to describe the effect of alloying the nickel surface with silver on carbon formation and the competition between carbon-carbon coupling and carbon oxidation, including carbon stability at the step, barriers to gateway carbon formation reactions, and diffusion of key carbon-containing and oxygen-containing species. Finally, the thermochemistry and kinetics of selected carbon-containing intermediates on the Ni(111) surface are presented.

The final chapter of this thesis is dedicated to recommendations for future work in areas related to the topics discussed in the preceding chapters.

Chapter 2. The Steam Methane Reforming Reaction

2.1 Hydrogen Production through Steam Methane Reforming

The production of hydrogen has long been of interest due to its importance as a feedstock in the chemical industry for applications such as ammonia and methanol production as well for hydro-treatment in oil refineries.[13, 14] More recently, interest has also turned to consideration of hydrogen as a potential energy-carrier in future energy infrastructures, principally because of increasing awareness of the environmental and health impacts of carbon dioxide emissions.[15] Hydrogen serves as an energy transport mechanism, obtained from direct energy sources and oxidized as a carbon-free energy source at the point of use. As such, hydrogen is recognized as a potential fuel for applications ranging from fuel cells in automobiles to direct combustion for electricity generation.[16, 17] The use of hydrogen for the production of ammonia is also relevant to low-carbon energy sources as it is an important component in fertilizer production that could be required for future biofuel markets.

Hydrogen is generally produced through either 1) reforming or gasification of fossil fuels and biomass or 2) electrolysis of water.[13] Reforming of fossil fuels is responsible for most of the hydrogen produced worldwide.[11, 18] In fact, steam methane reforming (SMR) accounts for 95% of the hydrogen produced in the United States.[19] Steam methane reforming (Equation 1) with water-gas shift (Equation 2) proceeds via:

$$CH_4(g) + H_2O(g) \overset{\text{catalyst}}{\rightleftarrows} CO(g) + 3H_2(g) \qquad \Delta H_{298}=206 \text{ kJ/mol} \qquad (R1)$$

$$CO(g) + H_2O(g) \overset{\text{catalyst}}{\rightleftarrows} CO_2(g) + H_2(g) \qquad \Delta H_{298}=-41 \text{ kJ/mol} \qquad (R2)$$

Industrial steam methane reforming is typically carried out under temperatures ranging from 450-950 °C in ~10 m tubular reformers.[14] Researchers are investigating means of *in situ* separation of the carbon dioxide and hydrogen products via membrane reformers.[20-22] One product stream is composed of carbon dioxide and water (and trace gases), from which the water can be condensed producing a relatively pure carbon dioxide stream. The second product stream contains either pure hydrogen or a mixture of hydrogen, nitrogen and water, depending on the operation of the reformer and the intended use of the hydrogen. Hydrogen membrane reformers operate under Le Chatelier's principle, increasing the conversion of methane through the removal of hydrogen. Because the steam reforming reaction is

strongly endothermic and water-gas shift reaction is exothermic, maximum conversion in standard reformers is achieved through the application of two reformers in series, operating at different temperatures. However, it has been shown that a separate water-gas shift reactor may not be necessary when a membrane reactor is employed because the removal of hydrogen through the membrane may lead to sufficiently high CH_4 and CO conversions.[23]

When coupled with carbon sequestration techniques, hydrogen production via SMR may become an important step in reducing global carbon dioxide emissions while meeting energy demands. Combining steam methane reforming with value-added sequestration techniques such as enhanced gas recovery (where the carbon dioxide gas is pumped back into gas wells to increase natural gas production) may also contribute to the economic viability of hydrogen as a fuel.[16] In addition to traditional hydrogen production, the kinetics of the SMR and WGS reactions are an active area of research with regard to internal reforming in solid oxide fuel cells.[24-26]

2.2 Steam Methane Reforming Catalysts

In general, the performance of a catalyst is measured by its activity and selectivity. While activity pertains to the rate of turnover of all species on the surface, selectivity is related to the rate of production of one species compared to another. For example, a potential byproduct of SMR could be formaldehyde, a molecule that contains hydrogen and thus limits the amount of hydrogen gas produced by the reforming reaction.[27] Therefore, catalysts that exhibit high reforming activity with selectivity towards carbon monoxide or carbon dioxide products are desired in hydrogen production applications.

Catalytic metals with reasonably high activity for SMR include nickel and noble metals such as ruthenium, rhodium, palladium, iridium, and platinum.[28] Experiments by Kikuchi, et al. of SMR at atmospheric pressure and 600 °C found that the activity of SMR catalysts follows the order Rh,Ru > Ni > Ir > Pd ~ Pt.[29] Subsequent experiments by Rostrup-Nielsen, et al. of SMR on MgO supports at atmospheric pressure and 550 °C produced a similar reactivity trend of Ru, Rh > Ir > Ni > Pt, Pd.[30] Qin, et al. observed a trend of Ru > Rh > Ir > Pt > Pd for steam and CO_2 methane reforming on MgO supports at atmospheric pressure and a temperature range of 600-900 °C.[31] These observed trends have recently been supported by theoretical calculations reported by Jones, et al. where the reactivity trend Ru > Rh > Ni > Ir > Pt ~ Pd was found.[32] These calculations and experiments suggest a general trend for SMR catalysts of Ru and Rh being the most active, Ni and Ir having intermediate activity, and Pt and Pd having lower activity. Interestingly, recent experiments by Wei and Iglesia produce results in contradiction to

these previously observed and computed reactivity trends. Over a temperature range of 600-800 °C, Wei and Iglesia find the reactivity trend to be Pt[33] > Ir[34, 35] > Rh[36] > Ru[37], Ni[38]. Although it is not the most active catalyst for SMR, nickel is the preferred industrial catalyst for steam methane reforming because of its reasonably high activity, cost and availability.[14] However, nickel is susceptible to deactivation via carbon formation.[39, 40] While noble metals such as rhodium and ruthenium do not present the carbon deactivation concerns of nickel, they are rare and expensive metals.[31] Thus, there is interest in developing novel SMR catalysts that are similar in activity, cost and availability to nickel, but show increased inhibition to carbon formation.

For a given catalyst, the absolute activity is generally proportional to the available metal surface area of the dispersed metal. In addition, it is also known that the structure of the available surface area is an important contributor to catalyst activity. For example, the close-packed (111) nickel surface is less active to steam reforming than is the more open (110) surface.[41] It has been suggested that step sites are the main active sites in nickel-catalyzed steam reforming. Theoretical work has shown that the intermediate reaction barriers and thermodynamics appear to favor step sites, which has been supported by experiment.[39, 42] For example, steam reforming of ethane has been shown to correlate with step density of the catalyst (measured by N_2 adsorption), as shown in Figure 2-1.[43, 44] The inset shows that the correlation between activity and catalyst surface area is much less satisfactory than the step density correlation. The catalyst support can also play a role in activity through dispersion of the metal particles, mitigation of catalyst sintering, alteration of the catalyst's electronic properties, and potential participation in the surface reactions.

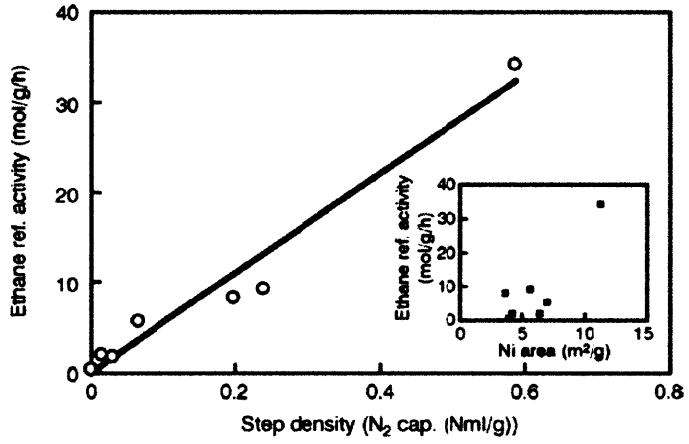

Figure 2-1. Surface Structure and Catalyst Activity: Ethane Reforming over Ni/Al_2O_3[44]

2.3 Kinetics of Steam Methane Reforming over Nickel Catalysts

Early work on the kinetics of nickel-catalyzed SMR focused on the development of a macroscopic, non-elementary rate law to describe the rate of methane consumption. Langmuir-Hinshelwood kinetics and the concept of a rate determining step (RDS) was applied in the work of Bodrov, et al.[45] The authors assumed that the dissociation of CH_4 to adsorbed CH_2 and H_2 gas was the RDS based on observations that the rate of reaction showed first order dependence on the partial pressure of methane in the gas phase. The rate law was derived for conditions near 900°C and 1 atm.

Later work by Khomenko, et al. also sought a non-elementary rate equation to describe SMR kinetics; however, this work avoided discussion of a rate determining step.[46] Instead, the authors applied the quasi steady-state approximation (QSSA) in the form of the Temkin identity to eliminate some terms and an assumed low surface coverage to eliminate others. The rate equation found in that work included temperature dependence (with constants regressed from experimental data over a range of 450-700°C). The following rate equation for the disappearance of methane was obtained:

$$r_{CH_4} = \frac{k\, p_{CH_4} p_{H_2O}\left[1-\frac{Q_R}{K_P}\right]}{f\left(p_{H_2O}, p_{H_2}\right)\left[1+K_W\frac{p_{H_2O}}{p_{H_2}}\right]}. \qquad \text{[Equation 2-1]}$$

In this equation, Q_R is the reaction quotient, K_P is the equilibrium constant of the methane to carbon monoxide steam reforming reaction, and K_W is the equilibrium constant of the water-gas shift reaction. The function $f(p_{H2O},p_{H2})$ is a polynomial in p_{H2O} and p_{H2} that contains three temperature-dependent constants. The rate equation was also shown to agree with the form of the results of Bodrov, et al. in the limit of "near-irreversibility" of SMR reaction at high temperatures. However, when tested at high pressure, the rate constant, k, in Equation 2-1 was found to be a function of pressure.

Rostrup-Nielsen introduced two-step kinetic and power law models to describe the kinetics of steam reforming of various hydrocarbons.[44, 47] With regard to steam methane reforming, Rostrup-Nielsen introduced the following rate expression:

$$r_{CH_4} = \frac{k\, p_{CH_4}}{\left[1 + K_H \sqrt{p_{H_2}} + K_W \frac{p_{H_2O}}{p_{H_2}}\right]^n}. \qquad \text{[Equation 2-2]}$$

This rate expression captured details of gas-phase dependence similar to the work of Khomenko, et al., but without the complicated functional dependence in the denominator. Rostrup-Nielsen's work in power-law models was extended by Tøttrup, et al. to describe steam reforming of n-heptane over nickel catalyst.[48]

Subsequent work by Xu and Froment applied the Langmuir-Hinshelwood kinetic form to describe steam reforming and water-gas shift kinetics over $Ni/MgAl_2O_4$. The authors applied thermodynamic criteria to reduce the number of possible mechanisms to three – adding to the water-gas shift and reforming reactions a third reaction where reforming produces CO_2 instead of CO. Twenty one sets of possible rate equations describing these three reactions were subjected to model discrimination and parameter estimation via statistical analysis using data from 280 measurements.[49] For each set of rate equations, one step was assumed to be rate-determining for each of the three reactions. The set of equations retained from the model discrimination produced three rate equations that were found to fit the experimental data well with the significant parameter estimates displaying thermodynamic consistency. The following equation (a linear combination of two of the three obtained rate expressions) was developed to describe the rate of disappearance of methane via steam reforming.

$$r_{CH_4} = \frac{\frac{k_1}{p_{H_2}^{2.5}}\left(p_{CH_4}p_{H_2O} - \frac{p_{H_2}^3 p_{CO}}{K_1}\right) + \frac{k_3}{p_{H_2}^{3.5}}\left(p_{CH_4}p_{H_2O}^2 - \frac{p_{H_2}^4 p_{CO_2}}{K_3}\right)}{\left(1 + K_{CO}p_{CO} + K_{H_2}p_{H_2} + K_{CH_4}p_{CH_4} + K_{H_2O}p_{H_2O}/p_{H_2}\right)^2} \qquad \text{[Equation 2-3]}$$

Although the agreement with experiment was good, Equation 2-3 cannot explain an observed decrease in reforming rate when steam is replaced by CO_2.[50] Also, the rate equation is restricted to a narrow range of parameters: temperatures of 500-575°C, pressures of 3-15 bar, and initial molar H_2O/CH_4 ratios of 3-5. It should be noted that the experiments of Xu and Froment were conducted at near-equilibrium conversions. As a result, reverse reaction effects were significant in their experiments.

Aparicio presented an alternative method of modeling steam methane reforming kinetics through microkinetic modeling.[50] Microkinetic modeling involves the study of catalytic reactions in terms of elementary chemical reactions that occur on the surface during the catalytic cycle.[51] Experimental

adsorption/desorbtion data are combined with estimates made for pre-exponential factors and activation energies from, for example, collision theory, transition state theory, and linear energy relationships such as the Evans-Polyani relation. An important distinction between macroscopic formulations like the Langmuir-Hinshelwood and microkinetic modeling is that microkinetic models generally include no assumptions about rate determining steps or surface concentrations to simplify the model.[52] The model is adjusted through altering the kinetic parameters or the proposed mechanism until a satisfactory fit to experimental data for the system of interest is obtained.

Prior to Aparicio's work, efforts to model the kinetics of the steam reforming reaction focused on macroscopic models like those presented above. However, macroscopic kinetics offer little to no insight about what is occurring on the catalyst surface. While they are useful for reactor design, they offer little information that can be used in catalyst design. Much of the power of microkinetic modeling lies in the information it provides about the surface in catalytic processes – information about which reaction steps are kinetically significant or rate limiting and which intermediates have significant or insignificant concentrations on the surface.[52]

Using this approach, Aparicio developed a microkinetic model consisting of 13 reversible reactions. The resulting model (below) was successful at predicting overall activation energies, reaction orders, and trends for several reactions. However, like many microkinetic studies, the many of the model's predictions are not quantitative, as predicted rates deviated by as much as an order of magnitude from experimental values.[50] As noted by the author, the value of microkinetic modeling lies less in quantitative modeling than in the contribution it can make to the general understanding of catalytic reaction mechanisms (e.g., rate limiting steps and important surface intermediates). For example, while no single step was concluded to be rate determining over all conditions examined (as assumed in previous studies), several steps were identified as potentially rate limiting as shown below in the mechanism obtained from the modeling.

1.	$CH_4 + 2^* \leftrightarrow CH_3^* + H^*$		(slow)
2.	$CH_3^* + * \leftrightarrow CH_2^* + H^*$		(slow)
3.	$CH_2^* + * \leftrightarrow CH^* + H^*$		(slow)
4.	$CH^* + * \leftrightarrow C^* + H^*$		
5.	$H_2O + * \leftrightarrow H_2O^*$		
6.	$H_2O^* + * \leftrightarrow OH^* + H^*$		
7.	$C^* + OH^* \leftrightarrow CHO^{**}$		(slow)
8.	$CO_2 + 2^* \leftrightarrow CO_2^{**}$		(equilibrium)
9.	$CO_2^{**} + H^* \leftrightarrow COOH^{**} + *$		(equilibrium)
10.	$COOH^{**} + H^* + 2^* \leftrightarrow CHO^{**} + OH^* + 2^*$		(slow)
11.	$CHO^{**} + 3^* \leftrightarrow CO^{**} + H^* + 2^*$		(slow)
12.	$CO^{**} \leftrightarrow CO + 2^*$		
13.	$2H^* \leftrightarrow H_2 + 2^*$		

By understanding which reactions are more critical in establishing the rate of reforming (e.g., the slow reactions), the catalyst designer may seek improved catalysts that enhance these steps. However, this search would require further microkinetic modeling of additional catalysts or estimates of how new catalysts would affect these key steps. In addition, treatment of deactivation mechanisms in microkinetic modeling is of particular use in the search for catalysts with longer-term stability than existing nickel catalysts, such as the microkinetic modeling of SMR with deactivation mechanisms by Chen, et al.[53]

One limitation of experimentally-parameterized microkinetic models is that the size (number of parameters to be fit, which scales with the numbers of reactions) should be kept small to help ensure the statistical significance of the fit parameters. There also exists some degree of covariance between the fit parameters in the microkinetic model. As a result, individual parameters or reactions should not be removed from one microkinetic model to be used as a unique quantity or for use as a "known" quantity in another microkinetic model. The complete set of parameters in an experimentally-fit microkinetic model should, in general, be considered unique to that model. The introduction of experimentally-measured quantities to the microkinetic model relaxes these constraints; however, the short-lived nature of the intermediates, the high temperature and pressure, and the complexities of heterogeneous catalysis make experimental measurement of the microkinetic model parameters extremely challenging or even impossible.

The use of computationally-determined quantities in the microkinetic model addresses many of these issues. Because the computed quantities are not fit, the model is limited in size only by the availability of computational resources and there the model parameters can be used along with other computationally-determined parameters from other microkinetic models. Chen et al. have recently employed the

activation exponential potential (UBI-QEP) approach and transition state theory to the microkinetic modeling of steam methane reforming.[54] Furthermore, density functional theory (DFT) has become a popular computational tool for describing heterogeneous catalysis, including many recent applications to methane reforming.

DFT-produced potential energy surfaces for one SMR pathway through C^* and O^* forming CO^* on the Ni(111) and Ni(211) surfaces were presented by Bengaard, et al.,[39] building on the work of Watwe, et al.[55] Their analysis offered important insight into the C* + O* → CO* pathway, but left other possible reaction pathways unexamined. Wang, et al.[56] and Zhu, et al.[57] investigated the thermochemistry of dry methane reforming (i.e., CO_2 reforming of CH_4) over Ni(111) using DFT. Their research included analysis of electronic energies (Wang, et al.) and Gibbs free energies (Zhu, et al.) along additional reforming pathways as well as the identification of activation barriers, but did not include a kinetic model that would facilitate the analysis of all surface pathways with flux and sensitivity analyses. In addition, Jones, et al. have recently investigated steam methane reforming over a variety of transition metal catalysts in an attempt to develop scaling relationships useful in studying reactivity trends.[32]

2.4 Nickel Catalyst Deactivation Mechanisms

To produce hydrogen on the scale necessary for automobile fuel, or an even greater scale for electricity generation, an affordable and abundant catalyst with long-term activity (e.g., a nickel bimetallic alloy with resistance to deactivation) is desired. Obtaining a molecular-level understanding of the deactivation mechanisms of nickel catalysts is important for more accurate modeling and the rational design of new bimetallic catalysts with longer-term activity. Nickel catalyst deactivation can occur through a variety of mechanisms such as sintering, oxidation, sulfur poisoning, and carbon formation, which are reviewed below.

Sintering

As the catalyst metal is heated, a thermodynamic driving force of total surface energy minimization leads to a growth in nickel particle size in a process known as sintering. Three possible mechanisms for nickel particle growth have been proposed: 1) particle migration where entire crystallites migrate over the support followed by coalescence, 2) metal transport species are emitted from one crystallite, migrate over the support and are captured by another crystallite, and 3) vapor transport between particles (at high

temperature).[58] The diffusion rates of metal atoms and small clusters as well as the partial pressure of gas phase species such as hydrogen and water have been shown to be important factors in determining sintering rates. Sintering can be controlled by avoiding hot spots in the catalyst (through reactor design and catalyst distribution) and application of suitable catalyst supports.

Oxidation

Oxidation of the metal atoms by gases in the reactor or surface intermediates can deactivate the reforming catalyst. In general, oxidation is not a concern for highly active catalysts because methane conversion is high and, as a result, hydrogen concentrations are high (a reducing environment). In membrane reformers, however, hydrogen concentrations could be low, particularly near the membrane if the hydrogen permeability rate is fast. In this environment, high ratios of water to hydrogen concentration could lead to metal oxidation and potential nickel catalyst deactivation. Thus, having carbon-resistant (see discussion below) catalysts that would allow for lower steam-to-methane operating ratios would be helpful in avoiding catalyst oxidation.

Sulfur Poisoning

Sulfur is a common, strong poison for nickel (and other Group-8) reforming catalysts.[14] It is therefore important that sulfur in the feed gas be removed. The degree of removal required is a function of reactor temperature because the adsorption of sulfur is an exothermic reaction between the metal surface and hydrogen sulfide gas. For example, while poisoning of the nickel catalyst occurs with about 5 ppm of sulfur in the feed gas at 800°C, only 0.01 ppm sulfur concentrations are sufficient to poison the catalyst at 500°C.[41]

Carbon Formation

Because of the highly endothermic nature of the steam reforming reaction, high reactor temperatures are generally required (~600-800 °C). At these temperatures, hydrogen production is favored; however; the downside of this is that catalyst-deactivating carbon formation is also favored at high temperatures.[59] There are three primary forms of carbon formation: pyrolytic coke, encapsulating carbon or gum, and whisker carbon.[14, 40, 41, 59]

Pyrolytic Coke

Pyrolytic coke (Figure 2-2A) is formed through a free radical process that results in the deposition of carbonaceous intermediates and coke on the catalyst and reactor internals.[59] The presence of higher hydrocarbons and olefins in the natural gas feed can increase pyrolytic coke formation. Pyrolytic coke is formed from gas-phase reaction. Unlike encapsulating coke and whisker carbon, pyrolytic coke is not catalytic in nature. Pyrolytic coke is undesirable because the condensed coke can encapsulate and deactivate the catalyst as well as clog the reactor internals leading to higher pressure drops. Because the formation of pyrolytic coke is a gas phase phenomenon, it is generally controlled through the adjustment of operating conditions and reactor control. Minimization of the heated space and dilution of the free radical concentration help to minimize coke formation.[59]

Encapsulating Carbon

Encapsulating carbon (Figure 2-2B), or gum, is formed through a catalytic process on the metal surface, but detailed knowledge about the formation of encapsulating carbon is limited.[53] Encapsulating carbon consists of a thin CH_x film or multiple layers of graphene covering nickel particles, representing the primary deactivation mechanism of the metal catalyst. Encapsulating carbon forms at lower temperatures than pyrolytic and whisker coke. One hypothesis for encapsulation is that methane dissociation on the surface yields highly reactive monatomic carbon (C*) that can either react to form gaseous CO or, if gasification is slow, polymerize to form C_β.[59] As the C_β polymer accumulates on the surface, encapsulation occurs.

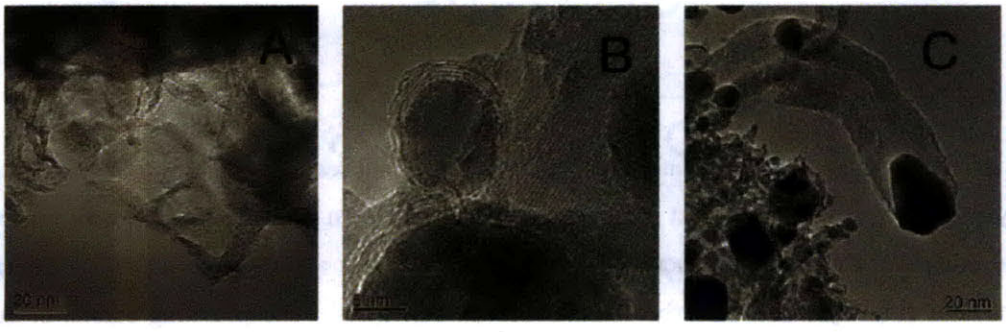

Figure 2-2. Electron microscopy images of pyrolytic carbon on a $MgAl_2O_4$ support (A), encapsulating carbon (B), and whisker carbon (C) on $Ni/MgAl_2O_4$ reforming catalysts (from Sehested[40])

Whisker Carbon

Whisker carbon (Figure 2-2C) is the carbon formation of primary concern in steam reforming.[14] A similar hypothesis to encapsulating carbon formation has been proposed to describe the initiation of whisker formation. Hydrocarbons dissociate on the metal surface and form adsorbed monatomic carbon, similar to the initiation of encapsulating carbon formation. However, in whisker carbon formation, it has been proposed that the carbon adatoms (i.e., adsorbed carbon atoms) dissolve into the metal particle. It is thought that they then diffuse through the particle where they nucleate into precursors of the carbon whisker or add to existing carbon whiskers at facets suitable for whisker formation on the rear interface (i.e., the support side of the particle).[14, 39]

There is debate, however, concerning the method of carbon transport to the rear surface in this mechanism. Recent DFT calculations suggest that the transport of carbon or carbon-containing species proceeds via the nickel surface and the nickel-graphite interface, not through the bulk phase.[40, 60] Whisker carbon formation does not necessarily deactivate the carbon catalyst like pyrolytic coke and encapsulating carbon. However, carbon whiskers have high mechanical strength and the catalyst particle is destroyed when the whisker hits the pore walls.[14] In addition, whisker formation results in higher reactor pressure drop.

Role of Step Sites in Carbon Formation

Similar to catalytic activity, it is believed that step sites play an important role in the nucleation of surface carbon formation routes of encapsulating and whisker carbon. High-resolution Transmission Electron Microscopy (HRTEM) paired with DFT calculations suggest that step sites are the preferred sites for carbon adsorption and act as growth centers for graphene layers.[61] As seen in Figure 2-3, the route to methane dissociation products, particularly to carbon adatoms, has lower barriers on Ni(211) than Ni(111). In addition, carbon adatoms are the most stable dissociation product of methane on Ni(211), resulting in an exothermic pathway to carbon adatoms at step sites, unlike the terrace. Also, note that the surface energy for a graphene layer (indicated by the dashed horizontal line in Figure 2-3) is lower than that of the carbon adatom (and all CH_x species). Therefore, there exists a thermodynamic driving force for the formation of a graphene layer over the nickel surface from adsorbed carbon-containing species, potentially leading to a graphene-covered surface (i.e., encapsulation and catalyst deactivation).

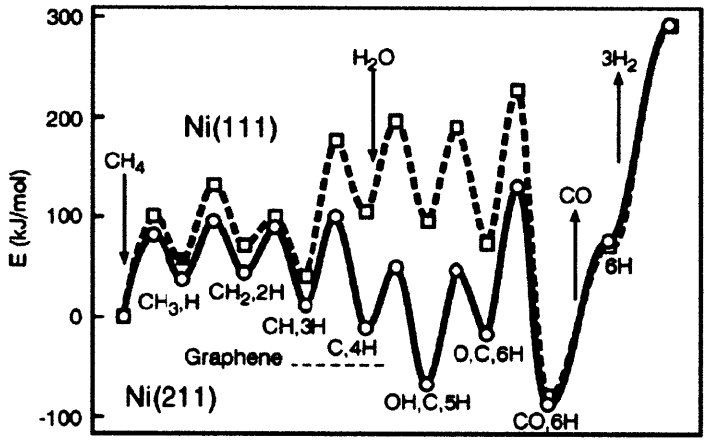

Figure 2-3. Calculated energies along the reaction path for steam reforming on Ni(111) and Ni(211) surfaces (from Bengaard, et al.[39])

At high temperatures, a single graphene plane can extend out from the particle and form a carbon nanotube. On the other hand, at lower temperatures it may be more favorable for new carbon layers to nucleate below the first graphene layer and grow through the addition of carbon atoms.[40] This process is proposed to be fundamental to whisker growth as the first layer of carbon is lifted from the nickel interface, growing the carbon whisker.[39] The common origin of each of these proposed carbon formation mechanisms provides insight into the important role that steps sites may play in carbon formation.

Minimization of Carbon Formation

Because of the limitations that carbon formation places on reactor operation and catalyst activity, minimization of carbon formation is an attractive research goal. Past efforts to limit carbon formation have included increasing coke gasification, ensemble size control, and prevention or limitation of carbon-formation precursors.[59] It has been shown that the type of catalyst support, such as oxide supports, can play a role in increasing coke gasification, which is an example of catalyst support participation in chemical reactions.[62] Similarly, steam methane reforming is typically operated at greater-than-stoichiometric ratios of steam to methane (e.g., 2.5:1) to provide excess oxygen on the surface to promote CO(g) formation over carbon formation.

The concept of ensemble size control is based upon the idea that the polymerization of adsorbed carbon adatoms (or other reactive carbon-containing intermediate species) requires an ensemble of sites that is

larger than that required for the steam reforming reaction. It is suggested that by limiting the number of sites in an ensemble through small amounts of sulfur adsorption, for example, coke formation might be retarded without significant impact on reforming rates (balancing coke minimization against sulfur poisoning of the catalyst).[63] This is known as the SPARG process, or Sulfur PAssivated ReforminG. Using a mean-field Langmuir kinetics expression, the rate of reforming or carbon formation on the sulfur-passivated surface is expressed as

$$r = r_o \left(1-\theta_s\right)^a , \qquad \text{[Equation 2-4]}$$

where r_0 is the rate on a non-passivated surface and θ_s is the fractional coverage of sulfur on the catalyst surface.[5] The factor a is suggested to be related to the ensemble size required for the reaction of interest. Experiments by Rostrup-Nielsen on steam methane reforming over nickel catalysts reveal that this ensemble factor is equal to 6.3 for the carbon formation process, but only 2.7 for the steam reforming process. The SPARG process exploits this difference in required ensemble size by preferentially inhibiting carbon formation over steam methane reforming through sulfur addition to the surface.

Techniques to minimize carbon formation often focus on the application of dopants or the creation of surface alloys to reduce coverage of carbon-containing intermediates (for example, at the step edge) or to slow the rate of carbon diffusion. Experiments and theoretical work have suggested that additives such as potassium, sulfur, and gold can block step sites and inhibit carbon nucleation.[39, 64, 65] Density functional theory calculations have shown that Ni/Au[66, 67] and Ni/Sn[68-70] surface alloys exhibit decreased carbon diffusion/nucleation. However, Ni/Au alloy is found to decrease the overall rate of reforming and its long-term stability is poor.[71] Like Ni/Au, Ni/Sn is also found to decrease the overall rate of reforming; however, more information is needed to assess its long-term stability.

Chapter 3. Computational Methods for Obtaining Thermochemical Properties in Heterogeneous Catalysis

3.1 Introduction

To gain a better fundamental understanding of the processes occurring on the catalyst surface under working conditions, we seek information about the coverage of surface species as well as the dominant reaction pathways on the catalyst surface. Computational chemistry, combined with statistical thermodynamics and transition state theory, can provide us with this information about surface species thermochemistry and kinetics. Through electronic structure calculations, computational chemistry allows us to obtain atomic-level understanding of the geometry of adsorbed species and transition states, the electronic binding energies of the species on the surface (as a function of coverage, if desired), and electronic reaction barriers of surface reactions. Through harmonic vibrational frequency analysis, frequencies can be computed that can be used to obtain partition functions for surface species and transition states through the application of statistical thermodynamics. The combination of the electronic thermochemical landscape with partition functions allows for the computation of surface thermochemistry and reaction rates at industrially-relevant temperatures and pressures. The thermochemistry and kinetics can be combined in a microkinetic model that allows for the computation of surface coverage as a function of reaction conditions, the investigation of dominant surface reaction pathways, and the identification of the rate-determining or rate-limiting step(s) in the reaction mechanism.

In the sections that follow, I will present an overview of performing electronic structure calculations for obtaining geometries, energies, and frequencies for the gas-phase and surface species involved in heterogeneous catalysis. Parameterization of the calculations is discussed, including details to the software packages employed in this work. In addition, I discuss the statistical thermodynamics required to obtain partition functions for the species involved in heterogeneous catalysis and how to use these partition functions to obtain thermodynamic properties. Particular detail is applied to the discussion of how the partition functions and thermodynamic properties for surface species are calculated differently for weakly-bound, mobile species than strongly-bound, localized species.

3.2 Density Functional Theory Calculations for Heterogeneous Catalysis

The Exchange Correlation Functional

DFT is the most widely used approach for performing quantum chemical calculations for the extended, many-electron systems present in metal catalysts. DFT provides a method for the calculation of the ground state electron density and total energy by solving the Kohn-Sham equations (one-electron time-independent Schrodinger equations) using only three spatial variables to define the electron density, rather than $3N_{electrons}$ spatial variables to define the locations of all electrons. The addition of an exchange correlation energy term to treat correlation effects improves the accuracy of DFT over similar methods such as the Hartree Fock Self-Consistent Field approach.[72, 73] Many exchange correlation functionals have been developed; however, those used to study metal catalysts are typically either a Local Density Approximation (LDA) or a Generalized Gradient Approximation (GGA). The LDA can often produce poor estimates for electronic binding energies and molecular geometries on metallic surfaces; however, GGA calculations have been shown to provide more accurate results.[73-75] In this work, I employ the revised Perdew-Burke-Ernzerhof (RPBE) functional of Hammer, et al.[76] The RPBE functional is an extension of the Perdew-Burke-Ernzerhof (PBE) GGA functional[77] and has been shown to reproduce experimental adsorption energies more reliably than other density functionals such as PBE or PW91 for adsorbates on various crystal surfaces, including nickel.[76]

Defining the Model of the Catalyst Surface Structure

The surface of a catalyst nanoparticle is non-uniform, containing multiple surface facets as well as surface defects, such as kinks and steps. Unit cells describing the (111) and (100) surface facets of a face-centered cubic (FCC) metal, such as nickel, are shown in Figure 3-1, along with a unit cell of the (211) surface, which can be used as a model to capture under-coordinated step edge atoms. Certain ad/desorption steps or surface reactions may be more facile on a given surface facet or defect, presenting the need to consider surface structure when modeling heterogeneous catalysis. A useful study was performed by Liu, et al. that presents general rules for predicting the surface structure where catalytic reactions such as C-H and C-O bond breaking/forming may occur.[78] When defining a model for the catalyst surface, the surface facets are typically modeled independently rather than incurring the computational expense of including all surface facets of interest in one surface model. A process for combining multiple surface facets into one kinetic model for the catalyst surface will be discussed later.

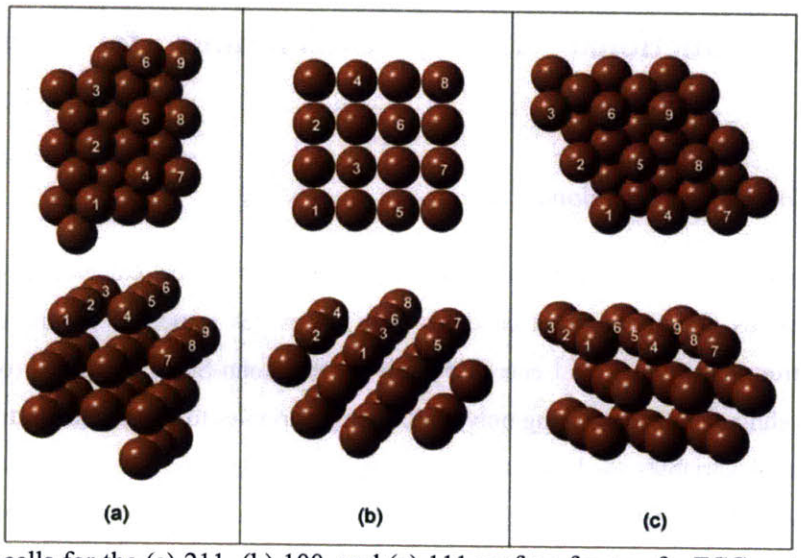

Figure 3-1. Unit cells for the (a) 211, (b) 100, and (c) 111 surface facets of a FCC metal. The top-layer of metal atoms for each surface is numbered for reference.

Catalyst nanoparticles typically range in size from a few nanometers to tens of nanometers. For a commercial catalyst, these nanoparticles are dispersed on a high-surface-area catalyst support, such as alumina and silica. In a world without computational limitations, one could explicitly model all catalyst and support atoms to obtain the desired thermochemistry and kinetics of the catalyst. However, each nanoparticle consists of hundreds to thousands of atoms, with catalyst support atoms being orders of magnitude greater. Current quantum chemical simulation packages can model approximately 100 atoms with reasonable accuracy and computational cost. This disconnect between the number of atoms we can model using DFT and the number of atoms present in the systems of interest presents the need for model catalysts for computational investigation.

Two models for treating the metal surface are cluster models and slab models. Cluster models apply finite ensembles of atoms to model the catalyst surface. While cluster models are computationally simpler to implement than slab calculations, the electronic structure of finite clusters can often be quite different than extended, semi-infinite surfaces and properties tend to converge slowly with respect to cluster size.[7] Cluster model calculations employ localized functions for basis sets, such as gaussians, atomic orbitals, or linearized muffin tin orbitals (LMTOs) because they satisfy the boundary condition of zero electron density at infinite distance from the metal cluster. For nanoparticles sufficiently large that all atoms cannot be included in the cluster at reasonable computational expense, slab models of the catalyst surface are usually preferred. In this work, the quantum calculations are performed exclusively

using the slab model approach. While convergence can still be slow, the electronic characteristics of the surface are better captured in slab calculations.[7] Slab models take advantage of periodic boundary conditions to model an extended surface in two dimensions, with the periodicity defined by the size of the unit cell. A supercell approach is applied to define the thickness of the slab and the separation of successive periodic slabs in the direction perpendicular to the surface. Slab model calculations also employ periodic basis sets, such as plane waves, to match the periodic boundary conditions. For either surface model, the size of the basis set should be chosen such that the energy predicted by the DFT calculations is reasonably well converged. The convergence of the binding energy of a hydrogen atom on Ni(111) as a function of plane wave cutoff (basis set size) is shown in Figure 3-2. It can be seen that the binding energy is reasonably well converged at plane-wave cutoff energies in excess of 300 eV for hydrogen, though note that larger basis set sizes are required for atoms such as oxygen.

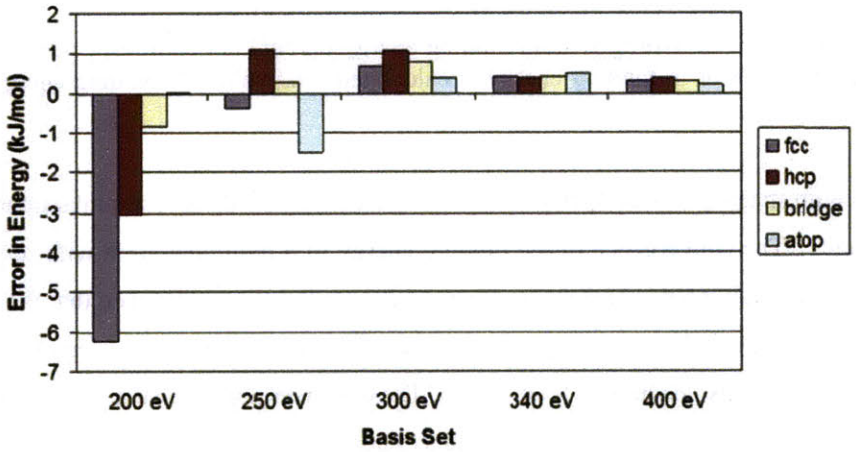

Figure 3-2. Convergence of hydrogen atom binding energy with respect to basis set, expressed as plane-wave cutoff energy. Error in binding energy is calculated relative to the binding energy computed with a plane-wave cutoff of 450 eV.

Consideration should also be given to the convergence of the DFT calculations with respect to surface model parameters, such as slab thickness, the size of the unit cell, and the vacuum spacing between successive periodic slabs in the direction perpendicular to the metal surface. Convergence with respect to slab thickness is straightforward, with the binding energy of adsorbates generally converging with increasing slab thickness. The convergence of the binding energy of a hydrogen atom on Ni(111) at various binding sites on the metal surface is shown in Figure 3-3. It can be seen that the binding energy is reasonably well-converged at three layers of metal atoms in the slab. The size of the unit cell is chosen to

minimize lateral interactions on the surface, with consideration given to the added computational expense of increased metal atoms in the unit cell.

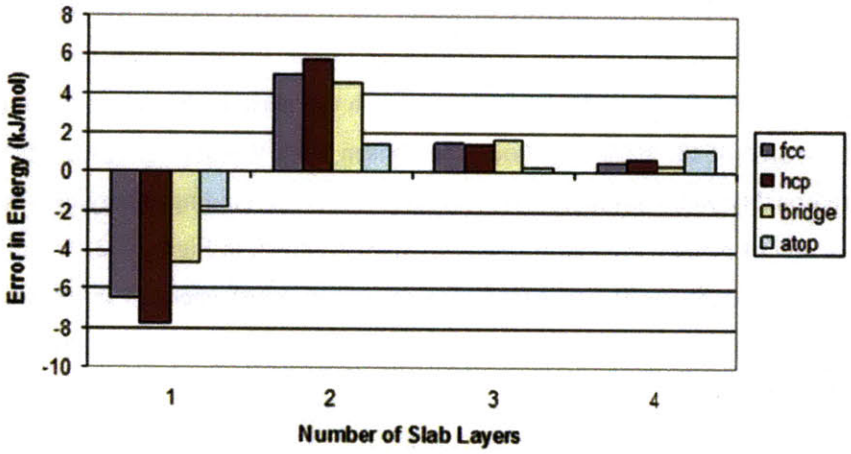

Figure 3-3. Convergence of hydrogen atom binding energy on Ni(111) with respect to slab thickness for various binding sites. Error in binding energy is calculated relative to the binding energy computed for five slab layers.

Finally, the vacuum spacing between periodic slabs is increased until there is minimal interaction between successive images. The convergence of the binding energy of a hydrogen atom with respect to vacuum spacing between successive Ni(111) slabs is shown in Figure 3-4. It can be seen that the binding energy is reasonably well-converged at a vacuum spacing of 6 Å, though there is not significant computation expense for increasing this spacing to 8 or 10 Å. These convergence calculations are performed with conventional counter-charges, which are used to cancel out any dipole interactions in the vacuum space.[79] Application of these counter-charges can reduce the amount of vacuum spacing required for convergence of energies. In general, calculations in this study are performed with approximately 10 Å between periodic slab images; however, the appropriate supercell parameters used for calculations in this work will be explicitly stated in subsequent chapters.

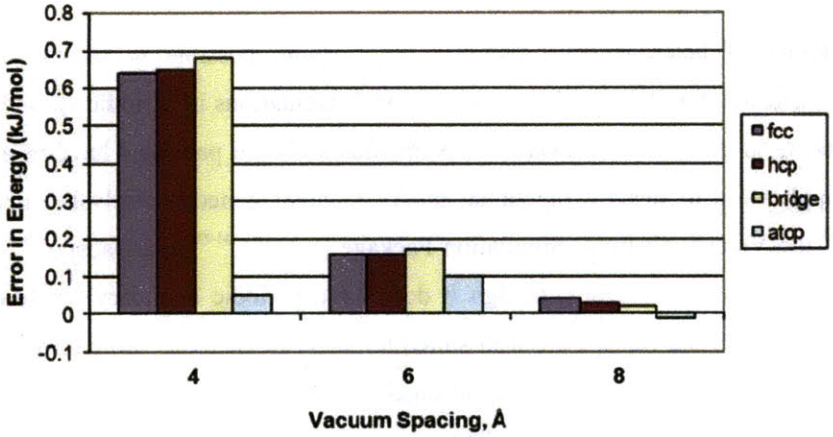

Figure 3-4. Convergence of hydrogen atom binding energy with respect to spacing between periodic Ni(111) slabs for various binding sites. Error in binding energy is calculated relative to 10 Å of vacuum spacing.

Treatment of Core Electrons

When modeling systems of metal atoms with many electrons, such as transition metals, significant computational expense can be saved by explicitly treating only valence electrons in the DFT calculations. Because the core electrons are not largely involved with bonding, reasonable accuracy can be achieved by approximating the core electron effect in the DFT calculations. Common methods for treatment of core electrons are the frozen core approximation, the pseudopotential method, and the projector-augmented wave method. In the frozen core approximation, the one-electron wave functions for the core electrons are not updated for each self-consistency iteration. Instead, the wave functions are 'frozen' to the functional form that the isolated, or non-interacting, atomic orbitals would have. The pseudopotential and projector-augmented wave methods are similar in that they completely remove the core electrons from the DFT calculations and introduce an effective potential in its place. The pseudopotential and projector-augmented wave methods are similar. For example, the pseudopotential energy functional can be obtained through a linearization of two terms of a slightly modified projector-augmented wave energy functional.[80] Both the pseudopotential method and the projector-augmented wave method yield accurate energies with good computational efficiency, though the projector-augmented wave method is found to have increased reliability for some magnetic systems.[80]

Software Packages for DFT Calculations of Heterogeneous Catalysis

Predictive modeling of heterogeneous catalysis has become possible in recent years due to the development of efficient, parallelized algorithms for DFT calculations in periodic systems combined with rapid improvements in computer hardware.[72] Numerous software packages have been developed that allow for the application of density functional theory to heterogeneous catalysis, such as Gaussian,[81] CRYSTAL,[82, 83] the Vienna Ab-Initio Simulation Package (VASP),[84-86] and Dacapo.[76, 87, 88] Gaussian is typically used for cluster calculations, though it does have periodic boundary condition functionality, while CRYSTAL, VASP, and Dacapo are well-suited for slab calculations. More information about these and other density functional theory software packages can be found in the review of density functional theory for transition metals prepared by Cramer and Truhlar.[89] For the density functional theory calculations performed in this work, I use both the Dacapo and VASP software packages, which are two of the most widely-used software packages for the investigation of heterogeneous catalysis.

Performing DFT Calculations using Dacapo

Dacapo is a planewave, periodic boundary condition density functional theory software package. Dacapo jobs are set up through use of a python script. All calculation parameters and commands are written in a single file, which can then be submitted for parallel calculations. These parameters are outlined below, along with classes that can be imported from the Atomic Simulation Environment (ASE), the computational framework from within which Dacapo is run. The description below is not intended to be an exhaustive review of all the capabilities of Dacapo, but rather an introduction to the setup of a Dacapo calculation. More details can be found at the Dacapo wiki, https://wiki.fysik.dtu.dk/dacapo. I provide the details below to provide points of reference that will make parsing the documentation more approachable.

Setting Atomic Positions and Size of Unit Cell

The atomic positions of metal atoms and adsorbates are set in Dacapo by defining on object (called atoms in the example below) using the built-in ASE classes `ListOfAtoms` and `Atom`. For example, the object atoms can first be initialized using an empty set of atoms and periodic boundary conditions through

```
atoms = ListOfAtoms([], periodic=True).
```

Then, metal or adsorbate atoms are added to the object using the append command. The syntax for this command is

```
atoms.append(Atom(Symbol,[a,b,c],magmom=mm))
```

where, Symbol is the periodic symbol for the atom of interest; a, b, and c are the lattice-vector-basis positions of the atom; and mm is a guess value for the magnetic moment of the atom. Alternatively, the Cartesian position of an atom can be assigned using parentheses rather than brackets. This is carried out for each metal and adsorbate atom to be placed in the unit cell. The size of the unit cell is defined using the built-in ASE class SetUnitCell

```
atoms.SetUnitCell([(1x, 1y, 1z),
                   (2x, 2y, 2z),
                   (3x, 3y, 3z)])
```

which is parameterized with the x,y,z Cartesian coordinates describing the three primitive lattice vectors for the unit cell.

Setting Calculation Parameters

The calculation parameters for a Dacapo simulation are set by defining the calculator object (calc) using the built-in ASE class `Dacapo`. The calculation parameters to be defined are the exchange correlation functional, the number of bands for the calculation (which should be in excess of half the number of valence electrons in the system), the Brillouin zone k-point integration grid, the planewave and density cutoff energies (these values are equal by default), the names of the *.nc and *.txt output files, and Boolean operators defining whether or not the calculation will be spin polarized and contain inter-slab dipole electrostatic decoupling. These parameters are set using the keywords shown below:

```
calc = Dacapo(xc=XCfunc,
              nbands=bands,
              kpts=(nkpts1, nkpts2, nkpts3),
              planewavecutoff=plwv,
              densitycutoff=dens,
              out=ncfile,
              txtout=txtfile,
              spinpol=do_spinpol,
              dipole=do_dipole).
```

In Dacapo, there are several exchange correlation (xc) functionals available for DFT calculations. The available functionals (with the appropriate XCfunc symbol in parentheses) are Vosko-Wilk-Nusair LDA

(LDA), Perdew-Wang 91 GGA (PW91), Perdew-Burke-Ernzerhof GGA (PBE), and the Revised Perdew-Burke-Ernzerhof GGA (RPBE).

The atomic positions previously defined in the object 'atoms' can then be attached to the Dacapo calculator object through

```
atoms.SetCalculator(calc).
```

Specifying Relaxed Atoms

Often, the user desires to relax only select atoms, freezing the positions of the remaining atoms. To do this, a mask object is utilized. In the object, Boolean operators are used to relax or freeze each x,y,z axis degree of freedom for each atom. A mask object is created using

```
mask = [[1x,1y,1z],[2x,2y,2z], … [nx,ny,nz] …, [Nx, Ny, Nz]]
```

where, nx, ny, and nz are the Boolean operators setting the dynamics of the x, y, and z axis degrees of freedom for the nth atom in a list of N total atoms. In this object, a nonzero value of an element corresponds to a frozen degree of freedom, while a value of zero corresponds to a relaxed degree of freedom. This mask object is then assigned to an object 'filter' using the built-in ASE class `FixCoordinates`, where it is attached to the atomic positions set previously using

```
filter = FixCoordinates(atoms,mask).
```

Performing the DFT Calculation for a Geometry Optimization

The DFT calculation is now ready to be run. To define the optimization technique, a dynamics object is created using the built-in ASE class corresponding to the desired optimizer. For example, to use the BFGS quasi-Newton optimization algorithm for a geometry optimization, the 'dyn' object is created as follows:

```
dyn = QuasiNewton(filter, fmax=f_criterion, logfilename=qnfile)
```

where, the convergence criterion is that the force on all individual atoms should be less than f_criterion and qnfile is the name of the log file that tracks convergence parameters. There are five optimization classes built into the Atomic Simulation Environment: BFGS (also associated with the synonym QuasiNewton), LBFGS, LBFGSLineSearch, MDMin, and FIRE.

Next, using the built-in ASE class `NetCDFTrajectory`, a trajectory object 'traj' is created and the initial atomic configuration in the object 'atoms' is written to a trajectory file 'trajfile' using

```
traj = NetCDFTrajectory(trajfile, atoms).
```

This object/file will be used to track the trajectory of the atoms during the optimization. The 'traj' object is attached as an observer to track the object 'dyn', which records the movement of atoms during the optimization, using the command

```
dyn.Attach(traj).
```

Finally, the optimization is started using

```
dyn.Converge.
```

Performing the DFT Calculation a Transition State Search

To obtain a transition state estimate, several techniques are available in Dacapo such as the Nudged Elastic Band (NEB) method, the Climbing Image Nudged Elastic Band (CI-NEB) method,[90] and the first-order saddle point search. The NEB method utilizes initial and final configurations to set the end-points of a reaction coordinate. The user specifies the number of NEB images that will be used to simulate the reaction path between the initial (reactant) and final (product) state. The user can specify these geometries based on intuition or simply linearly interpolate between the end-point images to parameterize the intermediate geometries. The NEB method performs geometry optimizations on the intermediate images, but against a "spring" force between adjacent images that ensures that the intermediate images do not simply fall back into either the reactant or product state. The NEB method does not rigorously

converge to a saddle-point, but instead results in a high-energy geometry that will approach the saddle-point energy. For rigorous conversion to a first-order saddle point, the CI-NEB can be a useful method. This simulation is initialized in a manner similar to the NEB; however, the algorithm allows the highest-energy image to be driven upward along the reaction coordinate by inverting the true force on this image along the tangent during the optimization such that the energy of the image is maximized along the band (and minimized in other directions), converging to the corresponding first-order saddle point.

If the reaction coordinate is not complicated or the user has a good initial guess for the transition state geometry (either through intuition or using a NEB calculation), then a first-order saddle point search is an excellent means for finding a transition state geometry. The Dacapo built-in first-order saddle point search method is a min-mode method, maximizing the energy along the mode corresponding to the lowest (i.e., most negative) eigenvalue. In our hands, we found a series of constrained optimizations (fixing the length of the bond that is breaking/forming) around the transition state geometry to be a quick means of obtaining an initial guess for a first-order saddle point search, rather than a NEB simulation which spends roughly as much computational time optimizing images away from the transition state as it does optimizing images near the transition state.[12] However, for non-intuitive reaction coordinates or complicated reaction paths, the NEB or CI-NEB would likely prove to be more useful methods.

These calculations are set up in a manner similar to that described above. Details for calling the desired transition state search technique are provided in the ASE manual available at https://wiki.fysik.dtu.dk/ase2/Dynamics. Note that the first-order saddle point search requires an initial guess of the Hessian. Running a NEB method calculation prior to a first-order saddle point search can provide the initial guess for the Hessian.

Performing Frequency Calculations

Once an optimized geometry or first-order saddle point is obtained, frequency calculations can be performed. A frequency calculation is set up similar to a geometry optimization job in that all parameters and commands are contained within one python script. Instead of defining a new geometry as was carried out for the geometry optimization calculation, the user can assign a previously-optimized geometry to the object 'atoms' using the ReadGeometry built-in ASE class. The geometry should be read in from the trajectory file resulting from the finished geometry optimization or first-order saddle point search. The calculation parameters are set in a manner identical to that for geometry optimizations. Before the frequency calculation is performed, it is useful to tighten the tolerances for more accurate derivatives

through finite difference calculations. The SetConvergenceParameters built-in ASE class can be used to adjust the tolerances. To run the frequency calculation, the built-in ASE class VibrationalCalculation is used.

Performing DFT Calculations using VASP

Like Dacapo, VASP is a planewave, periodic boundary condition density functional theory software package. VASP utilizes a setup where there are multiple files that must be assembled for a simulation. The documentation for VASP (http://cms.mpi.univie.ac.at/vasp/vasp/vasp.html) and the VASP Transition State Theory (TST) Tools (http://theory.cm.utexas.edu/vtsttools/) are detailed and straightforward. Therefore, I will review the files that are necessary for the calculations performed in this work along with some commentary; however, considerably more detail is available at the above references.

Performing Geometry Optimizations

For VASP geometry optimizations, the following files are needed:

INCAR – This file is used to set the calculation parameters such as optimization method, optimization tolerances, exchange correlation functional, planewave cutoff energy, spin polarization, etc.

KPOINTS – This file is used to set the Brillouin zone integration grid type (i.e., gamma-centered or Monkhorst-Pack) and k-point spacing.

POSCAR – This file is used to set the lattice vectors describing the unit cell as well as the atomic positions of all atoms in the unit cell. These positions can be specified as either Cartesian coordinates or lattice-vector-basis fractional coordinates. The degrees of freedom for each atom can be fixed or relaxed in this file as well using Selective Dynamics.

POTCAR – This file contains the core-electron representation information (i.e., pseudopotential or projector-augmented wave information) about each atom type defined in the POSCAR. This file is constructed by copying the potential

information from separate VASP files (for each atom/potential type) into one POTCAR file in the same order that the atom types appear in the POSCAR.

In VASP, the GGA exchange correlation functionals (set using the GGA tag in the INCAR file) available are the Perdew-Becke, Perdew-Wang 86, Langreth-Mehl-Hu, Perdew-Wang 91, Perdew-Burke-Ernzerhof, and revised Purdew-Burke-Ernzerhof. The revised Purdew-Burke-Ernzerhof (RPBE) functional is used for all VASP calculations in this study. In VASP, the optimization algorithm is set in the INCAR file using the IBRION tag. There are several built-in optimizers, which include the quasi-Newton (IBRION = 1), conjugate-gradient (IBRION = 2), and quick-min methods (IBRION = 3). Both the quasi-Newton and quick-min methods have force-based object functions, while the conjugate-gradient method has an energy-based object function. A force-based object function is intended to minimize the force below a specified criterion rather than finding a minimum in energy within a specified tolerance. The VTST Tools code provides several force-based optimizers, in addition to VASP's built-in optimizers. Once the VTST code is compiled along with VASP, these optimizers are available by setting the IOPT tag while setting the IBRION tag equal to 3 in the INCAR. These optimization methods include the Limited-memory Broyden-Fletcher-Goldfarb-Shanno (LBFGS) method (local or global), a force-based conjugate-gradient method, and a Fast Inertial Relaxation Engine (FIRE) method.

Performing Transition State Searches

For advanced transition state searches beyond standard NEB (such as climbing image NEB or first-order saddle point searches), additional code should be downloaded and installed from Graeme Henkelman's VASP TST Tools site (http://theory.cm.utexas.edu/vtsttools/). I will review the CI-NEB method and the Dimer method for finding transition states in VASP.

The CI-NEB method utilizes the same four files as a geometry optimization; however, there are multiple POSCAR files, one for each end point and intermediate image along the reaction coordinate. The KPOINTS and POTCAR files are not modified; however, the INCAR is modified to indicate that a CI-NEB job is desired (by setting ICHAIN = 0 and LCLIMB = .TRUE.), to specify the number of intermediate images using the IMAGES tag, and to specify the magnitude of the spring force between images for the elastic band calculation using the SPRING tag. Note that each POSCAR must be located in a separate subdirectory, numbered 00, 01, 02, etc. It is also recommended that no more than 4 to 5 intermediate images be used for the CI-NEB calculation for stable convergence. Also, if two local maxima are found during the CI-NEB calculation, it may be useful to alter the endpoints to remove the

lower-energy maxima from the CI-NEB reaction coordinate to ensure convergence to the proper saddle point geometry.

The Dimer method is a useful way to perform a first-order saddle point search in VASP.[91] The Dimer method is a min-mode following method, so the initial guess must be near the desired saddle point. Like Dacapo, this initial guess geometry to be used in the POSCAR file can be obtained through a NEB calculation, constrained optimizations, or intuition. The Dimer method utilizes the same four files as a geometry optimization, with the addition the MODECAR file. This file contains an initial direction for the dimer calculation and should be a guess at the lowest-curvature mode. If no MODECAR is specified (which is not advisable), a random search direction will be used. As part of the VTST Tools, Henkelman provides a script that can convert a NEB reaction path to a MODECAR for use in a Dimer calculation. Alternatively, for relatively straightforward reaction paths, I found simply stretching the bond that is breaking/forming and parameterizing the MODECAR with the vector describing this motion to be a successful method for creating the MODECAR without the need for NEB reaction coordinate information. When running a dimer calculation, no changes are required for the KPOINTS or POTCAR files are required; however, the INCAR must be modified to initialize the Dimer calculation (`ICHAIN = 1`, `IBRION = 3`, and `POTIM = 0`). Calculation parameters for the Dimer job can also be specified by the user if the default values are not desired. The parameters are explained in detail on the VTST Tools website.

For transition state searches (CI-NEB or Dimer calculations), it is important to use a force-based object function optimizer because the saddle-point search methods use a force projection to direct the solver toward the minimum energy path, which means that the energy is not always consistent with the force. Thus, it is recommended to use either the VASP built-in quasi-Newton or quick-min optimization method or one of the VTST code's optimizers, which have force-based object functions. The VTST code optimization methods have been analyzed by Sheppard, et al.[92] The global LBFGS method was found to be very effective for NEB and CI-NEB calculations. The force-based conjugate-gradient method and standard LBFGS methods were found to be efficient at finding minimum energy wells or saddle-points when the initial guess was near the well/saddle-point (accurate initial forces, which are required for accurate curvature information). When the initial guess is far from the minimum/saddle-point, methods that do not require curvature information such as the quick-min and FIRE methods are recommended, with the preferred method being the FIRE algorithm due to increased efficiency. For the VASP calculations performed in this work, the global LBFGS method was used for CI-NEB calculations while the standard LBFGS method was used for all Dimer calculations. The global implementation is preferred

for NEB and CI-NEB calculations because inter-image interactions can be included when calculating the inverse Hessian, resulting in greater optimization efficiency for multi-image calculations.[92]

Performing Frequency Calculations

Harmonic oscillator vibrational frequency calculations can be performed using the Dynamical Matrix method from Henkelman's VTST Tools. In addition to the four files used for geometry optimizations, the Dynamical Matrix method also requires a DISPLACECAR file. The DISPLACECAR file contains three entries for each atom in the system, defining the distance the atom will be displaced in each direction in the finite difference calculation. A typical displacement value is 0.001 Å. While the KPOINTS and POTCAR files require no modification, the INCAR should be modified to specify a Dynamical Matrix calculation (`ICHAIN = 1`, `IBRION = 3`, and `POTIM = 0`). In addition, the number of ionic relaxation steps (the `NSW` tag) must be defined such that it equals one more than the number of displacements to be performed (e.g., one more than three times the number of relaxed atoms). The one additional step is required to obtain the zero-displacement forces. Like frequency calculations in Dacapo, it is necessary to tighten tolerances for more accurate finite difference derivatives. In all VASP frequency calculations in this work, I apply a convergence tolerance of 1E-6 eV/Å on forces (compared to 1E-3 and 1E-4 eV/ Å for geometry optimizations and first-order saddle point searches, respectively). Note that an extremely effective parallelization strategy for Dynamical Matrix calculations is described on the VTST Tools website.

3.3 Obtaining Partition Functions for Heterogeneous Catalysis

The electronic structure calculations performed in software packages such as Dacapo or VASP provide 0 K electronic energies along with harmonic oscillator vibrational frequencies. Applying statistical thermodynamics to compute partition functions, the electronic energies and vibrational frequencies can be combined to arrive at thermodynamic quantities such as enthalpy, entropy, and free energy that provide the information necessary to model a system at industrially-relevant temperatures and pressures. In heterogeneous catalysis, it is necessary to describe the behavior of both gas phase species as well as species that exist on the surface. Due to differences in the degrees of freedom between gas phase and surface species, the partition functions that describe the species differ. Below, the partition functions for gas phase and surface species are introduced.

Partition Functions for Gas Phase Species

The total partition functions for gas phase species are calculated using standard formulas.[93] The total species partition function is expressed as a combination of the translational, rotational, and vibrational partition functions:

$$q_{tot} = q_{3D-trans} q_{rot} q_{vib}. \qquad [\text{ Equation 3-1 }]$$

The three-dimensional translational partition function takes the form

$$q_{\text{3D-trans}} = \left(\frac{2\pi M k_B T}{h^2}\right)^{\frac{3}{2}} \underline{V}_o = \left(\frac{2\pi M k_B T}{h^2}\right)^{\frac{3}{2}} \left(\frac{NkT}{P_o}\right), \qquad [\text{ Equation 3-2 }]$$

where M is the mass of the gas phase species, k_B is Boltzmann's constant, h is Plank's constant, and the (kT/P_o) term represents the standard state volume per molecule within which the species is translating (calculated using the standard state pressure, P_o). The rotational partition function for a non-linear polyatomic molecule takes the form:

$$q_{\text{rot}} = \left(\frac{1}{\sigma}\right)\left(\frac{8\pi^3 k_B T}{h^2}\right)^{\frac{3}{2}} I_x^{1/2} I_y^{1/2} I_z^{1/2}, \qquad [\text{ Equation 3-3 }]$$

where, I is the moment of inertia of the adsorbate about the subscripted axis and σ is the symmetry number (e.g., $\sigma = 2$ for CO_2). The remaining $3N_{atoms}$-6 (for non-linear polyatomic molecules of N_{atoms} atoms) or $3N_{atoms}$-6 (for linear polyatomic molecules of N_{atoms} atoms) degrees of freedom are treated using the harmonic oscillator vibrational partition function. The resulting vibrational partition function (with reference energy at the ground vibrational state) takes the form

$$q_{vib} = \prod_{i=1}^{\#\text{ Vib. Modes}} \left(\frac{1}{1-e^{-h\nu_i/k_B T}}\right) \qquad [\text{ Equation 3-4 }]$$

where ν_i is the frequency describing the i^{th} vibrational mode. Alternatively, the partition function can be written with a reference energy at the classical minimum (i.e., the bottom of the well), which takes the form

$$q'_{vib} = \prod_{i=1}^{\#\text{ Vib. Modes}} \left(\frac{e^{-h\nu_i/2k_BT}}{1-e^{-h\nu_i/k_BT}} \right) \qquad [\text{ Equation 3-5 }]$$

Finally, the total partition function, Q, for a system of N indistinguishable gas phase molecules, each with an individual partition function q_{tot} is expressed as

$$Q = \frac{q_{tot}^N}{N!}. \qquad [\text{ Equation 3-6 }]$$

Partition Functions for Surface Species

The following discussion of partition functions is taken primarily from a section of our previously published manuscript concerning SMR over Ni(111).[12] When a gas phase molecule adsorbs, one translational mode is converted to a surface-adsorbate vibrational stretching mode. If the DFT-predicted barrier to diffusion is large relative to the thermal energy available to the adsorbate (k_BT), then the other two translational modes can be well-described as frustrated translations, which behave like vibrations. On the other hand, if the DFT-predicted diffusion barrier is small compared to k_BT, the potential energy landscape felt by the adsorbate due to the surface appears nearly flat, and the adsorbate exhibits essentially free translation in two-dimensions. An analogous argument can be made for adsorbate rotation. It is generally found that the barriers for rotation and translation scale with the binding energy, thus the statistical mechanical treatments are divided into weakly bound and strongly bound cases. The process for obtaining thermodynamic properties is diagramed in Figure 3-5.

Strongly Bound, Localized Case.

Harmonic vibrational frequencies are computed via finite differences from analytical first derivatives. These frequencies are used to calculate the harmonic oscillator partition function for a species with reference energy at the ground vibrational state, which takes the form:

$$q_{HO} = \prod_{i=1}^{3N} \left(\frac{1}{1-e^{-h\nu_i/k_BT}} \right) \qquad [\text{ Equation 3-7 }]$$

where, N is the total number of relaxed atoms included in the frequency calculation and ν_i is the i-th frequency.

The total partition function for a system of N strongly-bound indistinguishable surface species distributed or a lattice of M labeled sites takes the form

$$Q = \frac{M! q_{tot}^N}{(M-N)!N!}. \qquad \text{[Equation 3-8]}$$

Note that the statistical factor formed by the factorials of M and N is an expression of the total number of unique molecular configurations for the system.

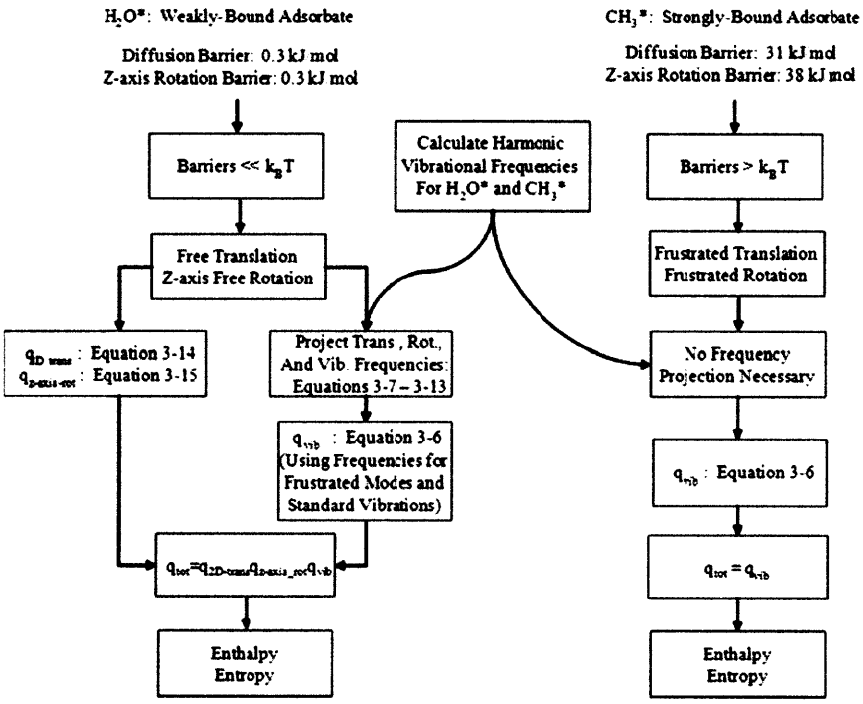

Figure 3-5: Procedure for Statistical Thermodynamic Treatment on Ni(111) at T = 800°C, $k_BT \sim 8$ kJ/mol

Weakly Bound, Mobile Case.

When the barrier for translation and/or rotation is much less than k_BT, the mode(s) can be treated as free motion. In order to treat the free motion of the adsorbates properly, it is necessary to identify the

vibrational modes corresponding to adsorbate translation and/or rotation relative to the surface. We first compute the Hessian using the same procedure as in the strongly bound case. To identify these translational/rotational modes explicitly and automatically, we separately project adsorbate translation and/or rotation about an axis out of the mass-weighted nuclear Hessian for these adsorbates. This procedure is completely analogous to that used to project out translation and rotation from the nuclear Hessian in most gas-phase quantum chemistry software packages/algorithms.

For adsorbate translation, movement in a direction (e.g., x-direction) can be projected out of the Hessian using a vector describing synchronized motion of the adsorbate atoms (in the x-direction) while the surface atoms do not move, in order to maintain alignment between the top-layer metal atoms which can move in the vibrational calculation with the lower-layer metal atoms which are fixed throughout. If we have N_{ads} adsorbate atoms with a combined mass of M and N total atoms, the vector of length $3*N$ becomes:

$$\langle t_x| = \frac{1}{\sqrt{M}}\left(\sqrt{m_1},0,0,\sqrt{m_2},0,0,...,\sqrt{m_{N_{ads}}},0,0,0,0,0,...,0,0,0\right), \qquad [\text{ Equation 3-9 }]$$

where, m_i is the mass of the i-th adsorbate atom. The inverse square root of the combined mass serves as a normalization factor. A similar vector can be constructed for motion in the y-direction, resulting in the projector:

$$\hat{P}_{trans} = |t_x\rangle\langle t_x| + |t_y\rangle\langle t_y|. \qquad [\text{ Equation 3-10 }]$$

For rotation, the situation is similar. When considering rotation of an adsorbate on a surface, we divide rotations into two classes: bond-breaking and bond-preserving. We define bond-breaking rotational modes as those that involve significant changes in the primary metal-adsorbate bond length as the atom rotates away from the metal surface, essentially breaking the metal-adsorbate bond. On the other hand, bond-preserving rotations describe modes where the primary metal-adsorbate bond remains more-or-less intact throughout the rotation. The barriers for bond-breaking rotations are generally quite high because of the stress placed on the metal-adsorbate bond; therefore, these modes are treated as harmonic oscillations. However, for the case of weakly-bound species, the bond-preserving rotational barrier may be considerably lower. When the barrier for this rotation is much less than k_BT, we treat the mode as free rotation (otherwise it too is treated as a harmonic oscillation). To isolate the free rotational mode (about

an axis described by the unit vector $\mathbf{v}_c$) from the remaining modes, the rotational projection vector of length $3*N$ is written as:

$$\langle r_c | = \left(\mathbf{r}_\mathbf{c}^1, \mathbf{r}_\mathbf{c}^2, \ldots, \mathbf{r}_\mathbf{c}^{N_{ads}}, 0,0,0, \ldots, 0,0,0 \right). \qquad [\text{ Equation 3-11 }]$$

The rotational projection vector, like the translational projection vector, should be normalized, which is performed numerically in our projection code. The projection vector has elements corresponding to the (x,y,z) coordinates of the i-th adsorbate atom given by:

$$\mathbf{r}_\mathbf{c}^\mathbf{i} = \sqrt{m_i} \left(\mathbf{R}_\mathbf{i} - \mathbf{R}_\mathbf{cm}^\mathbf{ads} \right) \times \left(-\mathbf{v}_c \right) \qquad [\text{ Equation 3-12 }]$$

where, m_i is the mass of the i-th adsorbate atom, $\mathbf{R}_\mathbf{i}$ are the nuclear coordinates of the i-th atom of the adsorbate, and $\mathbf{R}_\mathbf{cm}^\mathbf{ads}$ are the coordinates of the center of mass of the adsorbate. The metal atoms are ignored in the rotation and are each described by a row vector of zeros, (0,0,0), in Equation 3-11. The rotational projection vector is constructed analogously to the translational projection vector, taking the form:

$$\hat{P}_{rot} = |r_c\rangle\langle r_c|. \qquad [\text{ Equation 3-13 }]$$

The translational and rotational projection vectors are used to calculate the vibrational projection vector as follows:

$$\hat{P}_{vib} = \hat{I} - \hat{P}_{trans} - \hat{P}_{rot}. \qquad [\text{ Equation 3-14 }]$$

The projected vibrational frequencies are found by diagonalizing the projected mass-weighted Hessian, H_{vib}:

$$H_{vib} = \left(\hat{P}_{vib} \right)^T H \hat{P}_{vib}. \qquad [\text{ Equation 3-15 }]$$

In making these projections, we assume that there is little coupling between translational, rotational and vibrational modes, which is truer for weakly-bound adsorbates than for strongly-bound adsorbates. Therefore, we use projected frequencies for only weakly-bound adsorbates. Using these projected

frequencies, the appropriate partition functions for translation, z-axis rotation, and vibration can be calculated.

For free translation in two dimensions, the partition function takes the form:

$$q_{\text{2D-trans}} = \left(\frac{2\pi M_{ads} k_B T}{h^2} \right) \underline{\alpha}_o = \left(\frac{2\pi M_{ads} N k_B T}{h^2} \right) N^o_{sites} A \qquad [\text{ Equation 3-16 }]$$

where, $\underline{\alpha}_o$ is the standard state area of the box within which the molecule is translating, A is the surface area per binding site (5.365×10^{-20} m^2 for Ni(111) and Ni(211); 6.196×10^{-20} m^2 for Ni(100)) and N^o_{sites} is the standard state number of binding sites per adsorbate. For example, for a standard state coverage of one monolayer, the value of N^o_{sites} is one. The term $N^o_{sites} A$ defines the size of box that the molecule is free to translate within, analogous the gas phase standard state volume in the translational partition function.

For weakly bound species with a low barrier to rotation about an axis, the free rotation partition function takes the form:

$$q_{\text{rot}} = \sqrt{\left(\frac{8\pi^3 I k_B T}{\sigma^2 h^2} \right)} \qquad [\text{ Equation 3-17 }]$$

where, I is the moment of inertia of the adsorbate about the axis described by $\mathbf{v}_c$ and σ is the symmetry number (e.g., $\sigma = 2$ for CO_2). The harmonic oscillator partition function is applied to treat 1) frustrated translational/rotational modes with barriers too high to allow for free motion analysis as well as 2) all remaining standard vibrational modes. Using the projected frequencies from Equation 3-15, the harmonic oscillator partition function is calculated using Equation 3-7, but with product limits from 1 to ($3N - N_{free\ modes}$). As shown in Figure 3-5, the total partition function for a surface species, q_{tot}, is a product of the appropriate subspace partition functions q_{trans}, q_{rot}, and q_{vib}, which are calculated for one adsorbate in a single unit cell.

It should be noted that, as a consequence of periodic boundary conditions, the vibrational frequencies calculated in this manner include only motions where the adsorbate atoms, the surface metal atoms, and all of their periodic images move synchronously. This approximation eliminates many of the degrees of freedom found in the true system. The assumption is that the neglected frequencies do not change

significantly during the course of a reaction, leading to a cancellation of errors that makes these approximations tolerable.

Finally, the total partition function for a system of N indistinguishable weakly-bound surface species (with free translation) is expressed as

$$Q = \frac{q_{tot}^N}{N!} \qquad \text{[Equation 3-18]}$$

Note that Equation 3-18 is identical to Equation 3-6, reflecting the analogy between a weakly-bound surface species and a free two-dimensional gas. Note that unlike Equation 3-8, there is no statistical factor comprised of M and N because the weakly-bound adsorbates are not restricted to discrete binding sites on the surface, but rather can exist in a continuum of locations within the area A.

3.4 Obtaining Thermodynamic Properties from Partition Functions in Heterogeneous Catalysis

The values of enthalpy, entropy, and free energy are required to describe the behavior of a system at industrially-relevant temperatures and pressures. These quantities can be obtained directly from the partition function for the species of interest, as detailed below.

Gas Phase Species

The partition function of a species is related to thermodynamic properties through the Helmholtz free energy, $\underline{A}$, using

$$\underline{A} = -k_B T \ln Q. \qquad \text{[Equation 3-19]}$$

In differential form, the Helmholtz free energy of a pure gas phase species is expressed as

$$d\underline{A} = -\underline{S}dT - PdV + \mu dN, \qquad \text{[Equation 3-20]}$$

where μ is the chemical potential of the species and N is the number of gas phase molecules. As indicated by this differential form of Helmholtz free energy, the entropy of the species is calculated using

$$\underline{S} = -\left(\frac{\partial \underline{A}}{\partial T}\right)_{V,N}. \qquad [\text{ Equation 3-21 }]$$

Substituting Equation 3-6 and Equation 3-19 into Equation 3-21 relates the entropy of a gas phase species to the partition function for that species, yielding

$$\underline{S} = \frac{\partial}{\partial T}\left[k_B T \ln\left(\frac{q_{tot}^N}{N!}\right)\right]_{V,N}. \qquad [\text{ Equation 3-22 }]$$

Applying Stirling's approximation, removing volume from the partition function, and differentiating Equation 3-22 gives the following expression for the entropy of a gas phase species

$$\underline{S}^o = Nk_B\left[T\left(\frac{\partial \ln q_{tot}}{\partial T}\right)_{V,N} + \ln\left(\frac{q_{tot}' V_o}{N}\right) + 1\right]. \qquad [\text{ Equation 3-23 }]$$

Note that the term ($\underline{V}_o$ / N) can be replaced with ($k_B T$ / P_o) to compute the entropy at a standard state pressure. The internal energy is an explicit function of the external variables entropy, volume, and chemical composition (number of molecules) (i.e., $\underline{U} = \underline{U}(S,V,N)$). Thus, differential form of the internal energy, also called the fundamental equation of thermodynamics, takes the form

$$d\underline{U} = Td\underline{S} - Pd\underline{V} + \mu dN. \qquad [\text{ Equation 3-24 }]$$

The internal energy of a species is related to the Helmholtz free energy through a Legendre transform of internal energy with respect to (+T$\underline{S}$), taking the form

$$\underline{A} = \underline{U} - T\underline{S}. \qquad [\text{ Equation 3-25 }]$$

Substituting Equation 3-6, Equation 3-19, and Equation 3-23 into Equation 3-25 provides the relationship between the internal energy of a species and its partition function

$$\underline{U} = Nk_B\left[T^2\left(\frac{\partial \ln q_{tot}}{\partial T}\right)_{V,N}\right]. \qquad \text{[Equation 3-26]}$$

In computational studies, the energy computed through DFT calculations is a zero-Kelvin electronic energy. The relationship between electronic energy and internal energy is obtained by re-writing the partition function with energy referenced to the classical minimum from Equation 3-5 (giving the species an energy equal to the classical electronic energy of E_b obtained via electronic structure calculations) and performing the differentiation in Equation 3-26, giving

$$\underline{U} = NE_b + \frac{3}{2}Nk_BT + \frac{3}{2}Nk_BT + N\sum_i \frac{h\nu_i}{2} + N\sum_i \frac{h\nu_i}{\exp\left(\frac{h\nu_i}{k_BT}\right)-1} \qquad \text{[Equation 3-27]}$$

$$\underline{U} = N\left(E_b + U_{trans} + U_{rot} + E_{ZPE} + E_{Therm}\right)$$

where U_{trans} is the translational contribution to internal energy, U_{rot} is the rotational contribution to internal energy, E_{ZPE} is the zero-point energy correction, E_{Therm} is the thermal correction, and $\{\nu_i\}$ is the set of vibrational frequencies obtained via electronic structure calculations. The enthalpy of a species, $\underline{H}$, is defined as the Legendre transform of internal energy with respect to (-P$\underline{V}$), thus taking the form

□ EMBED Equation.DSMT4 $\underline{H} = \underline{U} + P\underline{V} = \underline{U} + Nk_BT.$ [Equation 3-28]

The ideal gas law is applied in Equation 3-28 to convert the PV term to Nk_BT. Note that enthalpy is a function of the extensive variables of entropy and chemical composition and the intensive variable pressure. An additional Legendre transformation of enthalpy with respect to (+T$\underline{S}$) yields the Gibbs free energy, $\underline{G}$, which is a function of the intensive properties of temperature and pressure and the extensive variable chemical composition

$$\underline{G}^o = \underline{H} - T\underline{S}^o. \qquad \text{[Equation 3-29]}$$

Substituting Equation 3-23 and Equation 3-28 into Equation 3-29 relates the Gibbs free energy of a species to its partition function, yielding

$$\underline{G}^o = Nk_B\left[T^2\frac{\partial \ln q_{tot}}{\partial T}\right]_{V,N} + Nk_BT - Nk_BT\left[T\left(\frac{\partial \ln q_{tot}}{\partial T}\right)_{V,N} + \ln\left(\frac{q_{tot}^{'}V_o}{N}\right)+1\right]$$

$$\underline{G}^o = -Nk_BT\ln\left(\frac{q_{tot}^{'}V_o}{N}\right) = -Nk_BT\ln\left(q_{tot}^{'}\frac{k_BT}{P_o}\right). \qquad \text{[Equation 3-30]}$$

The above extensive thermodynamic functions are converted to an intensive (per mole) basis by dividing by the number of gas phase molecules, producing

$$U = RT^2\left(\frac{\partial \ln q_{tot}}{\partial T}\right)_{V,N} = E_b + U_{trans} + U_{rot} + E_{ZPE} + E_{Therm}$$

$$S^o = R\left[T\left(\frac{\partial \ln q_{tot}}{\partial T}\right)_{V,N} + \ln\left(\frac{q_{tot}^{'}V_o}{N}\right)+1\right]$$

$$H = RT\left[T\left(\frac{\partial \ln q_{tot}}{\partial T}\right)_{V,N} + 1\right] \qquad \text{[Equation 3-31]}$$

$$G^o = -RT\ln\left(\frac{q_{tot}^{'}V_o}{N}\right) = -RT\ln\left(q_{tot}^{'}\frac{k_BT}{P_o}\right).$$

Strongly-Bound Surface Species

The thermodynamic quantities for strongly-bound adsorbates are derived analogously to those for the gas phase. The differential internal energy for an adsorbed lattice gas takes the form[94]

$$d\underline{U} = Td\underline{S} - \Phi dM + \mu dN, \qquad \text{[Equation 3-32]}$$

where Φ is essentially a pressure term, analogous to gas-phase pressure, but in units of energy here for the surface. In this equation, M (the total number of binding sites on the lattice) is the extensive property defining the size of the system, analogous to volume for the gas phase. Euler integration of Equation 3-32 (over the extensive properties $\underline{S}$, M, and N) yields the following expression for internal energy of a surface species

$$\underline{U} = T\underline{S} - \Phi M + \mu N. \qquad \text{[Equation 3-33]}$$

Obtaining Helmholtz free energy from the Legendre transform of internal energy with respect to (+T$\underline{S}$) yields a Helmholtz free energy expression identical to that for the gas phase, taking the form of Equation

3-25. Differentiating Equation 3-25 and substituting in Equation 3-32 provides the following description of differential Helmholtz free energy

$$d\underline{A} = -\underline{S}dT - \Phi dM + \mu dN. \qquad \text{[Equation 3-34]}$$

Analogous to the gas phase, the entropy of a tightly-bound surface species is defined as

$$\underline{S} = -\left(\frac{\partial \underline{A}}{\partial T}\right)_{M,N}. \qquad \text{[Equation 3-35]}$$

Substituting Equation 3-8 and Equation 3-19 into Equation 3-35 provides the following relationship between the entropy of a tightly-bound surface species and its partition function

$$\underline{S} = \frac{\partial}{\partial T}\left(k_B T \ln\left(\frac{M! q_{tot}^N}{(M-N)!N!}\right)\right)_{M,N}. \qquad \text{[Equation 3-36]}$$

Applying Stirling's approximation to Equation 3-36 (assuming $M >> 1$, $N >> 1$, and $M >> N$) and applying the product rule yields

$$\underline{S} = \ln\left(\frac{M}{M-N}\right)^M + N \ln q_{tot} + N \ln\left(\frac{M-N}{N}\right) + Nk_B T\left(\frac{\partial \ln q_{tot}}{\partial T}\right)_{M,N}. \qquad \text{[Equation 3-37]}$$

Performing the substitution of standard state number of binding sites per adsorbate $N^o_{sites} = M / N$, assuming $N^o_{sites} - 1 \approx N^o_{sites}$ (i.e., $N^o_{sites} >> 1$) yields

$$\underline{S}^o = Nk_B\left(T\left(\frac{\partial \ln q}{\partial T}\right)_{M,N} + \ln N^o_{sites} q_{tot} + \ln\left(\frac{N^o_{sites}}{N^o_{sites}+1}\right)^{N^o_{sites}}\right). \qquad \text{[Equation 3-38]}$$

Letting $N^o_{sites} = x + 1$ and applying the definition of Euler's constant[1] reduces the expression of entropy for a tightly-bound adsorbate to

[1] Limit as ($x \rightarrow \infty$) of $[1 + (1/x)]^x = e$

$$\underline{S}^o = Nk_B\left(T\left(\frac{\partial \ln q}{\partial T}\right)_{M,N} + \ln N^o_{sites} q_{tot} + \ln\left(1+\frac{1}{x}\right)^{x+1}\right)$$

$$\underline{S}^o = Nk_B\left(T\left(\frac{\partial \ln q}{\partial T}\right)_{M,N} + \ln N^o_{sites} q_{tot} + 1\right). \qquad \text{[Equation 3-39]}$$

Note that this equation is analogous to Equation 3-23, where the standard state number of binding sites per adsorbate (or the inverse of the standard state concentration of the tightly-bound adsorbate) replaces the ($\underline{V}_o$ / N) term (or the inverse of the standard state concentration of the gas phase species). The internal energy of a tightly-bound adsorbate is obtained analogously to that for a gas phase species, resulting in the expression

$$\underline{U} = Nk_B\left[T^2\left(\frac{\partial \ln q_{tot}}{\partial T}\right)_{M,N}\right]. \qquad \text{[Equation 3-40]}$$

The relationship between electronic energy obtained from electronic structure calculations and the internal energy is obtained by re-writing the partition function with reference energy at the classical minimum (giving the species a classical electronic energy of E_b obtained via electronic structure calculations relative to a common zero of energy) and performing the differentiation in Equation 3-40, giving

$$\underline{U} = NE_b + N\sum_i \frac{h\nu_i}{2} + N\sum_i \frac{h\nu_i}{\exp\left(\frac{h\nu_i}{k_B T}\right)-1}$$

$$\underline{U} = N\left(E_b + E_{ZPE} + E_{Therm}\right). \qquad \text{[Equation 3-41]}$$

Note that unlike the gas phase, the internal energy for a tightly-bound adsorbate has no contributions from translation or rotation.

The enthalpy is obtained by performing a Legendre transformation of internal energy with respect to the intensive/extensive variable pair (-ΦM), which is analogous to (-P$\underline{V}$) for the gas phase. The enthalpy of a tightly-bound adsorbate takes the form

$$\underline{H} = \underline{U} + \Phi M. \qquad \text{[Equation 3-42]}$$

From Equation 3-34, it is seen that Φ can be expressed as

$$\Phi = -\left(\frac{\partial \underline{A}}{\partial M}\right)_{T,N}. \qquad \text{[Equation 3-43]}$$

Substituting Equation 3-8 and Equation 3-19 into Equation 3-43 and applying Stirling's approximation provides the relationship between Φ and the other variables in the system, as shown below

$$\frac{\Phi}{k_B T} = \frac{\partial}{\partial M}\left(\ln \frac{M! q^N}{(M-N)!N!}\right)_{N,T}$$

$$\frac{\Phi}{k_B T} = \frac{\partial}{\partial M}\left(M \ln M - (M-N)\ln(M-N) - N \ln N + N \ln q\right)_{N,T} \qquad \text{[Equation 3-44]}$$

$$\frac{\Phi}{k_B T} = \ln M + 1 - \ln(M-N) - \left(\frac{M-N}{M-N}\right)$$

$$\frac{\Phi}{k_B T} = \ln\left(\frac{M}{M-N}\right).$$

The resulting expression is re-written in terms of N_{sites}, taking the form

$$\Phi M = k_B T \ln\left(\frac{M}{M-N}\right)^M$$

$$\Phi M = N k_B T \ln\left(\frac{N_{sites}}{N_{sites}-1}\right)^{N_{sites}}. \qquad \text{[Equation 3-45]}$$

Letting $N_{sites} = x + 1$ and applying the definition of Euler's constant to Equation 3-44 yields

$$\Phi M = N k_B T \ln\left(1 + \frac{1}{x}\right)^{x+1}$$

$$\Phi M = N k_B T. \qquad \text{[Equation 3-46]}$$

The resulting expression, $\Phi M = N k_B T$, is analogous to the ideal gas equation and can be viewed as the ideal localized lattice gas equation. Substituting this expression into Equation 3-42 yields an expression for the enthalpy of a tightly-bound adsorbate that is identical to that for a gas-phase species

$$\underline{H} = \underline{U} + Nk_B T. \qquad \text{[Equation 3-47]}$$

Performing a Legendre transformation of enthalpy with respect to (+T$\underline{S}$) and substituting in expressions for internal energy and entropy yields the relationship between the Gibbs free energy for a tightly-bound adsorbate and its partition function

$$\underline{G}^o = \underline{H} - T\underline{S}^o = \underline{U} + Nk_B T - T\underline{S}^o$$

$$\underline{G}^o = Nk_B T^2 \left(\frac{\partial \ln q_{tot}}{\partial T} \right)_{M,N} + Nk_B T - Nk_B T \left[T \left(\frac{\partial \ln q_{tot}}{\partial T} \right)_{M,N} + \ln\left(N^o_{sites} q_{tot} \right) + 1 \right] \qquad \text{[Equation 3-48]}$$

$$\underline{G}^o = -Nk_B T \ln\left(N^o_{sites} q_{tot} \right).$$

The above extensive thermodynamic functions are converted to an intensive (per mole) basis by dividing by the number of adsorbed molecules, producing

$$U = RT^2 \left(\frac{\partial \ln q_{tot}}{\partial T} \right)_{V,N} = E_b + E_{ZPE} + E_{Therm}$$

$$S^o = R \left[T \left(\frac{\partial \ln q_{tot}}{\partial T} \right)_{V,N} + \ln\left(N^o_{sites} q_{tot} \right) + 1 \right] \qquad \text{[Equation 3-49]}$$

$$H = RT \left[T \left(\frac{\partial \ln q_{tot}}{\partial T} \right)_{V,N} + 1 \right]$$

$$G^o = -RT \ln\left(N^o_{sites} q_{tot} \right).$$

Weakly-Bound Surface Species

The thermodynamic properties of weakly-bound surface species are derived similarly to those for gas-phase and tightly-bound surface species, but starting from a modified form of the differential internal energy, as suggested by Hill[94]. The term surface, or spreading, pressure (φ) is introduced, which is defined as

$$\varphi = \frac{\Phi}{A} = \frac{\Phi M}{\underline{\alpha}}, \qquad \text{[Equation 3-50]}$$

where, A is the area of a single binding site and $\underline{\alpha}$ is the area of the two-dimensional lattice. Recognizing that A is a constant intensive variable for a system, substituting Equation 3-50 into Equation 3-32 results in the following differential internal energy expression for a weakly-bound two-dimensional lattice gas

$$d\underline{U} = Td\underline{S} - \varphi d\underline{\alpha} + \mu dN. \qquad \text{[Equation 3-51]}$$

This expression is analogous to Equation 3-24 for a gas-phase species, but with surface pressure (φ) (rather than gas phase pressure, P) and the size of the box within which the molecule is translating defined by the area of the lattice ($\underline{\alpha}$) (rather than volume, $\underline{V}$). Similarly, substituting Equation 3-50 into Equation 3-46 yields the ideal lattice gas equation for a weakly-bound adsorbate, taking the form

$$\varphi A = Nk_B T. \qquad \text{[Equation 3-52]}$$

Thus by analogy to the gas-phase and strongly-bound surface species, the thermodynamic properties for a weakly-bound, freely-translating surface species take the form

$$\begin{aligned} U &= RT^2\left(\frac{\partial \ln q_{tot}}{\partial T}\right)_{\alpha,N} = E_b + U_{2D-trans} + U_{rot} + E_{ZPE} + E_{Therm} \\ S^o &= R\left[T\left(\frac{\partial \ln q_{tot}}{\partial T}\right)_{\alpha,N} + \ln\left(\frac{q_{tot}^{'}\alpha_o}{N}\right) + 1\right] \\ H &= RT\left[T\left(\frac{\partial \ln q_{tot}}{\partial T}\right)_{\alpha,N} + 1\right] \\ G^o &= -RT\ln\left(\frac{q_{tot}^{'}\alpha_o}{N}\right) = -RT\ln\left(q_{tot}^{'}N_{sites}^{o}A\right). \end{aligned} \qquad \text{[Equation 3-53]}$$

Note that in the Gibbs free energy expression, α_o defines the standard state area of the box within which the weakly-bound surface species is translating, completely analogous to $\underline{V}_o$ in Equation 3-31, the standard state volume of the box within which the gas-phase species is translating.

Chapter 4. Kinetic Modeling of Heterogeneous Catalysis

4.1 Introduction

To simulate heterogeneous catalysis, the thermodynamic quantities derived in Chapter 3 are combined with kinetic parameters such as Arrhenius pre-exponential factors and activation energies to develop a kinetic model. In this work, mean-field (MF) microkinetic modeling is applied to study heterogeneous catalysis. Microkinetic modeling is an attractive technique for obtaining detailed information about surface reactions and intermediates because it applies elementary reactions with no assumption of rate-determining step or most-abundant reaction intermediate (MARI).[52] In MF microkinetic modeling, a set of proposed elementary reactions and intermediate surface species is used to define the reaction mechanism. The microkinetic model is then parameterized either experimentally (e.g., through parameter estimation followed by data regression) or computationally (e.g., through DFT calculations). A drawback of experimental parameterization is that the size of the proposed mechanism must be kept reasonably small to ensure statistical significance of the parameters fit through experiment. Computational parameterization of the microkinetic model, on the other hand, allows for larger mechanisms, limited only by the computational resources available for computing the thermochemistry and kinetics of the elementary reactions and intermediate species.

Microkinetic modeling has become a popular tool, applied to study many heterogeneous catalytic systems such as ammonia decomposition over ruthenium[95] as well as ammonia synthesis over iron,[96] copper,[97] and ruthenium.[98] Microkinetic modeling has also been applied to the reaction of interest in this study, steam methane reforming and its reverse. Aparicio applied transient isotopic experimental studies to parameterize a microkinetic model for methane reforming over nickel,[50] which was built upon by Chen, et al., including the addition of deactivation effects.[53] While these studies focused on the methane reforming reaction, Alstrup also applied experimentally-parameterized microkinetic modeling to study the reverse reaction, CO methanation over nickel.[99] In addition to experiment, computation has also been applied to the parameterization of microkinetic models. Chen et al. have recently employed the activation exponential potential (UBI-QEP) approach and transition state theory to the microkinetic modeling of SMR.[54] Furthermore, density functional theory (DFT) has become a popular computational tool for describing heterogeneous catalysis, including many recent applications to methane reforming.[32, 39, 56, 57, 70]

Mean-field microkinetic modeling is employed in this work rather than kinetic Monte Carlo (KMC)[100-103] modeling due to the large size of the system of interest and the large computational expense of KMC. Implicit in the MF model is the assumption that the local concentration of a surface species can be described by the average concentration of that species on the surface. A physical interpretation of this assumption is that diffusion on the surface is fast relative to reaction, leading to diminishingly small concentration gradients. As will be discussed in subsequent chapters, diffusion barriers found for SMR over the nickel catalyst are generally considerably smaller than barriers to chemical reaction, offering some support for the use of the MF model. Also, the MF model is believed to be more accurate at lower surface coverages, due to the greater probability of a species "finding" a vacant site to which to diffuse.[104] At the high temperatures relevant to SMR, the surface is more likely to have a high concentration of vacant sites than it is at low temperatures (due to the entropic loss upon adsorption), further offering support for the use of the MF model. It should be noted, however, that the KMC model offers a more complete description of the catalytic process with fewer approximations and higher resolution to capture non-uniformity than the MF model; therefore, the MF model is considered less accurate, particularly in systems where co-adsorbate interactions are important.[105] As a result, the kinetic results from MF modeling are more useful in capturing trends than providing absolute accuracy. It should be noted that one drawback of the KMC model compared to the MF model is that the KMC model suffers from statistical sampling error, which is not an issue for the MF model.

In this chapter, Transition State Theory (TST) [106, 107] is applied to derive rate expressions for the reactions involved in heterogeneous catalysis, including partition functions, standard state corrections, and thermodynamic constraints for the reverse rate. Similar to the thermodynamic parameters in Chapter 3, rate expressions are presented to account for both mobile (weakly-bound) and localized (strongly-bound) adsorbates. In practice, the kinetic parameters obtained from these rate expressions are used to parameterize the mean-field microkinetic model. The microkinetic model is then combined with a reactor model to simulate heterogeneous catalysis and perform kinetic investigations such as flux analysis and sensitivity analysis. Flux analysis provides insight into the active reaction pathways on the catalyst surface while sensitivity analysis identifies the key reactions and species whose thermochemistry or kinetics have the greatest impact on the overall reaction rate. In this chapter, incorporation of the microkinetic model into a Continuously Stirred Tank Reactor (CSTR) and an ideal Plug Flow Reactor (PFR) will be discussed.

4.2 Overview of Transition State Theory for Gas Phase Rate Expressions

The rate at which a species disappears due to an elementary chemical reaction (e.g., A(g) + B(g) → C(g)) is expressed as

$$-\frac{dN_A}{dT} = \nu N_{AB^\dagger}, \qquad \text{[Equation 4-1]}$$

where N_A is the number of reactant molecules, ν is the frequency at which the reacting species crosses the reaction barrier and $N_{AB\dagger}$ is the number of transition state molecules. Transition state theory, which was developed through the work of Pelzer,[108] Wigner,[109] Eyring,[110] and Evans and Polanyi,[111] is used to describe the rate of the chemical reaction as

$$-\frac{dN_A}{dT} = \left(\frac{k_B T}{h}\right)\left(\frac{q_{AB^\dagger}}{q_A q_B}\right)\exp\left(\frac{-E_o}{RT}\right)N_A N_B. \qquad \text{[Equation 4-2]}$$

where, q_i is the partition function of the i^{th} species referenced to the energy at the ground vibrational state of i (i.e., zero-point energy), E_o is the reaction barrier from the zero-point energy of the reactants to the zero-point energy of the transition state, and all transition state molecules are assumed to proceed to product (i.e., the transmission coefficient is one). Transition state theory provides a framework for relating the number of transition state molecules to the number of reactant molecules. As discussed in the literature, the transition state theory formula can be expressed in terms of an effective chemical potential of the transition state through a quasi-equilibrium approximation, taking the form

$$\mu_A + \mu_B = \mu_{AB^\dagger}, \qquad \text{[Equation 4-3]}$$

where μ is the chemical potential of the subscripted component. Using this equilibrium relationship, the thermodynamic properties discussed in Chapter 3 can be used to relate the number of transition state molecules to reactant molecules, ultimately arriving at the rate expression shown in Equation 4-2. This approach provides a useful framework for the derivation of the rate expressions for the reactions of heterogeneous catalysis in the following sections.

Note that the partition functions in the rate expression in Equation 4-2 contain a translational partition function with an actual system volume term. To remove this dependence on actual system volume, the rate expression is converted from a number basis to a concentration basis by dividing out this volume dependence. The partition functions are then converted to standard state partition functions (calculated at the standard state volume), which introduces a standard state correction term. The resulting rate expression is

$$-\frac{d[A]}{dT}=\left(\frac{k_B T}{h}\right)\left(\frac{q^o_{AB^\dagger}}{q^o_A q^o_B}\right)\left(\frac{RT}{P_o}\right)\exp\left(\frac{-E_o}{RT}\right)[A][B]. \qquad \text{[Equation 4-4]}$$

From this rate expression, the rate coefficient for the chemical reaction takes the form

$$k_{for}=\left(\frac{k_B T}{h}\right)\left(\frac{q^o_{AB^\dagger}}{q^o_A q^o_B}\right)\left(\frac{RT}{P_o}\right)\exp\left(\frac{-E_o}{RT}\right) \qquad \text{[Equation 4-5]}$$

The rate coefficient can also be presented in its thermodynamic representation by re-writing Equation 4-5 to relate the equilibrium constant to the Gibbs free energy

$$k_{for}=\left(\frac{k_B T}{h}\right)\exp\left(\frac{-\Delta G^{o\dagger}}{RT}\right)\left(\frac{RT}{P_o}\right)=\left(\frac{k_B T}{h}\right)\exp\left(\frac{-\Delta H^{o\dagger}}{RT}\right)\exp\left(\frac{\Delta S^{o\dagger}}{R}\right)\left(\frac{RT}{P_o}\right), \qquad \text{[Equation 4-6]}$$

where $\Delta G^{o\dagger}$ is the change in Gibbs free energy (in units of energy per mole) from the reactants to the transition state, $\Delta H^{o\dagger}$ is the change in enthalpy, and $\Delta S^{o\dagger}$ is the change in entropy. The reverse rate coefficient is calculated through applying the equilibrium constraint. At equilibrium, the forward reaction rate equals the reverse reaction rate, giving

$$\begin{aligned} k_{for}[A][B] &= k_{rev}[C] \\ \frac{k_{for}}{k_{rev}} &= \frac{[C]}{[A][B]}. \end{aligned} \qquad \text{[Equation 4-7]}$$

Equating the chemical potential of A(g) and B(g) with C(g) gives the following equilibrium relationship

$$K = \left(\frac{q_C}{q_A q_B}\right) = \left(\frac{N_C}{N_A N_B}\right)$$
$$K = \left(\frac{q_C^o}{q_A^o q_B^o}\right)\left(\frac{RT}{P_o}\right) = \left(\frac{[C]}{[A][B]}\right). \qquad \text{[Equation 4-8]}$$

Substituting Equation 4-7 into Equation 4-8 and replacing the ratio of partition functions with the equivalent Gibbs free energy expression yields the following expression for the reverse rate coefficient.

$$k_{rev} = k_{for} \exp\left(\frac{\Delta G^o}{RT}\right)\left(\frac{P_o}{RT}\right) \qquad \text{[Equation 4-9]}$$

4.3 Rate Coefficients for Heterogeneous Catalysis from Transition State Theory

Rate coefficients for reactions occurring in heterogeneous catalysis are obtained by application of transition state theory in a manner analogous to that detailed for a gas phase reaction in the previous section. In this section, transition state theory is applied to obtain the rate coefficients for adsorption reactions (molecular and dissociative) as well as surface reactions (unimolecular and bimolecular). Mass transfer in the gas phase is assumed to be much faster than chemical reactions for adsorption/desorption. Special treatment is given to tightly-bound (localized) vs. weakly-bound (mobile) adsorbates, including consistent accounting of standard states. The rate expressions developed here are applied in mean-field microkinetic modeling to simulate heterogeneous catalysis.

Activated Molecular Adsorption Rate Coefficients

Activated molecular adsorption is represented by the following elementary reaction:

$$\mathrm{A(g)} + * \overset{A^{*\dagger}}{\rightleftharpoons} \mathrm{A*} \qquad \text{[Equation 4-10]}$$

Consistent with transition state theory, it is convenient to define an effective chemical potential of the transition state, which equals that of the reactant(s):

$$\mu_A = \mu_{A^{*\dagger}}. \qquad \text{[Equation 4-11]}$$

Below, the forward and reverse rate coefficients for molecular adsorption through a mobile (freely translating) and localized (tightly-bound) transition states are derived.

Localized Transition State

The partition function for the gas/surface system with a localized transition state, $A^{*\dagger}$, takes the form

$$Q = \left(\frac{M! q_A^{N_A} q_{A^{*\dagger}}^{N_{A^{*\dagger}}} q_*^{\left(M - N_{A^{*\dagger}} - \sum_i N_{i,ads}\right)} \prod_{i \neq A, A^{*\dagger}} q_i^{N_i}}{\left(M - N_{A^{*\dagger}} - \sum_{i \neq A^{*\dagger}} N_{i,localized}\right)! N_A! N_{A^{*\dagger}}! \prod_{i \neq A, A^{*\dagger}} N_i!} \right), \qquad \text{[Equation 4-12]}$$

where M is the total number of binding sites on the surface, N is the number of the subscripted species, $N_{i,ads}$ is the number of an adsorbed species (localized or mobile), and $N_{i,localized}$ is the number of a localized surface species occupying a binding site. This is the complete system partition function, though for the purposes of the analysis in this section, only the partition function's dependence on N_A and $N_{A^{*\dagger}}$ is of concern. The form of the partition function is modified from that detailed by Hill to include surface modes.[94] Note that in this form for the system partition function, the individual partition function for each surface species (mobile or localized) contains contributions from surface atoms, thus the exponent of q_* is dependent on the number of adsorbed species. The chemical potential of A(g) is unaffected by the surface, taking the form (q_A/N_A). The chemical potential of the transition state takes the form

$$\mu_{A^{*\dagger}} = \left(\frac{\partial \ln Q}{\partial N_{A^{*\dagger}}} \right)_{M,T,N_{i \neq A^{*\dagger}}} = \left(\frac{q_{A^{*\dagger}} \left(M - N_{A^{*\dagger}} - \sum_{i \neq A^{*\dagger}} N_{i,localized} \right)}{q_* N_{A^{*\dagger}}} \right) = \left(\frac{q_{A^{*\dagger}} N_*}{q_* N_{A^{*\dagger}}} \right). \qquad \text{[Equation 4-13]}$$

Equating the chemical potentials yields the following equilibrium constant when the partition functions are referenced to the ground vibrational state energies of the molecules

$$K^{\dagger} = \frac{N_{A^{*\dagger}}}{N_A N_*} = \frac{q_{A^{*\dagger}}}{q_A q_*} \exp\left(\frac{-E_o}{RT}\right). \qquad \text{[Equation 4-14]}$$

Through transition state theory, the rate expression takes the form

$$\frac{dN_{A^*}}{dT} = \left(\frac{k_B T}{h}\right)\left(\frac{q_{A^{*\dagger}}}{q_A q_*}\right) \exp\left(\frac{-E_o}{RT}\right) N_A N_*. \qquad \text{[Equation 4-15]}$$

Factoring out the volume from the translational contribution to the total partition function for the gas phase molecule and manipulating the surface species terms on both sides of the equation yields the following rate expression in concentration form

$$\frac{d[A^*]}{dT} = \left(\frac{k_B T}{h}\right)\left(\frac{q_{A^{*\dagger}}}{q_A q_*}\right) \exp\left(\frac{-E_o}{RT}\right)[A][*], \qquad \text{[Equation 4-16]}$$

where the concentration of the gas phase molecule is expressed in units of mole per volume while the concentration of the surface species (or vacant sites) is expressed in units of mole per area. The rate expression is then multiplied and divided by the standard state volume per mole of molecules (or RT/P_o) to form the standard state partition function for the gas phase molecule. The localized transition state molecule has no translational partition function; however, as was detailed in Chapter 3, a standard state of $N_{sites,o}$, the standard state number of binding sites per molecule, is introduced for the localized species. Finally, the concentration of vacant sites is converted to fractional coverage (θ_*) through use of the total concentration of binding sites, C_T. These modifications result in the following final form of the rate expression for molecular adsorption through a localized transition state

$$\frac{d[A^*]}{dT} = \left(\frac{k_B T}{h}\right)\left(\frac{q^o_{A^{*\dagger}}}{q^o_A q_*}\right)\left(\frac{RT}{P_o}\right)\left(\frac{C_T}{N^o_{sites}}\right) \exp\left(\frac{-E_o}{RT}\right)[A]\theta_*. \qquad \text{[Equation 4-17]}$$

This rate expression suggests the following form for the activated molecular adsorption rate coefficient through a localized transition state

$$k_{for} = \left(\frac{k_B T}{h}\right)\left(\frac{q^o_{A^{*\dagger}}}{q^o_A q_*}\right)\left(\frac{RT}{P_o}\right)\left(\frac{C_T}{N^o_{sites}}\right) \exp\left(\frac{-E_o}{RT}\right). \qquad \text{[Equation 4-18]}$$

Mobile Transition State

The partition function for the gas/surface system with a mobile transition state, $A^{*\dagger}$, takes the form

$$Q = \left(\frac{M! q_A^{N_A} q_{A^{*\dagger}}^{N_{A^{*\dagger}}} q_*^{\left(M - N_{A^{*\dagger}} - \sum_i N_{i,ads}\right)} \prod_{i \neq A, A^{*\dagger}} q_i^{N_i}}{\left(M - \sum_{i \neq A^{*\dagger}} N_{i,localized}\right)! N_A! N_{A^{*\dagger}}! \prod_{i \neq A, A^{*\dagger}} N_i!} \right). \qquad \text{[Equation 4-19]}$$

Taking partial derivatives with respect to N_A and $N_{A\dagger}$, referencing the individual partition functions to their ground vibrational state energy, and applying Equation 4-11 results in the following equilibrium expression:

$$K^{\dagger} = \frac{N_{A^{*\dagger}}}{N_A} = \frac{q_{A^{*\dagger}}}{q_A q_*} \exp\left(\frac{-E_o}{RT}\right). \qquad \text{[Equation 4-20]}$$

Thus, the rate expression for activated molecular adsorption involving a mobile transition state takes the form

$$\frac{dN_{A^{*\dagger}}}{dt} = \left(\frac{k_B T}{h}\right)\left(\frac{q_{A^{*\dagger}}}{q_A q_*}\right) \exp\left(\frac{-E_o}{RT}\right) N_A. \qquad \text{[Equation 4-21]}$$

Recall that the partition function for a mobile surface species contains a two-dimensional translational contribution $q_{2D\text{-}trans}$, which is defined in Equation 3-16. The standard state translational partition function for the mobile surface species is dependent upon the standard state area of the two-dimensional box within which it translates. The area of the box per translating molecule is defined at the standard state concentration of surface species as $N_{sites,o}{}^{*}A$ as described in Chapter 3. Applying this definition, the rate expression in Equation 4-21 is converted to a concentration basis, replacing the partition functions with standard state partition functions, which results in

$$\frac{d[A^*]}{dt} = \left(\frac{k_B T}{h}\right)\left(\frac{q^o_{A^{*\dagger}}}{q^o_A q_*}\right)\left(\frac{RT}{P_o}\right)\left(\frac{1}{N^o_{sites} A}\right)\exp\left(\frac{-E_o}{RT}\right)[A], \qquad \text{[Equation 4-22]}$$

where [A*] and [A] are the concentrations of the adsorbed transition state and gas-phase reactant in units of mol/area and mol/volume, respectively, and A is the area per mole of binding sites. To make unit consistency more apparent, the $(1/A)$ term is replaced with C_T, the total concentration of binding sites for the surface of interest, which produces the following form of the rate expression for activated molecular adsorption through a mobile transition state:

$$\frac{d[A^*]}{dt} = \left(\frac{k_B T}{h}\right)\left(\frac{q^o_{A^{*\dagger}}}{q^o_A q_*}\right)\left(\frac{RT}{P_o}\right)\left(\frac{C_T}{N^o_{sites}}\right)\exp\left(\frac{-E_o}{RT}\right)[A]. \qquad \text{[Equation 4-23]}$$

Note that Equation 4-23 does not contain a dependence on the vacant fraction of sites, which is consistent with other derivations of this rate expression.[5] It has been suggested that the mobile transition state model is only applicable at lower coverages where the transition state will be free to translate across the catalyst surface.[5] Thus, at high coverages (as the fraction of vacant sites approaches zero), this reaction would be expected to proceed at a diminishingly small rate. To capture these limits, a dependence on the fraction of vacant sites (θ_*) is added to the rate expression, taking the form

$$\frac{d[A^*]}{dt} = \left(\frac{k_B T}{h}\right)\left(\frac{q^o_{A^{*\dagger}}}{q^o_A q_*}\right)\left(\frac{RT}{P_o}\right)\left(\frac{C_T}{N^o_{sites}}\right)\exp\left(\frac{-E_o}{RT}\right)[A]\theta_*. \qquad \text{[Equation 4-24]}$$

Note that the forms of Equation 4-17 and Equation 4-24 are identical; however, the partition function for the mobile transition state in Equation 4-24 contains a contribution from the two-dimensional translational partition function (as well as a possible contribution from the free rotation partition function), unlike the partition function for the localized transition state in Equation 4-17 (where each mode is treated as a harmonic oscillator vibration). The contributions from translation/rotation result in a higher rate of adsorption for adsorption through a mobile transition state. Thus, while the form of the rate coefficient expressed in Equation 4-18 for activated molecular adsorption through a localized transition state is also valid for activated molecular adsorption through a mobile transition state, the values of the rate coefficients will differ because the partition functions describing the transition states differ.

Reverse Rate Coefficient

The reverse rate coefficient is obtained by applying the equilibrium constraint, which takes the form

$$k_{for}[A]\theta_* = k_{rev}[A^*]$$
$$\frac{k_{for}}{k_{rev}} = \frac{[A^*]}{[A]\theta_*}. \qquad \text{[Equation 4-25]}$$

Equating the chemical potential of A(g) and A* gives the following:

$$K = \left(\frac{q_{A^*}}{q_A q_*}\right) = \left(\frac{N_{A^*}}{N_A N_*}\right)$$
$$K = \left(\frac{q^o_{A^*}}{q^o_A q_*}\right)\left(\frac{RT}{P_o}\right)\left(\frac{1}{N^o_{sites}}\right) = \left(\frac{[A^*]}{[A][^*]}\right) = \left(\frac{[A^*]}{[A]\theta_*}\right)\left(\frac{1}{C_T}\right). \qquad \text{[Equation 4-26]}$$

Substituting Equation 4-25 into Equation 4-26 and replacing the ratio of partition functions with the equivalent Gibbs free energy expression results in the following expression for the reverse rate coefficient (or molecular desorption rate coefficient):

$$k_{rev} = k_{for}\exp\left(\frac{\Delta G^o}{RT}\right)\left(\frac{P_o}{RT}\right)\left(\frac{N^o_{sites}}{C_T}\right). \qquad \text{[Equation 4-27]}$$

To validate this expression, Equation 4-18 is substituted into the above equation, yielding

$$k_{rev} = \left(\frac{k_B T}{h}\right)\left(\frac{q^o_{A^{*\dagger}}}{q^o_A q_*}\right)\exp\left(\frac{-E_o}{RT}\right)\exp\left(\frac{\Delta G^o}{RT}\right). \qquad \text{[Equation 4-28]}$$

Making a further substitution of the individual partition functions (referenced to the energies of the molecules' ground vibrational states) for the Gibbs free energy results in

$$k_{rev} = \left(\frac{k_B T}{h}\right)\left(\frac{q^o_{A^{*\dagger}}}{q^o_{A^*}}\right)\exp\left(\frac{-E_{o,r}}{RT}\right), \qquad \text{[Equation 4-29]}$$

where $E_{o,r}$ is the reverse zero-point activation barrier, or the difference in energy between the zero-point energy of the transition state well and the zero-point energy of the product well. As is expected, this is

the result that would be obtained from applying transition state theory and the system partition function in Equation 4-12 and Equation 4-19.

Non -Activated Molecular Adsorption Rate Coefficients

Molecular adsorption of gaseous species often proceeds without an appreciable activation barrier. For example, the molecular adsorption of water onto nickel catalyst is viewed as a barrier-less reaction. For non-activated molecular adsorption, collision theory is applied, with the sticking coefficient (the fraction of collisions that result in an adsorbed product) assumed to equal to the fraction of vacant sites. This physical interpretation of this assumption is that a collision with the surface results in an adsorbed product when the collision occurs at a vacant site. Given this assumption, the rate coefficient for non-activated molecular adsorption becomes

$$k_{for} = \left(\sqrt{\frac{k_B T}{2\pi M_{ads}}} \right), \qquad \text{[Equation 4-30]}$$

where M_{ads} is the mass of the adsorbing molecule. The reverse rate coefficient for non-activated molecular adsorption is identical to that for activated molecular adsorption, which is shown in Equation 4-27.

Dissociative Adsorption Rate Coefficients

Dissociative adsorption occurs via the following elementary reaction:

$$A(g) + 2^* \overset{BC^{**\dagger}}{\rightleftharpoons} B^* + C^*. \qquad \text{[Equation 4-31]}$$

Localized Transition State

The partition function for this system takes the form

$$Q=\left(\frac{\left(M-N_{BC^{**\dagger}}-\sum_{i^{**}\neq BC^{**\dagger}}N_{i^{**}}\right)!q_A^{N_A}q_{BC^{**\dagger}}^{N_{BC^{**\dagger}}}q_*^{\left(M-2N_{BC^{**\dagger}}-\sum_i N_i\right)}\prod_{i\neq A,BC^{**\dagger}}q_i^{N_i}}{\left(M-2N_{BC^{**\dagger}}-\sum_{i\neq BC^{**\dagger}}N_{i,localized}\right)!N_A!N_{BC^{**\dagger}}!\prod_{i\neq A,BC^{**\dagger}}N_i!}\right). \quad [\text{ Equation 4-32 }]$$

Note that the factorial in the numerator includes the $N_{BC^{**\dagger}}$ term because the $BC^{**\dagger}$ transition state is assumed to occupy two binding sites.[112] This term is intended to capture the number of entities on surface, including binding sites. Thus, because $BC^{**\dagger}$ and other doubly-adsorbed species occupy two sites, they decrease the number of entities on the surface by one for each molecule. Note the presence of the factor of two in front of the $N_{BC^{**\dagger}}$ term in the exponent of q_* and in the factorial in the denominator, a consequence of the species being doubly-adsorbed. Also note that the $(c/2)^{N^{**\dagger}}$ term proposed by Romá, et al. is neglected in Equation 4-32. This is an approximate factor to account for the fact that a doubly-bound species can gain entropy due to orientation (e.g., left/right vs. up/down) as a function of the lattice connectivity, *c*. Neglecting this term does not affect the overall species equilibrium between reactants and products, but does ultimately lead to a slower forward and reverse rate (by a factor of (c/2)) than would be obtained if it were included.

Once again, transition state theory is applied, equating the chemical potentials of A(g) and $BC^{**\dagger}$, resulting in

$$K^{\dagger}=\frac{MN_{BC^{**\dagger}}}{N_AN_*^2}=\frac{q_{BC^{**\dagger}}}{q_Aq_*^2}\exp\left(\frac{-E_o}{RT}\right). \quad [\text{ Equation 4-33 }]$$

To obtain this expression, the quantity $(M\text{-}N_{BC^{**\dagger}}\text{-}\Sigma N_{i^{**}})$ was approximated as *M*, assuming that the concentration of doubly-bound species is small. Applying the method detailed above for activated molecular adsorption through a localized transition state, this equilibrium relationship results in the following rate expression

$$\frac{d[B^*]}{dT}=\left(\frac{k_BT}{h}\right)\left(\frac{q^o_{BC^{**\dagger}}}{q^o_Aq^2_*}\right)\left(\frac{RT}{P_o}\right)\left(\frac{C_T}{N^o_{sites}}\right)\exp\left(\frac{-E_o}{RT}\right)[A]\theta_*^2. \quad [\text{ Equation 4-34 }]$$

Thus, the rate coefficient for dissociative adsorption through a localized transition state takes the form

$$k_{for} = \left(\frac{k_B T}{h}\right)\left(\frac{q^o_{BC^{**\dagger}}}{q^o_A q^2_*}\right)\left(\frac{RT}{P_o}\right)\left(\frac{C_T}{N^o_{sites}}\right)\exp\left(\frac{-E_o}{RT}\right). \qquad \text{[Equation 4-35]}$$

Mobile Transition State

For dissociative adsorption through a mobile transition state, the system is described by the following partition function

$$Q = \left(\frac{M! q_A^{N_A} q_{BC^{**\dagger}}^{N_{BC^{**\dagger}}} q_*^{\left(M - N_{BC^{**\dagger}} - \sum_i N_{i,ads}\right)} \prod_{i \neq A, A^{*\dagger}} q_i^{N_i}}{\left(M - \sum_{i \neq A^{*\dagger}} N_{i,localized}\right)! N_A! N_{A^{*\dagger}}! \prod_{i \neq A, A^{*\dagger}} N_i!}\right). \qquad \text{[Equation 4-36]}$$

Equating the chemical potentials of A(g) and $BC^{**\dagger}$ that are derived from this partition function results in

$$K^{\dagger} = \frac{N_{BC^{**\dagger}}}{N_A} = \frac{q_{BC^{**\dagger}}}{q_A q^2_*}\exp\left(\frac{-E_o}{RT}\right). \qquad \text{[Equation 4-37]}$$

Recalling that the partition function for the mobile species contains a contribution from the two-dimensional translational partition function, the equilibrium constant results in the following rate expression for dissociative adsorption through a mobile transition state:

$$\frac{d[B^*]}{dT} = \left(\frac{k_B T}{h}\right)\left(\frac{q^o_{BC^{**\dagger}}}{q^o_A q^2_*}\right)\left(\frac{RT}{P_o}\right)\left(\frac{C_T}{N^o_{sites}}\right)\exp\left(\frac{-E_o}{RT}\right)[A]. \qquad \text{[Equation 4-38]}$$

As was found for molecular adsorption through a mobile transition state, the rate expression has no dependence on the concentration of vacant sites. However, consistent with the modification of the molecular adsorption rate coefficient, Equation 4-38 is modified to include dependence on the fraction of vacant sites. This will ensure that the rate of adsorption limits to zero as the surface becomes filled and the fraction of vacant sites approaches zero. Because the products of the dissociative adsorption must occupy two sites, the rate expression is given second-order dependence. The resulting rate expression is

$$\frac{d[B*]}{dT} = \left(\frac{k_B T}{h}\right)\left(\frac{q^o_{BC**\dagger}}{q^o_A q^2_*}\right)\left(\frac{RT}{P_o}\right)\left(\frac{C_T}{N^o_{sites}}\right)\exp\left(\frac{-E_o}{RT}\right)[A]\theta^2_*. \qquad \text{[Equation 4-39]}$$

From the form of this rate expression, it is seen that the rate coefficient for dissociative adsorption through a mobile transition state is identical to that for adsorption through a localized transition state (Equation 4-35).

Reverse Rate Coefficient

The reverse rate coefficient is constrained through the equilibrium expression, taking the form

$$k_{for}[A]\theta^2_* = k_{rev}[B*][C*]$$
$$\frac{k_{for}}{k_{rev}} = \frac{[B*][C*]}{[A]\theta^2_*} \qquad \text{[Equation 4-40]}$$

Equating the chemical potential of A(g) with B* and C* gives the following equilibrium relationship

$$K = \left(\frac{q_{B*}q_{C*}}{q_A q^2_*}\right) = \left(\frac{N_{B*}N_{C*}}{N_A N^2_*}\right)$$
$$K = \left(\frac{q^o_{B*}q^o_{C*}}{q^o_A q^2_*}\right)\left(\frac{RT}{P_o}\right)\left(\frac{1}{N^o_{sites}}\right)^2 = \left(\frac{[B*][C*]}{[A][*]^2}\right) = \left(\frac{[B*][C*]}{[A]\theta^2_*}\right)\left(\frac{1}{C_T}\right)^2 \qquad \text{[Equation 4-41]}$$

Substituting Equation 4-40 into Equation 4-41 and replacing the ratio of partition functions with the equivalent Gibbs free energy expression yields the following expression for the reverse rate coefficient for dissociative adsorption (or the associative desorption rate coefficient).

$$k_{rev} = k_{for}\exp\left(\frac{\Delta G^o}{RT}\right)\left(\frac{P_o}{RT}\right)\left(\frac{N^o_{sites}}{C_T}\right)^2 \qquad \text{[Equation 4-42]}$$

Surface Reaction Rate Coefficients

An example of a surface reaction takes the form of the following elementary reaction:

$$A^* + * \overset{BC^{**\dagger}}{\rightleftharpoons} B^* + C^*. \qquad \text{[Equation 4-43]}$$

Localized Transition State

The partition function for this system takes the form

$$Q = \left(\frac{\left(M - N_{BC^{**\dagger}} - \sum_{i^{**} \neq BC^{**\dagger}} N_{i^{**}} \right)! q_{A^*}^{N_{A^*}} q_{BC^{**\dagger}}^{N_{BC^{**\dagger}}} q_*^{\left(M - N_{A^*} - 2N_{BC^{**\dagger}} - \sum_i N_i \right)} \prod_{i \neq A^*, BC^{**\dagger}} q_i^{N_i}}{\left(M - N_{A^*} - 2N_{BC^{**\dagger}} - \sum_{i \neq A^*, BC^{**\dagger}} N_{i,localized} \right)! N_{A^*}! N_{BC^{**\dagger}}! \prod_{i \neq A^*, BC^{**\dagger}} N_i!} \right). \qquad \text{[Equation 4-44]}$$

Note that as was discussed for dissociative adsorption through a localized transition state, the transition state in this dissociative surface reaction is treated as occupying two sites because the products will occupy two sites. This means that the term $N_{BC^{**\dagger}}$ appears in the factorial expression in the numerator of the system partition function to properly account for the number of entities on the catalyst surface. Equating the chemical potentials of the transition state and reactant yields the following equilibrium expression, assuming that the concentration of doubly-bound species on the surface is small

$$K^{\dagger} = \frac{MN_{BC^{**\dagger}}}{N_{A^*} N_*} = \frac{q_{BC^{**\dagger}}}{q_{A^*} q_*} \exp\left(\frac{-E_o}{RT} \right). \qquad \text{[Equation 4-45]}$$

Applying this equilibrium constant and transition state theory results in the following rate expression for a dissociative surface reaction through a localized transition state

$$\frac{d[B^*]}{dT} = \left(\frac{k_B T}{h} \right) \left(\frac{q^o_{BC^{**\dagger}}}{q^o_{A^*} q_*} \right) \exp\left(\frac{-E_o}{RT} \right) [A^*] \theta_*. \qquad \text{[Equation 4-46]}$$

Thus, the rate expression for dissociation on the surface takes the form

$$k_{for} = \left(\frac{k_B T}{h} \right) \left(\frac{q^o_{BC^{**\dagger}}}{q^o_{A^*} q_*} \right) \exp\left(\frac{-E_o}{RT} \right). \qquad \text{[Equation 4-47]}$$

Mobile Transition State

The partition function for the system takes the form

$$Q = \left(\frac{(M)! q_{A^*}^{N_{A^*}} q_{BC^{**\dagger}}^{N_{BC^{**\dagger}}} q_*^{\left(M - N_{A^*} - 2N_{BC^{**\dagger}} - \sum_i N_i\right)} \prod_{i \neq A^*, BC^{**\dagger}} q_i^{N_i}}{\left(M - N_{A^*} - \sum_{i \neq A^*} N_{i,localized}\right)! N_{A^*}! N_{BC^{**\dagger}}! \prod_{i \neq A^*, BC^{**\dagger}} N_i!} \right). \qquad \text{[Equation 4-48]}$$

Equating the chemical potentials of the transition state and reactant yields the following equilibrium expression

$$K^{\dagger} = \frac{N_* N_{BC^{**\dagger}}}{N_{A^*}} = \frac{q_{BC^{**\dagger}}}{q_{A^*} q_*} \exp\left(\frac{-E_o}{RT}\right). \qquad \text{[Equation 4-49]}$$

Applying this equilibrium constant and transition state theory results in the following rate expression for a dissociative surface reaction through a mobile transition state

$$\frac{dN_{B^*}}{dT} = \left(\frac{k_B T}{h}\right)\left(\frac{q_{BC^{**\dagger}}}{q_{A^*} q_*}\right) \exp\left(\frac{-E_o}{RT}\right)\left(\frac{1}{N_*}\right) N_{A^*}. \qquad \text{[Equation 4-50]}$$

Assuming a generally low surface coverage, the number of vacant sites is set equal to the total number of binding sites, *M*. Factoring out the area-dependence from the two-dimensional translational partition function contribution to the transition state partition function and introducing standard state corrections results in the following concentration-dependent rate expression

$$\frac{d[B^*]}{dT} = \left(\frac{k_B T}{h}\right)\left(\frac{q^o_{BC^{**\dagger}}}{q^o_{A^*} q_*}\right)\left(\frac{N^o_{sites}}{N^o_{sites} A}\right) \exp\left(\frac{-E_o}{RT}\right) \theta_{A^*}. \qquad \text{[Equation 4-51]}$$

Noting that the value of $(1/A)$ is equivalent to C_T, the total concentration of binding sites per unit area, this rate expression is re-written as

$$\frac{d[B*]}{dT} = \left(\frac{k_B T}{h}\right)\left(\frac{q^o_{BC**\dagger}}{q^o_{A*} q_*}\right)\exp\left(\frac{-E_o}{RT}\right)[A*]. \qquad \text{[Equation 4-52]}$$

In order for the dissociation to occur, the A* species must be adjacent to a vacant site. To capture this effect, a first order dependence on the fraction of vacant sites is introduced to the rate expression, which results in

$$\frac{d[B*]}{dT} = \left(\frac{k_B T}{h}\right)\left(\frac{q^o_{BC**\dagger}}{q^o_{A*} q_*}\right)\exp\left(\frac{-E_o}{RT}\right)[A*]\theta_*. \qquad \text{[Equation 4-53]}$$

Thus, the rate coefficient for dissociation of an adsorbed species through a mobile transition state is identical in form to that for dissociation through a localized transition state, shown in Equation 4-47.

Reverse Rate Coefficient

The reverse rate coefficient is constrained through the equilibrium expression, taking the form

$$k_{for}[A*]\theta_* = k_{rev}[B*][C*]$$
$$\frac{k_{for}}{k_{rev}} = \frac{[B*][C*]}{[A*]\theta_*}. \qquad \text{[Equation 4-54]}$$

Equating the chemical potential of A* with B* and C* gives the following equilibrium relationship

$$K = \left(\frac{q_{B*} q_{C*}}{q_{A*} q_*}\right) = \left(\frac{N_{B*} N_{C*}}{N_{A*} N_*}\right)$$
$$K = \left(\frac{q^o_{B*} q^o_{C*}}{q^o_{A*} q_*}\right)\left(\frac{1}{N^o_{sites}}\right) = \left(\frac{[B*][C*]}{[A*][*]}\right) = \left(\frac{[B*][C*]}{[A*]\theta_*}\right)\left(\frac{1}{C_T}\right). \qquad \text{[Equation 4-55]}$$

Substituting Equation 4-54 into Equation 4-55 and replacing the ratio of partition functions with the equivalent Gibbs free energy expression yields the following expression for the reverse rate coefficient for a dissociative surface reaction (or the associative surface reaction rate coefficient)

$$k_{rev} = k_{for} \exp\left(\frac{\Delta G^o}{RT}\right)\left(\frac{N^o_{sites}}{C_T}\right) . \qquad \text{[Equation 4-56]}$$

General Form for Activated Reaction Rate Coefficients

Combining the rate coefficients derived in the preceding sections, a general form for the forward and reverse rate coefficients for adsorption/surface reaction are expressed as

$$k_{for} = \left(\frac{k_B T}{h}\right) q^{o\dagger} \prod_{\#R} \left(q_i^o\right)^{\nu_i} \exp\left(\frac{-E_o}{RT}\right)\left(\frac{P_o}{RT}\right)^{\sum_{\#R} \nu_{i,gas}} \left(\frac{C_T}{N^o_{sites}}\right)^{\sum_{\#R} \nu_{i,ads}+1}$$

$$k_{rev} = k_{for} \exp\left(\frac{\Delta G^o}{RT}\right)\left(\frac{RT}{P_o}\right)^{\sum_{\#R,\#P} \nu_{i,gas}} \left(\frac{N^o_{sites}}{C_T}\right)^{\sum_{\#R,\#P} \nu_{i,ads}} , \qquad \text{[Equation 4-57]}$$

where *#R* and *#P* refer to summations over the total number of reactants and products, respectively, ν_i is the stoichiometric coefficient of an entity (gaseous, adsorbed, or vacant site), $\nu_{i,ads}$ is the stoichiometric coefficient of an adsorbed species (this does not apply to vacant sites), and $\nu_{i,gas}$ is the stoichiometric coefficient of a gas phase species.

Interfacet Diffusion Rate Coefficients

In the kinetic modeling in this work, a molecule, such as CH_3, is treated as different species when adsorbed on different surfaces (e.g., $CH_3{}^*_{111}$ vs. $CH_3{}^*_{100}$). Therefore, the diffusion of an adsorbed molecule from one surface facet to another is treated as a reaction in the kinetic model because it involves the disappearance of a species from one surface facet and the appearance of a species on another facet. An approach analogous to that applied above for other surface reactions is applied to derive the rate coefficients for interfacet diffusion. The partition function is written considering only the interfacial binding sites between two adjoining surface facets, with each surface having M_{Int} interfacial sites. The transition state, $A^{**\dagger}$, corresponding to the diffusion of a molecule A at the interface of facet 1 (with total number $N'_{A^*,1}$) to the interface of neighboring facet 2 (with total number $N'_{A^*,2}$) is assumed to occupy two interfacial sites, one on each facet. The statistical factor describing the number of configurations for $N'_{A^{**\dagger}}$ transition state molecules bridging the interface, $\{N'_{i,1}\}$ adsorbates at the interface surface 1, and $\{N'_{i,2}\}$ adsorbates at the interface on surface 2 is expressed as

$$\Omega = \binom{M_{Int}}{N'_{A^{**\dagger}}} \binom{M_{Int} - N'_{A^{**\dagger}}}{\{N'_{i,1}\}} \binom{M_{Int} - N'_{A^{**\dagger}}}{\{N'_{i,2}\}}.$$

$$\Omega = \frac{M_{Int}!\left(M_{Int} - N'_{A^{**\dagger}}\right)!\left(M_1 - N'_{A^{**\dagger}}\right)!}{\left(M_{Int} - N'_{A^{**\dagger}}\right)!N'_{A^{**\dagger}}!\left(M_{Int} - N'_{A^{**\dagger}} - \sum N'_{i,1}\right)!\prod\left(N'_{i,1}!\right)\left(M_{Int} - N'_{A^{**\dagger}} - \sum N'_{i,2}\right)!\prod\left(N'_{i,2}!\right)} \quad \text{[Equation 4-58]}$$

$$\Omega = \frac{M_{Int}!\left(M_{Int} - N'_{A^{**\dagger}}\right)!}{\prod_{f_s=1,2}\left[\left(M_{Int} - N'_{A^{**\dagger}} - N'_{A^*,f_s} - \sum_{i\neq A^*} N'_{i,f_s}\right)!N'_{A^*,f_s}!\prod_{i\neq A^*} N'_{i,f_s}!\right]N'_{A^{**\dagger}}!},$$

where f_s is the index for the surface facets. Taking into account the statistical factor Ω, the partition function for this system takes the form

$$Q = \frac{M_{Int}!\left(M_{Int} - N'_{A^{**\dagger}}\right)!\prod_{f_s=1,2}\left(q_{A^*,f_s}^{N'_{A^*,f_s}} q_{*,f_s}^{\left(M_{Int} - N'_{A^{**\dagger}} - N'_{A^*,f_s} - \sum_{i\neq A^*} N'_{i,f_s}\right)}\right) q_{A^{**\dagger}}^{N'_{A^{**\dagger}}} \prod_{f_s=1,2}\left(q_{i,f_s}^{N'_{i,f_s}}\right)}{\prod_{f_s=1,2}\left[\left(M_{Int} - N'_{A^{**\dagger}} - N'_{A^*,f_s} - \sum_{i\neq A^*} N'_{i,f_s}\right)!N'_{A^*,f_s}!\prod_{i\neq A^*} N'_{i,f_s}!\right]N'_{A^{**\dagger}}!}. \quad \text{[Equation 4-59]}$$

Equating the chemical potentials of the reactant A^*_1 and the transition state results in the following expression:

$$K^{\dagger} = \frac{N'_{A^{**\dagger}} M_{Int}}{N'_{A^*,1} N'_{*,2}} = \frac{q_{A^{**\dagger}}}{q_{A^*,1} q_{*,2}} \exp\left(\frac{-E_o}{RT}\right). \quad \text{[Equation 4-60]}$$

Applying transition state theory, the number-based rate equation for interfacet diffusion therefore takes the form

$$-\frac{dN'_{A^*,1}}{dt} = \left(\frac{k_B T}{h}\right)\left(\frac{q_{A^{**\dagger}}}{q_{A^*,1} q_{*,2}}\right)\exp\left(\frac{-E_o}{RT}\right)\left(\frac{1}{M_{Int}}\right) N'_{A^*,1} N'_{*,2}. \quad \text{[Equation 4-61]}$$

Note that this rate expression is written considering only the interfacial sites between two adjoining surface facets. Considering that these equations will be applied in a mean-field model, the fractional coverage of a species on surface 1 along the interface is assumed to be equal to the overall fractional coverage of that species on surface one. The physical interpretation of this assumption is that intrafacet diffusion is sufficiently fast that the interface will see the effective concentration of the entire surface. Thus, an adsorbate A^*_1 located at the interface between facets 1 and 2 diffuses to the average vacant site fraction on facet 2. Also, note that the change (due to interface diffusion) in the number of A^*_1 molecules

at the interface ($dN'_{A^*,1}/dt$) is equal to the change in the number of this species on the overall surface ($dN_{A^*,1}/dt$). Therefore, Equation 4-61 is converted to a fractional coverage basis, with the fractional coverage of each species corresponding to that species' overall fractional coverage on the facet of interest

$$-\frac{dN_{A^*,1}}{dt} = -\frac{dN'_{A^*,1}}{dt} = \left(\frac{k_B T}{h}\right)\left(\frac{q_{A^{**\dagger}}}{q_{A^*,1} q_{*,2}}\right)\exp\left(\frac{-E_o}{RT}\right) M_{Int}\theta'_{A^*,1}\,\theta'_{*,2}$$

$$-\frac{d\theta_{A^*,1}}{dt} = \left(\frac{k_B T}{h}\right)\left(\frac{q_{A^{**\dagger}}}{q_{A^*,1} q_{*,2}}\right)\exp\left(\frac{-E_o}{RT}\right)\left(\frac{M_{Int}}{M_1}\right)\theta_{A^*,1}\theta_{*,2}, \qquad \text{[Equation 4-62]}$$

where M_1 is the total number of sites on surface 1. This form of the rate expression is then converted to a concentration basis, consistent with the other rate expressions in the model, by multiplying both sides of Equation 4-62 by the total concentration of sites on surface 1, resulting in

$$-\frac{d[A^*_1]}{dt} = \left(\frac{k_B T}{h}\right)\left(\frac{q_{A^{**\dagger}}}{q_{A^*,1} q_{*,2}}\right)\exp\left(\frac{-E_o}{RT}\right)\left(\frac{M_{Int}}{M_1}\right)[A^*_1]\theta_{*,2}. \qquad \text{[Equation 4-63]}$$

The forward rate coefficient for inter-facet diffusion from facet 1 to facet 2 takes the form

$$k_{for} = \left(\frac{k_B T}{h}\right)\left(\frac{q_{A^{**\dagger}}}{q_{A^*,1} q_{*,2}}\right)\exp\left(\frac{-E_o}{RT}\right)\left(\frac{M_{Int}}{M_1}\right). \qquad \text{[Equation 4-64]}$$

The ratio M_{Int} / M_1 represents the probability of a binding site on facet 1 bordering a binding site on facet 2. The ratio is equivalent to the "inhomogeneity parameter," $\omega_{1,2}$, applied by Cwiklik to the problem of mean field modeling of diffusion on non-uniform surfaces.[113] However, Cwiklik's derivation (based on the one-center approximation) details only the case where $M_1=M_2$ and his equations are unclear for cases where $M_1 \neq M_2$. The above derivation is general for any value of M_1 and $M_2 > M_{int}$.

Note that had the rate expression been written in terms of the appearance of A* on surface facet 2 rather than the disappearance of A* on surface facet 1, the rate expression would have taken the form

$$\frac{d[A^*_2]}{dt} = \left(\frac{k_B T}{h}\right)\left(\frac{q_{A^{**\dagger}}}{q_{A^*,1} q_{*,2}}\right)\exp\left(\frac{-E_o}{RT}\right)\left(\frac{M_{Int}}{M_1}\right)\left(\frac{C_{T,2}}{C_{T,1}}\right)[A^*_1]\theta_{*,2}, \qquad \text{[Equation 4-65]}$$

where C_T is the total concentration of sites on the surface facet of interest. Thus, the rate coefficient must be modified accordingly depending on which surface species is being accounted for.

Reverse Rate Coefficient

The reverse rate for this process is calculated by applying the overall reaction equilibrium expression, which takes the form

$$k_{for}[A^*_1]\theta_{*,2} = k_{rev}[A^*_2]\theta_{*,1}$$
$$\frac{k_{for}}{k_{rev}} = \frac{[A^*_2]\theta_{*,1}}{[A^*_1]\theta_{*,2}}. \qquad \text{[Equation 4-66]}$$

Equating the chemical potential of A^*_1 with A^*_2 gives the following equilibrium relationship (given the same standard state concentration of species on the two surfaces and using the same zero of energy when computing the partition functions):

$$K = \left(\frac{q_{A^*,2}q_{*,1}}{q_{A^*,2}q_{*,1}}\right) = \left(\frac{N_{A^*,2}N_{*,1}}{N_{A^*,1}N_{*,2}}\right)$$
$$K = \left(\frac{q^o_{A^*,2}q_{*,1}}{q^o_{A^*,1}q_{*,2}}\right) = \left(\frac{[A^*_2][^*_1]}{[A^*_1][^*_2]}\right) = \left(\frac{[A^*_2]\theta_{*,1}}{[A^*_1]\theta_{*,2}}\right)\left(\frac{C_{T,1}}{C_{T,2}}\right). \qquad \text{[Equation 4-67]}$$

Substituting Equation 4-66 into Equation 4-67 and replacing the ratio of partition functions with the equivalent Gibbs free energy expression yields the following expression for the reverse rate coefficient for interfacet diffusion

$$k_{rev} = k_{for}\exp\left(\frac{\Delta G^o}{RT}\right)\left(\frac{C_{T,1}}{C_{T,2}}\right). \qquad \text{[Equation 4-68]}$$

4.4 Kinetic Modeling of Heterogeneous Catalysis using a Continuously-Stirred Tank Reactor Model

The Continuously-Stirred Tank Reactor (CSTR) model is useful for performing sensitivity and flux analyses to identify key reactions or intermediates and determine the dominant reforming pathway on the catalyst surface. The CSTR model can be solved reasonably quickly, making it an attractive approach for these analyses which may require multiple runs under varying conditions. In the CSTR model, reactants at some initial concentration flow into a perfectly mixed reactor with uniform (reacted) species concentrations, shown in Figure 4-1. The species flow out of the reactor at the same concentration as they exist in the reactor. The CSTR model is posed in steady-state algebraic form for a single reaction as[114]

$$\tau_{res} = \frac{C_{A,o}X_A}{-r_A}[=]\frac{\text{moles of A reacted}}{\text{rate of disappearance of A}}, \qquad \text{[Equation 4-69]}$$

where τ_{res} is the residence time of the CSTR, $C_{A,o}$ is the initial concentration of species A, X_A is the conversion of species A, and $-r_A$ is the rate of disappearance of species A, following the form of a chosen rate expression. Note that the notation C_A is equivalent to the previous notation for concentration of [A].

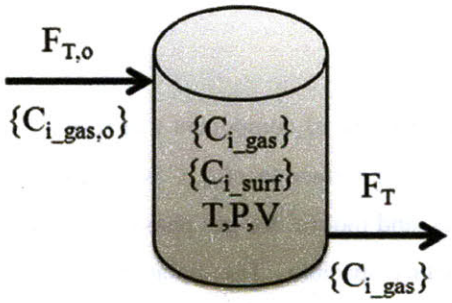

Figure 4-1. Flow Diagram of a Continuously Stirred Tank Reactor with inlet flow rate $F_{T,o}$ at concentrations $\{C_{i\_gas,o}\}$ and outlet flow rate F_T at concentrations $\{C_{i\_gas}\}$.

For multiple reactions, a system of such equations is solved to determine the final concentrations of each species at a given residence time. For sufficiently long residence times, the set of concentrations is expected to approach those defined by the equilibrium constraints for the system. However, when many species are present, finding a solution to this set of algebraic equations without excellent initial guesses

for final species concentrations (or conversions) can be a difficult task for standard solvers such as `fsolve` in MATLAB. Therefore, in this work, I pose the CSTR equations as a series of time-dependent design equations and integrate to a time $t_{end} >> \tau$ to find the steady state solution for the system of equations. In the kinetic model, there are gas phase species and adsorbed species. In addition, a molecule adsorbed on one surface facet (such as the (111) facet) is treated as a separate species than the same molecule adsorbed on a different surface facet (such as the (100) facet). The reactions in the kinetic model can be categorized as either 1) the adsorption/desorption of a species onto/from a surface facet, 2) a surface reaction involving the reaction of surface species from adsorbed reactant(s) to adsorbed product(s) on a single surface facet, and 3) the diffusion of an adsorbed surface species from one surface facet to another. The diffusion between surface facets is treated as a reaction in the model because it involves the dis/appearance of a surface species from/on a surface facet. If the kinetic model of interest only contains one surface facet, the third reaction family is not considered and the summations over multiple surface facets in the equations below disappear.

The molar rate of change for a surface species i on surface facet f_s is expressed as a sum of the rate of change due to reaction (Equation 4-70) and the rate of change due to inter-facet diffusion (Equation 4-71).

$$r_{i_{f_s},\text{Rxn}} = \sum_{j \text{ on } f_s} \nu_{j,i} \left[k_{j,f_s} \prod_{l=1}^{S_R} C_{l,f_s}^{-\upsilon_{j,l}} - k_{-j,f_s} \prod_{l=1}^{S_P} C_{l,f_s}^{\upsilon_{j,l}} \right], \qquad \text{[Equation 4-70]}$$

where $\nu_{j,i}$ is the stoichiometric coefficient of component i in reaction j, k is the rate coefficient for the forward (j) and reverse ($-j$) reactions on surface facet f_s, C is the concentration (in fractional coverage for vacant sites, mol/m^2 for adsorbates, and mol/m^3 for gas phase species) of component l (on surface facet f_s when the subscript l denotes a surface species). The molar rate of change for species i due to diffusion to/from surface facet f_s from/to another facet of the catalyst, f_t, is described as

$$r_{i_{f_s},\text{Diff},f_{s,t}} = -\left(\frac{\alpha_{f_t}}{\alpha_{f_s}}\right) r_{i_{f_t},\text{Diff},f_{s,t}} = -k_{i,f_{s,t}} C_{i_{f_s}} C_{*_{f_t}} + k_{i,-f_{s,t}} C_{i_{f_t}} C_{*_{f_s}}, \qquad \text{[Equation 4-71]}$$

where α is the surface area of the subscripted facet, subscripts $f_{s,t}$ and $-f_{s,t}$ indicate forward and reverse diffusion from surface facet f_s to facet f_t, and the subscript * represents a vacant site (recall that the concentration of vacant sites is expressed in terms of fractional coverage). Note that Equation 4-71

describes diffusion to/from facet f_s from/to one other facet and must be summed over all facets $f_{t,t\neq s}$ to capture all inter-facet diffusion, resulting in a total rate of change for species i on surface facet f_s of

$$\frac{dC_{i_{f_s}}}{dt} = r_{i_{f_s},\text{Rxn}} + \sum_{t\neq s} r_{i_{f_s},\text{Diff},f_s,t} \qquad \text{[Equation 4-72]}$$

For flowing gaseous species, the molar rate of change for a species is expressed as a sum of the rate of change due to adsorption/desorption and rate of change due to flow into/out of the reactor. The total molar rate of change for gaseous species i is expressed as

$$\frac{dC_i}{dt} = \sum_s \left(\frac{\alpha_{f_s}}{V}\right) r_{i,\text{Ads},f_s} + \frac{C_{i,in}}{\tau_{res,o}} - \frac{C_i}{\tau_{res}}, \qquad \text{[Equation 4-73]}$$

where V is the volume of the reactor, $r_{i,\text{Ads},fs}$ is the net rate of change of gas phase species i due to adosprtion/desporption onto/from surface facet f_s, $\tau_{res,o}$ is the user-specified zero-conversion residence time of the CSTR, and $C_{i,in}$ is the inlet concentration of gaseous species i. Note that the value $r_{i,\text{Ads/Des},fs}$ is calculated using Equation 4-70, where $r_{i,\text{Ads/Des},fs}$ is equal to $-r_{i,fs,\text{Rxn}}$ and i_{fs} is the product of the adsorption of gas phase species i onto surface facet f_s.

The zero-conversion residence time is equal to the actual reactor residence time for systems with no net change in moles upon reaction. For reactions where there is a net change in number of moles upon reaction, the two residence times are approximately equal at low conversions; however, to allow for the investigation of larger conversions, the actual reactor residence time, τ_{res}, is calculated as:

$$\tau_{res} = \frac{n_T}{F_T} = \left(\frac{PV}{RT}\right)\left(\frac{1}{F_T}\right) = \left(\frac{PV}{RT}\right)\left(\frac{1}{F_{T,o}}\right)\left(\frac{1}{1+\Delta F/F_{T,o}}\right) = \left(\frac{\tau_{res,o}}{1+\Delta F/F_{T,o}}\right), \qquad \text{[Equation 4-74]}$$

where n_T is the total number of gas phase moles in the CSTR, F_T is the total molar flow rate out of the reactor, ΔF is the change in molar flow rate from the initial feed to the outlet of the CSTR, and the subscript o represents an initial, or zero-conversion, quantity. With specific regard to the overall reactions studied in this work (the steam methane reforming reaction paired with water gas shift), the change in

number of moles upon reaction at a specific methane conversion is expressed as a function of initial and final methane mole fractions, $y_{CH4,feed}$ and y_{CH4}, through

$$\frac{\Delta F}{F_{T,o}} = \left(\frac{y_{CH_4,feed} - y_{CH_4}}{0.5 + y_{CH_4}} \right). \qquad \text{[Equation 4-75]}$$

The complete set of time-dependent CSTR equations (one for each gas phase or surface species) must then be solved using a differential equation solver, time-stepping to steady state for a specified zero-conversion residence time. In this work, ODE15s in MATLAB is employed.

4.5 Kinetic Modeling of Heterogeneous Catalysis using an Ideal Plug Flow Reactor Model

In this work, an ideal Plug Flow Reactor (PFR) model (Figure 4-2) is used to simulate research reactors for comparison to available experimental data. The PFR design equation is obtained from the species conservation equation in cylindrical coordinates, assuming no r or θ dependence, which takes the form[115]

$$\frac{\partial C_i(t,z)}{\partial t} = -\frac{\partial v_z C_i(t,z)}{\partial z} + D\frac{\partial^2 C_i(t,z)}{\partial z^2} + R_{v,i}\left(\{C(t.z)\}\right), \qquad \text{[Equation 4-76]}$$

where z is the spatial coordinate corresponding to the axis of the tubular reactor and $R_{v,i}$ is the volumetric rate of production of gas-phase species i. Note that the volumetric rate of production is a function of a set of concentrations, including both flowing gaseous species and stationary surface species. In the ideal PFR, dispersion is assumed to be negligible when compared to convection and reaction, resulting in the following design equation

$$\frac{\partial C_i(t,z)}{\partial t} = -\frac{\partial v_z C_i(t,z)}{\partial z} + R_{v,i}\left(\{C(t.z)\}\right), \qquad \text{[Equation 4-77]}$$

Discretizing Equation 4-77 in the z-coordinate results in the following differential equation describing the time evolution of concentration for a finite segment of the reactor

$$\frac{dC_{i,z_k}}{dt} = -\left(\frac{v_{z_k} C_{i,z_k} - v_{z_{k-1}} C_{i,z_{k-1}}}{\Delta z}\right) + R_{v,i,z_k}\left(\{C_{z_k}\}\right), \qquad \text{[Equation 4-78]}$$

Assuming an ideal gas and isothermal/isobaric operation, the velocity at a given point z_k is calculated as follows, taking advantage of an equation like Equation 4-75

$$v_{z_k} = \frac{V_{flow,z_k}}{A_{eff}} = \frac{F_{T,z_k} / C_T}{\varepsilon A} = \left(\frac{RT}{P\varepsilon A}\right) F_{T,o}\left[1 + \frac{\Delta F}{F_{T,o}}\right], \qquad \text{[Equation 4-79]}$$

where A_{eff} is the gas-containing cross-sectional area of the reactor, ε is the void fraction of the catalyst and packing, A is the cross-sectional area of the reactor, $V_{flow,zk}$ is the volumetric flow rate at z_k, and C_T is the total gas phase concentration.

The PFR design equation is next modified to replace the discretization in the z-coordinate with discretization by mass of catalyst. The mass of catalyst is related to the z-coordinate through

$$\Delta W = \rho_{cat,eff} A \Delta z, \qquad \text{[Equation 4-80]}$$

where ΔW is the mass of catalyst in reactor length Δz and $\rho_{cat,eff}$ is the effective density of the catalyst in grams of catalyst per volume of reactor (W_{total} / V_{total}). Substituting Equation 4-80 into Equation 4-78 results in the following W-discretized form of the PFR design equation

$$\frac{dC_{i,k}}{dt} = \left(\frac{\rho_{cat,eff}}{\varepsilon}\right)\left(\frac{RT}{P}\right)\left(\frac{F_{T,k-1}C_{i,k-1} - F_{T,k}C_{i,k}}{\Delta W}\right) + R_{v,i,k}\left(\{C_k\}\right), \qquad \text{[Equation 4-81]}$$

The rate of production of species i is calculated using Equation 4-70 for a multi-faceted catalyst surface, using the following relationship to correct the units from mol/m^2-s to mol/m^3-s

$$R_{v,i,k} = \sum_s \left(\frac{\alpha_{f_s}}{V}\right)\left(\frac{dC_{i,f_s,k}}{dt}\right)_{\text{Reaction}} = \sum_s \left(\frac{\hat{\alpha}_{f_s}\rho_{cat}}{\varepsilon}\right)\left(\frac{dC_{i,f_s,k}}{dt}\right)_{\text{Reaction}}, \qquad \text{[Equation 4-82]}$$

where $\hat{\alpha}$ is the total area of facet f_s per unit catalyst mass. Defining a new PFR residence time variable, τ_{PFR}, the ideal PFR design equation becomes

$$\frac{dC_{i,k}}{dt} = \left(\frac{C_{i,k-1}}{\tau_{PFR\_res,z_{k-1}}} - \frac{C_{i,k}}{\tau_{PFR\_res,z_k}} \right) + \sum_s \left(\frac{\hat{\alpha}_{f_s} \rho_{cat}}{\varepsilon} \right) \left(\frac{dC_{i,f_s,k}}{dt} \right)_{\text{Reaction}}, \qquad \text{[Equation 4-83]}$$

where

$$\tau_{PFR\_res,k} = \left(\frac{P}{RT} \right) \left(\frac{\varepsilon}{\rho_{cat}} \right) \left(\frac{\Delta W}{F_{T,k}} \right). \qquad \text{[Equation 4-84]}$$

As described previously for the CSTR model, the molar flow rate for the system studied in the present work (steam methane reforming coupled with water gas shift) is related to the methane mole fraction and the initial molar flow rate through the equation

$$F_{T,k} = F_{T,o} + \Delta F_k = F_{T,o} \left(1 + \frac{y_{CH_4,o} - y_{CH_4,k}}{0.5 + y_{CH_4,k}} \right). \qquad \text{[Equation 4-85]}$$

Note the similarity between Equation 4-83, the axially-discretized ideal PFR design equation, and Equation 4-73, the CSTR design equation. This similarity reveals that applying axial discretization to the PFR design equation and neglecting dispersion results in a series of CSTRs where the number of CSTRs is determined by the number of discretizations, with each reactor section described by Equation 4-83 (Figure 4-2).

For the PFR, the residence time is no longer user-specified, but is instead defined by the reactor conditions and molar flow rate in the section of interest. To solve for the concentration profiles in the PFR, each of the $N_{sections}$ CSTRs is integrated to steady-state (in a manner identical to that for the single CSTR described in Section 4.4), in succession from $k = 1$ to $k = N_{sections}$, subject to the constraint that the sum of the catalyst mass per section over all sections is equal the total mass of catalyst in the PFR. After the first section is solved using the PFR feed conditions, the outlet species concentrations from section $k - 1$ serve as the feed composition for section k.

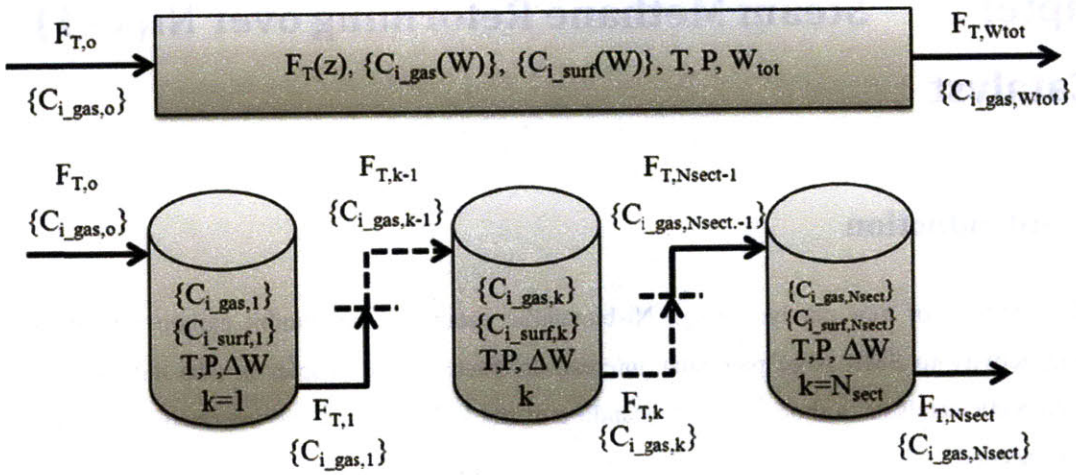

Figure 4-2. (Top) Diagram of a Plug Flow Reactor, with inlet flow rate $F_{T,o}$ at gas concentrations $\{C_{i\_gas,o}\}$ and outlet flow rate $F_{T,Wtot}$ at concentrations $\{C_{i\_gas,Wtot}\}$. The PFR contains a total mass of catalyst W_{tot}. (Bottom) Diagram of PFR approximated as a series of $N_{sections}$ CSTRs, each with a mass of catalyst ΔW. The outlet flow from reactor section k-1 serves as inlet flow to reactor k. The sum of ΔW over all $N_{sections}$ reactors is equal to W_{tot}.

Chapter 5. Steam Methane Reforming over Ni(111) Catalyst

5.1 Introduction

The development of new catalysts (e.g., Ni-bimetallic catalysts) that inhibit carbon formation while retaining activity to SMR is of particular interest, as discussed in Chapter 2. To aid the search for improved SMR catalysts, a thorough understanding of the key reactions and intermediates occurring on nickel is needed. In this chapter, a comprehensive, *ab initio* microkinetic model for nickel-catalyzed steam methane reforming on Ni(111) is presented. DFT and statistical thermodynamics are used to calculate the thermochemistry of SMR at industrial reforming conditions (800°C, 10 bar). Much of the power of microkinetic modeling lies in the information it provides about the surface in catalytic processes – information about which reaction steps are kinetically significant or rate-limiting and which intermediates have significant or insignificant concentrations on the surface.[52] Via flux and sensitivity analysis, the kinetic model is used to identify key reaction intermediates and steps that control catalytic productivity.

A catalyst particle is composed of many crystal faces, all of which could potentially show activity to the steam reforming reaction. The Ni(111) surface, also referred to as the Ni terrace, is known to be catalytically active[116] and is the most stable facet of Ni crystallites. It has also been shown that step sites play an important role in catalysis (of ethane reforming) on the nickel surface,[14] and the effects of these surface sites (and perhaps others) as well as catalyst support effects would need to be included to completely model a commercial Ni catalyst. It has been suggested that carbon formation begins when carbon adatoms nucleate at the step or defect sites, forming graphene layers, which blocks these sites from catalytic activity.[61, 117, 118] Abild-Pedersen, et al. reported that beyond a certain carbon coverage, the dissociation of methane will be dominated entirely by the terrace activity (significantly diminishing the overall rate of steam reforming).[42] It has also been suggested that promoters (such as Au doped on the Ni surface) tend to block these step sites.[39] As a result, both the step and the terrace may play an important role in steam reforming and the carbon formation mechanisms, depending upon the degree of carbon nucleation or dopant metal concentration on the catalyst surface. An increased understanding of the reactions taking place on both the step and the terrace will offer insight into the competition between SMR and carbon formation on the Ni catalyst. As a first step toward this comprehensive understanding, a ortant to this discussion. If these realectronic Structure Calculation Parameters and Methods

5.2 Electronic Structure Calculation Parameters and Methods

Planewave DFT calculations are performed with the software package Dacapo.[76, 87, 88] A 2x2 unit cell (corresponding to 0.25 ML coverage of adsorbates) is used along with a three-layer slab of the (111) facet of a FCC crystal of nickel atoms at the experimental lattice parameter (3.52 Å). Vacuum spacing equivalent to four nickel layers is used to separate successive images of the slab, and adsorption is allowed on only one side of the slab. Conventional counter-charges are used to cancel out the dipole interactions in the vacuum space.[79] The RPBE functional[76] is employed with spin polarization. The RPBE functional has been shown to be more accurate than other functionals such as PW91 or PBE in calculating heats of adsorption for molecules relevant in this study.[7] Core electrons are described using ultrasoft pseudopotentials[119] and the valence states are expanded in a basis set of plane waves with an energy cutoff of 340 eV. The Brillouin zone is sampled by a (6,6,1) k-point Monkhorst-Pack grid. Tests of grid sampling and slab/vacuum thickness indicate that the resulting energies are appropriately converged (generally within 1 kJ/mol and no more than 2 kJ/mol) for the parameters chosen in this study. Note that tests of basis set size show that while binding energies are not fully converged for all species at a cutoff energy of 340 eV, surface reaction energies and activation barriers are found to be converged to within less than 2 kJ/mol when compared to a cutoff energy of 600 eV.

In geometry optimizations, all adsorbate atoms and the top layer of metal atoms are relaxed. When necessary to avoid significant periodic-image interactions (such as hydrogen bonding between an adsorbate and its adjacent periodic image), a larger 2x3 unit cell is used. The stability of each adsorbate is studied at each of the binding sites shown in Figure 5-1, with the most stable geometry being used in subsequent calculations.

Initial estimates of transition states for both reactions and diffusion are obtained using the traditional nudged elastic band (NEB) approach, utilizing 7 images (including the endpoints). For reactions where more accuracy is desired, the transition state is refined using more images in the NEB study, or, preferably, by a first-order saddle point search.The NEB activation barrier is refined by performing constrained optimizations where the bond length corresponding to the reaction coordinate is fixed at intermediate distances between the bond lengths in the two successive images at the peak of the NEB calculation. The geometry that is the highest in energy is then used as an initial guess in a min-mode-following first-order saddle point search, using the built-in capability of Dacapo. For some reactions such as CH*+O*, this method was found to be more computationally efficient than Dacapo's built-in Climbing-Image NEB (CI-NEB) method on the 2x2 unit cell and without good initial guesses for the

transition state geometry. Harmonic vibrational frequency analysis is carried out on the resulting transition state geometry to confirm that it is a first-order saddle point. The level of refinement of for each reaction's activation barrier is denoted in Table 5-4.

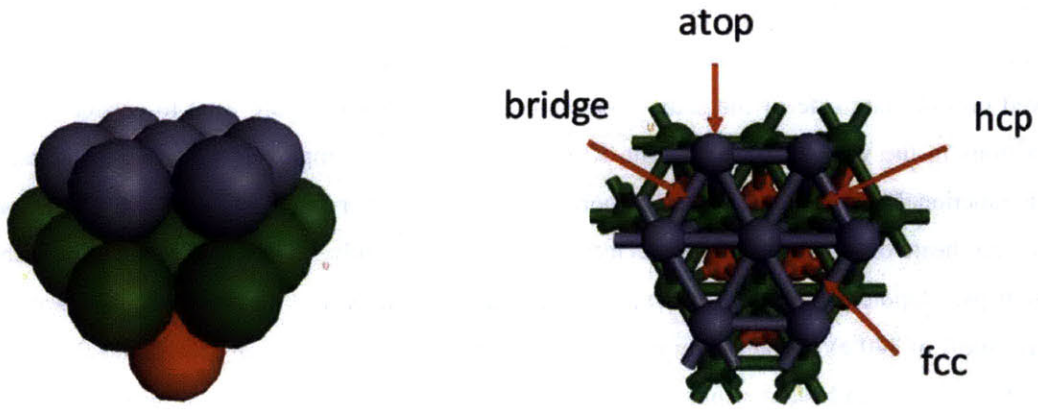

Figure 5-1. Three-layers of a Ni(111) slab, side view (left) and top view (right). The four distinct binding sites on the (111) surface – atop, bridge, hcp, and fcc - are labeled.

5.3 Steam Methane Reforming Thermochemistry over Ni(111)

Density functional theory calculations are used to predict the binding energies of all possible surface intermediates that can be formed from the combination of one molecule of $CH_4(g)$ and one of $H_2O(g)$. In addition, possible surface intermediates for the formation of $CO_2(g)$ are investigated. The mechanism that is explored is shown in Figure 5-2.

The DFT adsorption energy for each molecule in its most stable binding site is listed in Table 5-1. In addition to binding energy, it is also useful to examine barriers to diffusion (translation) and rotation for adsorbates. When binding energy is low, translational and/or rotational barriers can also be small. Because of their low diffusion barriers (Table 5-2), H_2O^*, CO_2^*, and CH_3OH^* are treated as free translators on the Ni(111) surface. Also, H_2O^* is the only species found to exhibit a rotational barrier much less than k_BT and is treated as a free rotator. Finally, the H-H transition state is treated as a free translator (based on previous experimental results, as discussed later). All remaining adsorbates (and remaining transition states when appropriate) are treated as harmonic oscillators. An electronic energy diagram of selected surface pathways is shown in Figure 5-3.

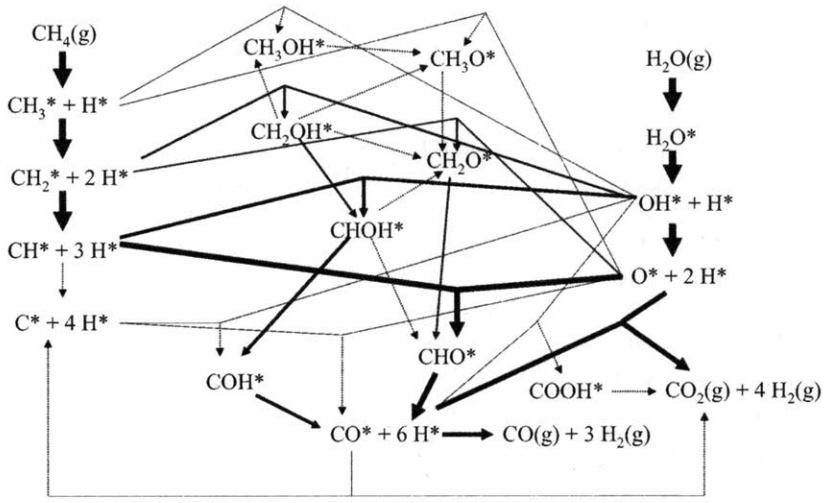

Figure 5-2. Proposed Steam Methane Reforming Mechanism on Ni(111) Surface (Line weights are indicative of steady state flux computed for each pathway at T=800°C, P=10 bar, initial H_2O:CH_4 ratio of 2.5, and 70% CH_4 conversion.)

Using the partition functions obtained from the statistical thermodynamic analysis detailed above, enthalpy, entropy, and Gibbs free energy values for each reaction in the proposed steam reforming mechanism are calculated, as shown in Table 5-4. The standard state for each adsorbate is 1 ML coverage at 800°C and 1 bar. Using plane-wave DFT, the overall enthalpy of the steam reforming reaction (reaction R1) is computed to be 243 kJ/mol compared to an accepted experimental value of 226 kJ/mol, derived from the Active Thermochemical Tables (ATcT).[120] This discrepancy in heat of reaction values results in a DFT-predicted equilibrium constant that is a factor of 6 from the expected value at 800°C. Fundamentally, this arises from the fact that the DFT heats of adsorption and DFT heats of reaction for surface reactions are inconsistent with the actual thermochemistry. At least one of these quantities must be adjusted to make the model consistent with known gas phase thermochemistry. Therefore, adjustments to the calculated thermochemical values are made to bring the results closer to expected experimental values through two different methods. The computed entropy is very close to the experimental value[120], so only the enthalpy is adjusted.

Table 5-1: Binding Energies, ΔE_{ads}^{*}, for Adsorbates in their Most Stable Binding Sites on Ni(111).

Species	ΔE_{ads} (eV)	Binding Site
H	-2.8	fcc
C	-6.00	hcp
O	-4.5	fcc
H_2	[b]	[b]
OH	-2.5	fcc
H_2O	-0.02	[e]
CO	-1.5	hcp
CH_4	[c]	[c]
CH_3	-1.3	fcc
CH_2	-3.3	fcc
CH	-5.9	hcp
CHO	□1.8	hcp
COH	-2.1[a]	hcp
CH_2O	-0.2	atop
CHOH	-2.4	fcc
CH_3O	-1.9	fcc
CH_3OH	-0.03	atop
CH_2OH	-1.0	atop/bridge
COOH	-2.3	atop/bridge
CO_2	0.03[d]	[e]

* Classical electronic binding energy from DFT calculations at a cutoff energy of 340 eV, consistent with previous work using the RPBE functional.[7] [a] COH(g) is unstable and dissociates. Binding energy is relative to CHO(g). [b] H_2 adsorbs dissociatively to two H adatoms. [c] CH_4 adsorbs dissociatively to CH_3 and H adatoms. [d] Species shows positive binding energy, within expected DFT error of ~10-20 kJ/mol. For consistency with other reforming models, the species is treated as a weakly-bound species in this analysis. [e] Species shows no discernable site preference.

Table 5-2: Partition Functions for Adsorbates on Ni(111) at T=800°C, Standard Pressure = 1 bar, and 1 ML Standard State Coverage

Adsorbate	Diffusion Barrier* (kJ/mol)	Q_{ads}† (1 adsorbate per 2x2 unit cell)	$Q_{ads,ZPE}$‡ (1 adsorbate per 2x2 unit cell)
H	13	4.7E7	1.3E9
C	50	3.4E8	4.4E9
O	48	6.7E8	6.7E9
OH	21	5.8E8	9.4E10
H_2O	0.3	2.1E11[a]	6.1E14[a]
CO	10	6.4E10	2.0E12
CH_3	31	9.1E6	5.9E11
CH_2	14	7.0E7	1.6E11
CH	46	6.8E7	1.5E10
CHO	13	2.4E9	1.3E12
COH	34	7.2E9	5.7E12
CH_2O	10	1.1E8	2.0E12
CHOH	25	7.8E8	1.1E13
CH_3O	10	5.8E7	3.5E13
CH_3OH	0.4	2.0E9[b]	2.7E16[b]
CH_2OH	19	1.7E8	9.9E13
COOH	25	2.5E9	9.5E12
CO_2	0.3	2.3E13[b]	3.0E15[b]
Slab	-	1.4E8	5.4E8

† Non-projected harmonic oscillator partition functions with zero of energy at the classical minimum, unless otherwise noted. ‡ Non-projected harmonic oscillator partition functions with zero of energy at the zero point energy, unless otherwise noted. * Diffusion barriers are estimated using a 3-image NEB study with relaxed adsorbate atoms and 1st-layer metal atoms. [a] Treated as free translation and free rotation about the principle axis resembling z-axis rotation. All remaining modes were treated as harmonic oscillations. [b] Treated as free translation, with remaining modes as harmonic oscillations.

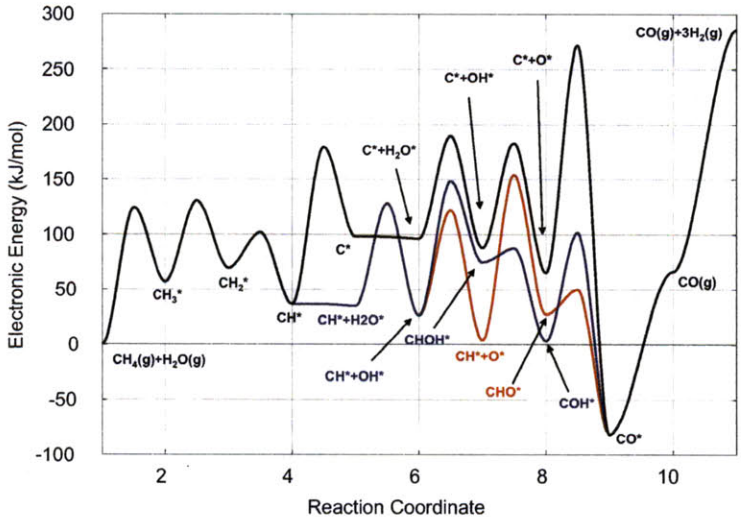

Figure 5-3. Electronic energies of selected pathways [relative to CH4(g) + H2O(g)] on the Ni(111) surface. The H* and H2O(g) species needed to balance the reactions have been omitted to simplify the notation.

Experimentally-Adjusted Heats of Adsorption

Method 1

As shown in Figure 5-4, experimental heats of formation for gas phase species (from the ATcT) and the DFT-predicted heats of adsorption are used to calculate experimentally adjusted heats of reaction for the surface reactions through thermodynamic cycles. This method results in equilibrium conversion that matches experimental values at the temperature of interest. However, when the energetics of the surface intermediates are effectively adjusted in this way, the energies of the transition states must also be adjusted, and it is not possible to maintain the computed reaction barrier for both the forward and the reverse reaction consistent with the original DFT calculation. Also, use of this method implies a greater confidence in the accuracy of DFT-predicted heats of adsorption than the DFT-predicted heats of surface reactions, a dubious assertion. In general, bond dissociation energies are much harder to predict using quantum chemistry than are reaction energies because the prediction of reaction energies typically benefits from partial cancellation of errors between the bonds formed and the bonds broken.

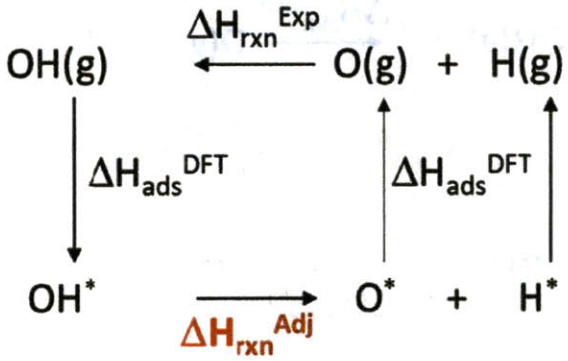

Figure 5-4. Diagram of the experimentally-adjusted heats of reaction thermodynamic cycle employed for the reaction OH* + * → O* + H*. The value shown in red is calculated using an experimental quantity for the gas phase heat of reaction and DFT-computed values for the heats of adsorption of the gas phase species.

Method 2

Known experimental heats of adsorption for one carbon-, one oxygen-, and one hydrogen-containing gas phase species (in this case, H, O, and CO – see Table 5-3) are used to produce experimentally adjusted heats of adsorption. The heat of adsorption data used in the calculations are valid for 25°C. To correct these heats of adsorption to values at 800°C, the DFT-predicted changes in adsorption energy with temperature are added to each value. Using thermodynamic cycles (shown in), these temperature-corrected heats of adsorption are combined with DFT-predicted heats of reaction (for the surface reactions) at 800°C to calculate experimentally adjusted heats of adsorption for the remaining species.

The enthalpy of the steam reforming reaction calculated through this method is 226 kJ/mol at 800°C, which is in agreement with the value calculated from the ATcT. Because DFT-predicted heats of reaction are used in the thermodynamic cycles, thermodynamic consistency between the forward and reverse reaction barriers is maintained for all surface reactions. However, the DFT-predicted reaction barriers cannot be maintained for both the adsorption and desorption reactions. Only the adsorptions of CH_4(g) and H_2(g) (the activated adsorptions) are affected by this inconsistency. The adsorption value is fixed at the DFT-calculated value and the desorption barrier is adjusted. In the case of hydrogen, the reaction barrier for associative desorption increases from the DFT-calculated value of 77 kJ/mol to an adjusted barrier of 99 kJ/mol. For methane, the reaction barrier for associative desorption increases from the DFT-calculated value of 72 kJ/mol to an adjusted barrier of 119 kJ/mol.

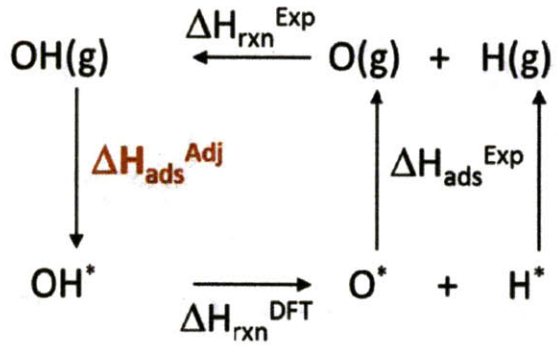

Figure 5-5. Diagram of the experimentally-adjusted heats of adsorption thermodynamic cycle employed for the reaction OH* + * → O* + H*. The value shown in red is calculated using an experimental quantity for the gas phase heat of reaction, experimental quantities or previously experimentally-adjusted heats of adsorption for the other heats of adsorption in the cycle, and DFT-computed values for the heat of reaction for the surface reaction.

Table 5-3: Experimentally Adjusted (Method 2) Heats of Adsorption, ΔH_{ads}^{Adj}, Compared to DFT Heats of Adsorption, ΔH_{ads}^{DFT}, for SMR Gas Phase Species on Ni(111).

Species	$\Delta H_{ads,25°C}^{Exp}$ (kJ/mol) [a]	$\Delta(\Delta H_{ads}^{DFT})$ (kJ/mol)†	$\Delta H_{ads,800°C}^{Adj}$ (kJ/mol)	$\Delta H_{ads,800°C}^{DFT}$ (kJ/mol)
CH_4	-	-	13	60
H_2O	-	-	-18	3
H_2	-	-	-92	-71
H	-266 [121]	-3	-269	-249
O	-470 [122]	1	-469	-427
CO	-13 [123]	9	-121	-135
CH_2O	-	-	-51	-7
CH_3OH	-	-	-43	-6
CO_2	-	-	-28	-3

† The DFT-predicted change in heat of adsorption from 25°C to 800°C.
[a] Determined from experimental data, combined with gas phase heats of formation data from the Active Thermochemical Tables when necessary

Table 5-4: Thermochemistry at 800°C and Kinetic Model Parameters* for SMR (1 bar standard pressure and 1 ML coverage) including Method 2 Heats of Adsorption Adjustments.

	Reaction	ΔH (kJ/mol)	ΔS (J/mol-K)	A †	E_a (kJ/mol) ‡
1:	$H_2(g) + 2* = 2H*$	-92	-129	1.1E3	4
2:	$H_2O(g) + * = H_2O*$	-18	-83	2.8E2	0
3:	$CO(g) + * = CO*$	-121	-132	2.3E2	0
4:	$CH_4(g) + 2* = CH_3* + H*$	13	-124	1.0E1	129
5:	$CH_2O(g) + * = CH_2O*$	-51	-157	2.2E2	0
6:	$CH_3OH(g) + * = CH_3OH*$	-43	-110	2.1E2	0
7:	$CO_2(g) + * = CO_2*$	-28	-103	1.8E2	0
8:	$CH_3* + * = CH_2* + H*$	3	-1	5.1E13	66
9:	$CH_2* + * = CH* + H*$	-38	-14	9.0E12	26
10:	$CH* + * = C* + H*$	54	-2	2.2E14	135
11:	$\square_2O* + * = OH* + H*$	-9	-58	1.4E11	89
12:	$OH* + * = O* + H*$	-33	-18	9.4E12	82
13:	$C* + O* = CO* + *$	-144	33	3.4E19	206
14:	$C* + OH* = COH* + *$	-83	15	9.8E17	126
15:	$CH* + O* = CHO* + *$	25	17	7.6E17	151
16:	$CH* + OH* = CHOH* + *$	48	8	3.5E17	123
17:	$CHO* + * = CO* + H*$	-115	13	9.4E12	20
18:	$COH* + * = CO* + H*$	-95	0	4.0E12	86
19:	$CHOH* + * = CHO* + H*$	-57	-9	7.5E13	66
20:	$CHOH* + * = COH* + H*$	-77	4	4.8E12	8
21:	$CH_2* + O* = CH_2O* + *$	28	-4	2.3E17	131
22:	$CH_2O* + * = CHO* + H*$	-42	8	4.8E13	31
23:	$CH_2O* = CHOH*$	15	16	1.0E13[a]	175[c]
24:	$CH_2* + OH* = CH_2OH* + *$	17	3	1.1E17	85
25:	$CH_2OH* + * = CHOH* + H*$	-6	-9	6.7E12	35
26:	$CH_2OH* + * = CH_2O* + H*$	-22	-25	4.7E12	59
27:	$CH_2OH* = CH_3O*$	-38	-11	1E13[a]	189[c]
28:	$CH_2OH* + H* = CH_3OH* + *$	-21	31	3.2E17[a]	143[b]
29:	$CH_3* + O* = CH_3O* + *$	15	9	1.1E18	152
30:	$CH_3O* + * = CH_2O* + H*$	17	-14	1.0E13[a]	99[c]
31:	$CH_3* + OH* = CH_3OH* + *$	-1	33	3.2E17[a]	125[c]
32:	$CH_3OH* + * = CH_3O* + H*$	-17	-42	1.0E13[a]	96[b]
33:	$CO* + OH* = COOH* + *$	63	-37	3.2E17[a]	111[b]
34:	$COOH* + * = CO2* + H*$	-69	51	1.0E13[a]	97[b]
35:	$CO* + O* = CO2* + *$	27	32	3.2E17[a]	149[b]
36:	$CO* + CO* = C* + CO2*$	171	-1	3.2E17[a]	326[b]

* Arrhenius pre-factors and activation energies are "temperature independent" and are regressed from the TST rate coefficient over a range of 800-1200K. † All pre-factors are in MKS units of length/number-s (e.g., m/s for Reaction 1 and m^2/mol-s for Reaction 13). The pre-factor is calculated via the statistical thermodynamic treatment presented in this study unless otherwise noted. ‡ Activation energy calculated by finding the first-order saddle point energy on a 3-layer slab unless otherwise noted. [a] Arrhenius pre-factor is approximated as k_BT/h (~1E13 s^{-1} at 800°C), divided by the total concentration of sites (3.095E-5 mol/m^2) when appropriate (e.g., bimolecular reactions). [b] Activation energy is an electronic energy obtained via NEB on a 2 layer slab. [c] Activation energy is an electronic energy obtained via NEB and refined by a series of constrained optimizations on a 2 layer slab.

Method 2, the experimentally adjusted heats of adsorption method, is preferred over Method 1, the experimentally adjusted heats of reaction method. The second method results in inconsistency between computed forward and reverse reaction barriers only for some adsorption steps, instead of all surface reaction steps. The inconsistency is preferred at an adsorption step because this is not a branching point in the mechanism and will therefore have little impact on the reaction pathway on the surface, a focus of this study. In addition, Method 2 relies on DFT-predicted heats of surface reactions rather than DFT-predicted heats of adsorption, which is preferred in terms of accuracy due to presumably greater cancellation of error (e.g., of the metal-adsorbate bond) in surface reaction prediction. As shown in Table 5-3, there are large discrepancies between the DFT-predicted values for heat of adsorption ($\Delta H_{ads,800°C}^{DFT}$) and those calculated via Method 2 ($\Delta H_{ads,800°C}^{Adj}$) for species such as O and H. Therefore, we use values computed by Method 2 as input for our kinetic studies.

Comparison to Previous Studies

The electronic energy results for CH_x intermediates and transition states compare well with those of Bengaard, et al.[39] with the exception of the electronic energy calculations for the barriers of CH_4(g) adsorption and the reaction of C^* and O^* to form CO^*. The discrepancy in the case of methane adsorption seems to be a result of the different unit cell size used in the analyses, with the 3x3, 5-layer unit cell used by Bengaard (for this reaction) yielding a more accurate estimate than the 2x2, 3-layer unit cell used here. The discrepancy in CO^* may be due to error introduced by their constrained optimization search versus the first-order saddle point search employed here (constrained optimizations will yield approximate transition state energy estimates, which are refined in this work via first-order saddle point searches). Additional surface pathways that pass through CH_xO^* species were compared to the results of Wang, et al.[56] While there are discrepancies in the intermediate species binding energies that are likely attributable to their use of the PBE functional and the use of the RPBE functional in the DFT calculations for this work, the computed electronic energy landscapes are generally similar. Like Wang, et al., the calculations presented here find that pathways through CHO^* and $CHOH^*$ have intermediates that are lower in energy than the direct formation of CO* pathway studied by Bengaard, et al. In addition, the calculations presented here agree (with discrepancies often less than 10 kJ/mol and at most 18 kJ/mol) with the electronic reaction barriers obtained by Wang, et al. for the reforming pathway through CHO^* that is shown in Figure 5-3 (the only pathway for which Wang, et al. reported activation barriers).

5.4 Kinetic Modeling of Steam Methane Reforming over Ni(111)

Because there are multiple pathways similar in intermediate energies and with barriers that are comparable, a kinetic model is employed to discern dominant reforming pathways and sensitive reactions in the reaction network. The kinetics of SMR are investigated at 800°C and 10 bar pressure with a H_2O:CH_4 ratio of 2.5 and reactor residence time of 60 seconds, which (with the present model) corresponds to 70% methane conversion. Entropic effects at this elevated temperature are significant, with total predicted surface coverage of only 23% at steady state. Three species, H*, CO* and H_2O*, make up most of this with predicted coverages of 15%, 7.5% and 0.1%, respectively. Other important adsorbates (in descending order of coverage) are predicted to be O*, CH*, and OH*. All surface coverages are listed in Table 5-5.

Table 5-5: Surface Coverage of Adsorbates at Steady State under the Conditions Described in Figure 5-2.

Adsorbate	Percent Coverage
H*	15
CO*	7.7
H2O*	0.11
O*	3.5E-02
CO2*	7.5E-03
CH*	5.5E-03
OH*	Ï.4E-03
CH2*	8.5E-05
C*	5.0E-05
COH*	3.7E-05
CH3*	2.6E-05
CHO*	8.2E-07
CH3OH*	1.8E-08
CH3O*	4.0E-09
COOH*	1.4E-09
CHOH*	7.9E-10
CH2O*	6.2E-10
CH2OH*	2.2E-10

At low surface coverage, dissociations are highly favored. In SMR, the primary reaction types of interest are dehydrogenation and oxygen-addition. In dehydrogenation reactions within our mechanism, cleaving of a C-H bond is generally predicted to have a smaller barrier than O-H bond cleavage on Ni(111). Also, oxygen-addition (or OH-addition) reactions are predicted to see considerably higher barriers than dehydrogenation reactions. These observations can be combined to predict the behavior of molecules such as CH_xOH, for example. The concentration of CH_xOH species will likely be higher for small values

of x than large values because species are driven to dissociate. Also, because it is easier to remove a hydrogen from carbon than oxygen, it is more likely CH_xOH will form $CH_{(x-1)}OH$ than CH_xO. Such trends can be confirmed by performing flux analysis.

Flux analysis was carried out by tracking the appearance and disappearance of each surface intermediate within the kinetic model (Figure 5-2). This analysis reveals the most important features of the kinetics. The Ni(111) catalysis begins with the adsorption of $H_2O(g)$ and the dissociative adsorption of $CH_4(g)$. Water progressively dissociates from H_2O^* to OH^* to O^*, with the ratio of O^*:OH^* being approximately 20:1 for the conditions shown in Figure 5-2 (because of the greater surface stability of O^* and the high concentration of vacant sites).

Once methane has dissociatively adsorbed onto the surface, the removal of two additional hydrogen atoms to form CH^* occurs relatively easily, with a free energy barrier of approximately 60 kJ/mol for the first hydrogen atom and approximately 30 kJ/mol for the second. However, the high instability of carbon adatoms on the Ni(111) surface means that the removal of the final hydrogen atom to form a carbon adatom exhibits a much larger, 115 kJ/mol free-energy barrier. Furthermore, the reaction of C^* with O^* to form CO^* has an even higher free energy barrier of 170 kJ/mol, so this pathway is not predicted to play a major role in the catalytic turnover. The pathway involving C^* and OH^* forming COH^* and then CO^* is more favorable, but the low surface concentrations of both C^* and OH^* make this pathway unimportant despite the smaller barrier of 120 kJ/mol. Under the conditions presented here, our model predicts most C^* that is formed recombines with H^* to form the more stable CH^*.

Instead, the kinetics favor the combination of CH^* with either O^* or OH^*, with free energy barriers of 150 kJ/mol and 130 kJ/mol, respectively. Though both barriers are higher than the barrier to removing the final hydrogen in CH^*, these barriers are lower than the $C^* + O^*$ barrier for the $CH^* \rightarrow C^* \rightarrow CO^*$ pathway, and both pathways' intermediates are overall lower in free energy than those from any other route.

In fact, roughly 87% of the total reaction flux is predicted to involve the reaction of CH^* with an oxygen-containing species. The intermediates CH^* and O^* were found to combine to form CHO^*, which subsequently decomposes to form CO^* and H^*. This single route is predicted to dominate all others on the surface, accounting for approximately 56% of the total predicted reaction flux. Even though this route involves a higher barrier than many other pathways to CO^*, its low overall free energy combined with the high surface concentrations of CH^* and O^* make it more favorable than other routes.

The second-most active pathway (~31% of the predicted flux) includes the formation of $CHOH^*$ from CH^* and OH^* with subsequent reaction to COH^*. With its smaller reaction barrier, $CHOH^*$ is more easily formed from CH^* than CHO^*, but the low concentration of OH^* slow this pathway. Once $CHOH^*$ is formed, it almost entirely decomposes to COH^*. As discussed above, the C-H bonds typically break more readily than O-H bonds in the CH_xOH species, and COH^* is thermodynamically more stable than CHO^*.

Approximately 12% of the flux is found to involve the reaction of CH_2* with either O* or OH*, with the reaction forming CH_2OH^* favored 2.5:1 for the conditions analyzed here. This is an instance where the reaction with OH^* is more dominant than the reaction with O^* despite the higher surface concentration of the oxygen adatom. This result appears to be a consequence of the considerably larger Gibbs free energy barrier for the addition of CH_2^* and O^* of 140 kJ/mol compared to the 100 kJ/mol barrier for the reaction of CH_2^* with OH^*. These pathways through CH_2^* are predicted to be less important than the CH^* pathways because of the lower surface concentration of CH_2^*. The CH_2O* intermediate is found to form CHO* while the CH_2OH* intermediate is found to form COH* through the CHOH* intermediate. This again demonstrates the preference for C-H bond cleavage over O-H bond cleavage.

In all cases CHO* and COH* decompose into CO* and H*. By reacting with an oxygen-containing species before removing all the hydrogen atoms on the carbon, the adsorbate avoids the unstable (at least on Ni(111)) C* adatom in all of these major pathways. These species then desorb (molecularly for CO* and associatively for H*) to form the gas phase products. Essentially all CO_2(g) is formed from the reaction of CO* with O*. The pathway through COOH* that has been mentioned in the literature[50, 53] is not found to be important under these conditions. Finally, note that the branching ratios among these key pathways are sensitive to error and DFT may not be accurate enough to precisely distinguish between pathways that are relatively close in energy. To summarize, the kinetic simulations for SMR on Ni(111) based on DFT calculations suggest that a mixture of pathways are involved in the SMR reaction. The dominant pathway involves the decomposition of methane to CH^* and water to O^*, which then combine to form CHO^*. After losing the last hydrogen in CHO^*, hydrogen, carbon monoxide, and carbon dioxide gases are produced. However, one cannot neglect the $CHOH^*$ pathway, and even CH_2O^* and CH_2OH^* are predicted to play a minor but nontrivial role in the SMR process. Note that these results are for the Ni(111) surface and do not consider the effects of step sites.

Sensitivity analysis is performed by perturbing the rate coefficient for each reaction by a factor of 100 (up and down). The mechanism is found to be most sensitive to downward perturbations in the rate coefficient of CH_4(g) adsorption. The reaction mechanism is also found to be sensitive to perturbations of

the reaction forming CHO^* from CH^* and O^* and the reaction forming $CHOH^*$ from CH^* and OH^*. To a lesser extent, the reaction of CH_2^* and O^* forming CH_2O^* and CH_2^* and OH^* forming CH_2OH^* are also found to be sensitive. The sensitivity analysis reveals that in addition to methane adsorption, formation of the CH_xO^* complex is a key step in the reforming process and enhancing steps that promote its formation will increase the overall rate of reforming by providing a pathway to CHO^* or COH^* formation on Ni(111). Reactions involving the CHO^* species on Ni(111) have been studied in detail by Pistonesi, et al.[28] Interestingly, the CHO^* species has also been found to be an important intermediate in hydrocarbon oxidation over Rh, Pt. and Pd catalysts.[124, 125]

The most abundant decomposition product of methane on the Ni(111) surface is found to be CH^*. It is considerably more stable than C^* on this surface. Therefore, the CH^* intermediate could be a key species in carbon formation mechanisms (e.g., CH^* diffusion to step sites and subsequent reaction with carbon/graphene), and could be a useful starting point for carbon formation mechanism investigations. These studies can then be extended to Ni-bimetallic alloys to investigate their effect on carbon formation and overall reforming activity.

To explore the effects of DFT error, the sensitivity of the model to errors in binding energy is examined by de/stabilizing individual species energy by 20 kJ/mol and once again observing rate of hydrogen production. Two cases were run for each species, one where forward reaction barriers were held fixed and one where the reverse reaction barriers were held fixed as the reactant well energy was perturbed by ±20 kJ/mol. The model was found to be most sensitive to species highest in surface coverage, such as H^* and CO^*, as well as reactants preceding large reaction barriers, such as CH^* and O^*.

The sensitivity of the species high in surface coverage is a direct result of de/stabilizing perturbations in binding energy causing increases/decreases in the fraction of vacant sites available for reaction. However, the binding energy of both H^* and CO^* were fixed using experimental data – so DFT error related to these species is not a significant concern. For species such as CH^* and O^* that are part of a reactant pool preceding a large reaction barrier, the sensitivity is only seen when the forward barrier is fixed. In these cases, stabilizing the reactant increases its surface coverage, thereby increasing the reaction rate through the rate-limiting reaction (such as $CH^* + O^* \rightarrow CHO^*$). When the reverse barrier is fixed instead of the forward barrier, the increase or decrease in species surface coverage is found to offset the increase or decrease in reaction barrier.

However, while the hydrogen production rate shows sensitivity to these species binding energies, the SMR mechanism described above is not greatly changed. Under binding energy perturbations, the majority of the flux continues to pass through the reaction of CH^* with O^* to form CHO^*. If the OH^* species is stabilized, then the reaction of $CH^* + OH^*$ to form $CHOH^*$ becomes more dominant. Likewise, stabilization of the CH_2^* species (or destabilization of the CH^* species) increases the flux of the reaction leading to the formation of CH_2OH^*. However, in all of these cases, the reactions of $CH^* + OH_x^*$ remain the dominant reforming pathways.

5.5 Impact of the Statistical Mechanical Treatment

Often in the literature, entropic effects are neglected or roughly approximated. In this study, statistical thermodynamics, as detailed in Chapter 3, are applied to calculate thermodynamic quantities at realistic temperatures and pressures. In particular, this approach allows for the consistent accounting of entropy throughout the reaction network. It is useful to examine what impact this treatment has on the results of this study. From the data in Table 5-4, the dissociation of OH^* to form O^* and H^* is downhill in enthalpy by 33 kJ/mol. However, it can also be seen that there is an 18 J/mol-K entropic penalty for dissociation of OH^* to O^* and H^*. Because of the high temperatures associated with industrial reforming, this entropic penalty is significant (~20 kJ/mol in Gibbs free energy at 800°C). Note that the standard state entropic penalty listed above is equivalent to the thermal entropic penalty at 800°C. Configurational entropy will contribute further to the entropic penalty with an additional 13 J/mol-K entropic penalty at steady state for the dissociation of OH^*.

To illustrate the impact of accurately accounting for entropy, it is useful to construct a comparative kinetic model where complete entropic effects are not included. A model is constructed using the entropies of adsorption calculated in this study (so that the surface concentrations would be on the appropriate order of magnitude) but assuming zero entropy change for surface reactions along with enthalpies of reaction approximated by electronic energy changes. When entropy of surface reactions is not taken into account, the O^* fractional coverage is found to increase by 3 orders of magnitude (at the same temperature, pressure, and reactor residence time), causing large increases in flux through the $CH_x^* + O^*$ reactions. The importance of the $CH^* + OH^*$ reaction is underestimated in this entropy-free model when compared to the results of our full kinetic model that included entropic contributions, with a reduction in flux through this reaction from ~31% to ~7% of the total reforming flux. The dissociations of H_2O^* and OH^* are the reactions most affected by ignoring entropy-of-reaction on the surface. Other

reactions (Table 5-4) have high entropies of reaction; however, their importance in the overall reaction network under these conditions is much less than that of water dissociation reactions. In addition, because the entropy of reaction is low for many reactions, the relative stabilities of many reactant and product pools are changed little by neglecting the entropy change.

However, the above analysis does not address one of the most important advantages of the thermodynamic treatment applied in this study - obtaining reasonable surface coverages as a function of temperature. At industrially relevant temperatures, the entropies of adsorption have a large impact on the total surface coverage – which is particularly important in cases such as the analysis of the competition between carbon-carbon and carbon-oxygen reactions (i.e., carbon formation vs. methane reforming). If no experimental estimates of entropy of adsorption are available (and the thermodynamic treatment applied here is not performed), then obtaining reasonable surface coverages is unlikely. For example, if in addition to setting entropies of surface reactions equal to zero, the entropies of adsorption are set equal to zero, the predicted surface coverage would exceed 95%, a considerable contrast to our predicted results of 20-25% coverage when entropy is considered.

5.6 Comparison of Computational Results to Available Experimental Data

When applied to an ideal plug flow reactor, the microkinetic model developed in this study predicts overall SMR rates that are approximately three to four orders of magnitude slower than experimentally-measured reforming rates using commercial supported catalysts.[49] A likely contributor to this disagreement is the fact that the model presented here pertains only to the Ni(111) catalyst surface, which is but one of many facets of a commercial catalyst. In particular, the suggestion that step sites are the most active reforming sites[14] when not deactivated by carbon formation or dopant metals suggests that a Ni(111) reforming model would under-predict overall reforming rates. Therefore, a reforming model that includes contributions from step sites would be necessary before useful comparison to experimental reforming rates on commercial catalysts can be made. In addition, the reported reaction energies and activation barriers are calculated at specific conditions (e.g., 0.25 ML coverage of the species of interest). These energies could be different at another coverage or in the presence of other species.

However, the purpose of this study is not to model the overall reforming rate, but to gain an increased understanding of the SMR over Ni(111). In particular, we are interested in the competition between surface pathways as well as the rate-limiting steps of the reaction network on the Ni(111) surface. Therefore, the results presented here are compared to single-crystal Ni(111) data to evaluate the accuracy of the computational methods employed here.

Previous investigation of CH_3^* decomposition on the Ni(111) surface by high-resolution electron energy loss spectroscopy (HREELS) led to the conclusion that CH_3^* is less stable on the surface than CH^*+2H^*.[116] The authors also concluded that the barrier from CH_2^* to CH^* is likely on order of or smaller than the barrier from CH_3^* to CH_2^* because CH_2^* was not observed on the surface. Both of these observations are consistent with the results of our computational investigation, suggesting that the computational methods are sufficient to obtain reasonable estimates of relative energies on the surface (at least for the case of methane decomposition), which is important for analysis of reforming pathways on the surface. Similar comparisons would be necessary for other reaction pathways to make a comprehensive assessment.

Single-crystal Ni(111) hydrogen adsorption/desorption data[121, 126] provide another point of comparison of our computational methods to experimental data. Applying the same definition of sticking coefficient as the experimental investigators, we obtain a sticking coefficient estimate for hydrogen adsorption of 0.13 (at T=150°C using Arrhenius parameters regressed from computed transition state theory rate coefficients over a range of 25°C to 275°C, which is similar to the temperature range of the experimental investigations) when the transition state is treated as a free translator. The treatment of free motion is based upon experimental observation[127] and also justified by the weak binding and Ni-adsorbate bond length of the transition state. This value for hydrogen sticking coefficient is consistent with the experimentally obtained value of 0.1 to 0.2[121] and the "rough estimate" by Christmann, et al. of 0.25. The present work predicts the pre-exponential factor for hydrogen desorption to be 0.77 cm^2/atoms-s, with a reverse barrier (after experimental adjustment of hydrogen's heat of adsorption) of 98 kJ/mol. Experimentally obtained values for the desorption pre-exponential factor are 0.2[121] and 0.08[126] cm^2/atoms-s while the values obtained for the reverse activation barrier are 95.0[121] and 96.2[126] kJ/mol. The model presented here appears to over-estimate the desorption pre-exponential factor, which may be a result of treating the adsorbed product, H^*, as completely immobile using a harmonic oscillator partition function when in fact it likely has some hindered motion on the surface. Note that because this model slightly over-estimates both the pre-exponential factor and the reverse activation barrier, the reverse rate coefficient is still in close agreement with the experimentally determined value.

5.7 Conclusions and Recommendations

Density functional theory calculations are performed using the planewave, periodic boundary condition simulation package Dacapo to model the thermochemistry of steam methane reforming over Ni(111). A statistical thermodynamic treatment is applied throughout to obtain values for enthalpy and entropy under realistic reforming conditions. The thermochemical data are combined with electronic activation barriers from Dacapo to develop a microkinetic model to simulate SMR over Ni(111). True saddle points are found for the important reactions, avoiding the uncertainty in conventional NEB estimates of reaction barriers. Flux and sensitivity analysis are used within the kinetic model to determine the dominant reforming pathway. The primary pathway involves CH_4(g) adsorption and decomposition to CH* in addition to H_2O(g) adsorption and decomposition to 2H* and O*. The rate-limiting steps are found to be the addition of CH* to O* to form CHO* and the addition of CH* to OH* to form CHOH*. The decomposition of CHOH* is found to lead to COH*, which along with CHO* subsequently decomposes to form CO*. The statistical mechanical treatment applied in this study allows for consistent accounting of entropy, which is found to be important in obtaining reasonable surface coverages of reaction intermediates – a factor that can influence the determination of active reforming pathways on the catalyst surface.

The combination of electronic structure calculations and the statistical mechanical treatment applied here predicts several instances of single crystal Ni(111) data well. This gives confidence in this approach for modeling heterogeneous catalysis. In addition, analyzing multiple pathways, not just the most straightforward, proved to be important as multiple reforming pathways are found to be active. It should be noted that only the combinations of one CH4(g) and one H2O(g) molecule are considered for the primary SMR reaction in this model, and other pathways are possible. However, it is also found that larger species like CH_2O, CH_2OH, CH_3O, etc. are present in low concentrations due to the large driving force for dissociation at the low coverages (and high vacant fraction) found at the elevated temperatures associated with SMR. As such, limiting the analysis to pathways through molecules with one carbon and one oxygen molecule is not as alerting as it might otherwise be. Despite the good agreement with single-crystal Ni(111) data, the overall rate of SMR (on multi-faceted commercial nanoparticle catalysts) is under-predicted by three to four orders of magnitude. Thus, it is suspected that the model is missing important contributions, with the contribution of other surface facets to the SMR reaction being a key area of interest.

Chapter 6. Steam Methane Reforming over Multi-Faceted Ni Catalyst

6.1 Introduction

In the previous chapter, steam methane reforming was investigated on the Ni(111) surface. In this chapter, the role of additional surface facets in SMR is investigated. While the reforming pathway through direct formation of CO* from C* and O* has been studied at the nickel step edge,[32, 39] other potential pathways (Figure 6-1) have remained largely unexplored on nickel surfaces other than the (111) facet. In this chapter, the multiple-pathway analysis of SMR over Ni(111) is extended to develop an ab initio microkinetic model of steam methane reforming over a multi-faceted nickel catalyst.

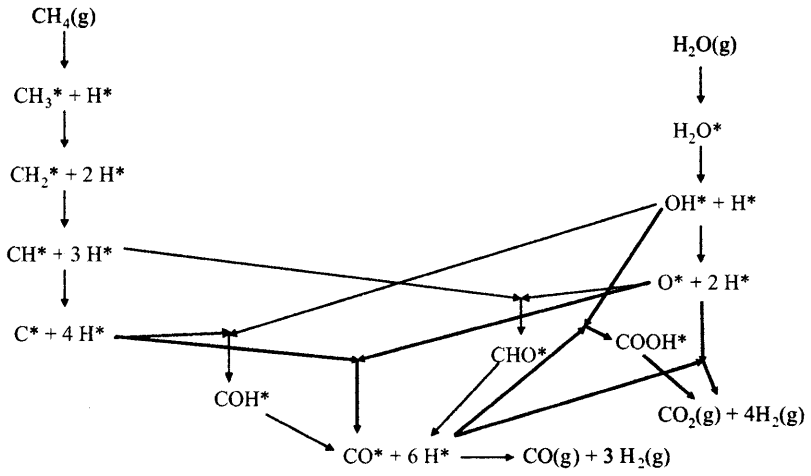

Figure 6-1. Steam Methane Reforming mechanism investigated on Ni(111), Ni(211), and Ni(100)

In this chapter, the effects of the Ni(111), Ni(100) and Ni(211) surface facets are included (Figure 3-1). The Ni(111) and Ni(100) surface facets are the most abundant facets of nickel and the Ni(211) surface is employed as a surrogate surface to model the effects of under-coordinated step-edge sites. Density functional theory, statistical thermodynamics and transition state theory are used to compute the thermochemistry and kinetics of the mechanism shown in Figure 6-1 on each of these surfaces. The thermochemical and kinetic values for each surface are combined in a mean-field, microkinetic model to

simulate SMR at industrial reforming conditions over a multifaceted nickel catalyst. The microkinetic model is used to investigate the primary reforming pathways, including the relative activity of each surface facet to the reactions included in the mechanism. The microkinetic model provides insight into the rate-limiting reactions as well as the most dominant surface species on each surface facet. In addition, incorporation of the microkinetic model into a plug-flow reactor model allows for comparison of the model's results to experimentally-observed rates of methane conversion.

6.2 Computational Methods

Electronic Structure Calculation Parameters and Methods

Plane wave, periodic boundary condition DFT calculations are performed in the Vienna Ab Initio Simulation Package (VASP).[84-86] The calculations consider three model surfaces: the (111), (100), and (211) surface facets (see Figure 3-1) of a FCC crystal of nickel atoms at the experimental lattice parameter (3.52 Å). For (111) surface calculations, a supercell consisting of a 3x3 unit cell of three layers of metal atoms with approximately 10 Å of vacuum spacing between periodic images of the metal slab is employed. The supercell used to model the (100) surface facet consists of a 2x2 unit cell, also with three layers of metal atoms with approximately 10 Å of vacuum spacing separating periodic slab images. The "clock" reconstruction of the (100) surface is not considered in this study.[128] The (211) surface facet is modeled using a 3x1 unit cell of nine layers of metal atoms (e.g., the three atoms in a row of the top-most level of atoms each have a different z-coordinate, making nine layers for a unit cell that is three atoms deep per row), with periodic images of the metal slab being separated by approximately 12 Å of vacuum spacing. The application of a dipole correction to electro-statically decouple the periodic slabs is not employed after test cases found its effect to be less than 1 kJ/mol in binding energy. A 15^3 $Å^3$ cube unit cell is used to study isolated gas phase atom and molecules.

In our DFT calculations, we use the RPBE[76] functional with spin polarization. The RPBE functional has been shown to be more accurate than other functionals such as PW91 and PBE in calculating heats of adsorption on nickel for molecules relevant in this study.[7] Projector-augmented wave (PAW) potentials[129] are used to describe the effect of core electrons, while the valence states were expanded with an energy cutoff of 400 eV. The Brillouin zone is sampled by (3,3,1), (4,4,1), and (4,3,1) k-point Monkhorst-Pack grids for the (111), (100), and (211) surface facets, respectively. Convergence tests were conducted when

choosing the selected values energy cutoff, slab thickness, and k-point spacing and energies were found to be reasonably well converged for the stated values of these parameters.

In geometry optimizations and first-order saddle point calculations for reaction transition states, all adsorbate atoms and the top layer of metal atoms are relaxed. First-order saddle point calculations for transition state geometries are carried out using the dimer method.[91] In some cases, initial guess geometries for the dimer calculations are obtained using the climbing-image nudged elastic band (CI-NEB) method.[90] Geometry optimizations are carried out until the change in energy between successive ionic relaxations is less than 1E-4 eV. First-order saddle point searches are considered converged when all forces are less than 1E-3 eV/Å.

Harmonic vibrational frequency analysis is performed on stable adsorbate and transition state geometries to obtain frequencies for calculation of kinetic parameters. In addition, frequencies for the transition states are used to confirm that the negative mode for each transition state corresponds to the desired reaction coordinates. The vibrational frequency calculations are performed using the dynamical matrix code[130] in VASP, with a tighter convergence parameter of 1E-6 eV/Å on forces to ensure better-converged frequencies.

Species Thermochemistry

The enthalpy, entropy, and Gibbs free energy are computed for each species as a function of temperature. The partition functions used to calculate thermodynamic quantities are taken from Chapter 3. Partition functions are applied to describe translation and rotation as either free or frustrated (e.g., two dimensional gas with free translation vs. a tightly bound adsorbate that is localized on the surface). Of the adsorbates included in the current mechanism, only H_2O* and CO_2* are found to be weakly-bound, freely rotating and translating molecules. Consistent with the Ni(111) investigation reported in the previous chapter, the transition state for hydrogen adsorption is treated as freely translating.

The experimentally-adjusted heats of adsorption procedure described in the previous chapter is applied to the calculated heats of adsorption for the (111) surface in the present study. The experimentally-adjusted heats of adsorption for the (211) and (100) surfaces are computed by adding the difference in DFT-computed binding energies for a species on the surface of interest and the species on the (111) surface to the experimentally-adjusted heat of adsorption for that species on the (111) surface.

Estimation of Fractional Coverage of Each Surface Facet

To obtain a theoretical prediction of equilibrium particle shape, the nickel nanoparticle is assumed to be a truncated octahedron with eight hexagonal (111) and six square (100) facets on its surface. The truncated octahedron shape has been shown to be a reasonable equilibrium model for nanoparticles with surface energies similar to those exhibited by nickel.[131] The atoms along the interfaces where (111) facets intersect with other (111) or (100) facets are assumed to be unstable and lost into solution, thus creating step edges. This assumption is consistent with previous computational investigation and experimental observation.[132,8] The thermochemistry and kinetics of the step edge atoms are modeled using the (211) surface facet.

The total number of step edge atoms is approximated as the sum of edge and vertex atoms on the truncated octahedron. The number of (111) atoms, (100) atoms, and step edge atoms are calculated using the appropriate equations reported by Li, et al., which are functions of n_{squ} and n_{hex}, the number of edge atoms along the (111)-(100) and (111)-(111) interfaces, respectively.[131] From Li, et al., $N_{vertex} = 24$,

$$N_{surf,111} = 4\left[\left(n_{squ} + n_{hex}\right)\left(n_{squ} + n_{hex} - 9\right) + 2n_{squ}n_{hex} + 14\right], \qquad \text{[Equation 6-1]}$$

$$N_{surf,100} = 6\left(n_{squ} - 2\right)^2, \qquad \text{[Equation 6-2]}$$

and

$$N_{edge} = 12\left(2n_{squ} + n_{hex} - 6\right). \qquad \text{[Equation 6-3]}$$

Note that an error exists in Equation 2.1 of Li, et al. (corresponding to Equation 6-1 here), where the factor of 4 should be placed outside the left bracket, not inside. The particle size is calculated from the average of the distances from the center of the particle to the center of a (111) facet ($D_{(111)}$) and to the center of a (100) facet ($D_{(100)}$), assuming a nickel lattice parameter of a = 3.52 Å. These lengths are related by the ratio

$$\frac{\gamma_{(100)}}{\gamma_{(111)}} = \frac{D_{(100)}}{D_{(111)}}, \qquad \text{[Equation 6-4]}$$

where γ is the surface energy of the subscripted facet. The values used for the surface energy of Ni(100) and Ni(111) are 2.88 J/m^2 and 2.44 J/m^2, respectively.[133] The individual lengths are calculated from the equations

$$D_{(100)} = \left(\frac{1}{2}\right)\left(\frac{a}{2}\right)\left(2n_{squ} + 2n_{hex} - 4\right), \qquad \text{[Equation 6-5]}$$

and

$$D_{(111)} = \left(\frac{1}{2}\right)\left(\frac{a\sqrt{3}}{3}\right)\left(2n_{squ} + n_{hex} - 3\right). \qquad \text{[Equation 6-6]}$$

Microkinetic Model

A mean-field kinetic model is constructed by combining the computed thermochemical and kinetic values for each surface facet with the surface facet fractional abundance data gained through particle shape analysis. The kinetic model is used to gain an understanding of reforming pathways, through sensitivity analysis, and the relative degree of rate limitation of the reactions in the mechanism, through sensitivity analysis. For flux and sensitivity analyses, a continuous-stirred tank reactor (CSTR) formulation is employed. For comparisons to fixed-bed reactor studies, a plug-flow reactor (PFR) formulation is employed. The reactions in the kinetic model can be categorized as either 1) the adsorption/desorption of a species onto/from a surface facet, 2) a surface reaction with all species on a single surface facet, and 3) the diffusion of an adsorbed surface species from one surface facet to another. The diffusion between surface facets is treated as a reaction in the model because it involves the dis/appearance of a surface species from/on a surface facet. The equations used to formulate the model are described in detail in Chapter 4. For Ni(111) and Ni(211), the value of total concentration of sites (C_T) is 3.10 x 10^{-5} mol/m^2. For the (100) surface, the value of C_T is 2.68 x 10^{-5} mol/m^2. For all surfaces, it is assumed that there exists one binding site per surface nickel atom.

Because diffusion in this system generally involves lower activation barriers than surface reactions, the diffusion in the mean-field model will often be considerably faster than surface reactions. Thus, obtaining accurate pre-exponential factors for diffusion is not as important as obtaining the pre-factors for adsorption and surface reactions. For inter-facet diffusion, all pre-factors are estimated to be 1×10^{12} s^{-1}, which is an approximate value chosen based on frequencies for frustrated translation of a few hundred wave numbers (based upon frequency projections performed for frustrated translation on the Ni(111) surface, following the method described previously[12]). Though the pre-factor is estimated, the correction ($M_{Int,fs,i}/M_{fs}$) in the inter-facet diffusion rate coefficient from Chapter 4 is still applied.

6.3 Estimation of the Fraction of Each Surface Facet of the Nickel Nanoparticle

In order to account for differences in the relative abundance of each surface facet, the fraction of each surface facet as a function of particle size is calculated as an input for the kinetic model. The equilibrium shape of the nickel particle is assumed to be a truncated octahedron with Ni(111) and Ni(100) facets. The relative stability of these facets is used to determine the relative abundance of the binding sites, with the boundaries between the facets being treated as Ni(211) step edges. The resulting surface fraction of each facet is shown in Figure 6-2. For an approximately 7 nm particle size, the fraction of each surface facet is found to be 0.74, 0.15, and 0.11 for Ni(111), Ni(100), and the Ni(211) surfaces, respectively. In this work, comparisons are made to the SMR experimental data sets of Xu and Froment[49] as well as those of Wei and Iglesia[38]. The ~7 nm nickel particle size is consistent with the catalyst particles in the experiments of Wei and Iglesia. The catalyst particle size in the experiments of Xu and Froment is not provided and is assumed to equal that of Wei and Iglesia's nickel catalyst for the calculations in this work.

A comparison of the truncated octahedron-predicted fractions to the results of full Wulff constructions, up to a particle size of approximately 10 nm, is shown in Figure 6-2. The Wulff construction data, which are considered a more accurate prediction of equilibrium particle shape, were obtained via personal communication with A. Hellmann from calculations conducted to support the investigation of particle size effect in the oxygen reduction reaction.[132] The truncated octahedron data agree reasonably well with the data from full Wulff constructions, particularly for the Ni(111) surface and the (211) nickel step edge. While there exists some discrepancy for the Ni(100) surface, the two methods produce better agreement

with increasing particle size. The truncated octahedron method is applied in the present work because of its computational ease (algebraic equations) and reasonable accuracy relative to full Wulff constructions, particularly for nanoparticles with diameters in excess of 5 nm.

There are eight hexagonal (111) facets and six square (100) facets on the surface of a truncated octahedron. Half of the edges on the surface are between a square face and a hexagonal face, while the other half are between two hexagonal faces. Thus, treating the edge atoms as a (211) step edge (as described above in computational methods), all step edge atoms border at least one (111) facet and one-half of the step edge atoms border a (100) facet. This information is useful in defining the ratio of interfacial sites to total binding sites of a given facet term in the rate coefficient for inter-facet diffusion. For example, for the interface between the (111) facet and (211) step edge, all (211) step edge sites border a (111) site, so the ratio of interfacial sites to total (211) step edge binding sites is 1. The ratio of interfacial sites to (111) sites is calculated by multiplying the previous ratio, 1, by the ratio of the fraction of (211) sites to the fraction of (111) sites. For a 7 nm nickel particle, the result is 0.15 (i.e., 15% of the (111) binding sites border a step edge site). A similar procedure is carried out for the interface between the (100) facet and the (211) step edge sites. The resulting ratio of interface to (211) sites is 0.5, while the ratio of interface sites to (111) sites is 0.37.

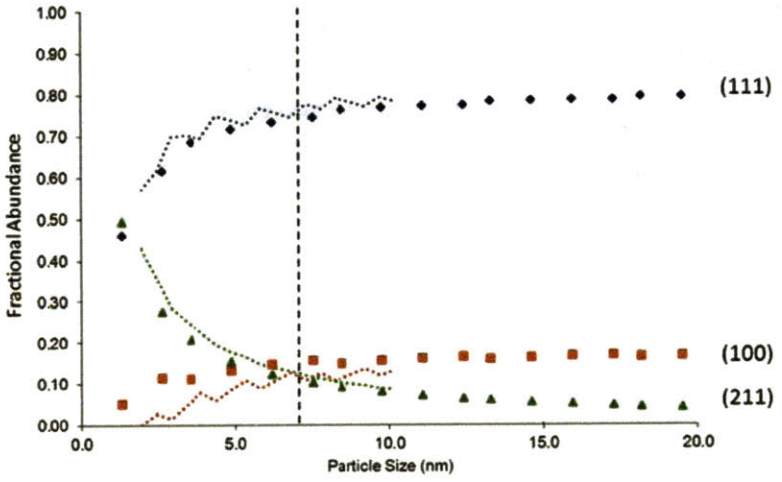

Figure 6-2. Fraction of each surface facet vs. particle size for the Ni(111) facet, Ni(100) facet, and step edges. Particle size used in the present study, 7 nm, is indicated by dashed vertical line for reference. Data are computed using a truncated octahedron model and are compared to full Wulff construction data (dotted lines), where available (data used for previously published results[132] provided via personal communication with A. Helmann).

6.4 Steam Methane Reforming Thermochemistry over Ni(111), Ni(100), and Ni(211)

Density functional theory calculations are used to predict the binding energies and electronic reaction energies for the surface intermediates and reactions shown in Figure 6-1. Binding energies for the species of interest are computed on the Ni(111), Ni(211), and Ni(100) surface facets. The resulting binding energies of the surfaces of interest are shown in Table 6-1. Because the H_2O*, COOH*, and CO_2* are not sensitive species in the mechanism and do not participate in any rate-limiting reactions, the binding energy obtained previously for these species on Ni(111)[12] is used in the present study (H_2O* is given this binding energy on all three surface facets).

In general, species are found to be more tightly bound on the (211) and (100) surfaces than on the (111) surface. In particular, carbon is significantly stabilized relative to the (111) surface because of increased coordination of the carbon atom along the step edge on the (211) surface and in a four-fold hollow binding site on the (100) surface. The Ni(100) binding energy results are generally consistent with available experimental data. The binding energy is predicted to be approximately the same for hydrogen on the (111) and (100) surfaces, which is consistent with experimental observations.[121, 127] The binding energy for CO is predicted to decrease slightly from the (111) to (100) surfaces, which is consistent with experiment that shows a decrease of 8 kJ/mol at similar coverages.[123] Finally, the binding energy of oxygen is predicted to be increase on the (100) surface relative to the (111) surface. Experimental results agree with this trend; however, there is more error for the oxygen binding energy than for CO* or H*, as DFT under-predicts the change in O* binding energy between the two surfaces by approximately 40 kJ/mol.[122]

Table 6-1: DFT-Predicted Species Binding Energies (kJ/mol) on Ni(111), Ni(100), and Ni(211)

Species	□i(111)	Ni(100)	Ni(211)
CH_3*	-137	-137	-171
CH_2*	-335	-356	-347
CH*	-576	-636	-600
CH* (0.25 ML) [a]	-	-635	-
CH* (0.5 ML) [a]	-	-595	-
C*	-613	-749	-706
C* (0.25 ML) [a]	-	-727	-
C* (0.5 ML) [a]	-	-692	-
H*	-255	-255	-257
H_2O* [d]	-2	-2 [c]	-2 [c]
OH*	-294	-314	-316
O*	-496	-527	-513
CO*	-151	-148	-154
CHO*	-164	-213	-176
COH* [b]	-191	-218	-177
COOH*	-217	-	-
CO_2* [d]	3	-	3 [c]

[a] Species is corrected for coverage-dependent effects. See Coverage-Dependent Binding Energies in Results and Discussion below for more detail. [b] COH* binding energy is relative to CHO(g). [c] Binding energy is assumed to equal the DFT-computed binding energy for this species on the (111) surface facet. [d] Ni(111) binding energy is taken from previously published value for that surface.[12]

Table 6-2: Experimentally-Adjusted Heats of Adsorption (kJ/mol) at 575°C

Species	Ni(111)	Ni(100)	Ni(211)
CH_3*	-180	-180	-213
CH_2*	-374	-396	-387
CH*	-568	-627	-591
CH* (0.25 ML) [a]	-	-626	-
CH* (0.5 ML) [a]	-	-586	-
C*	-591	-726	-683
C* (0.25 ML) [a]	-	-704	-
C* (0.5 ML) [a]	-	-669	-
H*	-268 [c]	-268	-270
OH*	-275	-296	-298
O*	-464 [c]	-495	-480
CO*	-124 [c]	-122	-128
CHO*	-192	-242	-204
COH* [b]	-215	-242	-201

[a] Species is corrected for coverage-dependent effects. See Coverage-Dependent Binding Energies in Results and Discussion below for more detail. [b] COH* heat of adsorption is relative to CHO(g). [c] Heat of adsorption is calculated from experimental quantity at 25 °C, which is then corrected to 575 °C using DFT-computed frequencies.

When obtaining thermodynamic quantities such as heats of reaction and entropies of reaction, the vibrational frequencies obtained previously for the Ni(111) surface[12] are used for the corresponding species on the Ni(100) and Ni(211) surface. Thus, the computed entropies of reaction are the same for a given reaction, regardless of the surface facet upon which it is occurring. Likewise, the zero-point energy and thermal corrections used in obtaining heats of reaction from the electronic reaction energies are the same for a given reaction, regardless of surface. The computed heats of reaction are a function of the surface facet upon which the reaction is occurring, but only because the electronic energies of reaction were computed for the reactions on each surface facet.

The heats of adsorption for species on the Ni(111) surface are adjusted using available experimental data and the computed heats of reaction for surface reactions, as described previously. Next, heats of adsorption for the Ni(211) and Ni(100) surfaces are estimated by adding the difference in the computed binding energy between the Ni(211) or Ni(100) and the Ni(111) surface to the experimentally adjusted heat of adsorption for a species on the Ni(111) surface. The resulting heats of adsorption for each species/surface are shown in Table 6-2 and the corresponding heats and entropies of reaction are shown in Table 6-3.

First-order saddle point searches are performed to obtain transition state geometries for methane adsorption and carbon-containing intermediates species oxidation (i.e., CO* formation from C* and O*, CHO* formation from CH* and O*, and COH* formation from C* and OH*). Where available, reaction barriers for reactions in the mechanism that are not evaluated in the present study are taken from previously published values, as indicated in the tables. Kinetic parameters for methane activation and the three investigated oxidation pathways (direct CO* formation through C* + O*, as well as formation of CO* through CHO* and COH* intermediates) are shown in Table 6-4.

Table 6-3: Heats and Entropy of Reaction for SMR over Multi-Faceted Ni at 575°C

Reactions	ΔH_{rxn} (kJ/mol)			ΔS_{rxn}[c]
	Ni(111)[12]	Ni(100)[d]	Ni(211)	(J/mol-K)
$H_2(g) + 2^* = H^* + H^*$	-94	-94	-97	-132
$H_2O(g) + * = H2O^*$	-12	-12	-12	-86
$CO(g) + * = CO^*$	-124	-122	-128	-135
$CH_4(g) + 2^* = CH_3^* + H^*$	1	1	-34	-130
$CO_2(g) + * = CO_2^*$	-26	-	-26	-91
$CH_3^* + * = CH_2^* + H^*$	6	-15	26	-2
$CH_2^* + * = CH^* + H^*$	-32	-70	-45	-15
$CH^* + * = C^* + H^*$	53	-22	-17	-3
$H_2O^* + * = OH^* + H^*$	-27	-47	-51	-60
$OH^* + * = O^* + H^*$	-20	-30	-16	-18
$C^* + O^* = CO^* + *$	-152	17	-47	33
$C^* + OH^* = COH^* + *$	-66	63	63	16
$CH^* + O^* = CHO^* + *$	31	72	58	18
$CHO^* + * = CO^* + H^*$	-130	-77	-122	12
$COH^* + * = CO^* + H^*$	-106	-77	-125	-1
$CO^* + OH^* = COOH^* + *$ [a]	77	-	-	-37
$COOH^* + * = CO_2^* + H^*$ [a]	-71	-	-	65
$CO^* + O^* = CO_2^* + *$ [b]	26	-	41	47
$CO^* + CO^* = CO_2^* + C^*$ [a]	178	-	-	14

[a] This water-gas shift reaction is included only on the Ni(111) surface. [b] This water-gas shift reaction is included only on the Ni(111) and Ni(211) surface facets. [c] Frequencies obtained previously for Ni(111) are used for all surfaces in present study, resulting in surface-independent entropies. [d] All heats of reaction for the Ni(100) surface are computed at the default computational coverage of 1/8 ML. Coverage-dependent effects for C* and CH* are not shown. These effects are calculated in the microkinetic model using the data in Table 6-2 and the method described in the Coverage-Dependent Binding Energies section below.

Methane adsorption is found to be have the lowest barrier on the Ni(211) surface, with a computed zero-point-corrected electronic barrier of 75 kJ/mol, which is in good agreement with the value of approximately 80 kJ/mol previously reported by Bengaard, et al.[39] The methane activation barriers on the Ni(100) and Ni(111) surface facets are found to be 98 kJ/mol and 111[12] kJ/mol, respectively. The activation barrier for the addition of C* and O* to form CO* is also reduced on the Ni(211) surface relative to the Ni(111) surface, decreasing from 199 kJ/mol to 157 kJ/mol. These results are in agreement with previous calculations and the general trend expected for methane adsorption and CO* formation on stepped surfaces.[39, 78] However, the barriers for CHO* and COH* formation are found to increase slightly on the Ni(211) surface relative to the Ni(111) surface. The CHO* and COH* formation reactions also exhibit larger activation barriers on the Ni(100) surface; however, the increase is more significant for CHO* formation, increasing from 128 kJ/mol on Ni(111) to 193 kJ/mol on Ni(100).

Table 6-4: Zero-Point-Corrected Activation Energies and Corresponding Pre-Factors at 575°C for SMR Reactions Investigated in the Present Study

Reactions	E_o (kJ/mol)			A (s^{-1})[a]		
	Ni(111)[12]	Ni(100)	Ni(211)	Ni(111)[12]	Ni(100)	Ni(211)
CH4(g) + 2* = CH3* + H*	111	98	75	7.3×10^{6}	8.1×10^{6}	7.6×10^{6}
C* + O* = CO* + *	199	200	157	4.2×10^{14}	7.1×10^{12}	1.0×10^{13}
C* + OH* = COH* + *	124	152	146	2.3×10^{13}	6.8×10^{12}	7.0×10^{12}
CH* + O* = CHO* + *	128	193	132	1.5×10^{13}	8.7×10^{12}	6.4×10^{12}
COH* + * = CO* + H*	81	88	40	2.0×10^{12}	9.9×10^{12}	3.8×10^{12}

[a] Calculated using $(k_B T/h)^*[q^{TS}/\Pi q_i]$, without standard state correction or concentration of sites term.

Comparisons of the thermochemistry (at 575°C) and reaction barriers of the pathways investigated in the present study on the Ni(100) and Ni(211) surfaces are shown in Figure 6-3 and Figure 6-4, respectively. While some activation barriers for carbon-containing intermediate species oxidation do increase, the significant stabilization of the intermediate species on the Ni(100) and Ni(211) surfaces leads to lower transition state energies relative to the energy of the gas phase reactants. On Ni(100), the lowest-energy pathway is through the COH* intermediate, followed by direction formation of CO* from C* and O*. However, as shown in Figure 6-3, the effective barrier for CO* formation from C* and OH* through COH* is only 20 kJ/mol less than the barrier for CO* formation from C* and O*. Also, as mentioned previously, the calculated O* energy disagrees with experimental values by 40 kJ/mol, introducing error that makes it less clear with C-O coupling reaction will be faster.

Like the Ni(100) surface, many intermediate species on Ni(211) are significantly stabilized relative to the Ni(111) surface. As shown in Figure 6-4, the lowest (electronic) energy pathway on the Ni(211) surface is through the CHO* intermediate, followed by the formation of COH* from C* and OH* and the direct formation of CO* from C* and O*. However, for the Ni(100) surface and particularly the Ni(211) surface, the differences between the investigated pathways are small, suggesting a kinetic model will be most useful in discerning the most favorable reforming pathways.

The results of our DFT calculations indicate that the Ni(100) and Ni(211) will provide an enhanced kinetic effect in the SMR reaction because of a significant stabilization of reaction intermediates as well as a reduction of the barrier to methane chemisorption and some carbon-containing intermediate species oxidation barriers. To gain a better understanding of the competition between these pathways, we next include these thermochemical and kinetic parameters in a kinetic model that will allow for flux and sensitivity analysis as well as comparison to experiment.

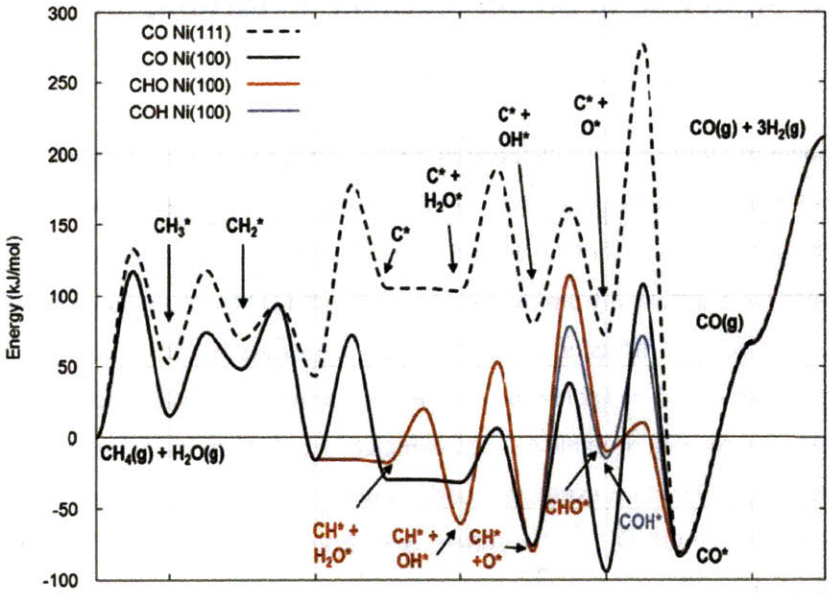

Figure 6-3. Electronic energies and activation barriers of SMR pathways [relative to $CH_4(g) + H_2O(g)$] on the Ni(100) surface compared to the pathway through C+O→CO on Ni(111). Some species labels are omitted to simplify notation.

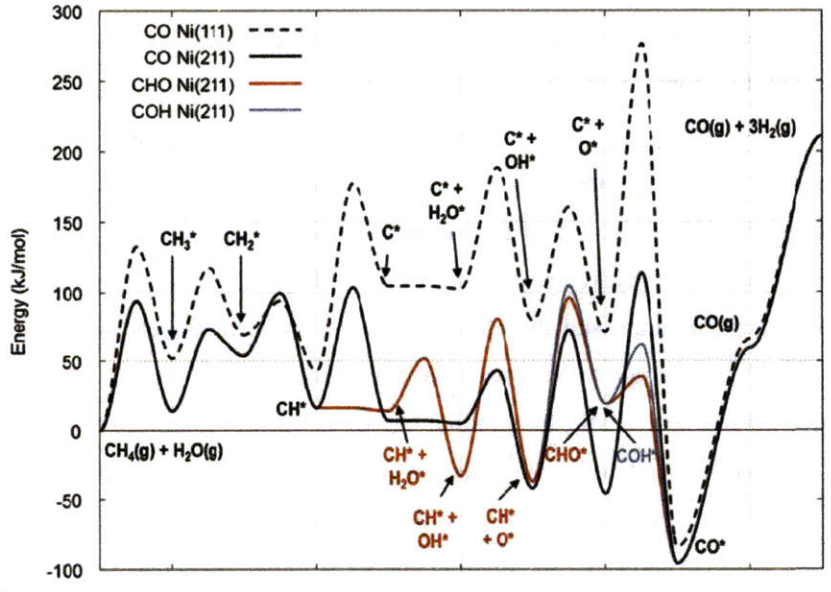

Figure 6-4. Electronic energies and activation barriers of SMR pathways [relative to $CH_4(g) + H_2O(g)$] on the Ni(211) surface compared to the pathway through C+O→CO on Ni(111). Some species labels are omitted to simplify notation.

6.5 Kinetic Modeling of Steam Methane Reforming over Multi-Faceted Nickel

The reactions shown in Figure 6-1 are included in a microkinetic model, combining the thermochemistry listed in Table 6-3 with the kinetic parameters listed in Table 6-7. In addition, two diffusion reactions are included for each species (except for COOH* and CO_2*, which are only included on the Ni(111) surface) to account for inter-facet diffusion from the Ni(111) to the Ni(211) surface and from the Ni(211) to the Ni(100) surface. The heats of diffusion are defined from the values listed in Table 6-2 and the estimated barriers for diffusion are listed in Table 6-6. The WGS reactions are studied using previously published kinetic parameters. As detailed in Table 6-7, the complete set of WGS reactions shown in Figure 6-1 are investigated on the Ni(111) surface using previously computed values.[12] Only the most facile reaction on the (111) facet, the CO* + O* → CO_2* reaction, is investigated on the (211) facet using a previously reported activation barrier.[134]

Coverage-Dependent Binding Energies

At the high temperatures investigated in the present work, coverage of species is generally low (Table 6-5) because of significant entropic effects. However, C* and CH* are found to have sufficiently large binding energies on the Ni(100) surface to result in coverage well in excess of the default computational coverage for the Ni(100) surface of 1/8 monolayer (ML). At the conditions described below for the CSTR formulation, the coverage of C* is predicted to be greater than 0.95 ML. Consequently, the binding energies of C* and CH* are corrected for coverage-dependent effects using the data listed in Table 6-2 . The species H* is also found to exist at relatively high coverages under certain conditions (such as high conversion where hydrogen partial pressure is large); however, the binding energy of H* is not a strong function of coverage and therefore coverage-dependent effects are ignored. The binding energy for C* and CH* is assumed to be constant at coverages less than 1/8 ML. For the range from 1/8 ML to 1/4 ML and 1/4 ML to 1/2 ML, the binding energy is linearly interpolated between the computed endpoints. The coverage-dependent binding energies are implemented by adjusting the heat of reaction for all reactions involving C* and/or CH* as appropriate depending on the species' coverages at the time step of interest. For both C* and CH*, the binding energy is found to decrease with increasing coverage. As a result, the coverage of each species is found to decrease as a result of the introduction of coverage-dependent binding energies. For example, the fractional coverage of C* is predicted to decrease from 0.95 with no coverage-dependence to 0.30 ML when coverage-dependent effects are included. Under the conditions examined in the present study, no species surface coverage was found to exceed 0.5 ML, so

corrections above this coverage are not implemented. Note that no additional adsorbate-adsorbate interactions are included in the present model.

CSTR Formulation for Flux and Sensitivity Analysis

We investigate the microkinetic model using a CSTR to quickly investigate parallel competing pathways on the catalyst surface (both the competition between individual surface facets and the competition among parallel reactions on a given surface facet). The kinetics of SMR are investigated at 575°C and 10 bar total pressure with a H_2O:CH_4 ratio of 2.5 and a reactor residence time of 1 second, which with the present model corresponds to approximately 5% methane conversion. In the simulation, there are $1.83x10^{-6}$ total moles of nickel binding sites. The fractional abundance of each type of site is taken from the surface facet analysis presented above.

The steady state coverage of vacant sites and selected reaction intermediates for each surface facet is shown in Table 6-5. The Ni(111) surface coverage is consistent with values obtained in our previous investigation of this surface with the surface being mostly vacant and the most abundant reaction intermediate being H*, with a predicted fractional coverage of approximately 0.19 and a fraction of vacant sites equal to 0.78. The Ni(100) surface is predicted to be more concentrated with surface species, with a fraction of vacant sites equal to 0.36 after coverage-dependent effects for C* and CH* (the most abundant reaction intermediates on this surface) are included. The Ni(211) surface is also found to be more concentrated with surface species than the Ni(111) surface; however, most intermediates are predicted to be less stable on this surface than on the Ni(100) surface, which results in a larger fractional coverage of vacant sites at 0.68. The most abundant reaction intermediate on the Ni(211) surface is predicted to be H* followed by C*.

Table 6-5: Fractional Surface Coverage of Vacant Sites and Selected Reaction Intermediates at ~ 5% CH_4 Conversion, 575 °C, Steam:Methane = 2.5

Species	Ni(111)	Ni(100)	Ni(211)
Vacant	$7.8x10^{-1}$	$3.6x10^{-1}$	$6.8x10^{-1}$
C*	$1.8x10^{-7}$	$3.0x10^{-1}$	$7.5x10^{-2}$
CH*	$1.2x10^{-4}$	$2.2x10^{-1}$	$2.8x10^{-3}$
H*	$1.9x10^{-1}$	$7.7x10^{-2}$	$1.9x10^{-1}$
O*	$1.1x10^{-3}$	$4.0x10^{-2}$	$1.1x10^{-2}$
OH*	$1.3x10^{-4}$	$1.1x10^{-3}$	$2.8x10^{-3}$
CO*	$1.9x10^{-2}$	$6.7x10^{-3}$	$3.0x10^{-2}$

Table 6-6: Diffusion Barriers[a] (kJ/mol) on the Multi-Faceted Nickel Surface

Species	Ni(111) to Ni(211)	Ni(211) to Ni(100)
CH3*	25[b]	25[b]
CH2*	25[b]	25[b]
CH*	46	119
C*	50	196
H*	13	13[c]
H2O*	0.3	0.3[c]
OH*	25[b]	19
O*	48	61
CO*	10	3
CHO*	13	13[c]
COH*	25[b]	25[b]

[a] Diffusion barriers are calculated on the larger facet across which molecules must diffuse (i.e., Ni(111) and Ni(100)). Ni(111) values are taken from barriers calculated for previously published results.[12] Ni(100) values are calculated in the present study and are defined as the difference in adsorption energies between a bridge binding site and a hollow binding site on the Ni(100) surface. [b] Diffusion barrier is not explicitly calculated and is assumed to equal 25 kJ/mol. [c] Diffusion barrier is not calculated and is assumed to equal the barrier calculated for the Ni(111) surface.

The most active surface facet for dissociative methane adsorption is predicted to be the stepped Ni(211) surface, accounting for 95% of the methane adsorption on the catalyst surface. The subsequent CHx* species dissociations are found to occur quickly at step sites as well as on the Ni(100) surface. The Ni(211) surface is predicted to be the preferred surface for adsorbed water dissociation to OH* and H*, while the final dissociation of OH* to O* and H* is predicted to be more facile on the Ni(111) surface. It should be noted, however, that the current kinetic parameters for water dissociation on the Ni(100) surface are approximated as being equal to the parameters on the Ni(211) surface; thus, predictions of dissociation products of H_2O* on the Ni(100) surface are uncertain. And, as noted above, the computed O* energy on Ni(100) surface used here differs significantly from the experimental number. While the H_2O dissociation kinetics are not sensitive parameters in the model, the stability of the O* intermediate can effect C-O coupling rates.

Table 6-7: Arrhenius Parameters[a] for SMR Kinetic Model over Multi-Faceted Ni

	Reactions	Ea (kJ/mol)			A[b]		
		Ni(111)	Ni(100)	Ni(211)	Ni(111)	Ni(100)	Ni(211)
1:	H2(g) + 2* = H* + H* [c]	11	11	11	$1.0x10^3$	$8.9x10^2$	$1.0x10^3$
2:	H2O(g) + * = H2O*	0	0	0	$8.6 \times T^{0.5}$	$8.6 \times T^{0.5}$	$8.6 \times T^{0.5}$
3:	CO(g) + * = CO*	0	0	0	$6.9 \times T^{0.5}$	$6.9 \times T^{0.5}$	$6.9 \times T^{0.5}$
4:	CH4(g) + 2* = CH3* + H*	133	117	94	$3.0x10^2$	$2.8x10^2$	$3.0x10^2$
5:	CO2(g) + * = CO2*	0	-	-	$5.5 \times T^{0.5}$	-	-
6:	CH3* + * = CH2* + H* [d]	66	59	59	$4.7x10^{13}$	$4.7x10^{13}$	$4.7x10^{13}$
7:	CH2* + * = CH* + H* [d]	25	46	46	$8.3x10^{12}$	$8.3x10^{12}$	$8.3x10^{12}$
8:	CH* + * = C* + H* [d]	135	88	88	$2.1x10^{14}$	$2.1x10^{14}$	$2.1x10^{14}$
9:	H2O* + * = OH* + H* [d]	87	38	38	$1.3x10^{11}$	$1.3x10^{11}$	$1.3x10^{11}$
10:	OH* + * = O* + H* [d]	82	114	114	$8.5x10^{12}$	$8.5 x10^{12}$	$8.5 x10^{12}$
11:	C* + O* = CO* + *	206	202	160	$3.3 x10^{19}$	$3.4 x10^{17}$	$4.9 x10^{17}$
12:	C* + OH* = COH* + *	126	154	147	$9.8 x10^{17}$	$3.3 x10^{17}$	$2.7 x10^{17}$
13:	CH* + O* = CHO* + *	131	195	134	$7.6 x10^{17}$	$3.9 x10^{17}$	$2.5 x10^{17}$
14:	CHO* + * = CO* + H* [c]	20	20	20	$9.2 x10^{12}$	$9.2 x10^{12}$	$9.2 x10^{12}$
15:	COH* + * = CO* + H* [e]	85	93	43	$3.6 x10^{12}$	$2.1 x10^{13}$	$6.1 x10^{12}$
16:	CO* + OH* = COOH* + * [f]	111	-	-	$3.2 x10^{20}$	-	-
17:	COOH* + * = CO2* + H* [f]	97	-	-	$1.0 x10^{16}$	-	-
18:	CO* + O* = CO2* + * [f]	149	-	142[g]	$3.2 x10^{20}$	-	$3.2 x10^{20}$
19:	CO* + CO* = CO2* + C* [f]	326	-	-	$3.2 x10^{17}$	-	-

[a] Unless otherwise shown, Arrhenius pre-factors and activation energies are temperature-independent, regressed over the range 500-575°C Values for the Ni(111) surface are computed from previously published values.[12] Pre-factors for non-activated molecular adsorption are shown with the appropriate temperature dependence. Pre-factors for all other adsorption reactions contain a standard state correction calculated at 575°C. [b] All pre-factors are in MKS units of length/number•s (e.g., m/s for reaction 1 and m^2/mol-s for reaction 11). [c] The activation energy and pre-exponential factor for this reaction is taken from the results obtained previously for the Ni(111) surface and is assumed to be the same for each surface in the model. The pre-exponential factor is corrected for the differing number of binding sites per unit area on the surfaces of interest. [d] The activation energy for the Ni(211) surface is taken from previously published values by Bengaard, et al (un-regressed).[39] The activation energy for the reaction on the Ni(100) surface is assumed to equal the activation energy on the Ni(211) surface. The pre-exponential factor obtained previously for the Ni(111) surface is used for all surfaces. [e] Because the kinetic model shows sensitivity to this reaction's barrier on the Ni(100) surface, that barrier was calculated in VASP. The barrier and pre-factor on the Ni(211) surface are assumed to equal the parameters obtained previously for the Ni(111) surface. [f] The Arrhenius pre-factor is estimated as k_BT/h, with appropriate unit corrections. [g] The activation barrier for this water-gas shift surface reaction is taken from a value previously published by Jiang, et al.[134]

The Ni(211) and Ni(100) surfaces are predicted to be the most active surfaces for the oxidation of carbon-containing intermediates. Each of the oxidation reactions included in the microkinetic model are found to be active pathways on the Ni(211) surface. At the conditions studied in the CSTR, approximately 27% of the adsorbed methane is converted to CO* through the direct-addition of C* and O* on the Ni(211) surface. Approximately 26% of the adsorbed methane is found to be converted to CO* through the

reaction of C* and OH* to form COH* on Ni(211), followed by 20% through the reaction CH* and O* to form CHO* also on Ni(211). Thus, the nickel step edge is predicted to be responsible for roughly 75% of the carbon-containing species' oxidation at these conditions. The primary oxidation reaction on the Ni(100) surface is predicted to be the formation of COH* from C* and OH*, accounting for the oxidation of 21% of the adsorbed methane. The pathways through the direct formation of CO* from C* and O* and the formation of CHO* from CH* and O* on Ni(100) are less active, accounting for the oxidation of 1% and 2% of the adsorbed methane, respectively. The remainder of the flux (3%) is accounted for through the formation of CHO* on Ni(111).

Discrete sensitivity analysis is performed to determine the rate-limiting reactions at the present conditions by adjusting the Arrhenius pre-factor up/down by a factor of 100 while observing changes in total methane conversion relative to the unperturbed reference case. This perturbation is equivalent to decreases/increases in the activation energy of approximately 30 kJ/mol at 575 °C. The overall rate of methane conversion is predicted to be most sensitive to methane adsorption (primarily at the nickel step edge) as well as the oxidation class of reactions, C* and CH* reacting with O* and OH* (primarily at the nickel step edge and on the Ni(100) surface). The methane adsorption reaction is found to be more sensitive to negative perturbations than positive, while the opposite is true for the oxidation reactions.

6.6 Comparison of Computational Results to Available Experimental Data

The microkinetic model is also studied in a plug flow reactor model to investigate methane conversion as a function of space time for comparison to available experimental data. To compare with the experimental results of Xu and Froment,[49] the system is modeled over a temperature range of 500-575 °C, at a pressure of 10 bar, a H_2O:CH_4 ratio of 3, and a H_2:CH_4 ratio of 1.25. The surface area of the catalyst is modeled as 7.2 m^2/g_{cat}, a reduction from the 9.3 m^2/g_{cat} cited by Xu and Froment for fresh catalyst, to account for catalyst deactivation reported in their study. The void fraction of the catalyst and diluent is modeled as 0.528, per the referenced study. The concentration of binding sites and fractional coverage of each surface facet used for the CSTR analysis are assumed to be applicable here. Measured fractions of sites, such as the ratio of step sites to terrace sites, were not reported by Xu and Froment.

The computational results obtained in this study are compared to the experimental results in Figure 6-5. While the multi-faceted kinetic model is slow relative to observed reforming rates, it represents a significant improvement over the previously published Ni(111) model. As expected, the presence of additional surface facets in the multi-faceted model results in considerably faster kinetics, as is shown in Figure 6-6b, where the multi-faceted model-predicted conversion at 575 °C is compared to the predicted conversion of the previously published Ni(111) model.

Methane adsorption has been demonstrated to be the rate-limiting SMR step at high temperatures by Wei and Iglesia.[38] As shown in Figure 6-6a, the present model predicts the forward rate of methane adsorption reasonably well, showing a considerable improvement over the Ni(111) model because of the importance of step sites in dissociative methane adsorption. The predicted methane adsorption rates from the multi-faceted model are computed at a fractional abundance of sites for the (111), (100) and (211) surfaces of 0.74, 0.15, and 0.11, respectively (chosen based on the particle size cited by Wei and Iglesia, 6.7 nm, and the fractional abundance of binding sites analysis presented above). In the calculation, the fraction of vacant sites is computed to be 0.75, 0.50, and 0.65 for the (111), (100), and (211) surfaces, respectively, at Xu and Iglesia's conditions.

However, despite the accurate prediction of Wei and Iglesia's rate of methane adsorption by the model, the overall rate of SMR (Figure 6-5 and Figure 6-6b) is under-predicted. Based on the sensitivity analysis presented above for the CSTR model, the carbon-containing intermediate species oxidation reactions at the nickel step edge and on Ni(100) as well as methane adsorption at the nickel step edge are the primary

sensitive reactions in the mechanism. Thus, the reasonably accurate prediction of methane adsorption rates but under-prediction of overall methane conversion rates suggests that one or more oxidation rates may be under-predicted by the current model. The under-prediction of the overall methane conversion rate is not necessarily (and likely not) solely a result of under-predicted oxidation rates. For example, the total fraction of step sites is approximated in the current model, and a higher fraction of step sites and/or Ni(100) sites on the actual catalyst would result in faster reforming rates. However, the rate-limitation of the C-O addition reactions at temperatures where it is not observed experimentally[38] is an indication that these rates are under-predicted to some degree by the present model.

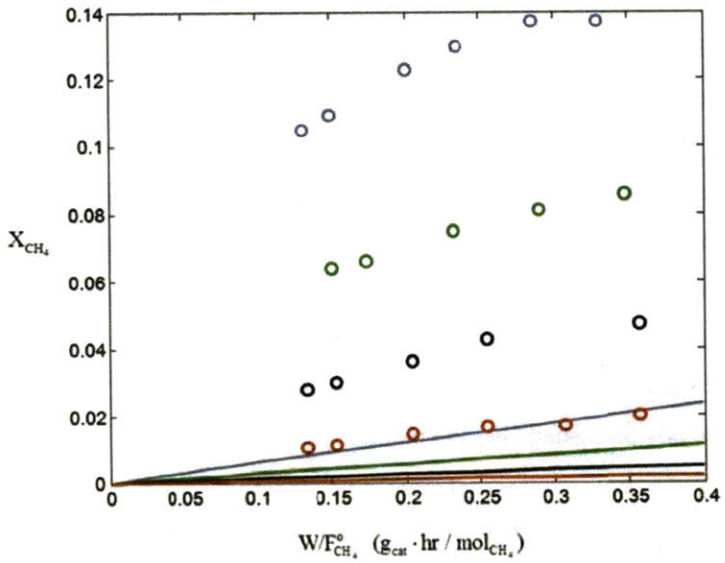

Figure 6-5. Comparison of computed conversion of methane vs. space time (solid lines) in an ideal PFR to experimental results of Xu and Froment (hollow circles) at (in order from bottom to top for both the experimental and predicted data sets) 500 °C, 525 °C, 550 °C, and 575 °C.

The degree of rate-limitation between methane adsorption and carbon-containing intermediate species oxidation is predicted to be a function of temperature. The free energy barriers for methane adsorption and the formation of CO* from C* and O* are found to increase and decrease, respectively, with increasing temperature. Therefore, at low temperatures, the oxidation reactions are predicted to be rate-limiting (with a lower fraction of the total flux through C* + O*) while methane adsorption is predicted to be rate-limiting at high temperatures (with a higher fraction of the total flux through C* + O*). This result is consistent with previous computations for these reactions[32] as well as the experimental observation[38] that methane adsorption is rate-limiting under high temperature conditions. As shown Figure 6-8, the methane adsorption transition state is predicted to be the highest point in the free-energy

landscape (the most rate-limiting) on the nickel step edge at high temperatures; however, not until higher temperatures than those where Wei and Iglesia found methane adsorption rate control (we predict a transition at approximately 800 °C, while Wei and Iglesia observe methane adsorption rate limitation at temperatures near 600 °C). These results present a general picture that at low temperatures, the oxidation of carbon-containing intermediate species is rate-determining, followed by a transition region of intermediate temperatures where there exists varying degree of rate control between methane adsorption and the oxidation reactions, followed by a high-temperature regime where methane adsorption reaction is the rate-determining step. A similar temperature-dependent transition in rate-limiting steps has been suggested for SMR over ruthenium catalyst.[135]

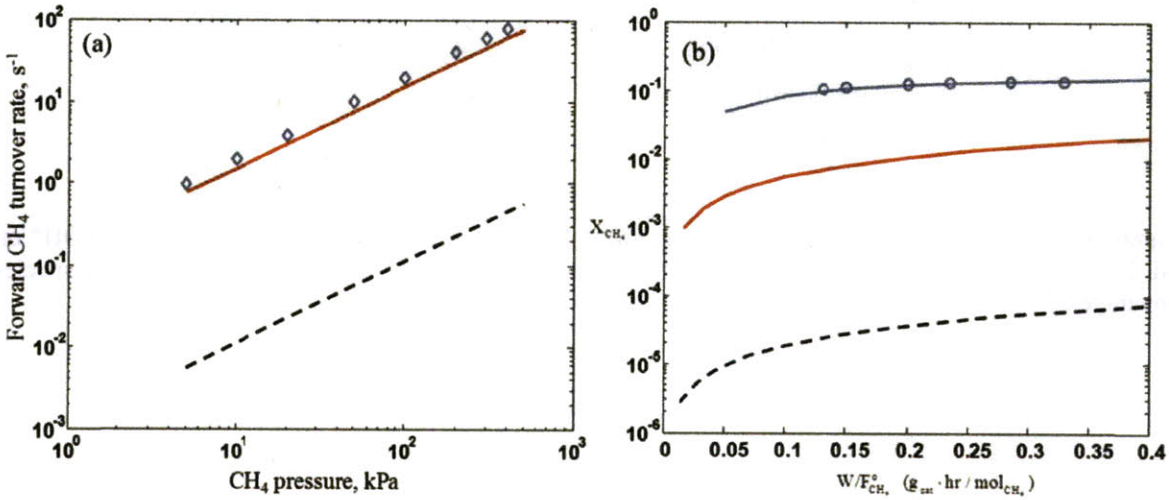

Figure 6-6. Forward CH_4 turnover rate vs. CH_4 partial pressure at 600 °C (a) as observed by Wei and Iglesia (open diamonds), predicted by the present model (line), and predicted by the previously published Ni(111) model (dashed line). Methane conversion vs. space time at 575 °C (b) as observed/modeled by Xu and Froment (open circles on line), predicted by the present model (line), and predicted by the previously published Ni(111) model (dashed line).

The transition state free energies of other carbon-species oxidation reactions such as COH* and CHO* formation are not found to be strong functions of temperatures. Thus, at high temperatures, the lowest-energy pathway is predicted to be through the direct reaction of C* and O* to form CO* on the Ni(211) surface. However, at lower temperatures as shown in Figure 6-8, the primary reforming pathway is predicted to shift from direct formation of CO*, with the lowest-energy pathways predicted to be through the hydrogen-mediated pathways of COH* and CHO* rather than direct formation of CO*, particularly the formation of COH* on the Ni(100) surface. However, at these lower temperatures, the oxidation

pathways are found to be rate-limiting and the flux through the pathways is not predicted to be sufficiently fast to agree with observed methane conversion rates.

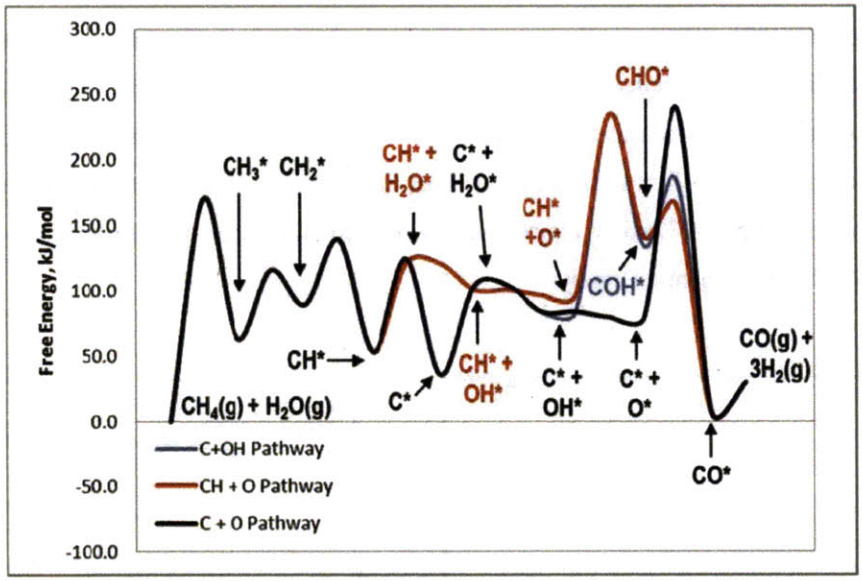

Figure 6-7. Vertical free energy (kJ/mol) diagram for SMR through C*+O*, CH* + O*, and C*+OH* on Ni(211) at 500 °C on Ni(211) with a standard state pressure of 1 bar and a standard state surface species coverage of 1 ML. Some species labels are omitted to simplify notation.

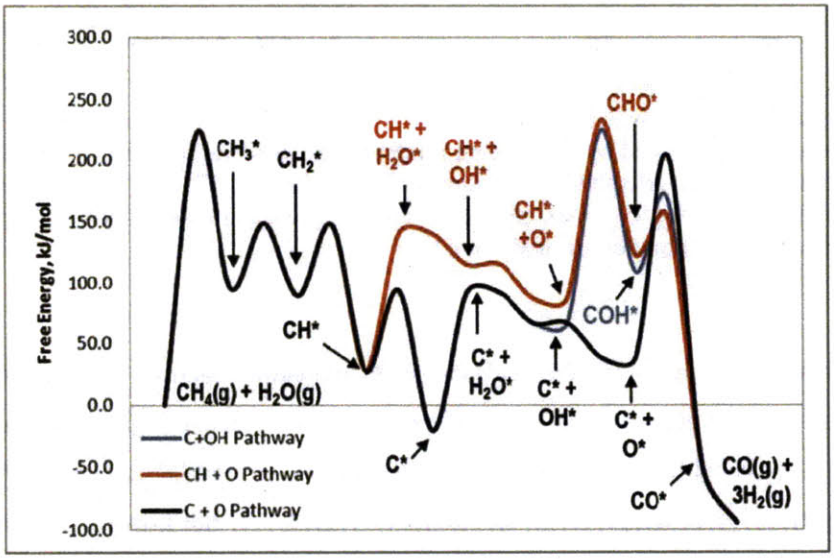

Figure 6-8. Vertical free energy (kJ/mol) diagram for SMR through C*+O* (black), CH* + O* (red), and C*+OH* (blue) on Ni(211) at 1000 °C on Ni(211) with a standard state pressure of 1 bar and a standard state surface species coverage of 1 ML.. Some species labels are omitted to simplify notation.

The apparent overestimation of the reaction barriers and/or under-estimation of the Arrhenius pre-factor for the oxidation reactions could be caused by several factors. First, while we have searched several configurations for these reactions at the step edge and have reported the lowest-energy transition state configuration, it is possible that there is another, lower-energy transition state configuration that we did not find. Similarly, it is possible that a surface feature not investigated here, such as a kink, presents a more facile route for oxidation (and sufficiently fast to overcome the site's likely low surface population). In addition, it is possible that a contribution to the under-prediction of the rates for these reactions is error in the DFT calculations for this reaction class. The error in predicting the binding energy for O* is found to be larger than for other species such as H*; however, the binding energy for CO* is reasonably well-predicted by the DFT calculations carried out in this study. For example, if the C-O transition state energy is well-predicted by DFT like the CO* binding energy, the error in treating the O* binding energy could lead to over-prediction of the C* + O* → CO* reaction barrier because, as shown in Table 6-1 and Table 6-2, the experimentally-adjusted heats of adsorption treatment leads to a destabilization of O* on Ni(211) by over 30 kJ/mol. However, the reaction barrier is not currently adjusted from the DFT-computed value because it is not known whether the transition state energy is well-predicted like CO*, or predicted with error, like O*. The apparent under-prediction of the C-O addition reaction rates presents an area for further research. In addition to the ability to more accurately predict SMR pathways, the carbon oxidation reactions represent an important branching point in understanding carbon formation (i.e., the competition between C-C coupling that leads to carbon formation and C-O coupling that oxidizes away carbon-containing intermediates). As we seek an improved understanding of the processes occurring on the catalyst surface, a physical description of this competition will be important in identifying the potential impact of new catalysts with regard to inhibition of carbon formation while retaining activity to the steam reforming reaction.

6.7 Conclusions and Recommendations

Density functional theory calculations are performed using the plane wave, periodic boundary condition Vienna Ab Initio Simulation Package to study the steam methane reforming reaction on a multi-faceted nickel catalyst, consisting of the Ni(111) surface, Ni(100) surface, and Ni step edges modeled using the Ni(211) surface. The introduction of additional facets to the microkinetic model describing SMR leads to a considerably improved description of overall methane conversion rates compared to our previously

published Ni(111) reforming model. However, while the rate of methane adsorption is captured reasonably well by the present model, the rate(s) of carbon-containing intermediate species oxidation reaction(s) appear to be under-predicted because the model predicts that the oxidation reactions are rate-limiting in regions where it is believed, based on experiment, that methane adsorption is the rate-determining SMR step. For temperatures in excess of 800 °C, the model correctly predicts that dissociative methane chemisorption has the highest degree of rate control. Like previous results for the Ni(111) surface, the reaction of CH* + O* to form CHO* is predicted to be an important reaction on the Ni(211) surface, along with C* + OH* to form COH* on the Ni(211) and Ni(100) surfaces. However, at higher temperatures, the dominant reforming pathway is predicted to be through the direct formation of CO* from C* and O* at the nickel step edge. The hydrogen-mediated pathways through intermediates such as COH* and CHO* are found to be active pathways in SMR at industrially-relevant temperatures, such as 800 °C; therefore, their inclusion in SMR kinetic models may be important. However, as a class of reactions, carbon-containing intermediate species oxidation rates appear to be under-predicted by the DFT methods applied in this study, suggesting further work is necessary to accurately capture these reactions. Describing these rates with reasonable accuracy is important for predicting the overall methane conversion rate in SMR as well as for understanding the competition between carbon oxidation and carbon-carbon coupling, which can lead to coking and catalyst deactivation.

The present work does not include lateral adsorbate-adsorbate interactions, except for the correction of C* and CH* binding energies for C*-C* and CH*-CH* interactions as a function of surface coverage up to 0.5 ML. Because surface coverage of species, particularly on the Ni(100) surface and to some extent on the Ni(211) surface, is significant, it is possible that adsorbate-adsorbate interactions may play an appreciable role in surface thermochemistry and/or kinetics. These effects are ignored in the present study; however, an extension of the work to include these effects could provide additional insight into the system, though at a significant computational expense for a mechanism of this magnitude. It has been shown that a mean-field model with lateral interactions can capture interesting physics of systems without the need for more expensive kinetic Monte Carlo calculations, though this is a function of surface coverage and surface heterogeneity.[105]

Chapter 7. Steam Methane Reforming over Ni/Ag Catalysts

7.1 Introduction

Alloying the nickel surface is regarded as a potential means for inhibiting carbon formation and associated catalyst deactivation during steam methane reforming. Research on bimetallic alloys, particularly surface alloys, suggests that it may be possible to "tune" catalyst properties by varying the type and concentration of an additive material to a base metal.[136, 137] Surface alloys are of particular interest, due to the potential of doping an inexpensive catalyst with small amounts of a more expensive metal that will reside largely at the surface, where catalysis occurs. Several Ni/M catalysts have been explored, with examples of the dopant metal, M, being gold, tin, and copper. Ni/Au surface alloys have been shown to inhibit carbon formation. While the mechanism responsible has not been conclusively determined, it has been shown that alloying the nickel catalyst with gold blocks nucleation sites and increases the barrier to diffusion of adsorbed carbon atoms.[66, 67] While gold inhibits carbon formation, it is also found to have the undesirable effect of decreasing the overall rate of steam methane reforming due to increasing the barrier for dissociative methane adsorption.[71] The Ni/Sn alloy has also been shown to inhibit carbon formation and preferentially slow carbon adatom diffusion relative to oxygen adatom diffusion.[68, 69, 138] Like Ni/Au, Ni/Sn is also found to decrease the overall rate of reforming due to an increase in the barrier for dissociative adsorption of methane.[70] It should be noted that the increased barrier for methane adsorption may also contribute to the decreased rate of carbon formation if the rate of carbon oxidation relative to methane dissociation is enhanced on the alloyed surface. Unlike Ni/Au and Ni/Sn, the Ni/Cu alloy was found to have increased activity to the steam methane reforming reaction relative to monometallic nickel (though carbon production rates were also found to increase).[139]

In this chapter, steam methane reforming over a multifaceted Ni/Ag surface alloy is explored. Like gold, silver is expected to have a high segregation energy in nickel, promoting the formation of the surface alloy, as shown in Figure 7-1. Therefore, silver is studied in only the top-most layer of atoms. Multiple alloy configurations are investigated using density functional theory to determine the most stable arrangement of surface atoms as a function of silver concentration. The most stable configurations are then investigated to obtain thermochemical and kinetic parameters for steam methane reforming over the multifaceted Ni/Ag surface at various silver concentrations.

Based on experimental observations[38] and the steam methane reforming over a multifaceted nickel catalyst results presented in the previous chapter, the primary focus of this Ni/Ag analysis is placed upon the rate-limiting reaction of dissociative methane adsorption. This reaction is studied at multiple silver concentrations on the three surface facets investigated for the multifaceted nickel catalyst, Ni(111), Ni(100), and Ni(211). In addition to this focus on the effects of alloying the nickel surface with silver on the dissociative methane adsorption barrier, thermochemistry and selected kinetics for the expanded mechanism are presented for the Ni/Ag (111) surface with ¼ ML Ag dopant.

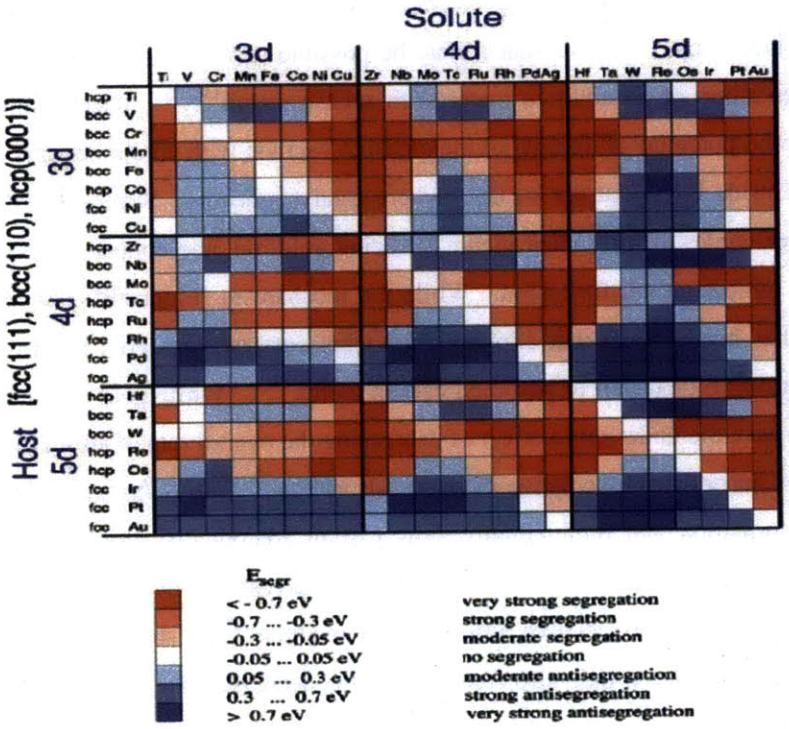

Figure 7-1. Calculated segregation energies on the most close-packed surface of all binary combinations of transition metals.[140]

7.2 Electronic Structure Calculation Parameters and Methodology

Both VASP and Dacapo are used to generate the results reported in this chapter. The results reported in Sections 7.4and 7.5 are obtained through calculations performed in VASP. The results reported in Section 7.6 are obtained through calculations performed in Dacapo. Note that the choice of one software package over another is a consequence of when the calculations were performed and should not be

interpreted to suggest that there are benefits of one simulation package over another with respect to the specific calculations being performed.

Electronic Structure Calculations in VASP

Plane wave, periodic boundary condition DFT calculations are performed in the Vienna Ab Initio Simulation Package (VASP).[84-86] The calculations consider three model surfaces: the (111), (100), and (211) surface facets of a FCC crystal of nickel atoms at the experimental lattice parameter (3.52 Å), shown in Figure 7-2. The Ni/Ag alloy is formed by replacing individual top-layer nickel atoms with silver atoms to obtain the desired degree of alloying. For (111) surface calculations, a supercell consisting of a 3x3 unit cell of three layers of metal atoms with approximately 10 Å of vacuum spacing between periodic images of the metal slab is employed. The supercell used to model the (100) surface facet consists of a 2x2 unit cell, also with three layers of metal atoms with approximately 10 Å of vacuum spacing separating periodic slab images. The (211) surface facet is modeled using a 3x1 unit cell of nine layers of metal atoms (e.g., the three atoms in a row of the top-most level of atoms each have a different z-coordinate, making nine layers for a unit cell that is three atoms deep per row), with periodic images of the metal slab being separated by approximately 12 Å of vacuum spacing. The application of a dipole correction to electro-statically decouple the periodic slabs was not employed, consistent with the VASP calculations reported in previous chapters. A 15^3 $Å^3$ cube unit cell was used to study isolated gas phase atoms and molecules. The RPBE[76] functional with spin polarization is employed. Projector-augmented wave (PAW) potentials[129] are used to describe the effect of core electrons, while the valence states are expanded with an energy cutoff of 400 eV. The Brillouin zone was sampled by (3,3,1), (4,4,1), and (4,3,1) k-point Monkhorst-Pack grids for the (111), (100), and (211) surface facets, respectively.

For geometry optimizations and first-order saddle point calculations for reaction transition states, all adsorbate atoms and the top layer of metal atoms are relaxed. First-order saddle point calculations for transition state geometries are carried out using the dimer method.[91] Geometry optimizations are carried out until the change in energy between successive ionic relaxations is less than 1E-4 eV. First-order saddle point searches were considered converged when all forces are less than 1E-3 eV/Å. Harmonic vibrational frequency analysis is performed on the resulting geometries to confirm that the negative modes of the transition states corresponded to the desired reaction coordinates as well as to obtain frequencies for calculation of zero-point energies. The vibrational frequency calculations are performed using the dynamical matrix code in VASP,[130] with a tighter convergence parameter of 1E-6 eV/Å on forces to ensure better-converged frequencies.

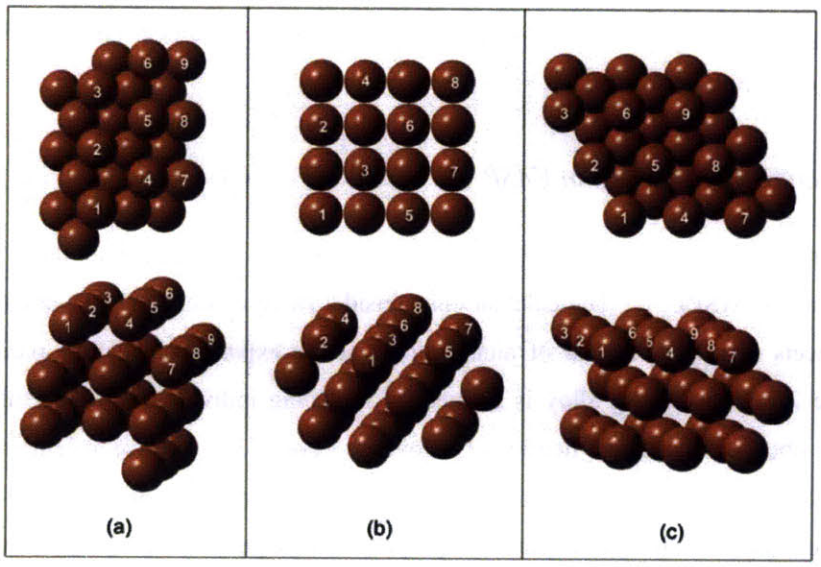

Figure 7-2. Unit Cells for the (a) 211, (b) 100, and (c) 111 Surface Facets of the Ni Catalyst

Electronic Structure Calculations in Dacapo

Planewave, periodic boundary condition DFT calculations are performed with the software package Dacapo.[76, 87, 88] For most calculations (unless otherwise specified), a 2x2 unit cell (corresponding to 0.25 ML coverage of adsorbates) is used along with a three-layer slab of the (111) facet of a FCC crystal of nickel atoms at the experimental lattice parameter (3.52 Å). The Ni/Ag alloy is formed by replacing individual top-layer nickel atoms with silver atoms to obtain the desired degree of alloying. Vacuum spacing equivalent to four nickel layers is used to separate successive images of the slab, and adsorption is allowed on only one side of the slab. Conventional counter-charges are used to cancel out the dipole interactions in the vacuum space.[79] The RPBE functional[76] is employed with spin polarization. Core electrons are described using ultrasoft pseudopotentials[119] and the valence states are expanded in a basis set of plane waves with an energy cutoff of 340 eV. The Brillouin zone is sampled by a (6,6,1) k-point Monkhorst-Pack grid.

In geometry optimizations, all adsorbate atoms and the top layer of metal atoms are relaxed. When necessary to avoid significant periodic-image interactions (such as hydrogen bonding between an adsorbate and its adjacent periodic image), a larger 3x3 unit cell is used. Initial estimates of transition states for both reactions and diffusion are obtained using the traditional nudged elastic band (NEB) approach, utilizing 7 images (including the endpoints). Transition state energies on the Ni/Ag surface are

found by performing first-order saddle point searches, beginning with an initial guess from the corresponding transition state on monometallic nickel. In some cases, constrained optimizations to find a better initial guess are required for conversion of the first-order saddle point search calculation. Harmonic vibrational frequency analysis is carried out on the resulting transition state geometry to confirm that it is a first-order saddle point.

7.3 Computational Methods

Ni/Ag Alloy Configurations

Density functional theory calculations are employed to determine the electronic energy penalty of alloying the nickel surface with silver (i.e., replacing a nickel atom with a silver atom). The segregation energy of silver in nickel is such that silver prefers to be on the nickel surface[140]; therefore, only surface alloys are considered in this study. Multiple surface concentrations of alloyed silver atoms are considered for each surface facet, as shown in Table 7-1. The electronic energy penalty of alloying the nickel surface with silver on a per silver atom basis, $\Delta E_{alloying}$, is calculated using Equation 7-1

$$\Delta E_{alloying} = \frac{\left(E_{Surf,Ni/Ag} - E_{Surf,Ni}\right)}{N_{Ag}} + \left(E_{Gas,Ni} - E_{Gas,Ag}\right), \qquad \text{[Equation 7-1]}$$

where N_{Ag} is the number of silver atoms alloyed with nickel per unit cell, $E_{Surf,Ni/Ag}$ and $E_{Surf,Ni}$ are the electronic energies of a Ni/Ag alloy slab and monometallic nickel slab, and $E_{Gas,Ni}$ and $E_{Gas,Ag}$ are the electronic energies of an isolated gas phase nickel and silver atom. For alloy configurations, enthalpic, entropic, and zero-point corrections are neglected.

Methane Adsorption Kinetics

Methane adsorption is believed to be the rate limiting step under the conditions considered for steam methane reforming in this study due to the measured lack of rate dependence on hydrogen partial pressure.[38] In addition, the analysis of steam methane reforming over a multifaceted nickel catalyst presented in the previous chapter suggests that while the computational methods employed described the rate-limiting methane adsorption reaction well, it seemed to under-predict the rate of carbon-containing species oxidation. Therefore, this analysis of SMR over Ni/Ag is performed under the assumption that

dissociative methane adsorption is the rate-determining step under the high-temperature conditions of interest. Thus, DFT calculations are performed to find the methane adsorption transition state geometries on the (211), (100), and (111) surface facets of monometallic and silver-alloyed nickel.

A competing parallel paths model is employed to investigate the effective kinetics of methane adsorption on the multifaceted monometallic and silver-alloyed nickel catalyst surface. For a model catalyst including N_{facets} surface facets, the total rate of dissociative methane adsorption is defined as (modified from Chapter 4):

$$r_{CH_4,total} = \sum_{i=1}^{N_{facets}} \alpha_i k_i \theta_i^2 [CH_4] = \sum_{i=1}^{N_{facets}} \alpha_i A_i \exp\left(\frac{-E_{a,i}}{RT}\right) \theta_{*,i}^2 [CH_4], \qquad \text{[Equation 7-2]}$$

where α is the area of the subscripted surface facet, $[CH_4]$ is methane gas concentration, A and E_a are the Arrhenius pre-factor and activation energy for dissociative methane adsorption onto the subscripted surface, and θ_* is the fraction of vacant sites on the subscripted surface. For the model catalyst in this work, N_{facets} is equal to three, accounting for the (211), (100), and (111) surface facets. The area of each surface facet is calculated from the fractional abundance of each surface facet, f_i, using the equation

$$\alpha_i = \frac{f_i n_T}{C_{T,i}}, \qquad \text{[Equation 7-3]}$$

where n_T is the total number of moles of binding sites on the catalyst surface (measured, for example, through hydrogen chemisorption). The rate coefficient for dissociative methane adsorption, k, onto surface i is defined from transition state theory as:

$$k_i = \frac{k_B T}{h} \frac{q_{TS,i}^o q_{*,i}}{q_{CH_4}^o q_{*,i}^2} \left(\frac{RT}{P_o}\right) \left(\frac{C_{T,i}}{N_{sites,o}}\right) \exp\left(\frac{-E_{o,i}}{RT}\right), \qquad \text{[Equation 7-4]}$$

where q is the partition function for the transition state (TS), gas phase CH_4, and the bare slab (*); C_T is the total concentration of binding sites on the subscripted surface facet; $N_{sites,o}$ is the standard state number of binding sites per molecule; P_o is the standard state pressure; and $E_{o,i}$ is the zero-point corrected activation barrier for dissociative methane adsorption. To obtain the temperature-independent Arrhenius

parameters in Equation 7-2, data generated using Equation 6-1 are regressed over a temperature range of 500 – 575 °C.

Taking the partial derivative of $\ln(r_{CH4,total})$ with respect to inverse temperature allows for the calculation of the effective activation energy for dissociative methane adsorption on the multifaceted model catalyst particle. Note that the fraction of vacant sites can vary among the surface facets included in the competing parallel paths model of the catalyst surface. Assuming that the vacant site fraction on a given surface facet does not change significantly over a narrow temperature range, it can be lumped with the temperature-independent Arrhenius pre-factor, resulting in a modified pre-factor A'_i. Applying the competing parallel paths model, the effective activation energy, $E_{a,eff}$, for methane adsorption onto the model multifaceted catalyst therefore takes the form

$$\frac{E_{a,eff}}{R} = -\frac{\partial \ln(rate)}{\partial\left(\frac{1}{T}\right)} = -\frac{\partial}{\partial\left(\frac{1}{T}\right)} \ln\left(\sum_{i=1}^{N_{facets}} \left(\alpha_i A'_i \exp\left(\frac{-E_{a,i}}{RT}\right)\right)\right) - \frac{\partial}{\partial\left(\frac{1}{T}\right)} \ln([CH_4])$$

$$\frac{E_{a,eff}}{R} = -\left(\frac{1}{\sum_{i=1}^{N_{facets}} \left(\alpha_i A'_i \exp\left(\frac{-E_{a,i}}{RT}\right)\right)}\right)\left(\sum_{i=1}^{N_{facets}} \left(\alpha_i A'_i \exp\left(\frac{-E_{a,i}}{RT}\right)\left(\frac{-E_{a,i}}{R}\right)\right)\right) - 0 \qquad \text{[Equation 7-5]}$$

$$E_{a,eff} = \frac{\sum_{i=1}^{N_{facets}} f_i \left(\frac{n_T}{C_{T,i}}\right) A'_i \exp\left(\frac{-E_{a,i}}{RT}\right) E_{a,i}}{\sum_{i=1}^{N_{facets}} f_i \left(\frac{n_T}{C_{T,i}}\right) A'_i \exp\left(\frac{-E_{a,i}}{RT}\right)}$$

Note that the n_T contribution from the area of each surface facet expression actually cancels out of Equation 7-5, but is shown for completeness. The lack of activation energy dependence on the total amount of catalyst present is an expected result. Also, note that the f_i term should be thought of as a fractional abundance of *active* sites for the subscripted surface facet. In this model, silver atoms that have replaced nickel atoms on the surface are not considered to be active binding sites. Thus, the effective fractional abundance of binding sites on the alloyed surface is actually the calculated value of f_i for the monometallic nickel surface multiplied by the fractional coverage of nickel on the alloyed facet (e.g., a calculated fractional coverage of Ni(211) sites of 0.06 on the monometallic nickel catalyst would result in $f_i = 0.04$ when the Ni(211) surface is alloyed with silver at 1/3 ML silver along the step edge).

7.4 Ni/Ag Alloy Configuration Results

Density functional theory calculations in VASP are used to determine the electronic energy penalty of alloying the nickel surface with silver, as shown in Table 7-1. This information is then used to determine the order in which each surface facet alloys as total silver concentration increases on the catalyst surface (assuming thermodynamic equilibrium).

Table 7-1: Energy Penalty for Alloying Nickel with Silver in Various Configurations

Surface Facet	Silver Coverage	Alloyed Position(s)[a]	$\Delta E_{alloying}$ (eV / Ag atom)
Ni/Ag(211)	1/9 ML (1/3 ML along step)	4	2.10
	1/9 ML	1	2.51
	2/9 ML (2/3 ML along step)	4,5	2.13
	3/9 ML (1 ML along step)	4,5,6	2.22
Ni/Ag(100)	1/8 ML	1	2.20
	3/8 ML	2,3,4	2.22
	3/8 ML	2,5,6	
	1/2 ML	2,4,6,8	2.24
	1/2 ML	1,3,6,8	2.44
Ni/Ag(111)	1/9 ML	1	2.50
	2/9 ML	4,9	2.50
	1/3 ML	2,4,9	2.49
	1/3 ML	1,4,5	2.53

[a] Atomic position, as indicated in Figure 7-2, at which a nickel atom is replaced with silver. Note that due to periodic boundary conditions symmetry, the listed atomic positions are not unique to the systems studied (e.g., positions 2,4,6 and 8 on the Ni/Ag(100) facet are identical to positions 1,3,5, and 7).

Among the surface facets studied, the energy penalty is lowest when alloying silver with the (211) facet of nickel. The energy penalty when alloying this facet to 1/3 ML silver coverage along the step edge (or 1/9 ML total coverage) is calculated to be 2.10 eV per silver atom. The lowest energy penalty for the addition of silver to the nickel surface is found to be along the step edge. For example, replacing an interior surface nickel atom (i.e., a nickel atom not at the top edge of the step) with silver results in an energy penalty of 2.51 eV per silver atom at 1/9 ML total coverage. As shown in Table 7-1, concentrating the surface in silver is found to increase the energy penalty, with the penalty increasing to 2.13 eV and 2.22 eV per silver atom at 2/3 ML and 1 ML silver coverage along the step edge, respectively. Due to the high energy penalty for replacing interior surface nickel atoms with silver, silver is found to collocate along the step edge rather than mix uniformly across the (211) facet.

The next most likely surface to alloy with silver is found to be the Ni(100) facet. The energy penalty for alloying this surface with silver is found to be 2.20 eV per silver atom at 1/8 ML total silver coverage. Like the (211) facet, concentrating the (100) facet with silver is found increase the energy penalty for alloying, which increases to 2.35 eV per silver atom at 3/4 ML total silver coverage. However, as shown in Table 7-1, the energy penalty for alloying the (100) facet is found to increase insignificantly from 1/8 ML to 1/2 ML total silver coverage, indicating the (100) facet has a reasonably high capacity for alloying with silver. The stability of silver atoms is found to be relatively insensitive to dispersion on the surface. Silver is found to prefer to a mixed phase with nickel on the (100) facet, as is shown in Table 7-1 for 1/2 ML silver coverage where the energy penalty is found to decrease when the silver atoms are dispersed (i.e., configuration of all nearest neighbors 1, 3, 6, and 8 is highest in energy penalty).

The least likely surface to alloy with silver is found to be the Ni(111) facet. Even at a reasonably low coverage of 1/9 ML silver, the energy penalty for replacing nickel with silver is found to be 2.50 eV per silver atom. The energy penalty is not found to increase significantly up to a coverage of 1/3 ML Ag. Once again, silver was found to prefer a dispersed phase rather than alloying with nearest-neighbor positions. Selected alloy configurations are shown in Figure 7-3, plotted left to right from most stable to least stable configuration (at an electronic energy level).

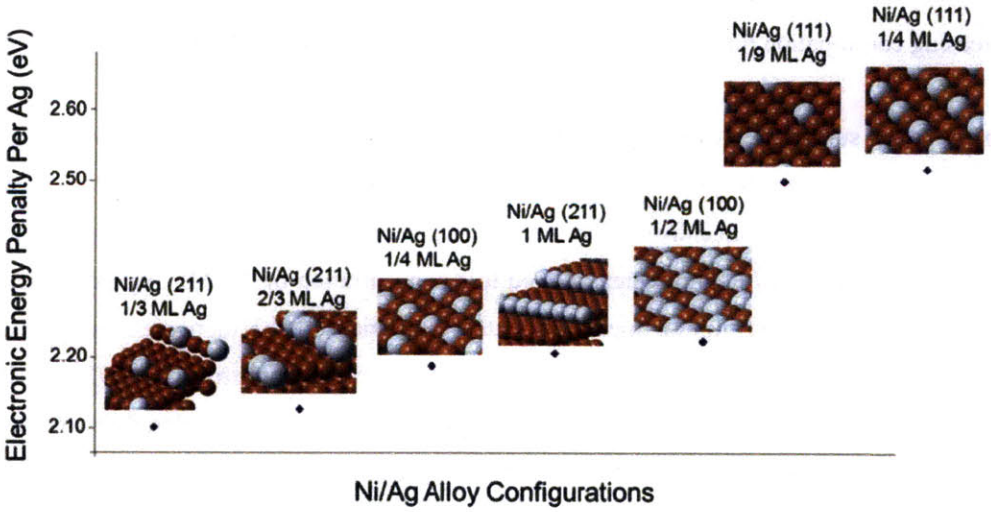

Figure 7-3. Ni/Ag surface alloy configurations plotted against the electronic energy penalty per Ag atom replacing a Ni atom.

The relative energy penalties calculated for these Ni/Ag alloy configurations indicate that as total silver concentration increases on the catalyst surface, the (211) facet's step edge will alloy first, followed by the (100) facet, and finally the (111) facet. Because the Ni-Ag interaction is unfavorable, the energy penalty for replacing a nickel atom with silver increases with increasing coordination number of the alloyed atom. The coordination number of surface atoms on each facet increases from 7 for the step edge atoms on the (211) facet, to 8 for the atoms on the (100) surface, and then 9 for the (111) surface atoms. Note that the interior surface nickel atoms on the (211) facet have a coordination number of 9 and are associated with an energy penalty of 2.51 eV per silver atom upon alloying, compared to 2.50 eV per silver atom for alloying with the similarly-coordinated nickel atoms on the (111) surface.

7.5 Dissociative Methane Adsorption Kinetics on a Multifaceted Ni/Ag Catalyst

The methane adsorption reaction on the monometallic and silver-alloyed (211), (100), and (111) nickel surfaces is studied using density functional theory calculations in VASP. The results of these calculations are shown in Table 7-2. The methane adsorption barrier is found to be lowest on the monometallic Ni(211) step edge, with a computed zero-point-corrected activation energy of 75 kJ/mol. The ZPE-corrected activation energy for adsorption is found to increase by 23 kJ/mol on the Ni(100) surface and 36 kJ/mol on the Ni(111) surface. These calculated barriers indicate a trend of increasing activation energy with increasing coordination number of the atom over which dissociative adsorption occurs.

Alloying the nickel surface with silver is found to increase the barrier for dissociative methane adsorption. The activation energy for adsorption on the (211) surface facet's step edge is found to increase by 9 kJ/mol when alloyed to a concentration of 1/3 ML Ag along the step edge. The calculated barrier increases by an additional 17 kJ/mol when alloyed to a concentration of 2/3 ML Ag along the step edge. The dissociative methane adsorption transition state geometries on the monometallic and Ag-alloyed (211) step edge are shown in Figure 7-4. Note that despite the high concentration of 2/3 ML silver at the step edge, the calculated barrier is 26 kJ/mol lower for adsorption at the step edge than over the interior, (111)-like atoms on the (211) surface. Alloying the (111) facet with 1/4 ML silver is found to increase the dissociative methane activation barrier by approximately 30 kJ/mol.

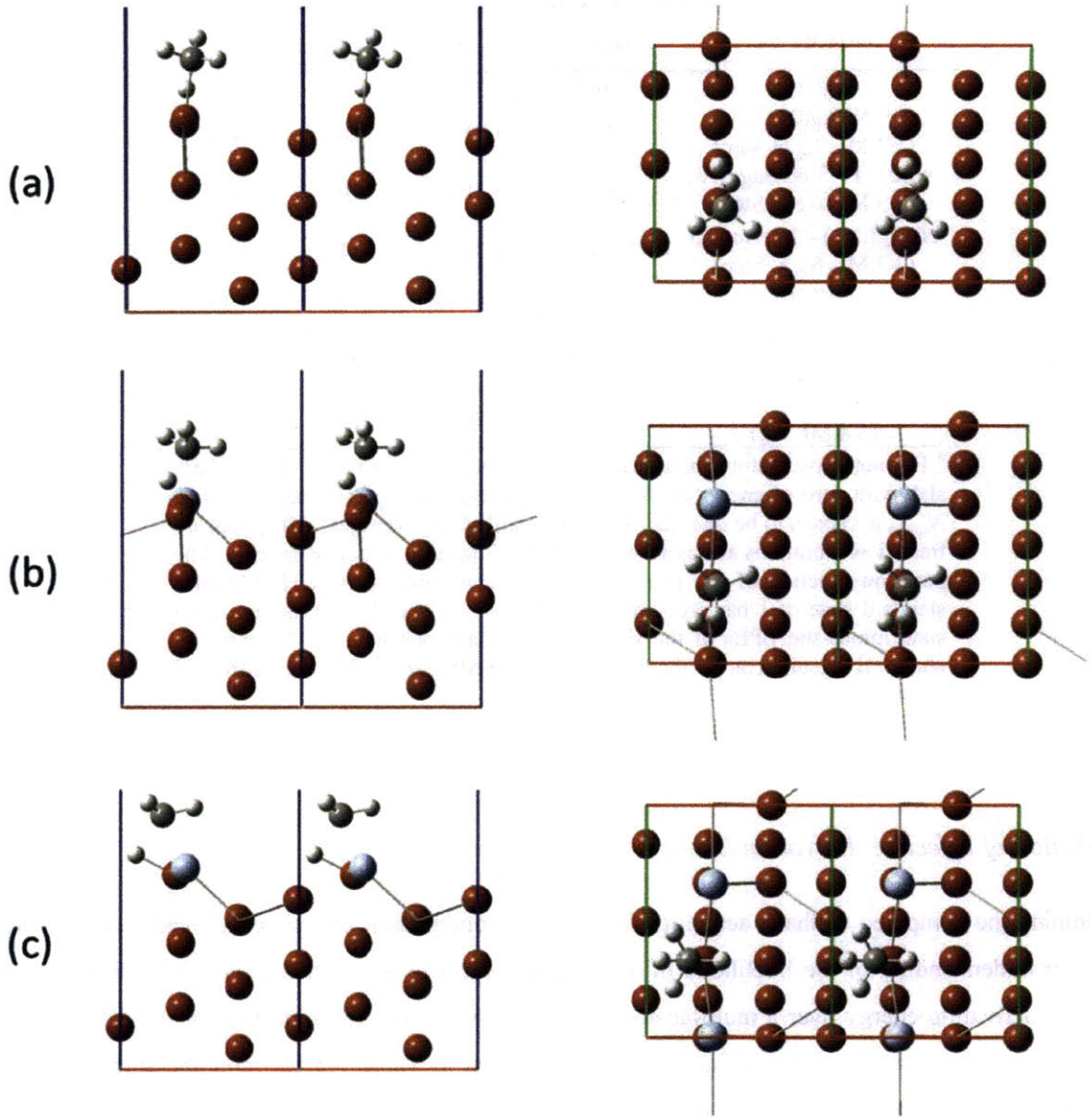

Figure 7-4. Side (left-hand column) and top (right-hand column) views of the dissociative methane adsorption transition state geometries on the step edges of (a) monometallic Ni(211), (b) Ni/Ag(211) at 1/3 ML Ag along the step edge, and (c) Ni/Ag(211) at 2/3 ML Ag along the step edge. The H atom that is leaving methane is located over a Ni-Ni bridge at the step edge on monometallic Ni(211) and Ni/Ag(211) at 1/3 ML Ag along the step edge (with the latter seeing the H shifted slightly toward the interior, away from the step edge). The transition state configuration is quite different for Ni/Ag(211) at 2/3 ML Ag along the step edge, with the leaving H atom positioned over an fcc site formed by two interior Ni atoms and one step edge Ni atom.

Table 7-2: Results of Dissociative Methane Adsorption Transition State Calculations

Surface Facet	$q_{*,ZPE}$ [a]	$q^{o}_{TS,ZPE}$ [a]	$E_{o,i}$ (kJ/mol)	ΔZPE^{TS} [b] (kJ/mol)
Ni(211)	□□0E16	2.3E20	75	-12
Ni/Ag(211) (1/3 ML Ag at Step)	2.0E17	1.8E21	84	-11
Ni(211) – Step Edge TS (2/3 ML Ag at Step)	1.3E18	3.3E21	101	-11
Ni/Ag(211) – Interior TS (2/3 ML Ag at Step)	1.3E18	2.3E21	127	-11
Ni(100)	1.1E15	5.4E18	98	-12
Ni(111)[12]	4.5E7	2.0E11	111	-12
Ni/Ag(111) [c] (1/4 ML Ag)	2.6E8	3.7E11	141	-11

[a] Harmonic oscillator vibrational partition function at T=575 °C for the bare slab with zero of energy at the zero point energy (ZPE) The standard state $N_{sites,o}$ is chosen to be one (i.e., 1 ML standard state coverage). All modes are treated as vibrations as described in Chapter 3 for tightly-bound species. The partition function of gas phase methane is calculated to be 1.1E10 with a standard state of 1 bar pressure and T=575 °C. [b] The ZPE of the transition state minus the ZPEs of the slab and gas phase methane. [c] The quantum chemical calculations for the Ni/Ag(111) (1/4 ML Ag) surface are performed in Dacapo.

Prediction of Effective Activation Energy

Combining the computed methane activation barriers on monometallic and silver-alloyed nickel surfaces with our understanding of the likelihood of each surface facet to alloy allows for the prediction of the effective activation energy over a multifaceted catalyst particle. The relevant data for the calculation of effective activation energy through Equation 7-5 are shown in Table 7-3 for monometallic nickel, 5% total silver surface coverage, and 25% total silver surface coverage. The resulting effective activation energies are compared to measured activation energies for these silver concentrations in Figure 7-5.

Assuming that the nickel catalyst particle takes a truncated octahedron shape, the method presented by Li, et al. (which detailed in the previous chapter) is used to calculate the fraction of (111), (100), and step edge (modeled using the (211) surface) binding sites.[131] For the purposes of this study, vertices/corners are treated as being equivalent to step edges. For a nominal particle size of 15 nm (with particle size being taken as twice the average of the lengths from the (100) and (111) facets to the center of the

particle), the fractions of (111), (100), and step sites are calculated to be 0.79, 0.16, and 0.05, respectively. These nickel site fractions are then multiplied by the fraction of nickel on each surface facet to calculate the value f_i. Note, for example, that the value of f_i is the calculated fraction of the subscripted surface facet for monometallic Ni, resulting in a sum of f_i values equal to on. On the other hand, at 5% Ag coverage, the sum over all f_i is 0.95, corresponding to 95% nickel on the catalyst surface. These results are shown in Table 7-3.

Table 7-3: Parameters Used for the Estimation of Effective Activation for Ni/Ag Catalyst

Silver Concentration	Surface Facet	(A_i) (m^3/mol-s)	$E_{a,i}$ (kJ/mol)	f_i (moles)	$\theta_{v,i}$
0%	Ni(211)	$7.7x10^6$	94	.05	0.7
	Ni(100)	$7.7x10^6$	117	30□ 0.4	0.4
	Ni(111)	$2.8x10^6$	124	.79	0.8
5%	Ni/Ag(211) (2/3 ML Ag at Step)	$2.6x10^5$	120	.02	0.8
	Ni(100)	$7.7x10^6$	117	.14	0.4
	Ni(111)	$2.8x10^6$	124	.79	0.8
25%	Ni(111)	$2.8x10^6$	124	.75	0.8

At 0% silver coverage, the choice of model surface facets is straightforward as the monometallic nickel (211), (100), and (111) surface facets are used to describe the methane adsorption kinetics. For the catalyst particle with 5% Ag on the surface, the Ni/Ag(211) facet with 2/3 ML silver along the step is used to describe step edge kinetics. Note the reduction of step edge active site fraction by two-thirds from 0.05 to 0.02 to account for silver atoms not being active for methane adsorption. Based upon the earlier alloy configuration analysis, the remaining silver is assumed to disperse on the (100) surface facet. However, because the resulting concentration would only be 1/8 ML Ag, the kinetics for this facet are assumed to be identical to the monometallic Ni(100) facet, though the added silver does lower the active site fraction on the Ni(100) surface from that of monometallic nickel (0.16 to 0.14). At 25% silver surface coverage, the step edge and (100) facets are assumed to be completely blocked with silver atoms. The remaining silver is assumed to disperse on the (111) facet with a total concentration on the (111) facet of approximately 5%. Because of the low silver coverage on the (111) facet, the 25% silver surface coverage particle is modeled as monometallic Ni(111). Based upon the results presented in Chapter 6 and Table 6-5, the vacant site fraction is assumed to be 0.8 for the (111) surface and, 0.4 for the (100) surface, and 0.7 for the (211) step edge. Because silver is found to destabilize adsorbates bound to neighboring nickel atoms, the vacant site fraction is assumed to increase from 0.7 to 0.8 for the (211) nickel facet when alloyed at 2/3 ML Ag along the step edge.

As shown in Figure 7-5, the results of this analysis compare well with measured activation energies for SMR over monometallic and silver-alloyed nickel catalysts by collaborators at NTNU.[141] The apparent activation energies are predicted to be 97, 122, and 124 kJ/mol for the Ni/Ag catalysts at 0%, 5%, and 25% silver surface concentrations, respectively. These values compare well with the measured values of 104, 120, and 127 kJ/mol. As was discussed in the previous chapter, experimental observations suggest that dissociative methane adsorption is the rate-limiting step in SMR over nickel catalysts at high temperature (for example, the experiments of Wei and Iglesia[38] were conducted at temperatures of approximately 600 °C and higher). The close agreement between the dissociative methane adsorption activation barrier and the measured experimental activation energy for the SMR reaction over Ni/Ag catalysts supports the notion that the methane adsorption step is also the key rate-determining step in SMR at high temperatures over Ni/Ag catalysts.

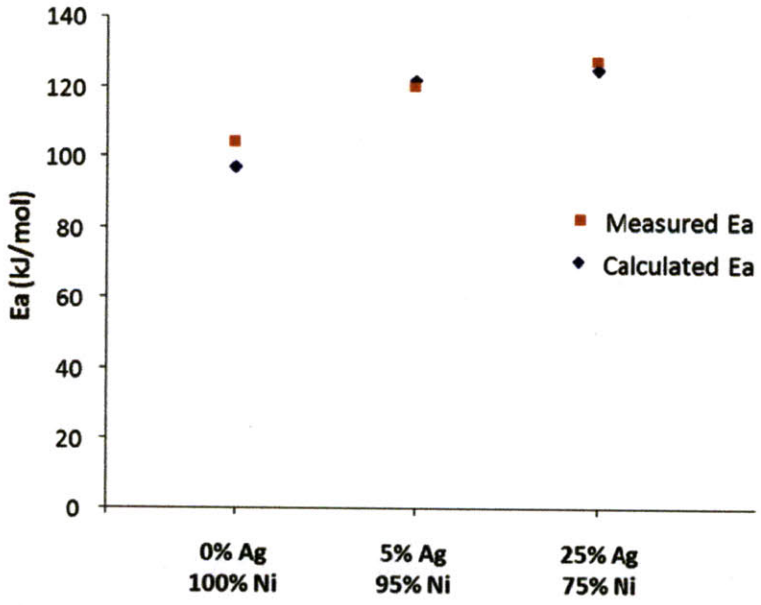

Figure 7-5. Comparison of Calculated and Measured Activation Energies for SMR over Monometallic and Silver-Alloyed Nickel Catalysts

7.6 Steam Methane Reforming Thermochemistry over Ni/Ag(111) with 1/4 ML Ag

The thermochemistry of selected intermediates on the Ni/Ag(111) with ¼ ML Ag are investigated using Dacapo. The binding energies represent the most stable geometry resulting from electronic structure calculations of the adsorbates at each of the binding sites shown in Figure 7-6 using a 2x2 2-layer unit cell. The most stable configuration (or configurations when the binding energies are within a few kJ/mol of each other) is then explored using a 2x2 3-layer slab. The resulting binding energies for the species are shown in Table 7-4.

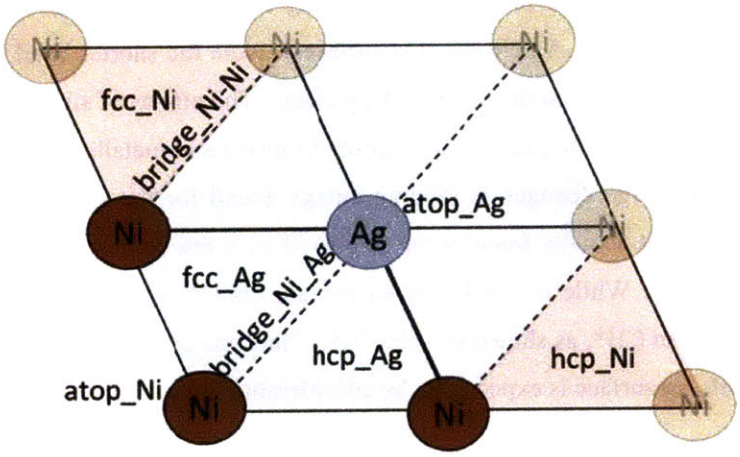

Figure 7-6. Ni/Ag(111) 1/4 ML Ag 2x2 unit cell with each unique class of binding sites labeled.

Table 7-4: Binding Energies of Species on the Ni/Ag(111) Surface at 1/4 ML Ag Coverage Compared to Species Binding Energy on Monometallic Ni(111)

Species	ΔE_{bind} (eV) Ni/Ag(0.25 ML)	Binding Site Ni/Ag(0.25 ML)	ΔE_{bind} (eV) Ni(111)	Binding Site Ni(111)
C*	-6.2	hcp_Ni	-6.0	hcp
CH*	-6.0	fcc_Ni	-5.9	hcp
CH_3*	-0.9	atop_Ni	-1.3	fcc
CHO*	-1.4	fcc_Ni	-1.8	hcp
CHOH*	-2.1	atop_Ni	-2.4	fcc
CO*	-1.5	hcp_Ni	-1.5	hcp
COH*	-2.0	hcp_Ni/fcc_Ni	-2.1	hcp
H*	-2.7	hcp_Ni/fcc_Ni	-2.7	fcc
O*	-4.5	fcc_Ni	-4.5	fcc
OH*	-2.2	fcc_Ni	-2.4	fcc

Note that, with the exception of C* and CH*, which see a slight increase in binding energy, the SMR intermediates are destabilized by the presence of Ag on the (111) facet. Also, note that with the exception of COH*, larger molecules are destabilized more than small molecules. This destabilization is found to be a function of Ag coverage, with adsorbates generally seeking to bind in a manner that maximizes their distance from Ag atoms (which is more possible for smaller molecules than larger molecules). For example, the binding energies of CH_3* and CHOH* are found to be -1.2 and -2.3 eV, respectively, when the Ag concentration is reduced to 1/6 ML (using a 2x3 unit cell rather than a 2x2 unit cell). At this lower silver coverage, these adsorbates can relax back into their preferred three-fold hollow site configurations rather than the atop binding position found for 1/4 ML Ag coverage. The CH_3* adsorbate is shown in Figure 7-7 on the 1/6 and 1/4 ML Ag Ni/Ag(111) surfaces. Note the shorter bond length (indicative of stronger bonding with the surface) on the 1/6 ML Ag surface. The effects of silver on binding energy are found to be fairly local, with binding energies returning to near-monometallic Ni(111) values at just 1/6 ML Ag, compared to the large changes in binding energy found for the species at 1/4 ML Ag. It is interesting to note that C* is actually found to be stabilized by a few tenths of an eV when the Ni(111) surface is alloyed with Ag. While this stabilization occurs, the C* + H* pair is still considerably less energetically favorable than CH*, as shown in Table 7-5. Thus, the equilibrium concentration of CH* on the Ni/Ag(111) 1/4 ML Ag surface is expected to be considerably higher than that of C*.

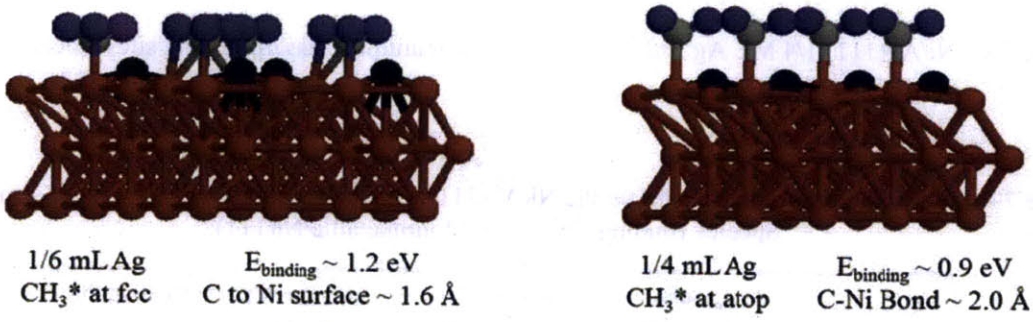

Figure 7-7. CH_3* on the Ni/Ag(111) surface at 1/6 and 1/4 ML Ag coverages. At the lower silver coverage, the CH_3* adsorbate can increase its distance from the alloyed silver atoms, resulting in a more tightly bound adsorbate to the catalyst surface with a correspondingly shorter bond length. The CH_3* binding site preference and binding energy at the lower silver coverage are similar to that of CH_3* on monometallic Ni, suggesting the effects of Ag on the surface are fairly local.

Table 7-5: Thermochemistry for Selected Reactions on Ni/Ag(111) at 1/4 ML Ag at T=575 °C, a Standard State Pressure of 1 bar, and an Adsorbate Standard State Coverage of 1 ML.

Reaction	ΔE (kJ/mol) Pure Ni	ΔE (kJ/mol) Ni-Ag (1/4 ML)	ΔH (kJ/mol) Ni-Ag (1/4 ML)	ΔS (J/mol-K) Ni-Ag (1/4 ML)
CH4(g) + 2* <--> CH3* + H*	57	85	85	-111
CH* + * <--> C* + H*	61	49	41	0
OH* <--> O* + H*	., H-50	-50	-62	-18
CH* + OH* <--> CHOH* + *	48	65	69	6
CH* + O* <--> CHO* + *	23	75	-78	-34
C* + OH* <--> COH* + *	-85	-80	-77	-10
C* + O* <--> CO* + *	-147	-112	-110	-21
CHOH* + * <--> CHO* + H*	-47	-40	-53	10
CHOH* + * <--> COH* + H*	-71	-96	-105	-15
CHO* + * <--> CO* + H*	-109	-138	-147	-13
COH* + * <--> CO* + H*	-85	-83	-94	12

The results in Table 7-5 show that the reactions that create larger products from smaller reactants (e.g., association reactions) have generally become more endothermic on the alloyed surface, reflecting the preferential destabilization of large molecules on the Ni/Ag(111) 1/4ML Ag surface. This is also true for the methane adsorption reaction because the stability of the reactant gas is unaffected by the presence of silver on the nickel surface. For example, the methane adsorption reaction has become more endothermic by 28 kJ/mol while the C*+O*, CH*+O*, and CH*+OH* addition reactions have become more endothermic by 35, 52, and 17 kJ/mol, respectively. Recall from Chapter 5 that the dissociative methane adsorption reaction and the reaction of CH*+O* → CHO* are found to be rate-limiting reactions on the Ni(111) surface. From an Evans-Polanyi argument, the increase in endothermicity of these key reactions upon alloying with silver will lead to an increase in the reactions' activation barriers.

Performing first-order saddle point searches, the expected trend of increasing activation barriers for these reactions is confirmed. As shown in Table 7-6, the barriers for dissociative methane adsorption, CH*+O*→CHO*, and CH*+OH*→CHOH* are found to increase by 28, 67, and 27 kJ/mol, respectively (for 2x2 unit cell calculations). In previous calculations on the monometallic Ni surface, the reaction barrier for the CH*+O* reaction was found to be sensitive to the size of the unit cell. As a result, this reaction was also investigated on a 3x3 Ni/Ag(111) unit cell at 1/9 ML Ag coverage. However, for proper comparison to the other reaction barriers in , the transition state on the 3x3 Ni/Ag(111) unit cell was placed in the same proximity to the alloyed Ag atom as on the 2x2 Ni/Ag(111) unit cell.

Table 7-6: Classical (Bottom of the Well) Electronic Energy Reaction Barrier for Selected SMR Reactions on Ni(111) and Ni/Ag(111) Surfaces.

Reaction	Unit Cell	E_b (kJ/mol) Pure Ni(111)	E_b (kJ/mol) Ni/Ag (1/4 ML Ag)[a]	$\Delta(E_b)$ (kJ/mol)
CH4(g) + 2* <--> CH3* + H*	2x2	124	152	28
CH* + O* <--> CHO* + *	2x2	150	217	67
CH* + O* <--> CHO* + *	3x3	131	192	61
CH* + OH* <--> CHOH* + *	2x2	122	149	27

[a] The 3x3 unit is doped with only one Ag atom, corresponding to a Ag coverage of 1/9 ML. However, the transition state is placed in a binding site adjacent to the Ag atom, resulting to a similar Ag effect on the transition state as seen on the 2x2 unit cell at 1/4 ML Ag coverage.

Because, as was mentioned previously, the effects of Ag are fairly local, the fact that the next-nearest Ag atoms are farther away on the 3x3 unit cell than on the 2x2 unit cell is thought to have negligible electronic impact on the transition state. (Note that using a 4x4 unit cell doped at 1/4 ML Ag would have been more straightforward, but at considerably greater computational expense.) As shown in Table 7-6, the activation barrier for the CH*+O*→CHO* reaction is found to decrease on the 3x3 Ni/Ag(111) unit cell relative to the 2x2 unit cell. However, note that the electronic effect of Ag on the transition state is relatively unchanged at 61 kJ/mol of destabilization on the 3x3 unit cell relative to 67 kJ/mol of destabilization on the 2x2 unit cell. Comparing the increases in the activation barrier for these reactions to their increases in endothermicity upon alloying indicates that each of the reactions follows an Evans-Polanyi relationship quite well, including on the alloyed surface.

7.7 Conclusions and Recommendations

DFT calculations are used to obtain the relative stability of multiple configurations of the Ni/Ag surface alloy at an electronic energy level. This information is used to predict the order in which the various surface facets will alloy with silver as a function of total silver coverage on the catalyst surface. The calculations suggest the step edge (modeled using the (211) surface facet) will be the first facet to alloy, followed by the (100) facet and finally the (111) facet. First-order saddle point searches are performed to obtain the dissociative methane adsorption activation barrier on each surface facet at multiple silver concentrations. The methane adsorption barrier is found to increase in the presence of silver, with the lowest barrier being on the alloyed step edge, followed by the Ni/Ag(100) surface and finally the Ni/Ag(111) facet. The methane adsorption barrier is studied in detail because previously reported

experimental evidence suggests that at high temperatures, the rate of SMR is controlled by the rate of dissociative methane adsorption. Combining the alloy stability data with the dissociative methane adsorption activation barriers therefore allows for predictions of the apparent activation energy of SMR over a multifaceted silver-alloyed nickel catalyst as a function of silver surface concentration. The resulting predictions agree well with measured SMR activation energies from fixed bed reactor studies conducted by collaborators at NTNU, confirming the model's prediction that alloying the nickel catalyst with silver results in a decrease in observed rate of steam methane reforming.

Thermochemistry and kinetics for multiple species and reactions on the Ni/Ag(111) surface at 1/4 ML silver coverage are also presented. Most adsorbates, particularly large adsorbates such as CHOH* and CH_3*, are destabilized by the presence of silver on the catalyst surface. It is found that in addition to increasing the barrier for dissociative methane adsorption, alloying the Ni(111) surface with silver also increases the barriers of key reactions such as CH*+O*→CHO* and CH*+OH*→CHOH*. The results represent a contribution toward a detailed kinetic model for the Ni/Ag catalyst. To perform detailed kinetic modeling of the alloyed catalyst, investigation of these species pathways on the (100) and (211) surface facets at multiple silver surface concentrations should also be carried out. Such calculations would be useful in gaining insight into the active reforming pathways on the silver-alloyed nickel catalyst. Such information would be particularly useful in investigating the competition between carbon formation and steam reforming; however, the ability to make predictions from these calculations is limited by the ability to accurately capture the rates for C-O addition reactions via DFT calculations (as discussed in the previous chapter for SMR over a multifaceted monometallic nickel catalyst).

Chapter 8. Carbon Formation during Steam Methane Reforming over Ni and Ni/Ag Catalysts

8.1 Introduction

Nickel catalysts are susceptible to deactivation via carbon formation during steam methane reforming. As discussed in Chapter 2, there are three categories of carbon formation: pyrolytic coke, encapsulating carbon, and whisker carbon. Pyrolytic coke is a gas-phase phenomenon that results in condensed coke that clogs the reactor internals. This form of coke is controlled through reactor design and operation (e.g. temperature control and gas distribution). Encapsulating carbon is formed by the polymerization of carbon-containing species on the catalyst surface into graphene or graphene-like sheets that can completely envelop and deactivate the catalyst. Whisker carbon formation is believed to begin in a manner similar to encapsulating carbon, but on surface facets suitable for the carbon growth to lift off of the catalyst surface. The whiskers grow through carbon addition at the catalyst surface, eventually lifting the catalyst particle off of its support, with the potential to crush the particle into the walls of the pore. The catalyst remains active during whisker carbon growth because much of the catalyst surface remains carbon-free; however, whisker carbon is the most concerning form of carbon formation because it can lead to catalyst destruction.

Encapsulating carbon and whisker carbon are initiated on the catalyst surface rather than in the gas phase; thus, the choice of catalyst can impact the degree of carbon formation observed during SMR. For example, ruthenium catalysts are not susceptible to deactivation during carbon formation. However, ruthenium catalysts are not employed for industrial SMR because of their scarcity and expense. As discussed in more detail in Chapter 2, it has been suggested that the process of carbon formation during SMR begins by dissociation of methane to carbon adatoms or other CH_x species. These species are then proposed to either diffuse across the catalyst surface or through the catalyst particle until they reach facets suitable for initiation of carbon formation or they reach existing carbon to which the diffusing species can add. When seeking to control carbon formation, there are three fundamental forms of control: thermodynamic limitation, kinetic limitation, and transport limitation.

Thermodynamic limitation of carbon formation refers to the driving force for producing carbon formation under reforming conditions. In addition to gas phase concentrations, the degree of thermodynamic limitation is also a function of the stability of the type of carbon formation of interest, which influences

the Gibbs free energy of reaction leading to the carbon formation, as well as the temperature of the system. Kinetic and transport limitation are similar in that both are related to the rate at which carbon is formed. For carbon-based deposits to form, the reactions leading to its deposition must occur at a rate that exceeds the rate at which the pre-cursors of carbon formation are oxidized away to form CO(g) and CO_2(g). Thus, understanding the competition between carbon-carbon addition vs. carbon-oxygen addition on the catalyst surface is important to predicting the effect of a particular catalyst on the likelihood of carbon formation. As shown in Figure 8-1, the free energy of the particular type of carbon formed is not a strong function of catalyst type. Thus, thermodynamic limitation of carbon formation is largely independent of the catalyst, while kinetic and transport limitations can be tuned by catalyst choice. However, note that catalyst choice can influence the type of carbon deposit formed, which does impact the thermodynamic constraints of the system. For example, the equilibrium constant of carbon formation has been shown to change with particle size for nickel catalysts as the type of carbon deposit formed changes (from more graphite-like to less graphite-like).[44] In the following sections, each of these modes of carbon formation limitation will be discussed with regard to nickel and nickel-silver catalysts. A detailed analysis of the thermodynamic driving force for carbon formation will be presented as well as illustrative cases pertaining to the competition between the rate of carbon oxidation and the rate of carbon-carbon coupling.

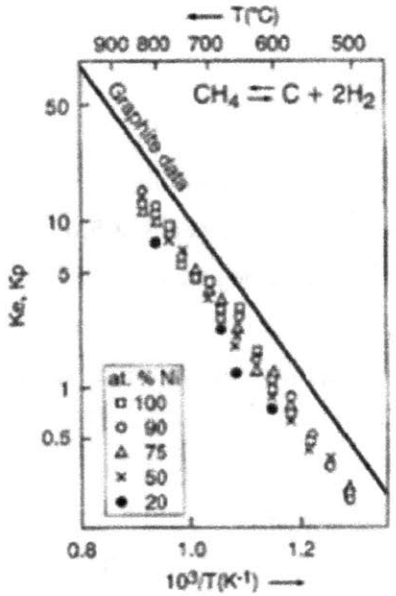

Figure 8-1. Equilibrium constant vs. temperature for the decomposition of methane to C(s) and H_2(g) for Ni/Cu catalysts at various copper concentrations. Note that the equilibrium constant is not a strong a strong function of copper content (from Rostriup-Nielsen, et al.[14]).

8.2 Thermodynamic Analysis of the Tendency to Form Carbon during SMR

Carbon formation may be controlled either by controlling the gas phase concentrations over the catalyst such that a thermodynamic driving force exists for carbon removal from the system via oxidation or by controlling the rate of carbon oxidation relative to carbon-carbon coupling. In practice, the gas phase concentration in the reactor is controlled by adjusting the initial steam to methane ratio and the initial hydrogen to methane ratio in the feed stream. In this section, a thermodynamic analysis of the tendency to form carbon will be presented. The overall process for carbon formation in SMR can be described through the following reactions:

$$CH_4(g) \rightleftharpoons C(s) + 2H_2(g) \qquad \text{[Reaction 8-1]}$$

$$2CO(g) \rightleftharpoons C(s) + CO_2(g) \qquad \text{[Reaction 8-2]}$$

$$CO(g) + H_2(g) \rightleftharpoons C(s) + H_2O(g) \qquad \text{[Reaction 8-3]}$$

Applying the Principle of Equilibrated Gas

It has been proposed that carbon formation can be controlled by ensuring that there is no thermodynamic driving force for carbon formation through these reactions at SMR equilibrium, through the principle of equilibrated gas.[47] It is suggested that the principle of equilibrated gas is valid for SMR reformers because of the low effectiveness factor of the catalyst in steam methane reforming.[14] A low effectiveness factor generally corresponds to a near-equilibrated gas inside most of the catalyst pores. Thus, the assumption that carbon formation follows the principle of equilibrated gas may be reasonable. The sum of Reaction 8-1 and the reverse of Reaction 8-3 results in the overall reaction for steam methane reforming while the sum of Reaction 8-2 and the reverse of Reaction 8-3 results in the overall reaction for the water-gas shift. Thus, after enforcing that SMR and WGS are equilibrated, only one of the three carbon formation reactions remains independent, which reduces the expression for the tendency to form carbon in the system to

$$\alpha_c = K_1 \frac{p_{CH_4}}{p_{H_2}^2} = K_2 \frac{p_{CO}^2}{p_{CO_2}} = K_3 \frac{p_{CO} p_{H_2}}{p_{H_2O}}, \qquad \text{[Equation 8-1]}$$

where α_c is a measure of the tendency to form carbon, K_i is the equilibrium constant of the subscripted reaction and p_i is the partial pressure of the subscripted component. When α_c is greater than one, there exists a driving force for carbon formation, while the carbon formation reaction is expected to run in reverse when the α_c is less than one. Thus, ideally, if the value of α_c is less than one during the whole course of reaction, no carbon will form. This means that a value of α_c equal to one is the limit of the carbon formation region. By adjusting the initial steam to methane ratio, the value of α_c in the equilibrated gas is shifted, allowing for thermodynamic control of carbon formation. When computing the equilibrium coefficients for these reactions, the thermodynamic properties of graphitic carbon are used. Perturbations can be applied to the thermochemistry to account for other forms of carbon. For example, Rostrup-Nielsen found increases in Gibbs free energy of approximately 1-3 kcal/mol for non-graphitic carbon deposits during SMR (such as carbon whiskers). However, using the thermochemistry of graphitic carbon should provide a conservative bound of the required conditions for carbon-free operation.

Using the Burcat thermodynamic data,[142] the initial steam to methane ratio that gives an α_c value of one is calculated as a function of temperature, pressure, and other species' concentrations in the feed. This is performed by setting the extent of reaction for the WGS and SMR reactions equal to the equilibrium extents of reaction and solving for the corresponding set of gas phase mole fractions that give zero extent of reaction for one of the three carbon formation reactions listed above (as mentioned earlier, only one of the three is independent when the WGS and SMR reactions are constrained at equilibrium). Following this approach, the limiting steam to methane ratio for no carbon formation at SMR and WGS equilibrium over a temperature range of 500 – 1000 °C at 1 bar and 10 bar pressure is shown in Figure 8-2 and Figure 8-3, respectively, at various initial hydrogen to methane ratios. Note that initial steam to methane ratios greater than the reported limits will also result in no carbon formation (when both the SMR and WGS reactions are equilibrated).

Figure 8-2 show that the initial steam to methane ratio required to ensure no carbon formation at SMR and WGS equilibrium reaches a peak at approximately 575 °C when no hydrogen is in the feed stream and the pressure is 1 bar. At temperatures in excess of 575 °C, the required initial steam to methane ratio decreases until reaching a fairly constant value of one at the high temperatures. Note that as hydrogen to

methane in the feed stream is increased, the required initial steam to methane ratio to prevent carbon formation decreases. This is an example of the carbon formation inhibition by hydrogen and why carbon formation is of increased concern in membrane reformers that remove hydrogen from the reformer. A similar trend is seen in Figure 8-3 at a pressure of 10 bar, but without a well-defined peak in required initial steam to methane ratio. Also note that the temperature range at 10 bar is different than that at 1 bar because the increased pressure shifts the physically-relevant equilibrium conditions at which there is zero carbon formation. Also note that, similar to the case of 1 bar pressure, the required ratios at 10 bar pressure converge to one at high temperatures, though at temperatures in excess of 2000 °C (thus these values are not shown because they represent a physically-unrealistic operating regime).

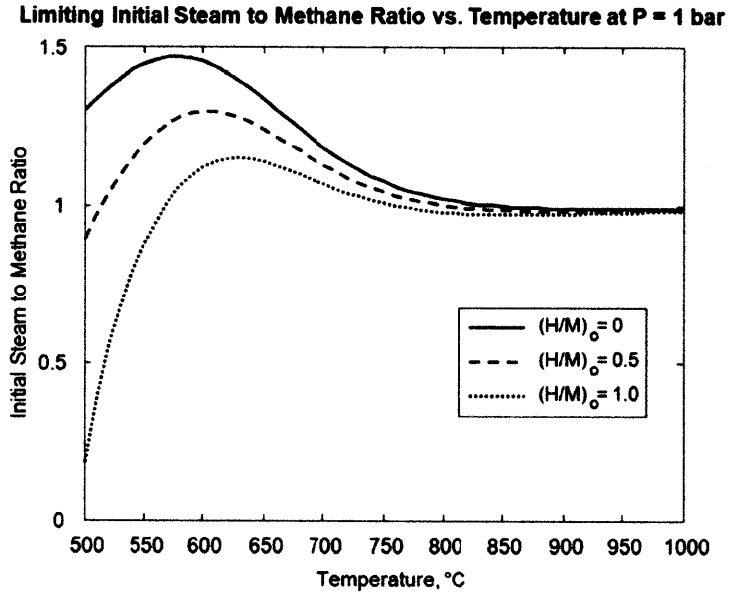

Figure 8-2. Required initial steam to methane ratios for zero carbon formation when WGS and SMR are equilibrated as a function of temperature at P = 1 bar. Ratios are calculated with initial hydrogen to methane ratios of 0, 0.5, and 1.0.

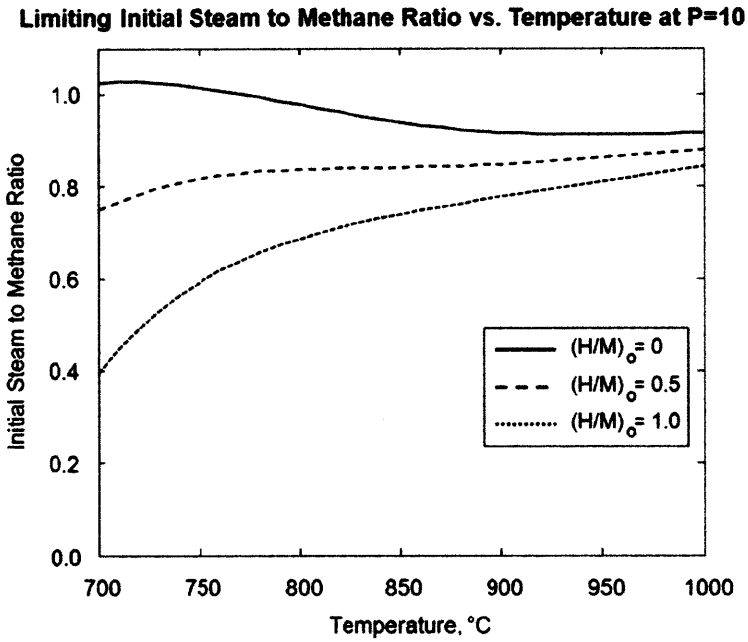

Figure 8-3. Required initial steam to methane ratios for zero carbon formation when WGS and SMR are equilibrated as a function of temperature at P = 10 bar. Ratios are calculated with initial hydrogen to methane ratios of 0, 0.5, and 1.0.

While data such as that presented in Figure 8-2 and Figure 8-3 provide an envelope of operating conditions to prevent carbon formation in an equilibrated gas, there can still be the potential for carbon formation due to complexities of the actual reformer. For example, temperature gradients that exist in the reactor as well as the catalyst particle complicate the α_c analysis as the equilibrium is a function of location within the reactor. Identifying and taking into account the most extreme carbon-formation environments would be necessary to define a more accurate operating envelope. In addition, while the principle of an equilibrated gas may apply to the pores of the catalyst, there will be external catalyst surfaces that are exposed to the bulk gas concentration rather than the nearly-equilibrated gas in the pores. This potential shortcoming of the equilibrated gas analysis motivates additional consideration of the reacting system's dynamics.

Analysis of Tendency to Form Carbon with Dynamic SMR Conversion

To account for reformer dynamics, the α_c analysis presented above is modified by relaxing the constraint on SMR equilibrium. The WGS reaction is observed to be fast relative to SMR and in equilibrium throughout the reformer;[38] therefore, the constraint on WGS equilibrium is retained. Because the WGS

reaction is formed through a linear combination of Reaction 8-2 and Reaction 8-3, the WGS equilibrium constraint results in the same α_c values for these two reactions. However, unlike the equilibrated gas analysis above, the tendency to form carbon due to Reaction 8-1 is not constrained to equal the value of α_c for the other carbon formation reactions. Therefore, the tendency to form carbon in the dynamic system is represented as

$$\alpha_{c_1} = K_1 \frac{p_{CH_4}}{p_{H_2}^2}$$

$$\alpha_{c_2} = \alpha_{c_3} = K_2 \frac{p_{CO}^2}{p_{CO_2}} = K_3 \frac{p_{CO} p_{H_2}}{p_{H_2O}}, \qquad \text{[Equation 8-2]}$$

where the gas phase partial pressures are a function of the SMR conversion and the WGS equilibrium constraint. For a given temperature, pressure and feed conditions, each value of α_c is calculated as a function of SMR conversion. Once again, a value of α_c greater than one for a reaction indicates a driving force for the production of carbon formation by that reaction while a value of α_c less than one indicates that there is a driving force for that reaction to remove carbon formation from the system. Because there are two values of α_c of interest in this system, there are three possible non-equilibrium operating regimes: 1) both α_c values are greater than one, indicating that carbon formation is thermodynamically favored, 2) both α_c values are less than one, indicating that carbon removal is favored in the system, and 3) the value of α_c for one reaction is greater than one while the value of α_c for the other reaction is less than one, indicating a kinetic competition for carbon formation. The values of $\alpha_{c,i}$ shown in Equation 8-2 are plotted from zero to equilibrium conversion of the SMR reaction in Figure 8-4 at a temperature of 600 °C, a pressure of 1 bar, and an initial steam to methane ratio of 1.45 with no hydrogen in the feed. This value for the steam to methane ratio is chosen based on the data in Figure 8-2; therefore, the α_c values are expected to converge to a value of one at equilibrium.

As shown in Figure 8-4, the value of α_c in the methane to carbon formation reaction decreases from a large value greater than one at low conversions when methane partial pressure is high and the hydrogen product has not yet formed in large concentrations. This value of this α_c is predicted to monotonically decrease until reaching an equilibrium value of one for the case of no hydrogen in the feed. Thus, there is a driving force for carbon formation from zero conversion to equilibrium conversion due to Reaction 8-1 under the conditions explored here. On the other hand, the value of α_c due to either Reaction 8-2 or Reaction 8-3 is predicted to be a small value less than one at low conversions when there is very little CO

product (because the WGS is constrained to be in equilibrium, reacting away much of the CO as it forms) and large concentrations of steam. This α_c is predicted to increase monotonically as methane conversion due to SMR increases until reaching a value of one at equilibrium for the case of no hydrogen in the feed. Thus, there is a driving force for these reactions to remove carbon formation from the system during SMR. As shown in Figure 8-4, when hydrogen is present in the feed at the same initial steam to methane ratio, the value of α_c is decreased at SMR equilibrium. This result indicates that higher concentrations of hydrogen in the process gas result in a decreased tendency to form carbon.

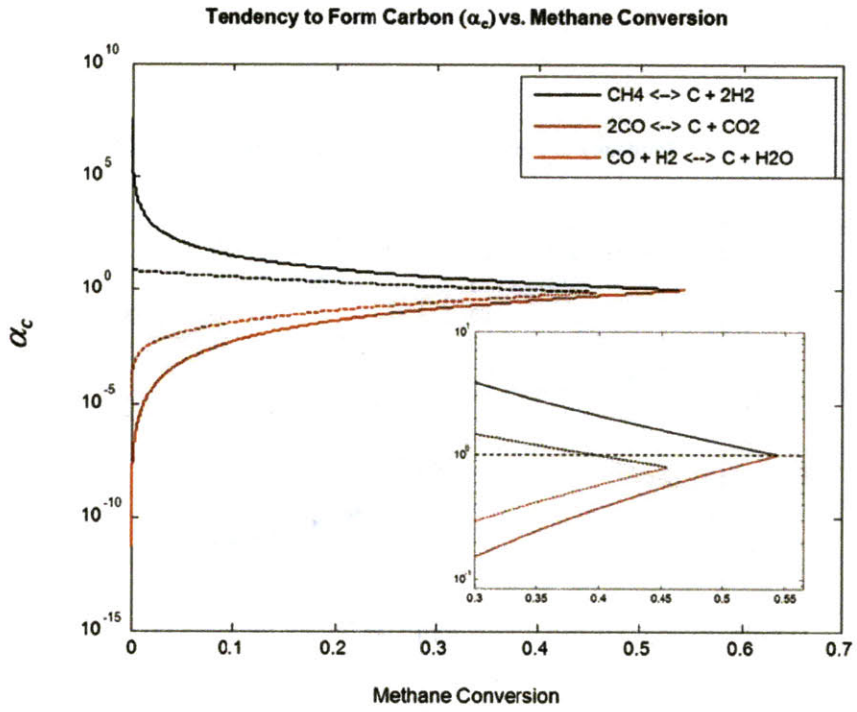

Figure 8-4. Tendency to form carbon vs. methane conversion during steam methane reforming (with WGS constrained to be in equilibrium) at T = 600 °C, P = 1 bar, and an initial steam to methane ratio of 1.45. The solid curves are for the case with no hydrogen in the feed while the dashed curve is for the case of an initial hydrogen to methane ratio of one. Reaction 8-1 runs forward while Reaction 8-2 and Reaction 8-3 run backward until SMR and WGS equilibrium are reached at ~55% methane conversion for the case of no hydrogen in the feed and ~45% methane conversion for the case with hydrogen in the feed. An inset is shown to provide more detail of α_c near SMR equilibrium. The value of α_c = 1 is shown in the inset as a horizontal dashed line.

As shown in Figure 8-5, increasing or decreasing the initial steam to methane ratio shifts the predicted value of α_c for the equilibrated gas. Figure 8-4 confirms that the limiting initial steam to methane ratio predicted in Figure 8-2 is a lower-limit for ensuring no carbon formation in the equilibrated gas. If the

initial steam to methane ratio is decreased below this limit, there exists a potential for carbon formation in the equilibrated gas. If the initial steam to methane ratio is greater than this limit, the value of α_c in the equilibrated gas is predicted to be less than one, indicating that carbon removal from the system is favored. However, even if carbon formation is not favored in the equilibrated gas, Figure 8-5 shows that carbon formation is possible prior to reaching SMR equilibrium. This analysis is performed with no hydrogen in the initial feed. If, for example, hydrogen were introduced to the feed the value of α_c at SMR equilibrium would shift down, as shown in Figure 8-4, but the situation is qualitatively the same: carbon formation is possible very close to equilibrium.

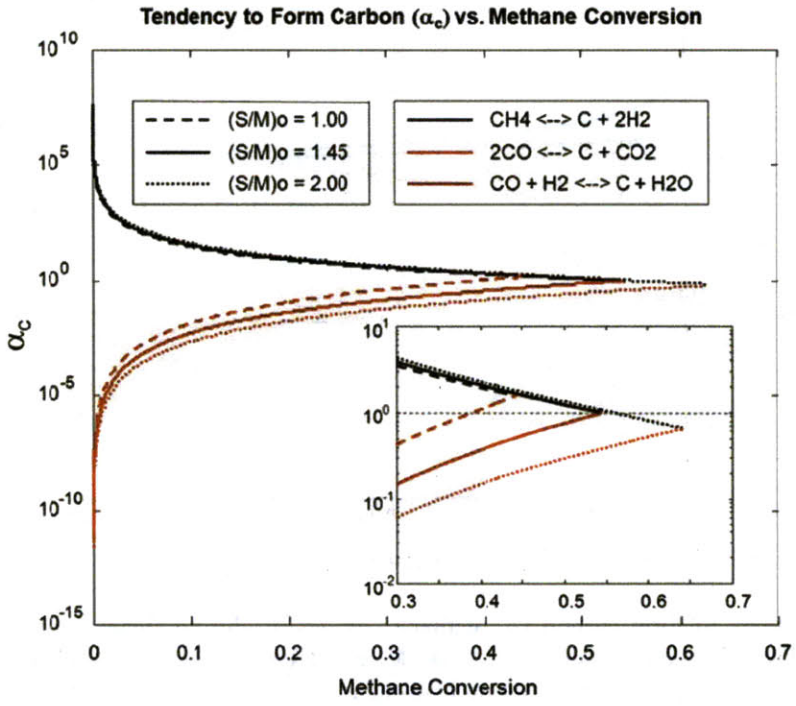

Figure 8-5. Tendency to form carbon vs. methane conversion during steam methane reforming (with WGS constrained to be in equilibrium) at T = 600 °C, P = 1 bar, and initial steam to methane ratios of 1.00, 1.45, and 2.00 (with no hydrogen in the feed). The curves of decreasing values of α_c are for Reaction 8-1. The curves of increasing α_c are for Reaction 8-2 and Reaction 8-3, which have equal values of α_c at a given set of conditions. The inset is a zoomed-in region near SMR equilibrium, which shows that as initial steam to methane ratio is increased, the system transitions from favoring carbon formation at SMR equilibrium to a region where carbon formation is thermodynamically forbidden. The dashed horizontal line in the inset represents a α_c value of one.

Unlike the equilibrated gas analysis, this dynamic perspective of carbon activities during SMR indicates that there exists a kinetic competition between carbon oxidation through Reaction 8-2 and Reaction 8-3 and carbon formation through Reaction 8-1 for the regions of catalyst exposed to non-equilibrated gas. Thus, if the rate that carbon formation (or carbon formation precursors) is produced is more than the rate of oxidation of carbon, then the regions of catalyst exposed to non-equilibrated gas would be expected to develop carbon deposits. A result of this analysis is that while an equilibrated gas α_c value of less than one is necessary for carbon-free operation, it may not be sufficient. For the portions of the catalyst exposed to the non-equilibrated gas with values of α_c such as those shown in Figure 8-5, the rate of carbon oxidation must exceed the rate of carbon-carbon coupling leading to carbon formation. Thus, higher steam to methane ratios may be required in the feed, which would increase the rate of carbon oxidation relative to the rate of carbon formation by increasing the concentration of O-containing species on the surface (due to water dissociation). This result is in agreement with the experiments of Chen, et al.[54] who reported initial steam to methane ratios required for no carbon formation in excess of the required ratios predicted for an equilibrated gas in Figure 8-2, which further suggests a kinetic competition between carbon oxidation and deactivating carbon formation. This competition will be discussed in more detail in the following sections.

Modifying the catalyst in a way that inhibits carbon-carbon coupling relative to carbon oxidation could decrease the steam to methane ratio required to ensure carbon-free operation in the regions of the catalyst exposed to non-equilibrated gas. This is desirable due to the large expense of creating excess steam for the reforming operations, providing motivation for the development of catalysts with increased inhibition to carbon formation. Also, though introducing hydrogen in the feed can produce more carbon-resistant reforming conditions, it is also desirable to limit the amount of hydrogen in the feed because excess hydrogen has a negative impact on methane conversion at SMR equilibrium. The competition between carbon formation and carbon oxidation can be adjusted by either altering the kinetics of the participating reactions or by manipulating the transport of key species such that the reactions become mass-transfer limited. These approaches will be discussed in the following sections.

8.3 Effect of Feed Gas Composition on the Rate of Carbon Formation

The analysis presented above indicates that for many regions of the catalyst bed, there exists a competition between carbon oxidation (to gas phase products) and carbon-carbon coupling leading to deactivating carbon formation. In practice, the initial steam to methane and hydrogen to methane ratios are adjusted to inhibit carbon formation. In this section, the multi-faceted microkinetic model for SMR

over nickel catalyst presented in Chapter 6 is used to investigate the surface coverage of adsorbed carbon and adsorbed oxygen on the Ni(211) facet during SMR in an isothermal, isobaric PFR. This facet is chosen because of its importance to the overall kinetics of SMR as well as its suspected role in carbon formation, which will be discussed later. Because a detailed carbon formation model is not available, the surface coverage of carbon is used to evaluate initial conditions least (or most) favorable for carbon formation. Regions of high carbon coverage would be expected to have a higher rate of carbon-carbon coupling than regions of lower carbon coverage. The coverage of carbon is found to be highest at the inlet of the reactor, decreasing as hydrogen partial pressure (due to SMR and WGS conversion) increases. Therefore, this limited analysis of coverage effects suggests that the rate of carbon formation is greatest at low SMR conversion. The coverage of carbon on the nickel catalyst as a function of initial steam to methane ratio and initial hydrogen to methane ratio is shown in Figure 8-6 for the case of low methane conversion (~ 5% to 10%) at 575 °C and 10 bar.

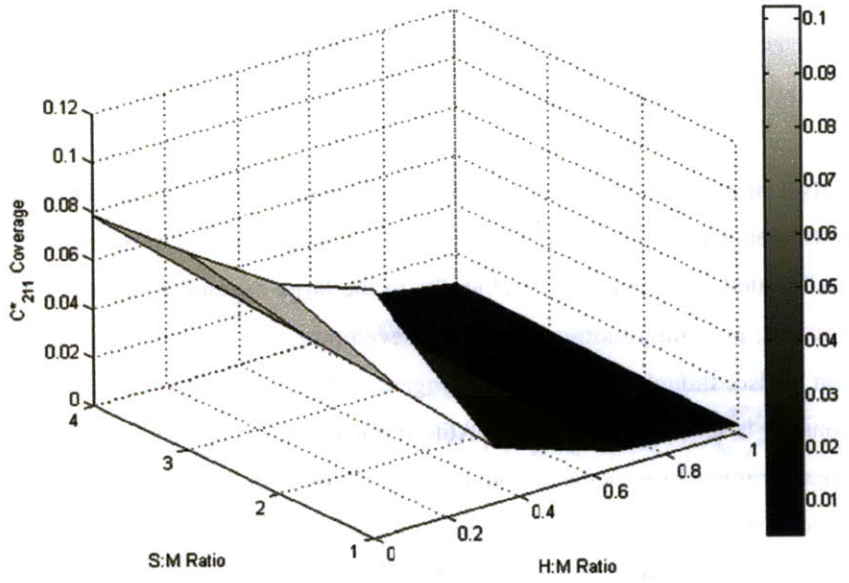

Figure 8-6. Adsorbed carbon fractional surface coverage on Ni(211) as a function of initial steam to methane (S:M) ratio and initial hydrogen to methane (H:M) ratio at low methane conversion (~5% to 10%), 575 °C, and 10 bar.

Figure 8-6 indicates that the surface coverage of carbon adatoms is found to decrease slightly with increasing steam to methane ratio in the feed; however, a much larger decrease in the surface coverage of

adsorbed carbon is seen with increasing hydrogen to methane ratio in the feed. Even small amounts of hydrogen in the feed (H:M ratios of ~ 0.2) are seen to have a reasonably significant impact on adsorbed carbon coverage. This analysis suggests that the forward rate of carbon-carbon coupling affected significantly by the presence of even small amounts of hydrogen in the feed stream, particularly because of the large ensemble size that has been reported for carbon formation (~6 sites).

In the absence of detailed modeling, some understanding of the effect of feed stream composition on the kinetic competition between carbon-carbon coupling and carbon oxidation can be obtained by comparing the coverage of adsorbed carbon to the coverage of adsorbed oxygen. The surface coverage of adsorbed oxygen as a function of initial hydrogen to methane ratio and initial steam to methane ratio is shown in Figure 8-7.

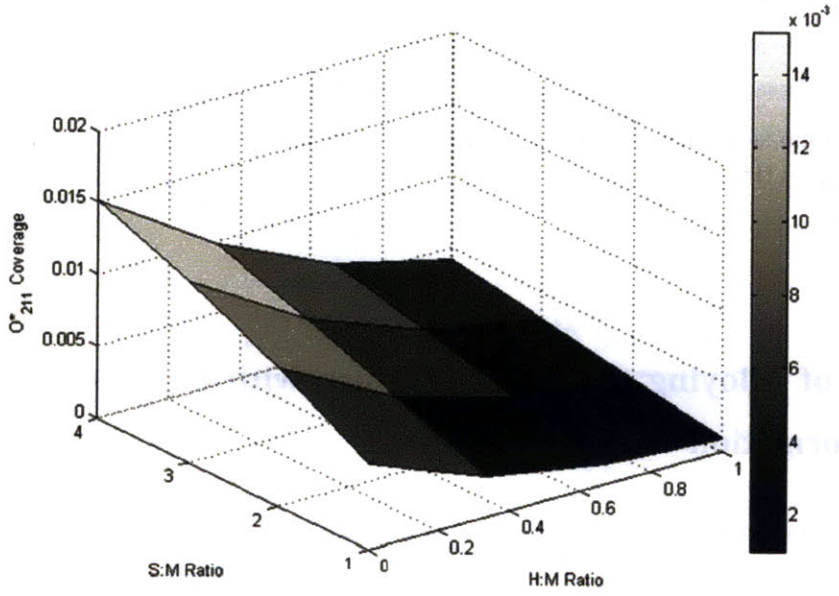

Figure 8-7. Adsorbed oxygen fractional surface coverage on Ni(211) as a function of initial steam to methane (S:M) ratio and initial hydrogen to methane (H:M) ratio at low methane conversion (~5% to 10%), 575 °C, and 10 bar.

The coverage of oxygen is predicted to increase with increasing steam to methane ratio in the feed stream while decreasing with increasing hydrogen to methane ratio in the feed. As expected, increasing the initial steam to methane ratio has a significant effect on the amount of adsorbed oxygen in the system.

Likewise, the rate of carbon oxidation will be enhanced due to the increased surface coverage of oxygen-containing species. In addition, while increased hydrogen in the feed stream is found to lower the surface coverage of oxygen and thus inhibit the rate of carbon oxidation, comparing Figure 8-7 to Figure 8-6 indicates that the surface coverage of carbon is more sensitive to increases in hydrogen partial pressure. In addition, given the larger ensemble size requirement that has been observed for carbon formation relative to SMR,[5] a decrease in the coverage of the reacting species leading to deactivating carbon formation (assumed in this analysis to be C* or related to the concentration of C*) would selectively inhibit carbon formation relative to carbon oxidation (which is first order in carbon-containing species).

The results of this surface coverage analysis indicate that carbon formation is inhibited by increased steam to methane ratio in the feed stream (due to significantly increased coverage of the oxygen-containing species required for carbon oxidation to SMR products) as well as increased hydrogen to methane ratio in the feed stream (due to a more significant decrease in the coverage of adsorbed carbon relative to adsorbed oxygen and the higher-reaction order that may be required for carbon formation relative to SMR). These predictions are consistent with experimental observations of the effect of initial steam to methane ratio and initial hydrogen to methane ratio on the rate of carbon formation during SMR over nickel catalysts.[54, 143]

8.4 Effect of Alloying the Nickel Surface with Silver on the Rate of Carbon Formation

As described in the preceding section, catalyst deactivation via coke formation can be controlled at static equilibrium by adjusting the gas-phase composition of the SMR feed stream. However, the issue of carbon formation becomes more problematic for a dynamic system where some regions of the reactor contain catalyst that is not exposed to equilibrated gas. In these regions of the reactor, there exists a kinetic competition between carbon formation and carbon removal via oxidation, even when high steam to methane or hydrogen to methane ratios are supplied to the reactor in the feed stream. This kinetic competition is diagramed in Figure 8-8. At the center of this diagram is the pool of carbon-containing species that leads to the formation of catalyst-deactivating carbon. It is at this point that carbon can either be oxidized away to gas-phase products via the pathways of region 2 of this diagram or undergo carbon-carbon coupling leading to the formation of carbon deposits via the pathways of region 3. By speeding the kinetics of region 2 or slowing the kinetics of region 3, carbon formation is kinetically inhibited. The

kinetics of region 1 are also relevant to the kinetic competition for carbon formation. If the kinetics of this region are slowed relative to carbon oxidation kinetics, then the concentration of methane dissociation products would decrease. Because the deactivating carbon formation kinetics have been demonstrated to have a require a higher ensemble size than SMR and the carbon oxidation reaction,[5] decreasing the concentration of carbon-containing intermediate species would selectively inhibit deactivating carbon formation by slowing the kinetics of region 3 relative to region 2. Initially, the reactions in region 3 involve slow nucleation of carbon formation, which is expected to scale as a high power of the concentration of the carbon pool species. However, after carbon formation has nucleated, it is expected to grow at a rate controlled by rate-limiting step(s) with a much lower dependence on the carbon pool species concentration.

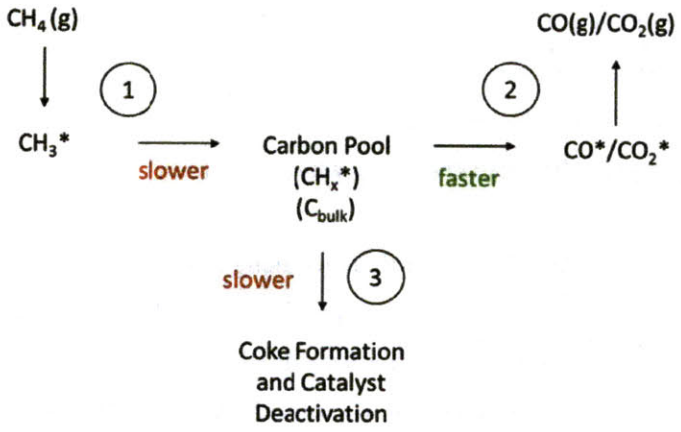

Figure 8-8. Diagram of the kinetic competition between carbon formation and carbon removal via oxidation during steam methane reforming. The kinetic modification that would lead to a decrease in the rate of carbon formation is labeled for each region (i.e., slower or faster methane dissociation, carbon oxidation, and carbon formation kinetics).

There are many reactions that make up the regions detailed in Figure 8-8. Several reaction pathways on multiple facets of the catalyst surface that describe the kinetics of regions 1 and 2 have been detailed in the preceding chapters. In addition, thermochemistry and kinetics of potential reactions in region 3 are detailed in this chapter. However, there are still many uncertain kinetic parameters that have not been explored in detail. Therefore, instead of a detailed, mechanistic model for carbon formation, a series of illustrative examples will be employed in the following sections to investigate the effect of alloying the nickel surface with silver on the kinetic competition leading to carbon formation. The illustrative cases

include modification of 1) reaction barriers, 2) stability of intermediate species, and 3) transport characteristics on the catalyst surface.

Effect of Alloying the Nickel Step Edge with Silver

Carbon Adatom Stability

As described in Chapter 2, it has been proposed that carbon adatom accumulation at the nickel step edge is an important step in the initiation of carbon formation. Carbon adatoms are predicted to be considerably more stable at the nickel step edge than on the Ni(111) surface (by almost 100 kJ/mol), increasing the carbon concentration and the probability of carbon-carbon addition reactions. Also, the nickel step edge leading to a Ni(111) terrace also presents an ideal configuration for carbon-carbon addition, with a distance of ~ 1.4 Å between the five-fold step binding site of carbon and the neighboring fcc binding site in the direction perpendicular to the step, which is close the preferred bond length in graphene of 1.42 Å.[144] Addition to the growing graphene sheet could then occur at the step edge or at the leading edge of the graphene on the Ni(111) surface, which have been studied by Abild-Pedersen, et al.[61]

When the nickel step edge is covered with 2/3 ML silver along the step edge, carbon adatoms adsorbed at the step edge are predicted to be destabilized by approximately 72 kJ/mol relative to the monometallic nickel step edge. As described in Chapter 7, the effects of silver are found to be fairly local. Consistent with this observation, the stability of carbon in a five-fold nickel binding site at the Ni/Ag step edge alloyed with 1/3 ML Ag is predicted to be only 4 kJ/mol less stable than carbon at the unalloyed step edge. Thus, there is a considerable difference in carbon binding energy between the 1/3 and 2/3 ML silver-alloyed nickel step edges. For comparison, the adsorbed geometries of carbon on the monometallic and silver-alloyed nickel step edge are shown in Figure 8-9.

On the monometallic nickel surface, the carbon adatom is five-fold coordinated, bonding with two nickel atoms on the bottom step, two nickel atoms on the top step, and one second-layer nickel atom below the top step. Because of this high degree of coordination with the nickel surface, the carbon adatom has a large degree of stability at the nickel step edge in comparison to the more tightly-packed Ni(111) surface where it has only three-fold coordination. When the nickel step edge is alloyed with silver at 2/3 ML silver, the carbon adatom loses one degree of coordination with a nickel atom at the top step. As a result, the C* molecule binds in the hcp site at the bottom step edge, further away from the step than C* binds on the unalloyed surface. At this position, the carbon adatom maintains four degrees of coordination with nickel atoms (three atoms on the plane of the bottom step and one atom along the top step), resulting in a

configuration that is more stable (by approximately 20 kJ/mol) than C* on the Ni(111) surface, but less stable than the monometallic nickel step edge. Interestingly, a terrace-like nickel atom along the plane of the bottom step is predicted to rise out of the surface by approximately 0.4 to 0.5 Å due to interaction with the carbon adatom, a process that is likely facilitated by the lower-degree of interaction between silver atoms and nickel atoms compared to the nickel-nickel interaction.

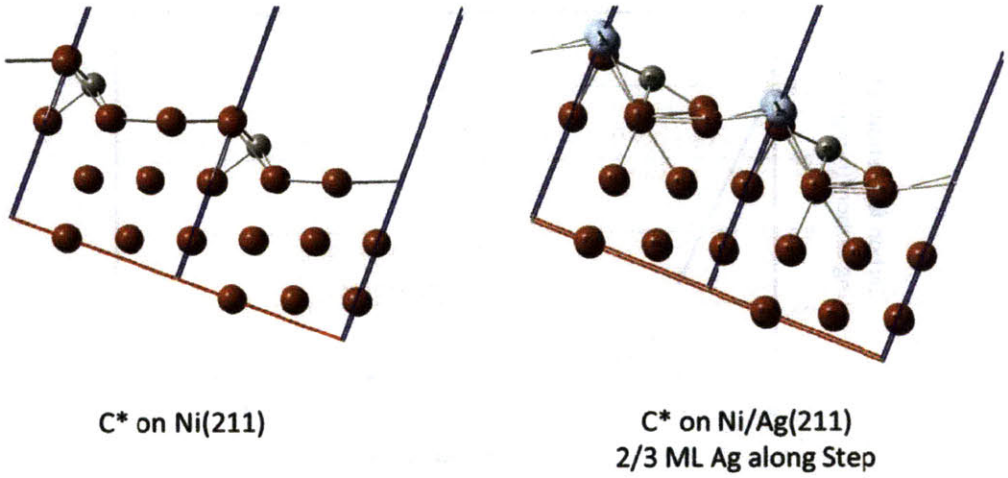

Figure 8-9. Geometries of adsorbed carbon on the Ni(211) surface and the Ni/Ag(211) surface with 2/3 ML Ag along the step edge. Carbon is five-fold coordinated with nickel on the monometallic nickel surface. On the silver-alloyed nickel surface, the carbon is pushed away from the step edge where it is four-fold coordinated.

Because the presence of silver at the nickel step edge destabilizes the carbon adatom, the concentration of carbon at the step is expected to decrease on the silver-alloyed nickel surface. For carbon formation nucleation, which has a higher-order dependence on carbon-containing intermediate species concentration than SMR, a decrease in the concentration of carbon-containing species would preferentially inhibit the reactions of region 3 of Figure 8-8 than the reactions of region 2. Therefore, this illustrative example of carbon adatom stability at the step edge indicates that nucleation of carbon formation may slow when the nickel step edge is alloyed with silver. This prediction is in agreement with experimental observations by collaborators at NTNU.[141] As shown in Figure 8-10, when the nickel catalyst is alloyed with silver, even at small concentrations, the rate of carbon formation is significantly inhibited. Based on the nickel/silver alloy stability analysis in Chapter 7, silver is expected to alloy first at the nickel step edge. The

observation that small amounts of silver alloyed with nickel significantly inhibit the rate of carbon formation is consistent with our predictions that the nickel step edge alloys first and that the presence of silver at the nickel step edge destabilizes carbon adatoms, which are precursors of carbon formation. The destabilization of carbon adatoms likely induces a kinetic effect due decreased rate of carbon-carbon addition at the step, which would be exacerbated if an ensemble of multiple carbon atoms is required to form a nucleation intermediate. A more complete analysis could be obtained by investigating carbon oxidation barriers on all alloyed facets for inclusion in a detailed microkinetic model.

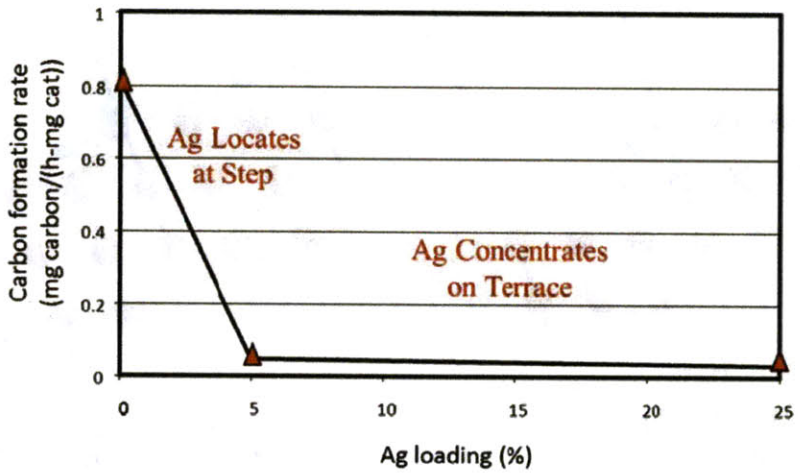

Figure 8-10. Experimentally-observed rate of carbon formation on nickel and silver-alloyed nickel catalysts at 5% and 25% total silver loading.[141] It is seen that a small amount of silver has a significant effect on the rate of carbon formation, supporting the suggestion that step sites play an important role in carbon formation.

Reaction Barriers at the Step Edge

The nickel step edge was shown to be a critical region on the catalyst for SMR activity in Chapter 6, and dissociative chemisorption of methane at the step edge is shown to be a rate-limiting reaction. As was discussed in Chapter 7, the barrier for dissociative methane adsorption is predicted by DFT to increase with increasing silver concentration along the step edge. Thus, an illustrative example of the effect of alloying the nickel step edge with silver is the slowing of methane dissociation and, as a result, the kinetics of region 1 in Figure 8-8. As was discussed above, slowing the kinetics region 1 is a metric that could lead to decreased carbon formation because it is expected to lead to a decrease in the steady-state concentration of pre-cursors to carbon formation (the result of which is analogous to that described above

for carbon adatom stability at the step edge). However, before this example of the effect of alloying the nickel step edge with silver can be understood more completely, additional investigation of the effect of alloying on carbon-oxidation reactions at the step edge is necessary. For example, if the rate of carbon-oxidation (region 2) is slowed comparably to that of methane dissociation (region 1), then the concentration of species in the carbon pool shown in Figure 8-8 would not necessarily decrease. Thus, the inhibition of methane dissociation is a potential metric indicating a decrease in the rate of carbon formation on the alloyed catalyst, but more analysis is necessary to evaluate the complete effect.

Effect of Alloying the Ni(111) Surface with Silver on Carbon Formation

As discussed in Chapter 7, the nickel catalyst will first alloy with silver at the step edge, followed by the (100) facet, and finally the (111) facet. In the preceding section, the stability of the carbon adatom was predicted to decrease in the presence of silver at the step edge. The stability of carbon-containing species on the silver-alloyed Ni(111) surface is also of interest as growing graphene sheets may propagate across this surface. Two illustrative metrics are analyzed to assess the impact of alloying the Ni(111) surface with silver. First, because the CH* intermediate is the most dominant methane dissociation product on the Ni(111) surface, the addition of CH* + CH* to form C_2H_2* is investigated as a precursor of carbon formation for potential kinetic effects of alloying the nickel surface with silver. For comparison, the changes in activation barriers for the addition of CH* and O* as well as CH* and OH* on the silver-alloyed Ni(111) surface that are reported in Chapter 7 are compared to the carbon-carbon coupling barrier increases computed here. Second, it is proposed that the carbon formation on the Ni(111) surface could be propagated by the addition of CH* to the growing carbon deposit (because CH* the most stable methane dissociation product on Ni(111) and is large in concentration relative to other methane dissociation products), while carbon formation would be removed by the oxidation of the carbon atoms to form CO* which can then desorb. Therefore, the effect of alloying the nickel surface with silver on the relative diffusion rates of the CH* and O* species is examined to offer an illustrative example of the effect of alloying the nickel catalyst with silver on transport across the catalyst surface.

Carbon-Carbon Coupling and Carbon Oxidation Reactions

The carbon- carbon addition reaction of CH* + CH* forming C_2H_2* is calculated via DFT in Dacapo to be exothermic by approximately 30 kJ/mol with a reaction barrier (from a first-order saddle point search) of approximately 81 kJ/mol. As discussed in Chapter 7, the presence of silver on the Ni(111) surface at ¼ ML coverage is found to preferentially decrease the stability of large molecules over small molecules because of increased interaction with the silver for large molecules. Consistent with this result, the CH*

+ CH* → C_2H_2* reaction is found to become endothermic on the Ni/Ag(111) 1/4 ML Ag surface, with an electronic energy of reaction equal to +69 kJ/mol, an increase of almost 100 kJ/mol relative to the unalloyed Ni(111) surface. Because the reaction has become more endothermic, an Evans-Polanyi relationship would suggest that the barrier for CH* coupling will increase on the alloyed surface, which is confirmed via a DFT first-order saddle point search. The activation barrier for CH* + CH* → C_2H_2* is predicted to be approximately 182 kJ/mol on the Ni/Ag(111) 1/4 ML Ag surface, which is an increase of approximately 100 kJ/mol (corresponding well to the increase of 100 kJ/mol in endothermicity).

The most active carbon-oxidation route on the Ni(111) surface were found to be CH* + O* → CHO* and CH* + OH* → CHOH* in Chapter 5. The electronic reaction energy and electronic reaction barrier for the reaction of CH* with O* were reported in Chapter 7 to increase by approximately 50 kJ/mol and 60 kJ/mol, respectively. For the CH* + OH* reaction, the reported increase in electronic reaction energy was less than that for CH* + O* at 17 kJ/mol, with a correspondingly lower increase in activation barrier of 27 kJ/mol. Thus, while alloying the Ni(111) surface with silver is found to increase the barriers of key carbon oxidation reactions, the predicted increase (~30-60 kJ/mol) is considerably less than the increase in activation barrier predicted for the carbon-carbon coupling reaction of CH* + CH* (~100 kJ/mol). Reflecting back to the dynamic SMR conversion α_c calculations, these carbon oxidation and carbon-carbon coupling reactions are related to the competition between the carbon-oxidizing and carbon-forming reactions shown in Figure 8-5. Because carbon-carbon coupling is predicted to be more inhibited by alloying the nickel surface with silver than carbon oxidation reactions, then this illustrates that the Ni/Ag catalyst may be a more carbon-tolerant catalyst than monometallic nickel. However, it is important to note that other surface facets such as the step edge and Ni(100) surface are important in carbon oxidation (as reported in Chapter 6) and the carbon-carbon coupling reaction investigated here is but one potential gateway to carbon formation. As a result, a more detailed analysis of the effect of silver on carbon oxidation and carbon-carbon coupling across the multiple facets present on the commercial catalyst could provide more insight into the competition between carbon formation and carbon oxidation and the carbon formation inhibition presented by the alloyed catalyst.

Carbon and Oxygen Transport on the Catalyst Surface

The analysis presented in the previous section focused on kinetic inhibition of carbon formation; however, it is also possible that carbon formation can be inhibited by altering the transport characteristics of species on the surface. If the barriers to diffusion of carbon-containing or oxygen-containing species become larger than the carbon-carbon coupling or carbon-oxidizing reaction barriers, then mass transfer

of species on the catalyst surface could become an important component in the analysis of carbon formation inhibition. To illustrate this, the diffusion barriers for the CH* species and O* species on the Ni/Ag(111) 2/9 ML surface are shown in Figure 8-11. Note that in the calculation, the position of the silver atoms is optimized on a bare slab and then fixed in constrained optimizations during diffusion simulations. In addition, in cases where the adsorbate is placed close to a silver atom, the x-y position of the adsorbate atom is sometimes constrained. These constraints are necessary to prevent significant diffusion of the silver atom or adsorbate atoms during the geometry optimization so that the desired configuration can be analyzed. Thus, this analysis should be viewed as a first-approximation. The 2/9 ML silver surface concentration was chosen so that non-alloyed binding sites would exist sufficiently far away from the silver atoms to allow for fairly unperturbed carbon oxidation or carbon-carbon coupling; however, the coverage is high enough to affect the calculated diffusion barriers of species across the alloyed surface. Note that to achieve a coverage of 2/9 ML silver on the (111) facet, the total concentration on the catalyst surface would likely have to approach 35-40% because the (211) and (100) facets will alloy first. Thus, this illustration of diffusion limitations is most relevant to cases of high silver doping. The design of the calculation is similar to the analysis of Nikolla, et al. for the tin-alloyed Ni(111) surface.[138]

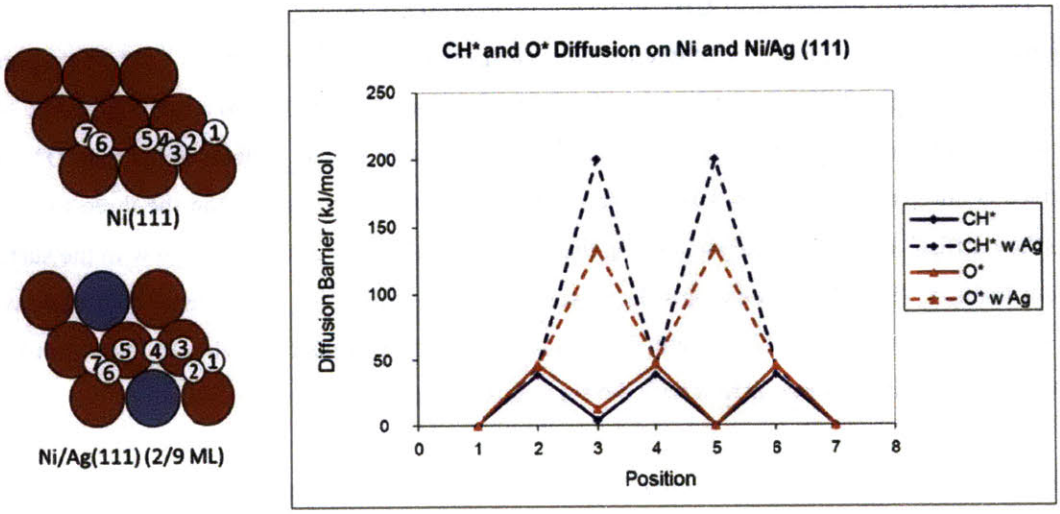

Figure 8-11. Diffusion barriers for CH* and O* on the monometallic and silver-alloyed Ni(111) surfaces. Note that the diffusion of CH* is inhibited considerably more than the diffusion of O* on the silver-alloyed Ni(111) surface. The energy of each species is calculated at the labeled positions (or equivalent mirror-image) and the diffusional barrier is calculated as the difference between the highest- and lowest-energy images.

The lowest-energy diffusion paths found in this analysis are in Figure 8-11. It can be seen that dispersed silver atoms on the nickel surface form a structure similar to a gate, increasing the diffusion barrier of adsorbates as they pass across the atop and bridge positions of nickel atoms, rather than the three-fold hollows on the unalloyed surface. While the CH* and O* species are predicted to have similar diffusional barriers on the monometallic Ni(111) surface, the barrier for diffusion of CH* on Ni/Ag(111) 2/9 ML is predicted to be approximately 70 kJ/mol higher than the barrier for O*. In addition, this diffusional barrier for CH* of approximately 200 kJ/mol is higher than the barrier predicted for CH* + CH* on monometallic Ni(111) of 81 kJ/mol or on Ni/Ag(111) 1/4 ML Ag of 182 kJ/mol, which suggests that diffusional limitations on the alloyed surface could be important. The diffusion barrier for O* on the alloyed surface is on the same order as the reaction barrier of CH* + O*, thus diffusional limitations are not as important for this reaction.

The result of this illustration of diffusion limitations is that the silver-alloyed nickel surface is found to preferentially inhibit CH* diffusion over O* diffusion (for this first-approximation model of the catalyst surface). Because the transport of CH* on the surface may be important to the overall rate of carbon formation growth, the increased inhibition of CH* diffusion relative to O* diffusion serves as an additional data point to suggest that carbon formation is inhibited by alloying the nickel surface with silver. The increased inhibition of CH* diffusion relative to O* diffusion on the silver-alloyed nickel surface may be related to the degree of interaction each species has with the surface. CH* was reported to have a binding energy of -5.9 eV on the Ni(111) surface in Chapter 5, relative to a binding energy of -4.5 eV for O*. Thus, the CH* species has a stronger interaction with the Ni surface atoms than O*. When the surface is alloyed and the adsorbates move to bridge and atop sites rather than the three-fold hollow sites as they diffuse across the catalyst surface, they lose a certain degree of interaction with the surface as their coordination with the surface atoms decreases from three (at the fcc or hcp three-fold hollow sites) to two (bridge) or one (atop). As a result, CH* is more destabilized than O* when it loses coordination with the surface because its interaction with the surface is stronger.

The particular system studied here is rather specific with regard to surface coverage and dispersion of silver on the catalyst surface. Thus, the results should be viewed as a general indication of diffusional limitations on the surface rather than precise predictions.

The kinetic and mass transfer arguments presented in this section are single-point illustrative metrics of the effect of alloying the nickel surface on carbon formation. The actual carbon formation process is more complex and the evaluation of additional carbon-containing intermediates as well as additional

carbon-formation reactions could give more insight into the competition between carbon formation and carbon oxidation. In the following section, a preliminary investigation of on carbon-containing species on the Ni(111) surface is presented.

8.5 Computational Investigation of Carbon-Containing Species on Nickel Catalyst

The thermochemistry and kinetics of carbon-containing species on the Ni(111) surface are investigated using DFT calculations in Dacapo. The analysis presented here represents a contribution toward building a more complete understanding of the thermochemistry and kinetics of the carbon formation reactions in region 3 of Figure 8-8. The resulting thermochemistry and reaction barriers are shown in Figure 8-12.

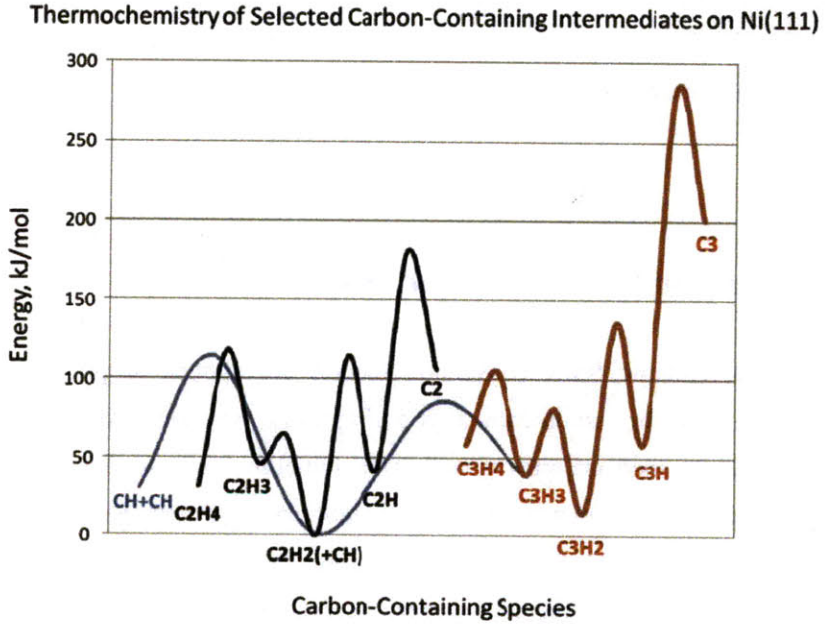

Figure 8-12. Electronic energy of selected carbon-containing intermediates on the Ni(111) surface. Pictured are C_1H_x, C_2H_x, and C_3H_x species. Reaction barriers for carbon-carbon coupling and hydrogen addition / dehydrogenation are also shown. Some CH* and H* species are omitted from labels to simplify the notation.

The activation barriers for C_2 and C_3 species dehydrogenation reactions are estimated by constructing an Evans-Polanyi plot using C_1 species' dehydrogenation reactions, which results in the relationship $E_a = 1.1*E_{rxn} + 69$ kJ/mol. To check the validity of this correlation, the dehydrogenation of HCCH* to form CCH* + H* is calculated through a first-order saddle point search (using a 2x3 unit cell for the H-CCH* transition state), resulting in an activation barrier of 103 kJ/mol, which compares well with the prediction from the Evans-Polanyi relationship of 114 kJ/mol.

The carbon-carbon addition reaction of CH* + CH* forming C_2H_2* is calculated via DFT to be exothermic by approximately 30 kJ/mol with a reaction barrier of approximately 81 kJ/mol. Our calculations are in agreement with experimental observations that C_2H_2* is more stable than 2 CH* on the Ni(111) surface.[116] The carbon-containing species on the Ni(111) surface are predicted to be more stable when hydrogenated, though a clear trend for stability vs. the degree of hydrogenation is not apparent. The order of stability for C_2 species is found to be (from most stable to least) $C_2H_2* > C_2H_4* > C_2H* \sim C_2H_3* > C_2*$. The order of stability for C_3 species if predicted to be $C_3H_2* > C_3H_3* > C_3H_4* \sim C_3H* > C_3*$. Our calculations suggest that C_2H_2 may be an important carbon pool species on the Ni(111) surface. Calculations on other Ni facets are needed to reach firmer conclusions, since it is likely that the thermochemistry will be significantly different at the step sites.

8.6 Conclusions and Recommendations

Equilibrated gas and a dynamic SMR conversion models are applied to provide insight into the thermodynamic driving force for carbon formation during steam methane reforming. It is shown that increasing the initial steam to methane ratio as well as the initial hydrogen to methane ratio can decrease the driving force for carbon formation in the SMR-equilibrated reformer gas. The equilibrated gas analysis is generally valid for the gas within the catalyst pores due to a low effectiveness factor for SMR catalysts. However, other regions of the catalyst may be exposed to the non-equilibrated reacting gas. For this gas, it is shown that the values of α_c describing the driving force for carbon formation are a function of SMR conversion. Under typical SMR conditions, one $\alpha_{c,i}$ value is found to be greater than one, while the other is found to be less than one. These values for the tendency to form carbon indicate that a competition between carbon-carbon coupling and carbon oxidation on the catalyst surface exists for many regions of the SMR reactor and that carbon formation is possible at most reaction conditions. This competition motivates investigating the kinetics and transport relevant to carbon formation and carbon

oxidation on the monometallic and alloyed nickel surface to assess the effect of alloying the surface on the relative rates of these reactions.

Several metrics/examples have been presented in this chapter to illustrate potential effects of modifying the kinetics and thermochemistry relevant to the competition between carbon formation and carbon oxidation by alloying the nickel surface with silver. The stability of carbon at the monometallic and silver-alloyed nickel step edge is investigated, leading to the conclusion that the presence of silver at the step edge significantly decreases the stability of carbon at the step. The result of this decrease in stability is a decrease in the rate of carbon-carbon coupling at the step, potentially leading to a decrease in the rate of carbon formation. In addition, the presence of silver on the Ni(111) surface facet is predicted to increase the barrier for CH* coupling to form C_2H_2* considerably more than it increases the barriers for carbon-containing species oxidation. This case illustrates that alloying the nickel surface with silver may preferentially inhibit carbon formation relative to carbon oxidation. Similarly, alloying the Ni(111) surface with silver is found to preferentially inhibit the diffusion of CH* species relative to O* species on the 2/9 ML Ag surface. The increase in diffusion barrier for CH* is sufficient to potentially limit the overall rate of carbon formation, introducing the possibility of mass transport limitations being important in the competition between carbon formation and carbon oxidation. Moving beyond these illustrative cases, a more detailed analysis of the transport mechanisms and kinetics of carbon formation and carbon oxidation would provide valuable insight into the competition between these reactions and the potential for carbon formation on the alloyed catalyst. However, the illustrative metrics analyzed here (carbon stability at the step, barriers to dissociative methane adsorption and gateway carbon formation reactions, and diffusion of key carbon-containing and oxygen-containing species) present a consistent picture that carbon formation is likely inhibited on the silver-alloyed nickel surface, which is consistent with experimental observation.

Chapter 9. Recommendations for Future Work

9.1 Steam Methane Reforming over Ni(111)

In in Chapter 5, the species thermochemistry was computed using a 2x2 unit cell at 1/4 ML species coverage. This unit cell and coverage was chosen based on being a reasonable description of the species on the surface at an affordable computational expense. Because the predicted coverage of most species is actually significantly lower than 1/4 ML, it is possible that some species, particularly larger species such as $CH_xO_yH_z$* species, would be better-represented using a larger unit cell (and resulting lower coverage) where less inter-image adsorbate-adsorbate interactions would be present in the calculation. The resulting energy would be more representative of the actual energy of the molecule on the catalyst surface.

In the gas phase, species in a system are generally located sufficiently far apart that their energy is well-represented using that of an isolated gas-phase molecule in vacuum. However, on the surface, interaction between species is much more common, particularly at high total coverage. On the Ni(111) surface, the coverage of species is generally found to be low (less than ~20% at the temperature and pressure investigated here). Therefore, using sufficiently large unit cells to ensure minimal inter-image adsorbate-adsorbate interactions in the DFT calculations is advisable. However, the coverage of H* species is approaching 15% under the conditions studied in Chapter 5. Thus, it might be interesting to include an extra H* species in the unit cells for other species when computing their thermochemistry or finding a first-order saddle point for a reaction. This is because the energies used in kinetic modeling should be representative of the energies of the species in the real system. The role of adsorbate-adsorbate interactions would be an interesting subject to research.

9.2 Steam Methane Reforming over a Multifaceted Nickel Catalyst

Thermochemistry and Kinetics

The role of adsorbate-adsorbate interactions and coverage effects could be even more interesting to explore on the multifaceted nickel surface of Chapter 6 than the Ni(111) surface modeled in Chapter 5. Because the Ni(211) and Ni(100) surfaces are found to bind species more tightly than the Ni(111) surface, the coverage of species is generally found to be higher on these surfaces. As a result, incorporation of coverage effects could be important. This was performed in Chapter 6 for the C* and CH* species on the Ni(100) surface; however, extending similar coverage effects to other species with reasonably high

coverage could be useful, though is only generally important for species with a coverage higher than that used in the DFT calculations. However, such a treatment would only account for the interaction of a species with itself in the model. Another interesting area of research would be the incorporation of unlike adsorbate-adsorbate interactions in the model. This analysis could also be interesting for observing the impact of non-reacting, but neighboring species on the transition states studied in the kinetic model.

Kinetic Modeling

It has been shown that a mean-field model with lateral interactions can capture interesting physics of systems without the need for more expensive kinetic Monte Carlo calculations, though this is a function of surface coverage and surface heterogeneity.[105] However, for systems with high coverage, it could be very useful to implement the kinetic model in a kinetic Monte Carlo formulation rather than a mean-field approach. For a system the size of the one studied in Chapter 6, this could be quite expensive. The expense comes not only in the Monte Carlo simulation, but also in obtaining all of the lateral interaction parameters required by the model. As a result, it may be necessary to decrease the size of the model and study only the species and reactions of most interest in the model. However, simplifications to the model made by drawing conclusions from mean-field modeling could result in species/reactions being removed from the model that would prove to be important in a kinetic Monte-Carlo simulation (i.e., the process of simplifying the model may not be straightforward).

Rate Limiting Reactions

As discussed in Chapter 6, C-O addition reactions are predicted to be rate-limiting at high temperatures where experimental observation suggests that only dissociative methane adsorption should be rate limiting. This disagreement between computational prediction and experimental observation is an interesting area for further research. Possible explanations for the disagreement include that the C-O addition barriers are being incorrectly predicted by the DFT methods employed in this work as well as possible errors in the thermochemistry leading to the reactants in these reactions, which would cause surface coverage of the species to be incorrectly predicted.

9.3 Steam Methane Reforming over Multifaceted Nickel/Silver Catalysts

Thermochemistry and Kinetics

In Chapter 7, the thermochemistry and kinetics of the expanded microkinetic model studied on the monometallic nickel surfaces are presented only for the Ni/Ag(111) surface. A clear extension of this work would be to study the thermochemistry and kinetics of these species on the other surface facets of the Ni/Ag surface at various silver concentrations, using the alloy stability analysis in Chapter 7 as a guide. The resulting thermochemistry and kinetics could then be combined with kinetic modeling to make more complete predictions about the kinetics of SMR over the Ni/Ag catalyst. Similar to the multifaceted nickel surface analysis, the ability to accurately model the C-O addition reactions on the silver-alloyed nickel surface would be important to maximize the information gained from such analysis.

9.4 Carbon Formation during Steam Methane Reforming over Nickel and Nickel/Silver Catalysts

Competition between Carbon Formation and Carbon Oxidation

In Chapter 8, a dynamic SMR conversion model of the tendency to form carbon indicated that the competition between carbon-carbon coupling and carbon-containing species oxidation is important to the control of carbon formation during SMR. Several metrics were presented in that chapter to discuss the effect of alloying the nickel surface with silver on carbon formation and the competition between carbon-carbon coupling and carbon oxidation. However, these metrics are not representative of all important intermediates/reactions in carbon formation or carbon oxidation, and additional analyses to study other reactions and intermediates is needed to obtain a more complete picture of the competition between these reactions.

In addition, the questions raised in Chapter 6 about the accuracy in capturing the barriers for carbon-oxygen addition reactions are extremely important to this discussion. If these reactions are not described with accuracy on the same order as that for carbon formation reactions, then quantifying the competition between the two reactions and the carbon formation inhibition of a particular catalyst will be difficult. If the carbon-oxygen addition reactions are described with reasonably accuracy, then the carbon formation and carbon oxidation reactions can be combined in a microkinetic model for simulation of the

competition between the reactions. Because the carbon formation product is largely localized and large diffusion barriers may be present on the alloyed surface, a mean field model may begin to break down. However, incorporation of a complete SMR and carbon formation microkinetic model into a kinetic Monte Carlo simulation would present a large computational challenge due to the large number of species and reactions in such a model.

Bibliography

1. Davis, B. H.; Ertl, G.; Knozinger, H.; Weitkamp, J., *Handbook of Heterogeneous Catalysis*. VCH, Weinheim, 1997; Vol. 1.
2. Lindström, B.; Pettersson, L. J., A Brief History of Catalysis. *CATTECH* **2003,** *7* (4), 130-138.
3. Wisniak, J., The history of catalysis. From the beginning to Nobel prizes. *Educ. Quim.* **2010,** *21* (1), 60-69.
4. Smil, V., Detonator of the population explosion. *Nature* **1999,** *400* (6743), 415-415.
5. Chorkendorff, I.; Niemantsverdriet, J. W., *Concepts of Modern Catalysis and Kinetics*. 2nd ed.; Wiley-VCH: 2007.
6. Somorjai, G. A., Modern Surface Science and Surface Technologies: An Introduction. *Chemical Reviews* **1996,** *96* (4), 1223-1236.
7. Hammer, B.; Nørskov, J. K., Theoretical surface science and catalysis--calculations and concepts. In *Advances in Catalysis*, Academic Press: 2000; Vol. Volume 45, pp 71-129.
8. Honkala, K.; Hellman, A.; Remediakis, I. N.; Logadottir, A.; Carlsson, A.; Dahl, S.; Christensen, C. H.; Nørskov, J. K., Ammonia Synthesis from First-Principles Calculations. *Science* **2005,** *307* (5709), 555-558.
9. Hellman, A.; Baerends, E. J.; Biczysko, M.; Bligaard, T.; Christensen, C. H.; Clary, D. C.; Dahl, S.; van Harrevelt, R.; Honkala, K.; Jonsson, H.; Kroes, G. J.; Luppi, M.; Manthe, U.; Nørskov, J. K.; Olsen, R. A.; Rossmeisl, J.; Skúlason, E.; Tautermann, C. S.; Varandas, A. J. C.; Vincent, J. K., Predicting Catalysis: Understanding Ammonia Synthesis from First-Principles Calculations. *The Journal of Physical Chemistry B* **2006,** *110* (36), 17719-17735.
10. Kandoi, S.; Greeley, J.; Sanchez-Castillo, M.; Evans, S.; Gokhale, A.; Dumesic, J.; Mavrikakis, M., Prediction of Experimental Methanol Decomposition Rates on Platinum from First Principles. *Topics in Catalysis* **2006,** *37* (1), 17-28.
11. Nørskov, J. K.; Christensen, C. H., Toward Efficient Hydrogen Production at Surfaces. *Science* **2006,** *312* (5778), 1322-1323.
12. Blaylock, D. W.; Ogura, T.; Green, W. H.; Beran, G. J. O., Computational Investigation of Thermochemistry and Kinetics of Steam Methane Reforming on Ni(111) under Realistic Conditions. *The Journal of Physical Chemistry C* **2009,** *113* (12), 4898-4908.
13. Solomon, B. D.; Banerjee, A., A global survey of hydrogen energy research, development and policy. *Energy Policy* **2006,** *34* (7), 781-792.
14. Rostrup-Nielsen, J. R.; Sehested, J.; Nørskov, J. K., Hydrogen and synthesis gas by steam- and CO2 reforming. In *Advances in Catalysis*, Academic Press: 2002; Vol. Volume 47, pp 65-139.
15. U.S. Department of Energy (DOE). National Hydrogen Energy Roadmap. Washington, DC, 2002.
16. Blok, K.; Williams, R. H.; Katofsky, R. E.; Hendriks, C. A., Hydrogen production from natural gas, sequestration of recovered CO2 in depleted gas wells and enhanced natural gas recovery. *Energy 22* (2-3), 161-168.
17. Jordal, K.; Bredesen, R.; Kvamsdal, H. M.; Bolland, O., Integration of H2-separating membrane technology in gas turbine processes for CO2 capture. *Energy 29* (9-10), 1269-1278.
18. Logan, B. E., Peer Reviewed: Extracting Hydrogen and Electricity from Renewable Resources. *Environmental Science & Technology* **2004,** *38* (9), 160A-167A.
19. U.S. Department of Energy. Hydrogen Production Fact Sheet. 2006.
20. Lægsgaard Jørgensen, S.; Nielsen, P. E. H.; Lehrmann, P., Steam reforming of methane in a membrane reactor. *Catalysis Today* **1995,** *25* (3-4), 303-307.
21. Bottino, A.; Comite, A.; Capannelli, G.; Di Felice, R.; Pinacci, P., Steam reforming of methane in equilibrium membrane reactors for integration in power cycles. *Catalysis Today* **2006,** *118* (1-2), 214-222.

22. Tong, J.; Matsumura, Y., Pure hydrogen production by methane steam reforming with hydrogen-permeable membrane reactor. *Catalysis Today* **2006,** *111* (3-4), 147-152.
23. Lattner, J. R.; Harold, M. P., Comparison of conventional and membrane reactor fuel processors for hydrocarbon-based PEM fuel cell systems. *International Journal of Hydrogen Energy* **2004,** *29*, 393-417.
24. Shishkin, M.; Ziegler, T., Oxidation of H2, CH4, and CO Molecules at the Interface between Nickel and Yttria-Stabilized Zirconia: A Theoretical Study Based on DFT. *J. Phys. Chem. C* **2009,** *113* (52), 21667-21678.
25. Mogensen, D.; Grunwaldt, J. D.; Hendriksen, P. V.; Dam-Johansen, K.; Nielsen, J. U., Internal steam reforming in solid oxide fuel cells: Status and opportunities of kinetic studies and their impact on modelling. *J. Power Sources* **2010,** *196* (1), 25-38.
26. Ingram, D. B.; Linic, S., First-Principles Analysis of the Activity of Transition and Noble Metals in the Direct Utilization of Hydrocarbon Fuels at Solid Oxide Fuel Cell Operating Conditions. *J. Electrochem. Soc.* **2009,** *156* (12), B1457-B1465.
27. Menon, P. G.; de Deken, J. C.; Froment, G. F., Formaldehyde as an intermediate in the steam reforming of methane. *Journal of Catalysis* **1985,** *95* (1), 313-316.
28. Pistonesi, C.; Juan, A.; Irigoyen, B.; Amadeo, N., Theoretical and experimental study of methane steam reforming reactions over nickel catalyst. *Applied Surface Science* **2007,** *253* (9), 4427-4437.
29. Kikuchi, E.; Tanaka, S.; Yamazaki, Y.; Morita, Y., Steam reforming of hydrocarbons on noble metal catalysts - 1. The catalytic activity in methane-steam reaction. *Bull Jpn Pet Inst* **1974,** *16* (2), 95-98.
30. Rostrup-Nielsen, J. R.; Hansen, J. H. B., CO2-Reforming of Methane over Transition Metals. *Journal of Catalysis* **1993,** *144* (1), 38-49.
31. Qin, D.; Lapszewicz, J., Study of mixed steam and CO2 reforming of CH4 to syngas on MgO-supported metals. *Catalysis Today* **1994,** *21* (2-3), 551-560.
32. Jones, G.; Jakobsen, J. G.; Shim, S. S.; Kleis, J.; Andersson, M. P.; Rossmeisl, J.; Abild-Pedersen, F.; Bligaard, T.; Helveg, S.; Hinnemann, B.; Rostrup-Nielsen, J. R.; Chorkendorff, I.; Sehested, J.; Nørskov, J. K., First principles calculations and experimental insight into methane steam reforming over transition metal catalysts. *Journal of Catalysis* **2008,** *259* (1), 147-160.
33. Wei, J.; Iglesia, E., Mechanism and Site Requirements for Activation and Chemical Conversion of Methane on Supported Pt Clusters and Turnover Rate Comparisons among Noble Metals. *Journal of Physical Chemistry B* **2004,** *108* (13), 4094-4103.
34. Wei, J.; Iglesia, E., Isotopic and kinetic assessment of the mechanism of methane reforming and decomposition reactions on supported iridium catalysts. *Physical Chemistry Chemical Physics* **2004,** *6* (13), 3754-3759.
35. Wei, J.; Iglesia, E., Structural and mechanistic requirements for methane activation and chemical conversion on supported iridium clusters. *Angewandte Chemie - International Edition* **2004,** *43* (28), 3685-3688.
36. Wei, J.; Iglesia, E., Structural requirements and reaction pathways in methane activation and chemical conversion catalyzed by rhodium. *Journal of Catalysis* **2004,** *225* (1), 116-127.
37. Wei, J.; Iglesia, E., Reaction pathways and site requirements for the activation and chemical conversion of methane on Ru-based catalysts. *Journal of Physical Chemistry B* **2004,** *108* (22), 7253-7262.
38. Wei, J.; Iglesia, E., Isotopic and kinetic assessment of the mechanism of reactions of CH4 with CO2 or H2O to form synthesis gas and carbon on nickel catalysts. *Journal of Catalysis* **2004,** *224* (2), 370-383.
39. Bengaard, H. S.; Nørskov, J. K.; Sehested, J.; Clausen, B. S.; Nielsen, L. P.; Molenbroek, A. M.; Rostrup-Nielsen, J. R., Steam Reforming and Graphite Formation on Ni Catalysts. *Journal of Catalysis* **2002,** *209* (2), 365-384.
40. Sehested, J., Four challenges for nickel steam-reforming catalysts. *Catalysis Today* **2006,** *111* (1-2), 103-110.

41. van Beurden, P. *On the catalytic aspects of steam methane reforming*; Energy Research Centre of the Netherlands (ECN): 2004.
42. Abild-Pedersen, F.; Lytken, O.; Engbæk, J.; Nielsen, G.; Chorkendorff, I.; Nørskov, J. K., Methane activation on Ni(1 1 1): Effects of poisons and step defects. *Surface Science* **2005,** *590* (2-3), 127-137.
43. Rostrup-Nielsen, J. R., Activity of nickel catalysts for steam reforming of hydrocarbons. *Journal of Catalysis* **1973,** *31* (2), 173-199.
44. Rostrup-Nielsen, J. R., *Steam Reforming Catalysts*. Danish Technical Press: Copenhagen, 1975.
45. Bodrov, I. M.; Apel'baum, L. O.; Temkin, M., Kinetics of the reaction of methane with water vapor on a nickel surface. *Kinetics and Catalysis* **1964,** *5*, 614-622.
46. Khomenko, A. A.; Apel'baum, L. O.; Shub, F. S.; Snagorskii, Y. S.; Temkin, M. I., *Kinetics and Catalysis* **1971,** *12*, 367.
47. Rostrup-Nielsen, J. R., *Catalytic Steam Reforming*. Springer-Verlag: Berlin, 1984.
48. Tøttrup, P. B., Evaluation of intrinsic steam reforming kinetic parameters from rate measurements on full particle size. *Applied Catalysis* **1982,** *4* (4), 377-389.
49. Xu, J.; Froment, G. F., Methane steam reforming, methanation and water-gas shift: I. Intrinsic kinetics. *AIChE Journal* **1989,** *35* (1), 88-96.
50. Aparicio, L. M., Transient Isotopic Studies and Microkinetic Modeling of Methane Reforming over Nickel Catalysts. *Journal of Catalysis* **1997,** *165* (2), 262-274.
51. Dumesic, J. A.; Trevino, A. A.; Milligan, B. A.; Greppi, L. A.; Balse, V. R.; Sarnowski, K. T.; Beall, C. E.; Kataoka, T.; Rudd, D. F., A kinetic modeling approach to the design of catalysts: formulation of a catalyst design advisory program. *Industrial & Engineering Chemistry Research* **1987,** *26* (7), 1399-1407.
52. Dumesic, J. A.; Rudd, D. F.; Aparicio, L. M.; Rekoske, J. E.; Trevino, A. A., *The Microkinetics of Heterogeneous Catalysis*. American Chemical Society: Washington, DC, 1993.
53. Chen, D.; Lødeng, R.; Anundskås, A.; Olsvik, O.; Holmen, A., Deactivation during carbon dioxide reforming of methane over Ni catalyst: microkinetic analysis. *Chemical Engineering Science* **2001,** *56* (4), 1371-1379.
54. Chen, D.; Lødeng, R.; Svendsen, H.; Holmen, A., Hierarchical Multiscale Modeling of Methane Steam Reforming Reactions. *Industrial & Engineering Chemistry Research* **2010,** *In Print.*
55. Watwe, R. M.; Bengaard, H. S.; Rostrup-Nielsen, J. R.; Dumesic, J. A.; Nørskov, J. K., Theoretical Studies of Stability and Reactivity of CHx Species on Ni(111). *Journal of Catalysis* **2000,** *189* (1), 16-30.
56. Wang, S.-G.; Cao, D.-B.; Li, Y.-W.; Wang, J.; Jiao, H., CO2 Reforming of CH4 on Ni(111): A Density Functional Theory Calculation. *The Journal of Physical Chemistry B* **2006,** *110* (20), 9976-9983.
57. Zhu, Y.-A.; Chen, D.; Zhou, X.-G.; Yuan, W.-K., DFT studies of dry reforming of methane on Ni catalyst. *Catalysis Today* **2009,** *148* (3-4), 260-267.
58. Sehested, J.; Gelten, J. A. P.; Remediakis, I. N.; Bengaard, H.; Nørskov, J. K., Sintering of nickel steam-reforming catalysts: effects of temperature and steam and hydrogen pressures. *Journal of Catalysis* **2004,** *223* (2), 432-443.
59. Trimm, D. L., Catalysts for the control of coking during steam reforming. *Catalysis Today* **1999,** *49* (1-3), 3-10.
60. Helveg, S.; Lopez-Cartes, C.; Sehested, J.; Hansen, P. L.; Clausen, B. S.; Rostrup-Nielsen, J. R.; Abild-Pedersen, F.; Norskov, J. K., Atomic-scale imaging of carbon nanofibre growth. *Nature* **2004,** *427* (6973), 426-429.
61. Abild-Pedersen, F.; Nørskov, J. K.; Rostrup-Nielsen, J. R.; Sehested, J.; Helveg, S., Mechanisms for catalytic carbon nanofiber growth studied by ab initio density functional theory calculations. *Physical Review B* **2006,** *73* (11), 115419.
62. Urasaki, K.; Sekine, Y.; Kawabe, S.; Kikuchi, E.; Matsukata, M., Catalytic activities and coking resistance of Ni/perovskites in steam reforming of methane. *Applied Catalysis A: General* **2005,** *286* (1), 23-29.

63. Alstrup, I.; Andersen, N. T., Statistical models for ensemble control by alloying and poisoning of catalysts : II. Comparisons with Monte Carlo simulations and with experimental results. *Journal of Catalysis* **1987,** *104* (2), 466-479.
64. Vang, R. T.; Honkala, K.; Dahl, S.; Vestergaard, E. K.; Schnadt, J.; Laegsgaard, E.; Clausen, B. S.; Norskov, J. K.; Besenbacher, F., Controlling the catalytic bond-breaking selectivity of Ni surfaces by step blocking. *Nat Mater* **2005,** *4* (2), 160-162.
65. Rostrup-Nielsen, J.; Nørskov, J., Step sites in syngas catalysis. *Topics in Catalysis* **2006,** *40* (1), 45-48.
66. Besenbacher, F.; Chorkendorff, I.; Clausen, B. S.; Hammer, B.; Molenbroek, A. M.; NÃ¸rskov, J. K.; Stensgaard, I., Design of a Surface Alloy Catalyst for Steam Reforming. *Science* **1998,** *279* (5358), 1913-1915.
67. Molenbroek, A. M.; Nørskov, J. K.; Clausen, B. S., Structure and Reactivity of Ni/Au Nanoparticle Catalysts. *The Journal of Physical Chemistry B* **2001,** *105* (23), 5450-5458.
68. Nikolla, E.; Holewinski, A.; Schwank, J.; Linic, S., Controlling Carbon Surface Chemistry by Alloying: Carbon Tolerant Reforming Catalyst. *Journal of the American Chemical Society* **2006,** *128* (35), 11354-11355.
69. Nikolla, E.; Schwank, J.; Linic, S., Promotion of the long-term stability of reforming Ni catalysts by surface alloying. *Journal of Catalysis* **2007,** *250* (1), 85-93.
70. Nikolla, E.; Schwank, J.; Linic, S., Comparative study of the kinetics of methane steam reforming on supported Ni and Sn/Ni alloy catalysts: The impact of the formation of Ni alloy on chemistry. *Journal of Catalysis* **2009,** *263* (2), 220-227.
71. Kratzer, P.; Hammer, B.; Norskov, J. K., A theoretical study of CH4 dissociation on pure and gold-alloyed Ni(111) surfaces. *The Journal of Chemical Physics* **1996,** *105* (13), 5595-5604.
72. Greeley, J.; Nørskov, J. K.; Mavrikakis, M., Electronic Structure and Catalysis on Metal Surfaces. *Annual Review of Physical Chemistry* **2002,** *53* (1), 319-348.
73. Kohanoff, J.; Gidopoulos, N. I., In *Handbook of Molecular Physics and Quantum Chemistry*, Wilson, S., Ed. John Wiley & Sons: Chichester, 2003; Vol. 2, Part 5, pp 532-568.
74. Hu, P.; King, D. A.; Crampin, S.; Lee, M. H.; Payne, M. C., Gradient corrections in density functional theory calculations for surfaces: Co on Pd{110}. *Chemical Physics Letters* **1994,** *230* (6), 501-506.
75. Hammer, B.; Jacobsen, K. W.; oslash; rskov, J. K., Role of nonlocal exchange correlation in activated adsorption. *Physical Review Letters* **1993,** *70* (25), 3971.
76. Hammer, B.; Hansen, L. B.; Nørskov, J. K., Improved adsorption energetics within density-functional theory using revised Perdew-Burke-Ernzerhof functionals. *Physical Review B* **1999,** *59* (11), 7413.
77. Perdew, J. P.; Burke, K.; Ernzerhof, M., Generalized Gradient Approximation Made Simple. *Physical Review Letters* **1996,** *77* (18), 3865.
78. Liu, Z.-P.; Hu, P., General Rules for Predicting Where a Catalytic Reaction Should Occur on Metal Surfaces: A Density Functional Theory Study of C-H and C-O Bond Breaking/Making on Flat, Stepped, and Kinked Metal Surfaces. *Journal of the American Chemical Society* **2003,** *125* (7), 1958-1967.
79. Bengtsson, L., Dipole correction for surface supercell calculations. *Physical Review B* **1999,** *59* (19), 12301.
80. Kresse, G.; Joubert, D., From ultrasoft pseudopotentials to the projector augmented-wave method. *Physical Review B* **1999,** *59* (3), 1758.
81. Frisch, M. J.; Trucks, G. W.; Schlegel, H. B.; Scuseria, G. E.; Robb, M. A.; Cheeseman, J. R.; Montgomery, J. A.; Vreven, T.; Kudin, K. N.; Burant, J. C.; Millam, J. M.; Iyengar, S. S.; Tomasi, J.; Barone, V.; Mennucci, B.; Cossi, M.; Scalmani, G.; Rega, N.; Petersson, G. A.; Nakatsuji, H.; Hada, M.; Ehara, M.; Toyota, K.; Fukuda, R.; Hasegawa, J.; Ishida, M.; Nakajima, T.; Honda, Y.; Kitao, O.; Nakai, H.; Klene, M.; Li, X.; Knox, J. E.; Hratchian, H. P.; Cross, J. B.; Bakken, V.; Adamo, C.; Jaramillo, J.; Gomperts, R.; Stratmann, R. E.; Yazyev, O.; Austin, A. J.; Cammi, R.; Pomelli, C.; Ochterski, J.; Ayala,

P. Y.; Morokuma, K.; Voth, G. A.; Salvador, P.; Dannenberg, J. J.; Zakrzewski, V. G.; Dapprich, S.; Daniels, A. D.; Strain, M. C.; Farkas, O.; Malick, D. K.; Rabuck, A. D.; Raghavachari, K.; Foresman, J. B.; Ortiz, J. V.; Cui, Q.; Baboul, A. G.; Clifford, S.; Cioslowski, J.; Stefanov, B. B.; Liu, G.; Liashenko, A.; Piskorz, P.; Komaromi, I.; Martin, R. L.; Fox, D. J.; Kith, T.; Al-Laham, M. A.; Peng, C. Y.; Nanayakkara, A.; Challacombe, M.; Gill, P. M. W.; Johnson, B. G.; Chen, W.; Wong, M. W.; Gonzalez, C.; Pople, J. A. *Gaussian 03*, Revision D.1; Gaussian, Inc.: Wallingford, CT, 2004.

82. Dovesi, R.; Orlando, R.; Roetti, C.; Pisani, C.; Saunders, V. R., The Periodic Hartree-Fock Method and Its Implementation in the Crystal Code. *physica status solidi (b)* **2000,** *217* (1), 63-88.

83. Dovesi, R.; Civalleri, B.; Roetti, C.; Saunders, V. R.; Orlando, R., *Ab Initio Quantum Simulation in Solid State Chemistry*. John Wiley & Sons, Inc.: 2005; p 1-125.

84. Kresse, G.; Hafner, J., Ab initio molecular dynamics of liquid metals. *Phys. Rev. B: Condens. Matter* **1993,** *47* (1), 558-61.

85. Kresse, G.; Furthmuller, J., Efficiency of ab-initio total energy calculations for metals and semiconductors using a plane-wave basis set. *Comput. Mater. Sci.* **1996,** *6* (1), 15-50.

86. Kresse, G.; Furthmueller, J., Efficient iterative schemes for ab initio total-energy calculations using a plane-wave basis set. *Phys. Rev. B: Condens. Matter* **1996,** *54* (16), 11169-11186.

87. Bahn, S. R.; Jacobsen, K. W., An object-oriented scripting interface to a legacy electronic structure code. *Computing in Science & Engineering* **2002,** *4* (3), 56-66.

88. *Dacapo*, 2.7.7. Available as open source software at http://wiki.fysik.dtu.dk/dacapo.

89. Cramer, C. J.; Truhlar, D. G., Density functional theory for transition metals and transition metal chemistry. *Physical Chemistry Chemical Physics* **2009,** *11* (46), 10757-10816.

90. Henkelman, G.; Uberuaga, B. P.; Jonsson, H., A climbing image nudged elastic band method for finding saddle points and minimum energy paths. *The Journal of Chemical Physics* **2000,** *113* (22), 9901-9904.

91. Henkelman, G.; Jonsson, H., A dimer method for finding saddle points on high dimensional potential surfaces using only first derivatives. *The Journal of Chemical Physics* **1999,** *111* (15), 7010-7022.

92. Sheppard, D.; Terrell, R.; Henkelman, G., Optimization methods for finding minimum energy paths. *The Journal of Chemical Physics* **2008,** *128* (13), 134106-10.

93. Jensen, F., *Introduction to Computational Chemistry*. 1999.

94. Hill, T. L., *An Introduction to Statistical Thermodynamics*. Addison-Wesley (1960), Dover Publications, 1986.

95. Tsai, W.; Weinberg, W. H., Steady-state decomposition of ammonia on the ruthenium(001) surface. *The Journal of Physical Chemistry* **1987,** *91* (20), 5302-5307.

96. Dumesic, J. A.; Trevino, A. A., Kinetic simulation of ammonia synthesis catalysis. *Journal of Catalysis* **1989,** *116* (1), 119-129.

97. Rasmussen, P. B.; Holmblad, P. M.; Askgaard, T.; Ovesen, C. V.; Stoltze, P.; Nørskov, J. K.; Chorkendorff, I., Methanol synthesis on Cu(100) from a binary gas mixture of CO2 and H2. *Catalysis Letters* **1994,** *26* (3), 373-381.

98. Hinrichsen, O.; Rosowski, F.; Muhler, M.; Ertl, G., The microkinetics of ammonia synthesis catalyzed by cesium-promoted supported ruthenium. *Chemical Engineering Science* **1996,** *51* (10), 1683-1690.

99. Alstrup, I., On the Kinetics of Co Methanation on Nickel Surfaces. *Journal of Catalysis* **1995,** *151* (1), 216-225.

100. Fichthorn, K.; Weinberg, W. H., Theoretical foundations of dynamical Monte Carlo simulations. *The Journal of Chemical Physics* **1991,** *95* (2), 1090-1096.

101. Dooling, D. J.; Broadbelt, L. J., Generic Monte Carlo Tool for Kinetic Modeling. *Industrial & Engineering Chemistry Research* **2000,** *40* (2), 522-529.

102. Jansen, A. P. J.; Lukkien, J. J., Dynamic Monte-Carlo simulations of reactions in heterogeneous catalysis. *Catalysis Today* **1999,** *53* (2), 259-271.

103. Reuter, K.; Frenkel, D.; Scheffler, M., The Steady State of Heterogeneous Catalysis, Studied by First-Principles Statistical Mechanics. *Physical Review Letters* **2004,** *93* (11), 116105.
104. Dooling, D. J.; Rekoske, J. E.; Broadbelt, L. J., Microkinetic Models of Catalytic Reactions on Nonuniform Surfaces: Application to Model and Real Systemsâ€ *Langmuir* **1999,** *15* (18), 5846-5856.
105. Dooling, D. J.; Broadbelt, L. J., Microkinetic models and dynamic Monte Carlo simulations of nonuniform catalytic systems. *AIChE Journal* **2001,** *47* (5), 1193-1202.
106. Laidler, K., *Chemical Kinetics.* 1987.
107. Steinfeld, J. I.; Francisco, J. S.; Hase, W. L., *Chemical Kinetics and Dynamics.* 2nd ed.; Prentice Hall: Upper Saddle River, New Jersey, 1998.
108. Pelzer, H.; Wigner, E., The speed constants of exchange reactions. *Zeitschrift für Physikalische Chemie* **1932,** *15*, 445.
109. Wigner, E., On the penetration of potential barriers in chemical reactions. *Zeitschrift für Physikalische Chemie* **1932,** *15*, 203.
110. Eyring, H., The activated complex and the absolute rate of chemical reactions. *J. Chem. Phys.* **1935,** *3*, 107.
111. Evans, M. G.; Polanyi, M., Some applications of the transition state method to the calculation of reaction velocities, especially in solution. *Trans. Faraday Soc.* **1935,** *31*, 875.
112. Roma, F.; Ramirez-Pastor, A. J.; Riccardo, J. L., Configurational entropy for adsorbed linear species (k-mers). *The Journal of Chemical Physics* **2001,** *114* (24), 10932-10937.
113. Cwiklik, L., Influence of surface diffusion on catalytic reactivity of spatially inhomogeneous surfaces - mean-field modeling. *Chemical Physics Letters* **2007,** *449* (4-6), 304-308.
114. Levenspiel, O., *Chemical Reaction Engineering.* 3rd ed.; John Wiley & Sons: New York, New York, 1999.
115. Deen, W. M., *Analysis of Transport Phenomena.* 1st ed.; Oxford University Press: New York, New York, 1998.
116. Yang, Q. Y.; Maynard, K. J.; Johnson, A. D.; Ceyer, S. T., The structure and chemistry of CH3 and CH radicals adsorbed on Ni(111). *The Journal of Chemical Physics* **1995,** *102* (19), 7734-7749.
117. Xu, J.; Saeys, M., Improving the coking resistance of Ni-based catalysts by promotion with subsurface boron. *Journal of Catalysis* **2006,** *242* (1), 217-226.
118. Kalibaeva, G.; Vuilleumier, R.; Meloni, S.; Alavi, A.; Ciccotti, G.; Rosei, R., Ab Initio Simulation of Carbon Clustering on an Ni(111) Surface: A Model of the Poisoning of Nickel-Based Catalysts. *The Journal of Physical Chemistry B* **2006,** *110* (8), 3638-3646.
119. Vanderbilt, D., Soft self-consistent pseudopotentials in a generalized eigenvalue formalism. *Physical Review B* **1990,** *41* (11), 7892.
120. Introduced by Rusic, B. P., R.E.; Morton, M.L.; von Laszevski, G.; Bittner, S.J.; Nijsure, S.G.; Amin, K.A.; Minkoff, M.; Wagner, A.F. *J. Phys. Chem. A.* **2004,** *108*, 9979-9997. More information can be found at the ATcT wiki, http://wiki.cogkit.org/index.php/Active_Thermochemical_Tables.
121. Lapujoulade, J.; Neil, K. S., Chemisorption of Hydrogen on the (111) Plane of Nickel. *The Journal of Chemical Physics* **1972,** *57* (8), 3535-3545.
122. Stuckless, J. T.; Wartnaby, C. E.; Al-Sarraf, N.; Dixon-Warren, S. J. B.; Kovar, M.; King, D. A., Oxygen chemisorption and oxide film growth on Ni{100}, {110}, and {111}: Sticking probabilities and microcalorimetric adsorption heats. *The Journal of Chemical Physics* **1997,** *106* (5), 2012-2030.
123. Stuckless, J. T.; Al-Sarraf, N.; Wartnaby, C.; King, D. A., Calorimetric heats of adsorption for CO on nickel single crystal surfaces. *The Journal of Chemical Physics* **1993,** *99* (3), 2202-2212.
124. Inderwildi, O. R.; Jenkins, S. J.; King, D. A., An Unexpected Pathway for the Catalytic Oxidation of Methylidyne on Rh{111} as a Route to Syngas. *Journal of the American Chemical Society* **2007,** *129* (6), 1751-1759.
125. Inderwildi, O.; Jenkins, S.; King, D., Mechanistic Studies of Hydrocarbon Combustion and Synthesis on Noble Metals. *Angewandte Chemie International Edition* **2008,** *47* (28), 5253-5255.
126. Christmann, K.; Schober, O.; Ertl, G.; Neumann, M., Adsorption of hydrogen on nickel single crystal surfaces. *The Journal of Chemical Physics* **1974,** *60* (11), 4528-4540.

127. Lapujoulade, J.; Neil, K. S., Hydrogen adsorption on Ni (100). *Surface Science* **1973,** *35*, 288-301.
128. Klink, C.; Olesen, L.; Besenbacher, F.; Stensgaard, I.; Laegsgaard, E.; Lang, N. D., Interaction of C with Ni(100): Atom-resolved studies of the ``clock" reconstruction. *Physical Review Letters* **1993,** *71* (26), 4350.
129. Blöchl, P. E., Projector augmented-wave method. *Physical Review B* **1994,** *50* (24), 17953.
130. Henkelman, G., *http://theory.cm.utexas.edu/vtsttools/dynmat/*
131. Li, H.; Zhao, M.; Jiang, Q., Cohesive Energy of Clusters Referenced by Wulff Construction. *The Journal of Physical Chemistry C* **2009,** *113* (18), 7594-7597.
132. Greeley, J.; Rossmeisl, J.; Hellmann, A.; Nørskov, J. K., Theoretical Trends in Particle Size Effects for the Oxygen Reduction Reaction. *Zeitschrift für Physikalische Chemie* **2007,** *221* (9-10), 1209-1220.
133. Jiang, Q.; Lu, H. M.; Zhao, M., Modelling of surface energies of elemental crystals. *J. Phys.: Condens. Matter* **2004,** *16* (4), 521-530.
134. Jiang, T.; Mowbray, D. J.; Dobrin, S.; Falsig, H.; HvolbÃ¦k, B.; Bligaard, T.; NÃ¸rskov, J. K., Trends in CO Oxidation Rates for Metal Nanoparticles and Close-Packed, Stepped, and Kinked Surfaces. *The Journal of Physical Chemistry C* **2009,** *113* (24), 10548-10553.
135. Jakobsen, J. G.; Joergensen, T. L.; Chorkendorff, I.; Sehested, J., Steam and CO2 reforming of methane over a Ru/ZrO2 catalyst. *Appl. Catal., A* **2010,** *377* (1-2), 158-166.
136. Greeley, J.; Mavrikakis, M., Alloy catalysts designed from first principles. *Nat Mater* **2004,** *3* (11), 810-815.
137. Groß, A., Reactivity of Bimetallic Systems Studied from First Principles. *Topics in Catalysis* **2006,** *37* (1), 29-39.
138. Nikolla, E.; Schwank, J. W.; Linic, S., Hydrocarbon steam reforming on Ni alloys at solid oxide fuel cell operating conditions. *Catalysis Today* **2008,** *136* (3-4), 243-248.
139. Huang, T.-J.; Jhao, S.-Y., Ni-Cu/samaria-doped ceria catalysts for steam reforming of methane in the presence of carbon dioxide. *Applied Catalysis A: General* **2006,** *302* (2), 325-332.
140. Ruban, A. V.; Skriver, H. L.; Nørskov, J. K., Surface segregation energies in transition-metal alloys. *Physical Review B* **1999,** *59* (24), 15990.
141. Personal communication from De Chen, Norwegian University of Science and Technology. Manuscript in preparation.
142. Burcat, A. http://garfield.chem.elte.hu/Burcat/burcat.html.
143. Sperle, T.; Chen, D.; Lødeng, R.; Holmen, A., Pre-reforming of natural gas on a Ni catalyst: Criteria for carbon free operation. *Applied Catalysis A: General* **2005,** *282* (1-2), 195-204.
144. Boukhvalov, D. W.; Katsnelson, M. I., Chemical functionalization of graphene. *Journal of Physics: Condensed Matter* **2009,** *21* (34), 344205.